N°d'ordre : 2924

THÈSE

présentée à

L'UNIVERSITÉ BORDEAUX I

ÉCOLE DOCTORALE DES SCIENCES PHYSIQUES ET DE L'INGÉNIEUR

par Pierre Lubin

POUR OBTENIR LE GRADE DE

DOCTEUR

SPÉCIALITÉ : MÉCANIQUE

****

Simulation des Grandes Échelles du déferlement plongeant des vagues
Large Eddy Simulation of plunging breaking waves

****

Soutenue le : 18 décembre 2004

Après avis de :

MM.	Stéphan T. Grilli	Professeur, University of Rhode Island	**Rapporteurs**
	Pierre Sagaut	Professeur, Université Paris 6	

Devant la commission d'examen formée de :

MM.	Pierre Fabrie	Professeur, Université Bordeaux 1	**Président**
	Stéphane Vincent	Maître de Conférences, ENSCPB	**Rapporteur**
	Pierre Sagaut	Professeur, Université Paris 6	**Examinateurs**
	Stéphan T. Grillit	Professeur, University of Rhode Island	
	Jean-Paul Caltagirone	Professeur, Université Bordeaux 1	
	Stéphane Abadie	Maître de Conférences, Université de Pau	

- 2004 -

Remerciements

Le travail présenté dans ce mémoire a été effectué au sein de l'Unité Mixte de Recherche Interétablissements Transferts Écoulements Fluides Énergétique (TREFLE UMR CNRS 8508), anciennement laboratoire de Modélisation Avancée des Systèmes Thermiques et des Écoulements Réels de l'École Nationale Supérieure de Chimie et de Physique de Bordeaux (MASTER - ENSCPB), en collaboration avec le Laboratoire des Sciences Appliquées au Génie Civil de l'Université de Pau et des Pays de l'Adour (LaSAGeC - UPPA), situé à Anglet.

En tout premier lieu, je tiens à exprimer ma sincère et profonde reconnaissance au professeur Jean-Paul Caltagirone, ancien directeur du laboratoire MASTER et directeur de thèse, pour la confiance qu'il m'a accordée et pour son soutien sans faille durant ces années de thèse. Je remercie tout aussi sincèrement Stéphane Abadie, co-directeur de cette thèse, sans qui je n'aurais pas été là. J'ai apprécié la liberté et l'indépendance que vous m'avez laissées.

Je tiens à exprimer toute ma gratitude envers les professeurs Stéphan Grilli et Pierre Sagaut de m'avoir fait l'honneur d'accepter d'être rapporteurs de cette thèse. Leurs commentaires et l'attention qu'ils ont portés à mon travail m'ont beaucoup touché. J'espère sincèrement que tout ce travail débouchera sur des collaborations très fructueuses.

J'adresse mes remerciements au professeur Pierre Fabrie pour m'avoir fait l'honneur et le plaisir de présider mon jury. Je tiens à exprimer toute ma gratitude envers Stéphane Vincent pour avoir accepté de juger ce travail et de participer à cette commission. Sans ta collaboration, cette thèse n'aurait pas été la même.

Je souhaite vivement remercier les différentes personnes avec lesquelles j'ai pu collaborer pendant ma thèse, au LMM de l'Université Paris VI (merci Pierre Sagaut pour le coup de main sur le canal), au CEA et au LEGI de Grenoble (gros merci à Hervé, Philippe, aux Pr. Éric Barthélémy et André Temperville pour leurs conseils et leur gentillesse !), au LaSAGeC d'Anglet (Phillipe et la clique de thésards en bâteaux !), au LSEET à Toulon (courage Déb !), à l'IMFT de Toulouse (Marie et ses Dominiques !), à l'ENS Cachan

(Frédéric Dias et Christophe, bordelais dorénavant !), à l'IRPHE et à l'ESIM de Marseille (merci pour votre gentillesse et votre disponibilité, Hubert et Olivier !), à Rhode Island (Stéphan et Richard, pour votre patience et votre disponibilité !), au DGO de Bordeaux (Philippe Bonneton, merci d'avoir transmis ma candidature à Stéphane Abadie, et Dr. Castellus, la bise aux Aussies), le LMF ce Centrale Nantes (Alain Clément, Bertrand Alessandrini, Lionel Gentaz et Pierre Ferrant qui m'ont donné le goût de la recherche, et le Joss toujours aussi motivé !).

J'exprime mes plus vifs remerciements aux professeurs Jean-Rodolphe Puiggali, directeur du laboratoire TREFLE, et Éric Arquis, ancien directeur du MASTER et directeur du site TREFLE - ENSCPB, pour leur soutien.

Je remercie également tous les membres du laboratoire qui ont su me supporter durant ces années. Stéphane Glockner, membre de la caste du petit personnel en tant que technicien, qui me gonfle avec son jazz, ses photos et l'Italie. J'espère quand même qu'on pourra peut-être un jour bosser ensemble ! Sincèrement, merci pour ton aide et ton soutien. Jean Toutain, pour tous ces bons moments partagés autour de ripailles, de matchs de rugby ou de soirées de jeux. Tu peux me redire ce qu'est une forme sesquilinéaire ? Le Jeannot, Maître de Stratégie en tous genres au Colon de Catane, même les pires... Deux heures pour finalement construire une route, est-ce bien raisonnable ? Marie-Paule, il paraît que tu sais faire des gâteaux ? Moi, je ne me souviens pas en avoir goûté... David, le seul et unique expérimentateur du labo. Avec le numérique, on inonde pas les couloirs du labo, nous... Stéphane Vincent, à la garde-robe aussi colorée que la mienne... Tu devrais demander des bras à Shiva pour faire tout ce que tu voudrais réaliser en recherche... À quand une publi sur les blagues capilotractées à deux balles ? Le pire c'est que ça me fait rire... Mejdi (Wednesday Night Fever), arrivé en cours de route. Bonne chance pour diriger cette joyeuse bande d'individus ! Mohammed, merci pour ton humour, ta bonne humeur et tes cours de rédaction en anglais ! À Guy, Nicolas et Serge du deuxième étage. Aziz, au sourire aussi large que celui de la Joconde, qui continue à venir picoler notre café... Un petit mot spécial pour l'équipe qui gère l'informatique, Bernard, Sandrine et Alain : pour les trois cent soixante jours de l'année où le réseau informatique fonctionne sans problème, merci ! Quant aux cinq jours qui restent, je vous hais !!!!

À la cohorte de thésards que j'ai cotoyé pendant ces années de thèse, je voudrais leur faire part de toute mon affection pour leur présence et les moments qu'on a pu partager. J'ai une pensée sincère envers la bande de surfeurs qu'on a composée et qui a splitté, chacun vers des horizons bien différents : Dr. K, qui ne taxe jamais une vague sauf celles sur lesquelles je pars, me pardonneras-tu pour ma magnifique traîtrise au Risk ?

Dr. Wood, bobo le chameau, merci pour les plans charniers en guise de réveille-matin (Qu'est-ce qui nous arrive ?...). Dessine-moi la mouche ravashyolle... Spéciale dédicace pour mon collègue de bureau, Dr. Sous, qui a supporté, au-delà de l'imaginable, mes goûts musicaux ravageurs pendant trois ans (voir bande originale ci-après). Maintenant, à cause de toi, j'écoute presque du reggae ! Merci pour tous les bons moments, les bonnes bouffes et le pogo au concert de FFF... Mr. Squale, créateur de Chômedu Productions, que j'espère très vite revoir pour faire parti du casting de la prochaine réalisation. Pour les sessions "engagements", les sessions à -10 degrés, les sessions magiques de l'automne 2001, les sessions de la Jenny avec les bétounes, les repas et les soirées détente-loisir... Cette page de ma vie restera longtemps dans ma mémoire. Vous me manquez, les gars...

Le Glôde, Cal de base et poisson rouge. T'as une tête de singe et t'as jamais vu la jungle ? Mais tu vas y retourner dans ta jungle, t'inquiète pas ! Et avec tes bibilles... Le Dric, maintenant Maître de Conférences (tout juste un mètre), le plus dur est derrière toi... Jamais vu quelqu'un qui aime autant jouer aux petits indiens... Fais attention à pas finir à poil dans la rue... Guiguit, futur Prix Nobel que tout le monde ignore ! Tu pourras toujours reviewé les blagues pour Carambar, Télé Z ou les articles sur les blagues à deux balles du Sieur Vincent... Sinon, à part le ping-pong, tu fais du sport ? Grégoire, pulvérisateur de café sur bureaux. Sinon, Amsterdam, c'est bien ? Stéphanie, qui aime les histoires d'eaux... Sans jeu de mots, Guiguit... Nirina, garde ton sourire et ta gentillesse, c'est rare un mec comme toi. Le Dric dit que tu es trop parfait et donc on te hait tous ! Nico, qui a supporté la collocation avec un roux dans son bureau pendant toute sa thèse ! Respect, mon gars ! Christophe, le roux en question, qui a supporté un gros barbu dans son bureau pendant toute sa thèse. Pépette, rousse aussi (no comment), qui a expérimenté le côté hard et douloureux de la thèse. Accroche-toi, c'est bientôt fini ! Cyril et Éric, broyeurs de mains à tout va... Delphine (de rien pour la LES), aux couleurs chamarées, qui a supporté nos commentaires sur ses tenues. Faut avouer, quand même, y'a pas idée... La bise à Matthieu "deux t, un h" ! Sylvain, qui pense comme un ingénieur, qui bosse comme un ingénieur, et dire que c'est l'élite de la France... Hamza, mon nouveau collègue de bureau qui me menace tous les jours de me traîner devant les tribunaux pour diffamations, mais faut avouer que t'as quand même de bien belles chevilles... Si tu continues à être sérieux comme ça, demande à Damien comment ça va se passer au niveau ambiance sonore... Étienne, bon basque de base au nom imprononçable, qui ne sort jamais de son bled qui est même pas sur la carte ! Hadji (pour l'accueil que tu m'as fait un certain jour dans ton bureau, ou souviens-toi les Journées Portes Ouvertes de Saint-Émilion...) et Fréd pour leur amitié sincère. En espérant que nos routes vont continuer à se croiser. La bise à Patricia, Sarah, Jihane, Thania, Maman Hadji, Mina et kiki !!! À tous ceux qui ont fréquenté l'appart' de la rue Saint-Genès, Juan, Tarzan, Le Brâle, Émilie, Guitoune,

Lolo, Papy, Wendy, Arnaud, etc. ! À Sylvain et Psylaw, pour tous les concerts ! À Nicolas Garcia qui m'a fait l'immense plaisir de venir d'Espagne pour assister à ma soutenance. Aux anciens thésards, Hugues et Jérôme qui nous ont montré l'exemple... À mes amis de Bruxelles, Marie-Noëlle, Liz et les rugbymen and women du BBRFC !

À mes parents, mes grands-parents, mon frère François et Florence, à qui je pense tous les jours et que j'aime profondément, pour les sacrifices qu'ils ont faits pour moi, sans lesquels je serais dans la Légion Étrangère !!! À ma famille, à qui j'aimerais pouvoir consacrer plus de temps. À ceux qui sont partis, qui me manquent, je dédie toutes mes pensées les plus sincères.

À ceux que je considère comme ma famille. Zazouille, ma grande sœur, Nono, Clara, notre filleule, et sa sœur Lexane qui vient de naître. Stéphane, mon frère, et Pascale, mes bons ténardiers... Mick et Gwen, Patrick et Natacha, Manpower et Fabienne, Gégé et Nath, Patoche... et leurs enfants Lia, Noé et Léna, et ceux qui arrivent...

À ma future belle-famille, à Élise (et sa coiffure) et Ahmed, à Tatie et Jean-Luc, à la nièce Sandrine, pour votre accueil et votre immense gentillesse. Pourtant, c'était pas gagné avec ma tête... Grâce à vous, je parle créole, et pas que du châtié...

Martiane, tu vas bientôt me dire "oui". J'ai pas l'intention de me calmer ou de faire moins de bruit, alors accroche-toi ! Je t'aime. C'est vrai que les opposés s'attirent. Je suis très fier de toi. À Pierrick et Hervelyne...

Des hectolitres de café ont été nécessaires pour arriver au bout de cette thèse, 8000 kms au compteur de mon vélo et 100 kilos sur la balance...

TAZ !
R.A.W.

P.S. : non, je ne suis pas impulsif... un peu Rock'n Roll...

Bande originale de la thèse : Psylaw, Lofofora, Rage Against The Machine, Fishbone, Downset., Refused, Rollins Band, L.U.N.G.S., Jr Ewing, Jimi Hendrix, Funkadelics, Poison The Well, Madball, Manhole, Minor Threat, Mr Bungle, Faith No More, Pearl Jam, Prong, NOFX, Mudvayne, Pantera, System Of A Down, 24-7 Spyz, Thumpasauras, The Workhorse Movement, Tool, Sick Of It All, Snot, Supergrass, Vision Of Disorder, Biohazard, Black Bomb A, Deftones, FFF, Houston Swing Engine, Helmet, etc.

Contents

Remerciements

Introduction Générale **1**

1 Literature review **7**

1.1 General flow representation 8

1.1.1 Breaker types classification 9

1.1.2 Plunging breaking waves 9

1.2 Large-scale vortices and turbulence generation 14

1.2.1 Experimental observations 14

1.2.2 Numerical studies 19

1.3 Scope of the present work 25

2 Methodology of the numerical tool: Aquilon **29**

2.1 Mathematical formulation of the problem 30

2.2 Numerical modelling 30

2.2.1 Boundary conditions treatment 30

2.2.2 Solid obstacles 31

2.2.3 Temporal discretization 32

2.2.4 Velocity-pressure uncoupling 33

2.2.5 Spatial discretization 34

2.2.6 Numerical resolution of the linear system 36

2.3 Numerical methods for the description of free surface flows 36

2.3.1 Interface tracking 36

2.3.2 Interface capturing 37

2.3.3 Calculation of the two-phase flow characteristics 40

2.4 Governing equations system for two-phase flows 41

2.5 Validation: two-dimensional two-phase Poiseuille flow 42

3 Large Eddy Simulation - LES **47**
3.1 Position of the problem . . . 48
3.2 Formulation of the one-phase model . . . 49
3.2.1 The filtering operation . . . 49
3.2.2 Classical filtered one-phase Navier-Stokes equations . . . 50
3.2.3 Physical subgrid-scale models . . . 51
3.2.4 Improvement of subgrid-scale models . . . 54
3.2.5 Explicit discrete filtering . . . 58
3.3 Simulation of the turbulent three-dimensional incompressible plane channel flow . . . 59
3.3.1 Computational domain and grid spacing . . . 59
3.3.2 Definitions . . . 60
3.3.3 Initial conditions and flow characteristics . . . 61
3.3.4 Boundary conditions . . . 63
3.3.5 Turbulent structures . . . 63
3.3.6 Results . . . 65
3.3.7 Conclusion . . . 70
3.4 Extension to the two-phase model . . . 71
3.4.1 Mathematical formulation for a filtered multi-fluid model . . . 71
3.4.2 Simpler one-fluid model for LES . . . 81

4 Validation and exploitation of the numerical model **85**
4.1 Breaking of a dam on a wet bottom . . . 86
4.1.1 The physical model . . . 86
4.1.2 Comparisons between numerical and experimental results . . . 87
4.1.3 Conclusions and perspectives . . . 88
4.2 A solitary wave propagating in a constant water depth . . . 88
4.2.1 Comparisons between numerical and analytical results . . . 89
4.2.2 Conclusions and perspectives . . . 92
4.3 Interactions between solitary waves . . . 92
4.3.1 Solitary waves colliding a vertical end-wall . . . 93
4.3.2 Head-on collisions between two solitary waves . . . 95
4.3.3 Conclusions and perspectives . . . 101
4.4 Solitary wave propagating over a submerged obstacle . . . 102
4.4.1 Comparisons with experimental results . . . 103
4.4.2 Conclusions and perspectives . . . 109
4.5 Solitary wave propagating and breaking over a submerged obstacle . . . 110

4.5.1 Comparisons with experimental results . . . 111
4.5.2 Conclusions and perspectives . . . 123
4.6 Solitary wave shoaling and breaking over a sloping beach . . . 125
4.6.1 Comparisons with numerical results . . . 125
4.6.2 Comparisons with experimental results . . . 133
4.6.3 Conclusions and perspectives . . . 139

5 Application to plunging breaking waves over a flat bottom 147
5.1 Two-dimensional plunging wave breaking simulations . . . 148
5.1.1 Initial conditions of the case study . . . 148
5.1.2 Overturning motion and general flow description . . . 152
5.1.3 Splash-up phenomenon . . . 157
5.1.4 Vortices occurrence . . . 164
5.1.5 Energy dissipation . . . 166
5.1.6 Conclusions and perspectives . . . 182
5.2 Three-dimensional plunging wave breaking simulations . . . 182
5.2.1 Preliminary considerations of the case study . . . 182
5.2.2 Free surface and vortex analysis . . . 185
5.2.3 Energy dissipation . . . 202

Conclusions et persepctives 207

A The adaptative augmented Lagrangian method 213
A.1 Introduction . . . 213
A.2 Uzawa algorithms for predictor velocity fields . . . 217
A.2.1 Standard augmented Lagrangian (SAL) . . . 218
A.2.2 Adaptative augmented Lagrangian (AAL) . . . 219
A.2.3 Numerical solver . . . 221
A.3 Simulation of three-dimensional multi-material flows . . . 221
A.3.1 The 2D Laplace law . . . 222
A.3.2 Flow induced by a spherical particle . . . 223
A.3.3 Wave breaking in shallow water . . . 224
A.4 Conclusions . . . 226
A.5 Acknowledgements . . . 226
A.6 Tables and figures . . . 227

B Analytical solution of the two-phase Poiseuille flow 235

C Solitary waves theories **239**

C.1 Description of the various theories 239

C.1.1 Boussinesq's solution - 1^{st} order 240

C.1.2 Grimshaw's solution - 3^{rd} order 241

C.1.3 Tanaka's exact solution 242

C.2 Comparison between the various theories 244

Bibliographie **255**

Introduction Générale

Le déferlement des vagues est un phénomène naturel fascinant et très spectaculaire qui joue un rôle de première importance dans les processus côtiers. Il est en effet à l'origine de courants très intenses et responsable de la majeur partie du transport sédimentaire dans cette zone par la mise en suspension de celui-ci. Les ouvrages côtiers sont en outre régulièrement soumis à des impacts, très violents et répétés, infligés par les brisants et le déferlement des vagues. L'état de la mer est la première chose que l'on voit de l'océan. Ce sont aussi les phénomènes qui nous rappelle que la nature a toujours le dernier mot. Aucune activité en mer ne peut ignorer les vagues.

Or, bien que largement étudié depuis une vingtaine d'années, le déferlement est un phénomène qui reste encore très difficile à appréhender.

La France métropolitaine possède environ 5 500 km de linéaire de côtes, et les DOM-TOM en possèdent près de 2 000 km, répartis comme suit :

- 1 948 km de plages (35 %)
- 1 316 km de marais et vasières (24 %)
- 1 548 km de côtes rocheuses découpées (28 %)
- 721 km de falaises (13 %)

L'environnement littoral est soumis à de très fortes pressions dues à la densité de population présente dans, ou à proximité de cette zone. 5 270 000 habitants occupent en permanence cet ensemble littoral, ce qui représente 10 % de la population sur 3 % du territoire, la population pouvant doubler, voire quadrupler ou décupler en période estivale. 35 % de la population se trouve dans 5 des grandes villes (Marseille, Nice, Le Havre, Toulon, Brest), 25 % dans 35 villes de 20 000 à 100 000 habitants et moins de 8 % habite dans des communes de 2 000 habitants. L'occupation du littoral est donc très importante, à savoir que 51 % du linéaire ctier est urbanisé dont 960 km de façon dense.

Cette forte densité de population implique inévitablement un impact non négligeable et de nombreuses dégradations mettant en péril le fragile équilibre de l'ensemble du système côtier.

On identifie une très forte activité économique dépendante non seulement de l'état des ressources vivantes (oiseaux, poissons, crustacés, coquillages, algues, etc.), mais aussi de l'état du linéaire côtier. En effet, de nombreuses plages doivent êre protégées ou réalimentées en sable pour satisfaire la population estivale et des ouvrages, tel que les digues, impliquent des modifications plus ou moins importantes du paysage côtier en terme d'esthétique. Ces interventions humaines sont cependant à double tranchant, à moyen comme à long terme, puisque la présence de ces structures artificielles va modifier à nouveau l'équilibre du système hydrodynamique, générant à nouveau des phénomènes d'érosion ou d'accrétion en déplaçant le problème dans le temps et dans l'espace.

Or, environ 850 km du littoral reculent de plus de 1 mètre par an (Fig. 1). Par exemple, on a pu relever une érosion de la Côte des Landes de 1 à 3 mètres par an. Outre l'élévation lente du niveau de la mer ou l'exploitation des matériaux meubles des dunes et des plages destinés à la voirie et à la construction, l'érosion du trait de côte est très fortement influencée par les activités humaines et l'action de la houle.

Le déferlement des vagues est donc un phénomène crucial à étudier à la vue de ces implications et conséquences sur notre environnement.

Plusieurs types d'approches peuvent être employés afin d'appréhender l'étude du déferlement des vagues.

L'étude analytique est limitée du fait de la complexité du phénomène et de la nécessité de faire un grand nombre d'approximations pour rendre le problème accessible. Cette partie a donc fait l'objet d'importantes avancées pour souligner les principales caractéristiques du déferlement plongeant, mais reste impossible à mettre en oeœuvre d'un point de vue pratique pour permettre une quelconque description du problème dans son intégralité.

L'étude expérimentale a été source d'un très grand nombre d'étude qui ont permis de visualiser et de mesurer la majeur partie des processus mis en jeu lors du déferlement des vagues. Les observations réalisées ont fait avancer la compréhension de la physique de l'écoulement et ses conséquences sur la zone littorale, en terme de courants induits, de mise en suspension du sédiment et des phénomènes d'érosion ou d'accrétion qui en découlent. Cependant, les mesures expérimentales restent très chères à réaliser du fait des coûts d'infrastructures et de matériels de mesures et d'acquisition. La complexité de l'écoulement rend délicates les observations : en effet, le caractère fortement tridimensionnel des processus physiques reste difficilement accessible et la qualité des mesures dépend

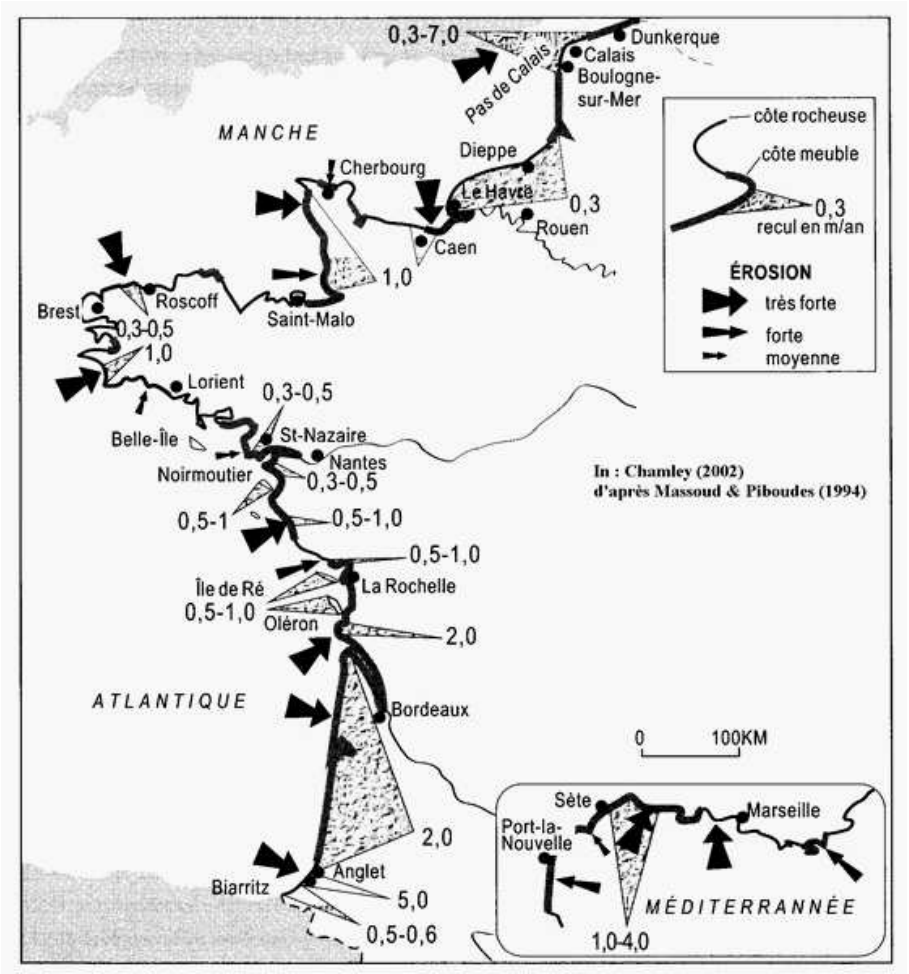

Figure 1: Représentation graphique de l'état d'érosion sus les côtes de France métropolitaine.

donc de la technique employée pour la visualisation. De plus, les campagnes de mesure *in situ* sont très ardues à mener pour des raisons évidentes de logistique et de matériel.

L'approche que nous avons donc choisi d'explorer est celle de la simulation numérique, et plus précisément de la Simulation numérique des Grandes Échelles (SGE - Large Eddy Simulation, LES). En effet, les récents progrès informatiques permettent d'envisager la simulation d'écoulements de plus en plus complexes, dans des échelles de temps et d'espace de plus en plus grands, avec une précision grandissante. Les algorithmes de résolution sont de plus en plus rapides pour une précision accrue. Or la description de la surface libre, le caractère tridimensionnel, diphasique et turbulent de l'écoulement résultant du déferlement, nécessitent des méthodes et des schémas numériques évolués et robustes. La simulation numérique est un moyen relativement accessible pour disposer d'une description très détaillé et complète de l'écoulement, en terme de champs de pression, de vitesse, etc.

L'objectif de cette thèse est, d'une part, d'implémenter et de valider la méthode de Simulation des Grandes Échelles au sein du code numérique Aquilon, et, d'autre part, d'appliquer cet outil à l'étude du déferlement plongeant des vagues. Ce type de déferlement a été choisi pour son aptitude à piéger et entraîner au fond une très grande quantité d'air. Il s'agit donc à la fois d'un cas physique trés intéressant à étudier, comme un grand défi pour décrire ce phénomène d'entraînement de l'air dans l'eau numériquement. L'intérêt est aussi esthétique, puisque le déferlement plongeant offre aux yeux des comportements trés spéctaculaires, tel que ces hautes gerbes de mousses, composées d'air et d'eau, créées par ces impressionnantes lèvres projetées lors du retournement de la vague.

Ainsi, ce travail de simulation numérique est donc à la portée d'un outil tel que celui qui est développé au laboratoire TREFLE-ENSCPB (anciennement MASTER-ENSCPB), basé sur la résolution des équations de Navier-Stokes en volumes finis.

Le document se présente en plusieurs parties.

Le premier chapitre va permettre de bien définir le problème, le situer dans le paysage de la recherche des vingt dernières années et d'évaluer les besoins en terme de questionnements et des besoins associés en terme de simulation numérique.

Le second chapitre va présenter l'outil de simulation Aquilon, ainsi que les méthodes et schémas numériques déjà disponibles. De plus, des avancées seront détaillées et validées. Un cas simple de validation consistant dans l'étude de l'écoulement bidimensionnel de Poiseuille diphasique entre deux plans parallèles illustrera le traitement des équations de Navier-Stokes dans leur formulation diphasique.

La méthode de la Simulation des Grandes Échelles sera introduite et définit dans le troisième chapitre. L'implémentation dans Aquilon est l'un des objectifs de cette thèse. Les modèles codés dans l'outil de simulation sont présentés et validés grâce au cas d'étude de l'écoulement incompressible turbulent dans un canal plan infini. Une étude analytique du filtrage des équations de Navier-Stokes en formulation diphasique est pour la première fois détaillée, afin de fournir une vision de la complexité de la méthode, pour l'instant trés largement simplifiée dans son application. Cette étude est actuellement en soumission dans sa version la plus aboutie (Labourasse et al., 2004).

Le quatrième chapitre va présenter de façon très détaillée les différents cas d'étude bi- et tridimensionnels qui serviront tout à la fois de cas de validation comme de cas d'études approfondies. Seront, entre autres, développés les cas de rupture de barrage sur fond mouillé, la propagation d'ondes solitaires, les interactions ondes/parois et ondes/ondes, ainsi que le déferlement d'ondes solitaires sur récifs immergés et plages inclinées. Des comparaisons avec des résultats numériques et expérimentaux permettront d'évaluer la validité et la précision de nos méthodes et de nos schémas numériques.

Le cinquième chapitre va concerner plus précisément le déferlement plongeant des vagues. Le déferlement d'ondes sinusoïdales de grandes amplitudes en domaines périodiques sera détaillé en deux, puis en trois dimensions, cette méthode s'étant déjà avérée très efficace pour la modélisation du problème nous concernant. Une description très précise de l'écoulement global sera fournie, en terme de retournement de l'onde et d'impact du jet plongeant. Une grande attention sera donnée quant au splash-up résultant et à la génération de grandes structures turbulentes. Une étude précise de la dissipation énergétique survenant lors du déferlement sera menée, confirmant l'importance du processus de l'entraînement de l'air dans l'eau. La partie préliminaire de cette partie a fait l'objet d'une publication, pour ce qui est de l'étude en trois dimensions (Lubin et al., 2003a).

Un conclusion clôturera cette travail. Des perspectives seront développés quant aux progrès et améliorations qui peuvent être amenés à cette travailétude, ainsi qu'aux travaux envisagés dans la continuité de cette thèse.

L'annexe A présentera de façon détaillée l'amélioration qui a été apportée à la méthode de résolution des équations de Navier-Stokes dans Aquilon et dont cette thèse a servi à la mise en lumière de la nécessité de cette avancée et à la validation. Ce travail a fait l'objet d'une publication (Vincent et al., 2004).

L'annexe B donne les détails de la solution analytique de l'écoulement bidimensionnel de Poiseuille diphasique entre deux plans parallèles, utilisée dans le deuxième chapitre.

L'annexe C présente de façon très détaillée les solutions analytiques, utilisées dans le quatrième chapitre, pour l'étude des ondes solitaires.

Chapter 1

Literature review

Introduction

Numerous problems motivated by fundamental research and applications from environmental and coastal engineering sciences require accurate description of wave breaking. A great effort of research is still leaded concerning wave transformation across the nearshore zone, risk assessments in terms of coastal and ocean structures resistance against periodical waves or tsunamis breaking and effects of turbulence in broken waves on sediment transport.

The general knowledge and understanding of turbulence generated by breaking waves have greatly been improved in the last two decades. Nevertheless, a lot of work still has to be done in many directions, where some aspects suffer from a lack of efficiency or remaining limitations. The surf zone is the place where highly complex hydrodynamics occur.

In the present chapter, the recent advances made in the field of modelling and simulation of the wave breaking phenomena have been reviewed. Areas requiring further research work have been identified. Motivations of the present study are summarized. We will detail the review concerning:

- the general flow description
- the overturning motion and plunging jet formation
- the large-scale structures generated during the breaking process and their influence on the sediment transport.

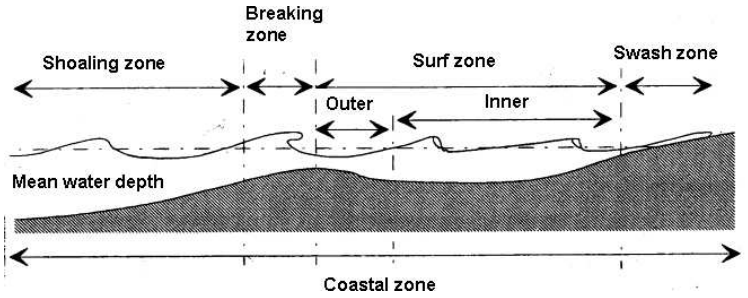

Figure 1.1: Sketch of the nearshore region (Abadie, 1998).

1.1 General flow representation

A schematic diagram of the flow structure in the nearshore region is shown in figure (1.1). The coastal zone is divided into four separate zones. Namely, the shoaling zone, the breaking zone, the surf zone and the swash zone.

In the shoaling zone, as the waves approach to the coastline, they start to deform. The wave height increases with the decrease of the wave celerity.

In the breaking zone, the incoming wave becomes unstable and starts breaking.

The surf zone is divided in two separate areas: the outer and inner regions. The outer surf zone starts at the breaking point. The flow is violently perturbed, highly unstationary and turbulence is spreading in the whole water column, from the free surface to the bottom. The inner surf zone starts when the flow becomes quasi-stationary and keeps on propagating towards the shore line.

Then, the wave runs up the beach in the swash zone.

The wave breaking phenomenon can be described as the transition from an irrotational particular motion, during wave steepening, overturning and plunging jet formation (Peregrine, 1983), to a rotational motion following jet impingement leading to a turbulent, chaotic flow motion.

It can also be characterized as the dramatic, complete and irreversible transformation of the organized motion of the incident wind-generated waves into motions of different types and scales, including large-scale coherent vortical motions and small-scale turbulence (Battjes, 1988). Once waves broke, a large amount of energy is released and turned into turbulence (Svendsen and Putrevu, 1996).

Surprisingly, the famous Leonardo da Vinci first reported in his notebooks a lot of observations about breaking waves, waterfalls, vortices in water and many other phenomena linked to coastal engineering sciences (McCurdy, 1942).

Regularly, during the last two decades, important reviews described and commented in details the general mechanisms involved in the breaking process (Peregrine, 1983) and the surf zone dynamics (Battjes, 1988; Svendsen and Putrevu, 1996). Liu (1999) gave an overview and discussion of the different numerical techniques which have been used for the interface tracking in numerical simulations of breaking waves, while Christensen et al. (2002) detailed the recent advances that have been made in the numerical modelling and the techniques of measurement for the study of the surf zone.

1.1.1 Breaker types classification

Galvin (1968) has identified, classified and described the different types of wave breaking:

- *spilling breaker*, where white foam, consisting of a turbulent air/water mixing, appears at the wave crest and spills down the front face of the propagating wave
- *plunging breaker*, where the front face of the steepening wave is observed to overturn. A plunging jet is ejected from the wave crest and splashes near the base of the wave
- *collapsing breaker*, where the crest of the steepening wave remains unbroken and the lower part of the front face explodes
- *surging breaker*, where, again, the crest of the steepening wave remains unbroken and advances up the beach.

It is usually admitted that there is a continuous gradation in type of breaking from spilling to surging (Fig. 1.2).

We choose to study plunging breaking waves as the potential for air entrainment is much greater than the other breaker types. Moreover, plunging breakers have the ability to entrain a large quantity of air at great depths, leading to long bubble residence time in the water column, which induces a large amount of energy dissipation (Chanson and Lee, 1997; Chanson et al., 2002).

1.1.2 Plunging breaking waves

The general processes involved in the wave steepening and subsequent breaking are now well known and has been fully described by numerous authors. For example, Peregrine (1983) has reported a complete review of the research work in this field.

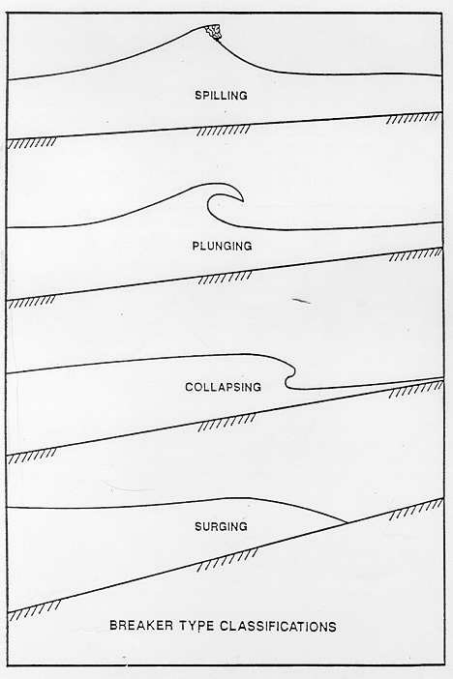

Figure 1.2: Breaker types classification (Galvin, 1968).

As it approaches to the beach, the propagating wave changes of form due to the decreasing of the water depth. The forward face of the wave steepens, its shape looses its symmetrical aspect.

Figure (1.3) shows a sketch of three main features of the overturning motion, located in three different regions of the steepening wave, before the face of the wave becomes vertical (Longuet-Higgins and Cokelet, 1976; Cokelet, 1979; Peregrine et al., 1980; Longuet-Higgins, 1982; Peregrine, 1983; New et al., 1985). The following features have been reported:

(i) high water-particle velocities are found at the crest of the steepening wave. The most commonly accepted criterium to identify the beginning of the plunging breaking process is when the maximum horizontal velocity component magnitude becomes greater than the initial wave celerity

(ii) high water-particle accelerations are located on the forward face of the wave. The acceleration field is directed from the water towards the air. The high water accelerations exceed the acceleration of gravity

(iii) low particle accelerations on the rear of the wave have a negative horizontal component.

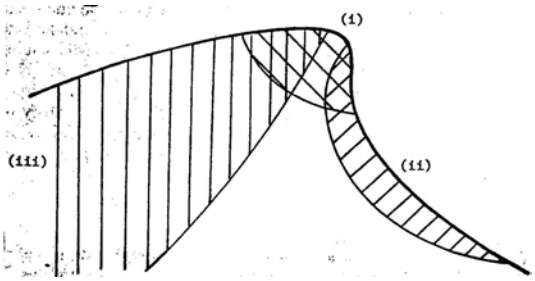

Figure 1.3: Sketch of the three dynamically significant regions in the steepening wave (Peregrine, 1983).

Figure 1.4: Overturning motion and plunging jet impact.

Once the front face of the crest steepens and becomes vertical, a jet of liquid is projected from the crest of the wave. The tongue of water thrown from the crest develops and free falls down forward into a characteristic overturning motion (Figs 1.4). This striking and powerful feature can be very spectacular: a massive amount of water is sometimes involved, generating a beautiful and high splash of white foam, the sound being also very impressive.

Longuet-Higgins (1982), New (1983), Greenhow (1983) have developed analytical solutions, called *loop models* to understand and describe the overturning motion of the wave.

Longuet-Higgins (1982) presented a mathematical solution characterized by the shape of a rotating hyperbola with asymptotes enclosing a steadily reducing angle (Fig. 1.5). The flow near the tip of the jet has also been described. Nevertheless, this solution does not take into account the rear part of the wave.

New (1983) fitted ellipses of large portions of the face in some computed solutions and pictures of waves. He showed that the ratio of the axes of the ellipses was always close to $\sqrt{3}$. This has been verified for waves breaking in both deep or shallow waters (Fig. 1.6).

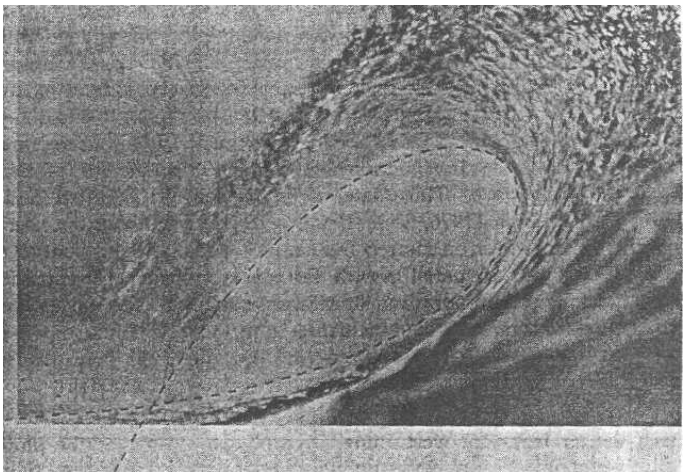

Figure 1.5: P_3 solution of Longuet-Higgins (1982) (dashed line) superposed on a breaking wave picture (Peregrine, 1983).

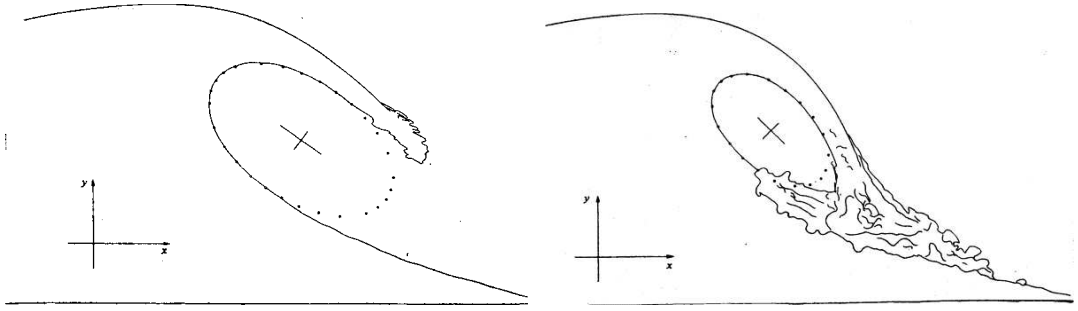

Figure 1.6: Laboratory waves of Miller (1976) and fitted ellipses of $\sqrt{3}$ aspect ratios (New, 1983).

Again, this solution describes the front faces of plunging breaking waves.

As both previous solutions do not take into account the rear part of the wave, Greenhow (1983) suggested a model combining both previous analytical developments. This has been shown to produce the forward face, loop, jet and rear of the wave in a very realistic way.

These analytical models allowed a great improvement in the description of the main features taking place during the plunging breaking process, but are limited to the jet formation and development.

Once the jet is ejected from the wave crest and plunges down, it hits the water at the plunge point (Figs 1.4 and 1.7). Chanson and Lee (1997) showed that the location of the plunging jet impact with the free surface is always above the still water level. The impact angle of the plunging jet with the free surface has been evaluated to be about 31.

Figure 1.7: Plunging jet impact and splash-up generation.

The plunging jet closes over the air to form a tube around which there is a considerable circulation. The flow degenerates rapidly into a turbulent motion of air and water.

Depending on the position of the plunge point, different breaker types can be observed. If the plunge point is located very near to the crest of the wave, the resulting splash is directed down the wave leading to a spilling breaker. Otherwise, if the jet is ejected farther towards the lower part of the face of the steepening wave, the wave becomes a plunging breaker.

The jet then entrains a pocket of gas and hits the forward face of the wave, forcing up a second jet, called *splash-up*. This splash-up can rise higher than the original wave.

Peregrine et al. (1980) first discussed about splashes in waterfalls and breaking waves, and tried to analyze a simplified mathematical model of a splash from a thin uniform jet of water impacting onto a thin layer of water at rest on a vertical plate. Peregrine (1983) then presented in figure (1.8) three possible modes of splash-up generation:

- mode (a): the jet rebounds, the front face of the wave acting like a solid body
- mode (b): the jet penetrates and pushes up the water from the previously undisturbed water
- mode (c): the jet penetrates, pushes up the water from the front face of the wave and participates to the formation of the splash-up

It has been usually observed that the original splash-up caused another splash-up to be projected forward over another tube of air, hitting the undisturbed water at a second plunge point. Miller (1976) showed these cycles of plunge and splash-ups which entrap pockets of air and create strong vortex-like motions in each cycle.

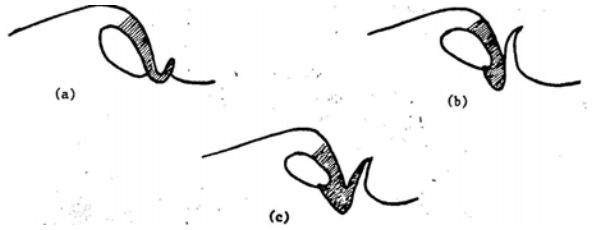

Figure 1.8: Sketches of the three possible modes of splash-up proposed by Peregrine (1983).

Both non-circular initial state and three-dimensional instabilities are responsible for the main large pocket of air having a relatively short life time (Peregrine, 1983). This tube of air sometimes collapses and the trapped air escapes through the free surface with a sudden spout of spray (Miller, 1976), while the air entrapped mixing with the water. It results a region with vortical motion and a high concentration of air bubbles rising gradually to the surface (Battjes, 1988).

It is important to be able to describe accurately the splash-up mechanism as it is responsible for a large amount of gas to be entrapped and entrained in the water, this, in turn, playing a great role in the wave energy dissipation.

Moreover, it has been shown that turbulence generated at this point depends on the type of large-scale structures which are generated. For example, when a sequence of vortices rotates in the same direction, the regions between them have a high shear rate, which results in a high rate of dissipation of the organized motion (Battjes, 1988).

Experiments show that the eddies contain a large amount of air bubbles which enhances the upwelling of sediment. Chanson and Lee (1997) observed that the rate of energy dissipation is increased with the bubble penetration depth and with the characteristic length of the plunging jet shear flow.

1.2 Large-scale vortices and turbulence generation

1.2.1 Experimental observations

The jet-splash cycles, occurring several times in a single breaker, are responsible for the generation of a sequence of large-scale coherent vortices. Some authors have worked to highlight the generation and the importance of the vortices during the wave breaking process. A review of this part of the research area has been presented by Battjes (1988).

The early experimental work of Sawaragi and Iwata (1974) gave an estimation of the

energy loss occurring during the breaking process, due to the motions of the vortices. Among the greatest work to keep in mind, Miller (1976) investigated experimentally the internal velocity field, indicating the importance of what he called *breaker vortices*, which size and strength are a function of breaker shape. Miller (1976) first highlighted the occurrence of the successive splash-ups. The process is observed to repeat, each successive splash-up and vortex being weaker than the preceding one. Some pictures indicate the formation of a large amount of air bubbles during the jet-splash-up cycles. The trajectories of the vortices centers during the breaking process and the wave propagation are shown.

Miller (1976) also illustrated that the vortices in plunging breakers significantly affect the bottom flow. He concluded a series of experiments by suggesting that sand bars are formed when the large-scale vortices created by plunging breaker are present in the flow, while they are erased by the translation effect of spilling breakers when the vortices are confined to the vicinity of the surface.

Nadaoka and Kondoh (1982) confirmed this difference between plunging and spilling breakers. A series of laboratory measurements have been conducted to identify the structure of the internal velocity field within the surf zone. Their measurements clearly indicate that the velocity field can be divided into two regions, the upper and the bottom layer. The mechanism of onshore-offshore motions of the bottom sand is very well described.

Nadaoka and Kondoh (1982) reminds that the velocity field is characterized by the existence of very active turbulence associated with air entrainment, which is responsible in wave energy damping in the surf zone. The presence of a strong mean flow and the asymmetry of orbital velocity profile control the transport of sand having been put into suspension by the turbulence. It appears in their measurements that the entrained air bubbles are contained mostly in the large structures and diffused towards the bottom due to these eddies.

An upper layer is identified, characterized by the presence of large-scale eddies associated with small-scale turbulence and entrained air bubbles, whereas the bottom layer is characterized by the coexistence of the small-scale turbulence originated from the upper layer and the bottom originated turbulence. Thus, Nadaoka and Kondoh (1982) showed that the Eulerian mean velocity within the surf zone is directed onshore above the through level, whereas it is directed offshore below the through level. This explains the observations of Miller (1976).

An early experimental and two-dimensional numerical comparison work has been published by Sakai et al. (1986), where plunging breakers on sloping beaches are studied. The existence of several vortices, having a horizontal axis of rotation (*co-rotative vortices* or

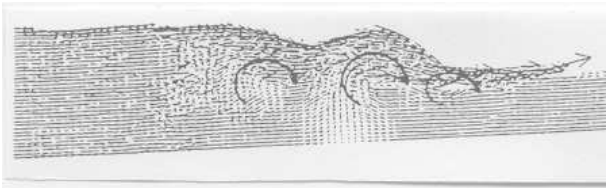

Figure 1.9: Two-dimensional numerical simulation of co-rotative vortices (Sakai et al., 1986).

clockwise revolving vortices), generated during the jet-splash cycles, has been confirmed as shown in figure (1.9).

Jansen (1986) studied the sequence of jet-splash motions in both spilling and plunging, investigating experimentally the kinematics of the aerated region located in the upper part of the broken waves.

Following the work of Miller (1976) and the review of Battjes (1988), Bonmarin (1989) studied experimentally the shape evolution of a plunging crest after breaking has started. The resulting splash-up phenomenon is fully observed and detailed, including its part in the air-entrainment process (Figs. 1.10). Some very interesting pictures show the co-rotative vortices and, more original, *counter-rotative vortices* or *anti-clockwise revolving vortices* generations.

In the same time, Nadaoka et al. (1989) published an important experimental work about the structure of turbulence and its role in the breaking wave dynamics within the surf zone. The results confirm the characteristic structures of large-scale horizontal eddies as found previously by some authors. *Obliquely descending eddies* or *slanting vortices* (Fig. 1.11), similar to these reported by Sakai et al. (1986), have also been visualized. These latest structures are shown to have a significant role in the generation of Reynolds stress and thus affect the deformation of the mean flow field. The horizontal vortices are shown to be unstable and the obliquely descending eddies are then developed. These eddies are then generally observed under spilling breakers or propagating bores, after the occurrence of plunging breakers.

More recently, Zhang and Sunamura (1990) examined experimentally the characteristics and the conditions of occurrence of vortices produced by breaking waves. These large-scale structures are classified into two types: oblique and horizontal vortices. Furthermore, the horizontal vortex is subclassified into four types, depending on the developmental characteristics of the vortex:

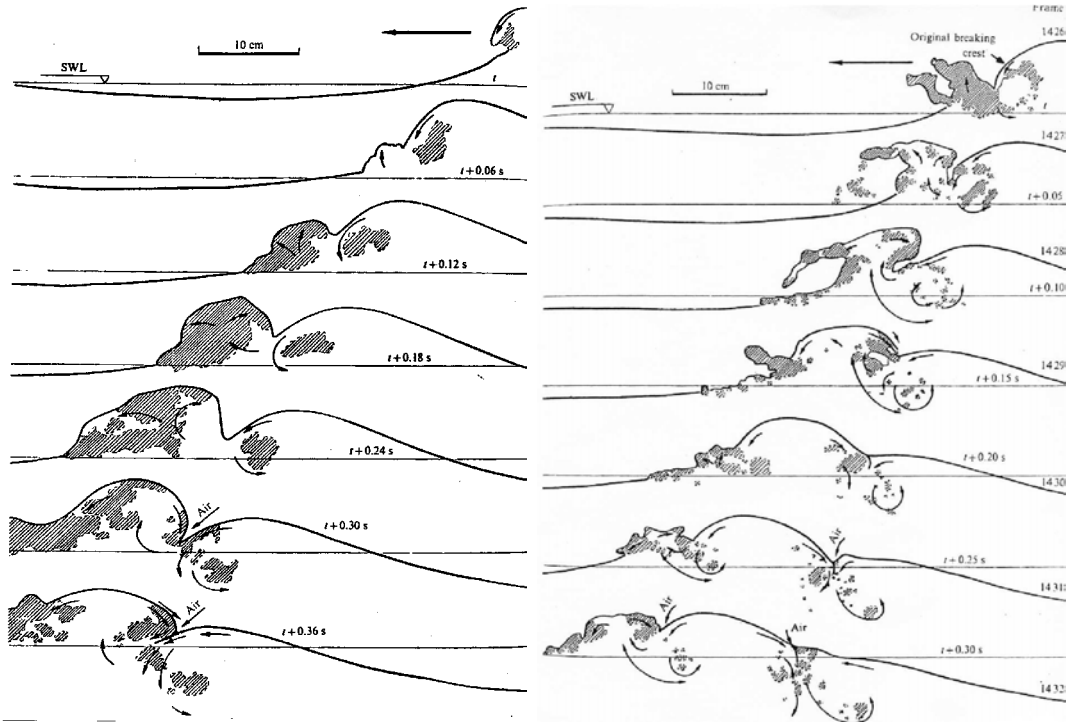

Figure 1.10: Generation and development of the splash-ups with air entrainment and large underwater structures commented by Bonmarin (1989).

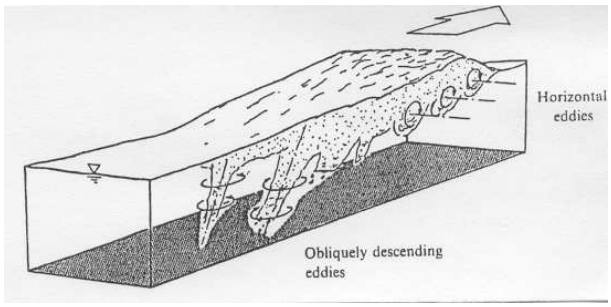

Figure 1.11: Sketch of the large eddy structures observed under breaking waves (Nadaoka et al., 1989).

- type A: formation of a horizontal vortex that will change to oblique vortices
- type B: formation of horizontal vortices that will develop in sequence
- type C: formation of a horizontal vortex that will disappear in a short time
- type D: formation of a horizontal vortex that will change rapidly to nonsystematic vortices

Lin and Hwung (1992) found from experimental measurements that the main mechanism driving the motion in the bubble region was the vortex system that was generated during the jet-splash cycles. The interactions between the jets, the vortices and the rising air bubbles are shown to be responsible for the vortex stretching occurrence.

Ting and Kirby (1994, 1995, 1996) studied experimentally turbulence transport in the surf zone under breaking waves. This study confirms previous observations and indicates that there are fundamental differences in the dynamics of turbulence between spilling and plunging breakers, which are related to the processes of wave breaking and turbulence production. It is shown that the sediment transport is found to be offshore under spilling breakers, while it is onshore under plunging breakers.

This is explained by the fact that, under a plunging breaker, a large amount of turbulence is generated over the whole water column immediately after the wave broke. Thus a large amount of sediment is brought into suspension. Since the high turbulence region travels with the wave top towards the shoreline, the sediment transport is onshore.

Under a spilling breaker, the turbulence remains in the upper region of the wave. Turbulence intensity and vertical variations of undertow are found to be much smaller in the spilling case than in the plunging case. In addition, offshore motion is maintained for a longer period of time than onshore motion. Thus the sediment put into suspension goes in the same direction than the undertow, *i.e.* in the offshore direction.

Nepf et al. (1995) investigated experimentally the occurrence of longitudinal cells under spilling breakers, but this is not in our concern.

Chanson et al. (2002) studied experimentally the mechanisms of air bubbles entrainment by plunging breakers. The results highlight strong vertical motions induced by the rising air bubbles. A high level of aeration is measured, depth-averaged void fraction of more than 10% next to jet impact in shallow waters being measured.

Melville et al. (2002) showed experimentally that both the kinetic energy of the flow and the vorticity decay approximately as t^{-1}. It was found that breaking generated at least one coherent vortex that slowly propagated downstream at a speed consistent with the velocity induced by its image in the free surface.

Christensen et al. (2002) summarized that the vertical of outer and inner surf zone regions could be divided into three parts: the upper, middle and lower regions.

In the upper region, a violent transformation of the wave top into turbulent flow structures occurs, these eddies breaking down and interacting with the flow in the middle region to produce much turbulence. The offshore-directed flow under the trough and the incoming wave motion interact with the exchange of turbulence and momentum. The undertow then interacts with the bed, as a wave-current boundary layer.

Many experimental work have been carried out to identify the role and nature of turbulence in the bottom boundary layer (Cox et al., 1996; Cox and Kobayashi, 2000; Cox and Anderson, 2001).

1.2.2 Numerical studies

Experimental visualizations and measurements are limited due to three major problems.

Firstly, optical techniques fail to give reliable predictions of the flow conditions in the aerated part of the broken waves. Some acoustic measurements have shown another possible way of non-intrusive experimental technique (Doering and Donelan, 1997), but this technique suffers from the same limitation. Secondly, three-dimensional techniques are not available yet, or not yet implemented for the wave breaking problem, so fully three-dimensional flow structure such as the obliquely descending eddies have not been completely described experimentally. Thirdly, experimental and *in situ* measurements require heavy structural and technical equipments, such as wave tanks, lasers, data probes, digital cameras, etc. A measurement campaign is then a very tedious task.

It is only a matter of time for the technical limitations to be overtaken, due to the rapid improvements of the technology. Nevertheless, there is a need for developing other complementary approaches for studying the breaking processes.

The recent progresses in applied mathematics and computer architectures offer the possibility of developing numerical models. The available numerical methods can be classified as wave-averaged models, Boussinesq models, models based on the potential flow theory. Models based on the Navier-Stokes equations, coupled with a mathematical treatment for the free surface and turbulence description are also reviewed.

Numerous models have been developed to describe the cross-shore processes and the propagation of waves in shallow water, such as the wave-averaged models and the Boussinesq models. This type of models yields a good prediction of the set-up and wave heights in the surf zone, the roller propagation or the sediment transport. Nevertheless, these models do not allow to describe the flow in details (see Madsen and Schäffer (1999) for a complete review).

Another way of tackling the surf zone problem is to simulate the flow with numerical tools based on potential flow theory. Most of the numerical studies have been carried out in two-dimensions. The early work of Longuet-Higgins and Cokelet (1976) is dedicated to the development of a mixed Eulerian-Lagrangian (MEL) approach combined with a boundary integral equation formulation (BIE). Cokelet (1979) and Peregrine et al. (1980) used the same method to give more details of the internal flow before breaking (see section 1.1.2). Similar studies have been reported by Vinje and Brevig (1981); Longuet-Higgins (1982); New et al. (1985); Dommermuth et al. (1988); Yasuda et al. (1997). These methods were only implemented in two-dimensional configurations.

Strongly nonlinear waves problems required very accurate and stable numerical methods. High-order boundary element methods (BEM) have then been developed to solve the equations in the MEL formulation. The accuracy of this numerical method allows to predict the evolution of nonlinear waves in numerous configurations (Grilli et al., 1997).

Grilli et al. (2001) proposed an accurate three-dimensional numerical method for the description of these strongly nonlinear waves over complex bottom topography. An application to the shoaling of a solitary wave up to the overturning motion was presented. A lot of applications of this method have proved its high accuracy (Guyenne and Grilli, 2003; Grilli et al., 2004).

Although its efficiency, this type of numerical method is limited to describe the wave evolution up to the jet ejection and does not allow to study the flow motion from the jet impact onto the forward face of the wave.

The most direct way to investigate numerically the complexity of the flow in the surf zone is then to solve the Navier-Stokes equations, usually used for aerodynamics, industrial and academic fluid mechanics. The method is able to calculate complex flows in complex geometries, its drawbacks being the numerical diffusion, induced by the numerical schemes used to discretize and solve the equations, and the large CPU time, which can be very time consuming when three-dimensional problems are tackled. Nevertheless, this method gives access to many reliable information about the velocity, acceleration and pressure fields under the broken waves. Moreover, distorted free surface can be accurately

described, in addition to the turbulence and transport properties.

A complete review concerning the free surface methods applied to the wave breaking problem has been published by Liu (1999).

The first method which has been implemented to simulate breaking waves is the lagrangian Marker-And-Cell (MAC) method (Sakai et al., 1986), as shown in figure (1.9). This method has then been improved by the Simplified Marker-And-Cell (SMAC) method (Takikawa et al., 1997) and the Surface Marker (SM) method (Christensen, 1996; Christensen and Deigaard, 2001). Samples results for velocity field showing obliquely descending eddies is shown in figure (1.12).

The most used method is the Volume Of Fluid (VOF) method, with or without interface reconstruction. Different methods for the interface reconstruction have been implemented. The Donor-Acceptor method, referred to as the Simple Line Interface Reconstruction (SLIC-VOF) method, is the first and simplest VOF algorithm which has been developed and thus used (Lemos, 1992; Lin and Liu, 1998a,b; Bradford, 2000; Zhao et al., 2004). An example of the overturning motion predicted using the SLIC-VOF method is shown in figure (1.13).

The SLIC-VOF method has then been improved by the more accurate Piecewise Linear Interface Construction (PLIC-VOF) (Abadie, 1998; Abadie et al., 1998; Chen et al., 1999; Abadie, 2001) and Semi-Lagrangian (SL-VOF) (Guignard, 2001; Guignard et al., 2001; Biausser, 2003) methods, as shown in figure (1.16). A recent improved scheme of the PLIC-VOF method, the Defined Donating Region (DDR-VOF) algorithm, has also been used by Hieu et al. (2004). Plunging jet generation and velocity field distribution predicted by DDR-VOF method is shown in figure (1.14).

Some very different methods are now recently implemented, involving numerical schemes to avoid the interface reconstruction: the Level Set method (Iafrati et al., 2001; Iafrati and Campana, 2003), as shown in figure (1.15) and the Lax-Wendroff Total Variation Diminishing (TVD) scheme (Lubin et al., 2003a).

The Navier-Stokes can be treated with or without turbulence models. The first and simplest way of solving the Navier-Stokes is the Direct Numerical Simulation, with the assumption that the mesh grid size used to discretized the numerical domain is sufficiently refined to take all the length-scales of the flow, which is in practice never the case. The majority of the work followed that method (Abadie, 1998; Abadie et al., 1998; Chen et al., 1999; Iafrati et al., 2001; Abadie, 2001; Guignard, 2001; Guignard et al., 2001; Watanabe and Saeki, 2002; Biausser, 2003; Iafrati and Campana, 2003) and gave very promising results for the overall flow description, including the shoaling and the breaking of the

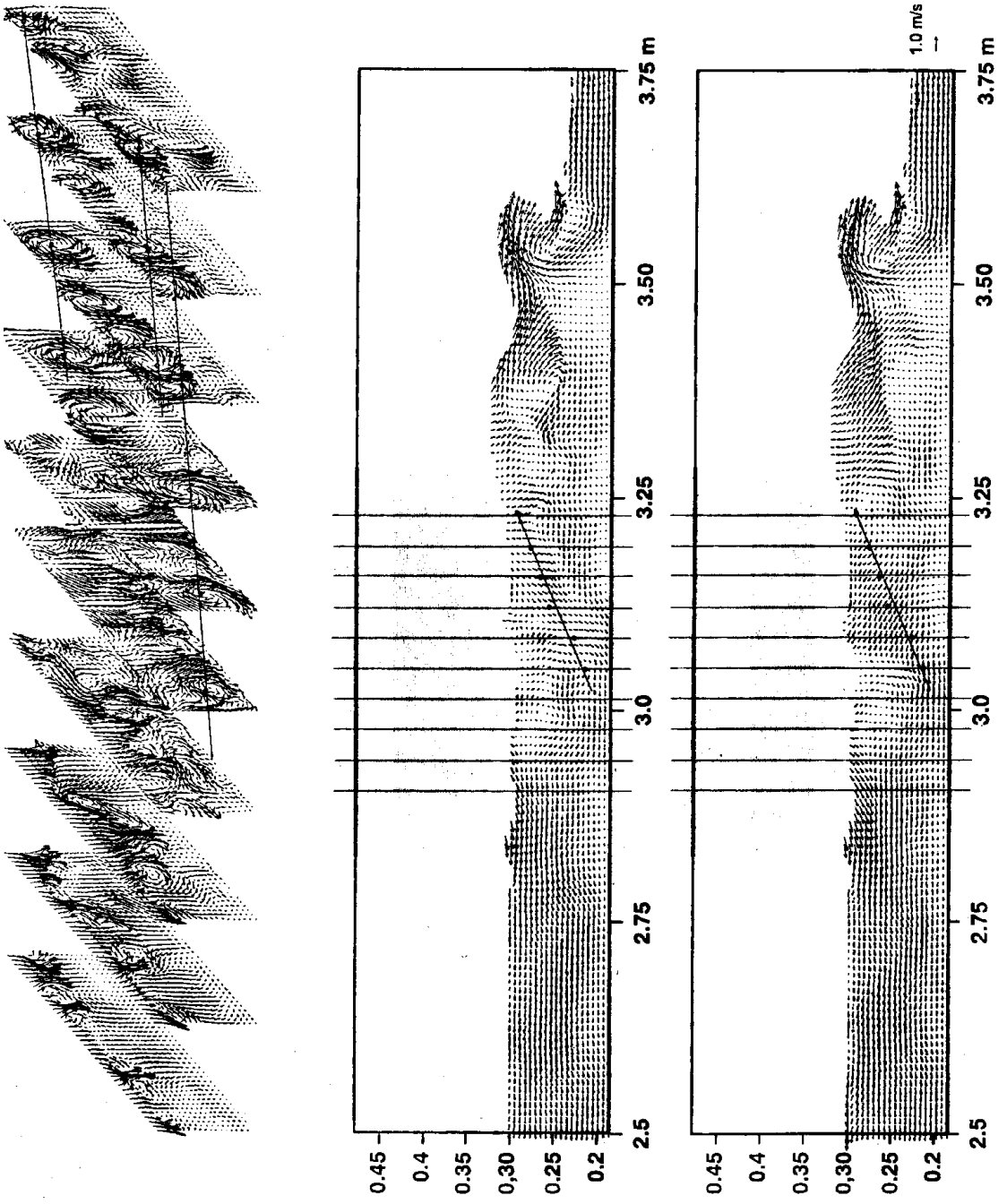

Figure 1.12: Velocity field showing obliquely descending eddies in a weak plunging breaker (Christensen and Deigaard, 2001). Simulation run with the SM method.

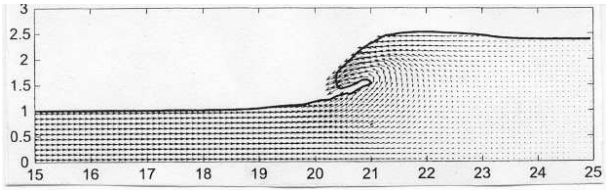

Figure 1.13: Overturning motion. The authors note that their numerical model does not account for the air entrainment (Zhao et al., 2004). Simulation run with the SLIC-VOF method.

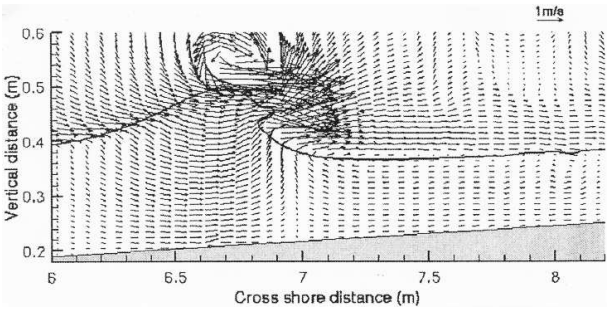

Figure 1.14: Plunging jet generation and velocity field distribution (Hieu et al., 2004). Simulation run with the DDR-VOF method.

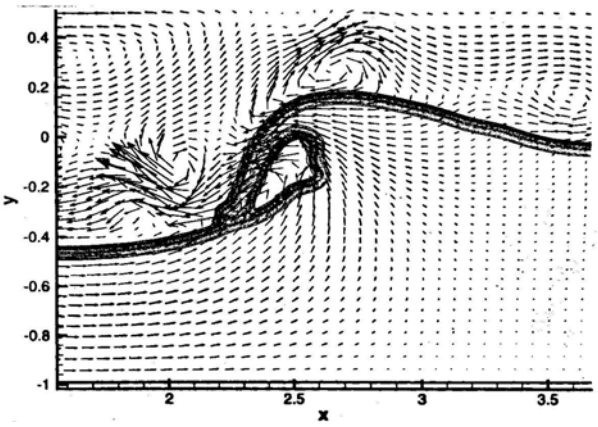

Figure 1.15: Velocity field in air and water at the jet impact (Iafrati et al., 2001). Simulation run with a Level Set method. Only one velocity vector over three is plotted.

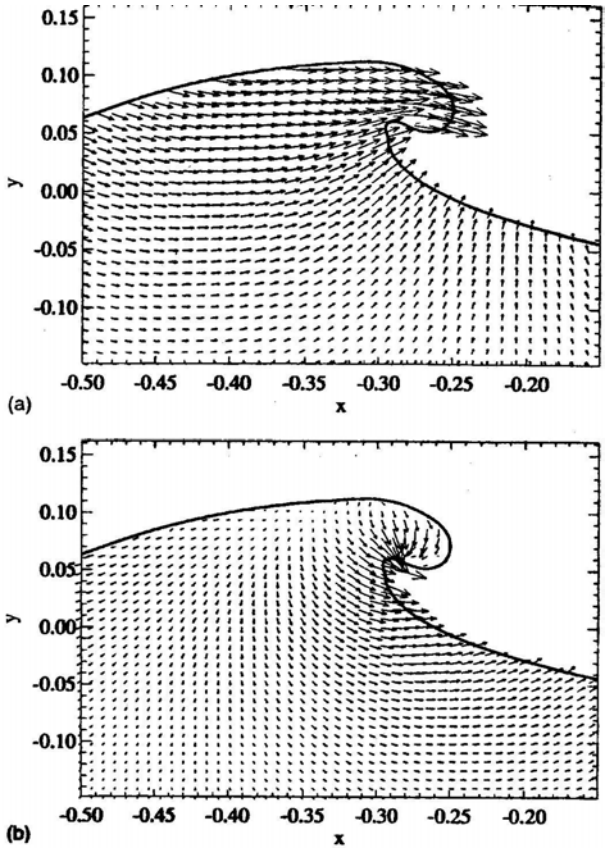

Figure 1.16: Close-ups showing the velocity (a) and acceleration (b) fields (Chen et al., 1999). Simulation run with the PLIC-VOF method. Only one vector over four is plotted.

waves. The turbulence is not described or analyzed, the main large-scale structures being shown as an illustration of the abilities of the numerical tools (Fig. 1.16). A majority of these studies consider theoretical fluids, more viscous and lighter than water.

Some recent work implemented the Reynolds Averaged Navier-Stokes modelling of the surf zone. Lemos (1992) used a $k-\epsilon$ model to represent the turbulent scales in the simulations. The turbulence levels were found to be overpredicted. Takikawa et al. (1997) used a $k-l$-like model and indicated that, in the upper region of the surf zone, the Reynolds stress is highly related to the vorticity and the skewness. Lin and Liu (1998a,b) brought a very great improvement in the understanding of the processes taking place in the surf zone, using again a $k-\epsilon$ model. The turbulence levels at breaking were found to be overestimated by 25% to 50%, as compared to the turbulence level measured by Ting and Kirby (1994). The results of the plunging case show a better agreement than the spilling case compared with the measurements reported by Ting and Kirby (1995, 1996). In the spilling case, the undertow was found to be sometimes in a completely

wrong prediction, directing towards the shore line. Bradford (2000) made a comparative study of three turbulence models, including the $k-\epsilon$ and the Renormalized Group (RNG) models. Similar results as those found by Lin and Liu (1998a,b) are shown, confirming the discrepancies for the spilling case and the agreement for the plunging case. It should be noted that the work of Lin and Liu (1998a,b) and Bradford (2000) do not take the air entrainment into account.

Except the recent promising simulations shown by Biausser (2003), all the previously cited work were two-dimensional simulations.

Another very recent way of simulating turbulence in breaking waves is the Large Eddy Simulation (LES) method. Turbulence is taken into account in the Navier-Stokes equations thanks to a turbulence model for the subgrid scales of the flow. Zhao and Tanimoto (1998) first implemented the LES method to breaking waves and showed very promising results compared to experimental measurements, considering a two-dimensional configuration. Christensen (1996) and Christensen and Deigaard (2001) first used a fully three-dimensional numerical tool based on the Navier-Stokes equations and studied spilling, weak and strong plunging breakers. Some very interesting visualizations and encouraging results describing the internal velocity field perturbed by three-dimensional vortices are shown (Fig. 1.12). Similar results were found by Watanabe and Saeki (1999) with three-dimensional numerical simulations of plunging breakers. Hieu et al. (2004) studied two-dimensional breaking waves, but they argue that the surface tension was not implemented in the numerical simulations, which involves that air entrainment was rather absent in the results. The numerical model was shown to be able to reproduce the wave breaking processes in shallow water (Fig. 1.14). Very recently, Zhao et al. (2004) implemented a new multi-scale method where the two-dimensional flow structures are fully resolved with a $k-l$ RANS approach, while the three-dimensional turbulence interactions are modelled with a three-dimensional subgrid-scale eddy viscosity model. A general good agreement with experimental data are shwon, improving significantly the RANS results of Lin and Liu (1998a,b) and Bradford (2000) in the spilling and plunging cases.

Nevertheless, as Lin and Liu (1998a,b) and Bradford (2000) stated, the air entrainment is not taken into account (Fig. 1.13).

1.3 Scope of the present work

Few elements can be highlighted from this presentation of the existing work.

The authors proved a great improvement in the numerical methods allowing to describe

with a very promising accuracy both the free surface and the turbulent flow structures general behavior, solving the Navier-Stokes equations. Nevertheless, all the authors agree to state that solving the Navier-Stokes equations in an air/water configuration is a real challenge, due to strong interface deformations and air entrainment. Thus, the effect of air has not been studied yet in details in most of the cited two- and three-dimensional simulations. Taking the mixture of air and water into account is one of the challenges of the coming years (Christensen et al., 2002). Some recent work heading in that direction (Brochini and Peregrine, 2001a,b) still have to be implemented.

Most of the published work are two-dimensional configurations. As already mentioned, running three-dimensional two-phase Navier-Stokes simulations is very demanding in terms of CPU time and computer facilities. Indeed, very refined mesh grids have to be used to ensure an acceptable free surface description. Above all, numerical simulations involving turbulence investigation require large number of mesh grid points to reach the small length-scales and thus to be reliable. Some studies, involving large sizes of numerical domains and small scales of turbulence and free surface deformations, are thus still unreachable.

The numerical methods are then a field of research where efforts and improvements have to be put into, in order to gain in accuracy and speed. The two-phase Navier-Stokes equations are discretized with numerical schemes which can be very diffusive, leading to imperfections and discrepancies.

Thus, the objective of our work is first to validate new numerical methods for solving the two-phase flow Navier-Stokes equations in air/water configurations. Then, some Large eddy simulation subgrid-scale models have been implemented in the numerical tool Aquilon, developed in our laboratory, and validated with many case studies.

We finally aim at describing the air entrainment and the internal velocity field under broken waves in two- and then three-dimensional configurations.

Summary and conclusion

We gave in this section the detailed description of the processes involved in the wave breaking phenomenon. A general overview of the recent advances is also described.

The three-dimensional and two-phase character, the small time and space-scales and the turbulent behavior of breaking waves make experimental and theoretical researches difficult to achieve. Since fully three-dimensional experimental techniques does not exist, 3D flow structures are therefore complicated to obtain with certainty. The recent progresses in applied mathematics and computer architectures offer the possibility of developing a numerical model based on the three-dimensional Navier-Stokes equations to study the breaking phenomenon. The interest of this approach is to provide a complete description of free surface and velocity evolutions which must lead to the understanding of energy dissipation and turbulent flow structures.

The process of wave breaking in shallow water is not completely described, due to its high complexity. The complete understanding requires an accurate description of phenomena such as the splash-up induced by the impact of the plunging jet, the air entrainment and the large-scale structures behavior. Since breaker types are not only visually different in shape, but also in the kind of vortices they induce and in the way turbulence will affect sediment transport, it is important to investigate and to demonstrate the ability of the numerical tool to accurately describe the breaking phenomenon, considering the two media, air and water. This is indeed a great difference between previously published work and the study we present in this document, as we will show large quantities of air entrainment in the water.

This work is then dedicated to an attempt for implementing a new method in an existing numerical tool for an accurate description of the previously detailed processes, in order to be able to predict precisely the complex flow occurring in the nearshore area. The originality of this work is to apply the Large Eddy Simulation technique to turbulent two-phase flows.

Moreover, we try to investigate the possibility to see fully three-dimensional structures as the main goal of our work is to study turbulence induced by breaking waves.

Chapter 2

Methodology of the numerical tool: Aquilon

Introduction

The breaking wave problem has been presented in the previous section. Analytical solutions are not available due to the high complexity of the flow. Numerical modelling of the wave breaking problem involves the solution of the Navier-Stokes equations of two-phase flows with strong free surface deformations and tearing. So we will use numerical methods to obtain approximate values for the different variables of the problem in a finite number of points of the domain (spatial and temporal). In the present study, a numerical code, Aquilon, developed in the TREFLE laboratory (formerly MASTER), is utilized.

In this chapter, the contribution of our work brought to the numerical code Aquilon is to validate an original augmented Lagrangian method for the resolution of the Navier-Stokes equations.

The scope of this chapter is thus to present the concepts and the numerical methods developed in Aquilon, as, for example:

- a unique mesh grid is used for a unique system of equations
- the system of equations is discretized using the finite volume method
- an original augmented Lagrangian method has been successfully tested to solve the system of equations
- some robust methods are able to handle accurately with interface reconnections in the modelling of three-dimensional two-phase flows

2.1 Mathematical formulation of the problem

We choose an Eulerian approach for handling the present problem. Let $\mathbf{u}$ be the velocity field vector, p the pressure, $\mathbf{g}$ the gravity vector, t the time, ρ the density and μ the dynamic viscosity. The conservation equation system for incompressible flows are the classical Navier-Stokes equations supplemented by the condition of incompressibility. This system can be written as follows (Eq. 2.1):

$$\begin{cases} \nabla \cdot \mathbf{u} = 0 \\ \rho \left(\dfrac{\partial \mathbf{u}}{\partial t} + (\mathbf{u} \cdot \nabla)\mathbf{u} \right) = \rho \mathbf{g} - \nabla p + \nabla \cdot [\mu(\nabla \mathbf{u} + \nabla^T \mathbf{u})] \end{cases} \tag{2.1}$$

2.2 Numerical modelling

The originality of the numerical tool Aquilon is the use of a mesh grid disconnected with the studied geometry, which allow us to treat globally a heterogeneous fluid/solid domain. Most numerical tools need to define a mesh grid which corresponds precisely to the studied geometry. This sometimes implies that the mesh grid has to be generated thanks to extra specialized softwares. Moreover, if some parameters concerning the geometrical shape or the numbering of the mesh cells is not well controlled, the linear systems will be badly preconditioned and so hard to solve.

Then, the concept of a unique grid consists in the projection of the studied geometry on a Cartesian rectangular mesh grid surrounding the whole physical domain (Khadra et al., 2000). This method allows to modify easily the geometry during the simulations and improves the preconditioning of the linear systems (Angot, 1989). However, the increased complexity of some geometries requires a refined mesh grid and, thus, a greater number of mesh grid cells. We will then use irregular mesh grids for a better local description.

2.2.1 Boundary conditions treatment

We use the concept of a unique system of equation which is solved in the whole numerical domain. Penalization terms are then added to the Navier-Stokes equations. The technique we use to impose boundary conditions is based on the work of Angot (1989) and Khadra (1994). The method consists in writing a generalized boundary condition as a surface flux:

$$-\left(\frac{\partial \mathbf{u}}{\partial \mathbf{n}}\right)_S = \mathbf{B}_\mathbf{u}(\mathbf{u} - \mathbf{u}_\infty) \tag{2.2}$$

where $\mathbf{B_u}$ is a matrix. It has to be noted that it is a vectorial formulation and then involves the three Cartesian components of the velocity vector $\mathbf{u}$. Then, the boundary condition is directly taken into account in equation (2.1) thanks to the extra term $\mathbf{B_u}(\mathbf{u}-\mathbf{u}_\infty)$.

Thanks to this penalization term, we can then impose a velocity in the numerical domain or on a lateral boundary. For $\mathbf{B_u}=0$, Neuman boundary conditions are modelled $\left(\frac{\partial \mathbf{u}}{\partial \mathbf{n}}\right)=0$, while some coefficients are chosen as $\mathbf{B_u}=+\infty$ to ensure Dirichlet boundary conditions imposed at the mesh grid points of the boundary.

We then have the following system of equations (Eq. 2.3):

$$\begin{cases} \nabla\cdot\mathbf{u}=0 \\ \rho\left(\dfrac{\partial \mathbf{u}}{\partial t}+(\mathbf{u}\cdot\nabla)\mathbf{u}\right) \quad +\mathbf{B_u}(\mathbf{u}-\mathbf{u}_\infty) \\ \qquad\qquad\qquad\qquad\qquad\qquad =\rho\mathbf{g}-\nabla p \ +\nabla\cdot[\mu(\nabla\mathbf{u}+\nabla^T\mathbf{u})] \end{cases} \tag{2.3}$$

in the numerical domain and equation (2.2) on the lateral boundaries.

2.2.2 Solid obstacles

As said in the previous section (2.2.1), we use the concept of penalization terms added to the general system of equations (Arquis and Caltagirone, 1984; Angot et al., 1999; Khadra et al., 2000). To deal with solid obstacles within the numerical domain, it is possible to use multi-grid domains, but it is often very much simpler to implement the Brinkamn theory: the numerical domain is then considered as a unique porous medium. The permeability coefficient K defines the capability of a porous medium to let pass the fluids more or less freely through it. If this permeability coefficient is great ($K\rightarrow+\infty$), the medium is equivalent to a fluid. If it is nil, we can model an impermeable solid. A real porous medium is modelled with intermediate values of K. It is possible to model moving rigid boundaries or complex geometries.

To take this coefficient K into account in our system of equations, we then add an extra term, called *Darcy term*, $\frac{\mu}{K}\mathbf{u}$. The momentum equations is then (Eq. 2.4):

$$\begin{cases} \rho\left(\dfrac{\partial \mathbf{u}}{\partial t}+(\mathbf{u}\cdot\nabla)\mathbf{u}\right) \quad +\mathbf{B_u}(\mathbf{u}-\mathbf{u}_\infty) \\ \qquad\qquad\qquad\qquad\qquad\qquad =\rho\mathbf{g}-\nabla p \ +\nabla\cdot[\mu(\nabla\mathbf{u}+\nabla^T\mathbf{u})]-\dfrac{\mu}{K}\mathbf{u} \end{cases} \tag{2.4}$$

2.2.3 Temporal discretization

An implicit treatment is applied to the system of equations previously introduced: the temporal discretization is achieved through a second-order Euler scheme, or GEAR scheme, on the time derivatives. The time interval is then discretized in a finite number of time steps $[t_n, t_{n+1}]$. The approximation of the variable ϕ at time t_n is written ϕ^n.

The approximation of the derivative term $\frac{\partial \phi}{\partial t}$ at time t_{n+1} is obtained from a Taylor-Series formulation truncated at an order N.

To attain a stationary solution for a given problem, it is necessary to iterate several times. At each time iteration, the real solution is temporally advanced of the quantity $\Delta t = t_{n+1} - t_n$, called *time step*.

The calculation of the time derivative at time t_{n+1} from the values obtained at the previous times can be achieved through a first-order Euler scheme, using the results from iteration n and based on a Taylor-Series formulation truncated at the order $N = 1$:

$$\left(\frac{\partial \phi}{\partial t}\right)^{n+1} = \frac{\phi^{n+1} - \phi^n}{\Delta t} \tag{2.5}$$

or through a second-order Euler scheme (GEAR scheme), using the results from iterations n and $n-1$ and based on the Taylor-Series development truncated at the order $N = 2$:

$$\left(\frac{\partial \phi}{\partial t}\right)^{n+1} = \frac{3\phi^{n+1} - 4\phi^n + \phi^{n-1}}{\Delta t} \tag{2.6}$$

The Gear scheme cannot be used at the first iteration, as ϕ^{n-1} is not known. This problem is avoided by using a Euler scheme for the first iteration The Euler scheme is preferably used for stationary flows, as the Gear scheme is mainly used for unstationary flows.

As we choose to treat implicitly the system of equations, all the time derivatives are evaluated at time t_{n+1}, except those coming from the temporal discretization calculated at time t_n and those where appear non-linearities.

The two main non-linearities appear in the calculation of the density ρ^{n+1} and viscosity μ^{n+1}, which depend on the position of the interface, and the term $(\mathbf{u}^{n+1} \cdot \nabla)\mathbf{u}^{n+1}$ in the momentum equations. This latest term is linearized by re-writing it as $(\mathbf{u}^n \cdot \nabla)\mathbf{u}^{n+1}$. An implicit discretization of the equations allow us to formulate the linearized problem as follows.

The quantities $\mathbf{u}^n$, $\mathbf{u}^{n-1}$ and p^n are supposed to be known. So, $\mathbf{u}^{n+1}$ and p^n are obtained by solving the linearized system (Eq. 2.7):

$$\left\{ \begin{array}{l} \nabla \cdot \mathbf{u}^{n+1} = 0 \\ \rho^n \left(\dfrac{\mathbf{u}^{n+1} - \mathbf{u}^n}{\Delta t} \; + \; (\mathbf{u}^n \cdot \nabla)\mathbf{u}^{n+1} \right) \; + \; \mathbf{B}_\mathbf{u}(\mathbf{u}^{n+1} - \mathbf{u}_\infty) \\ = \rho^n \mathbf{g} - \nabla p^{n+1} \; + \; \nabla \cdot [\mu^n (\nabla \mathbf{u}^{n+1} + \nabla^T \mathbf{u}^{n+1})] - \dfrac{\mu}{K} \mathbf{u}^{n+1} \end{array} \right. \tag{2.7}$$

It is well known that the time step effects the accuracy of the resolution from time step to time step, a small time step giving a precise solution but slow calculation and *vice versa*.

2.2.4 Velocity-pressure uncoupling

The approximation of the Navier-Stokes equations (2.1) is difficult, due to the velocity-pressure coupling and the incompressibility constraint. Indeed, there is no explicit equation which gives an approximation for the pressure field, so all the difficulty lies in its calculation.

We use the augmented Lagrangian method to do the uncoupling between velocity and pressure. The standard augmented Lagrangian method was first introduced by Fortin and Glowinski (1982). This predictor/corrector iterative method consists of solving an optimization problem by solving a velocity-pressure saddle point with an Uzawa algorithm (Uzawa, 1958). From an initial pressure field, the Navier-Stokes equations, modified with the introduction of the constraint of a nil divergence, are solved. A new pressure is calculated thanks to a modified equation of continuity.

The iterations of the augmented Lagrangian method, called m, are repeated until a numerical threshold controlling the constraint is reached, no boundary conditions being needed for the pressure.

This method is fully developed in appendix A. If M is the maximum number of iterations to be done, the algorithm can be summarized, as follows:

- Initializations : $(\mathbf{u}^{m=0}, p^{m=0}) = (\mathbf{u}^n, p^n)$

- For $m = 0$ to $M - 1$ do:

- Calculation of $\mathbf{u}^{m+1}$ solution of the equation:

$$\rho^n \left(\frac{\mathbf{u}^{m+1} - \mathbf{u}^m}{\Delta t} + (\mathbf{u}^m \cdot \nabla)\mathbf{u}^{m+1} \right) - r\nabla(\nabla \cdot \mathbf{u}^{m+1}) \; + \; \mathbf{B}_\mathbf{u}(\mathbf{u}^{n+1} - \mathbf{u}_\infty) =$$
$$-\nabla p^m + \rho^n \mathbf{g} + \nabla \cdot [\mu(\nabla \mathbf{u}^{m+1} + \nabla^T \mathbf{u}^{m+1})] - \frac{\mu}{K}\mathbf{u}^{m+1}$$

- Calculation of p^{m+1} from the equation:

$$p^{m+1} = p^m - r\nabla \cdot \mathbf{u}^{m+1}$$

- Solutions: $(\mathbf{u}^{n+1}, p^{n+1}) = (\mathbf{u}^{m=M}, p^{m=M})$

This standard augmented Lagrangian method had to be improved to deal with two- and three-dimensional unsteady, multimaterial problems. The ability of the modified method is developed and illustrated in appendix A. It has been proved to be efficient for the wave breaking problem, which is the main concern of our work.

2.2.5 Spatial discretization

Once we transformed the original system of differential equations, we have a system of uncoupled equations which has to be discretized on a defined grid.

A Finite-Volume method on a staggered mesh (Marker And Cell - MAC, (Harlow and Welsh, 1995)) is implemented to discretize the Navier-Stokes equations. This method is based on the determination of the values for the variables of the problem in a finite number of points in the numerical domain.

The numerical domain is cut into a finite number of mesh grid cells, or control volume, associated to each mesh grid point. The equations are then integrated on a control volume, centered on each mesh grid point where the scalar and velocity fields are located. The velocity components are located on the faces of the control volumes and the scalar fields on the edges of the mesh grid cells.

The use of a staggered mesh allow an easy calculation of pressure gradients and velocity divergence, and avoid pressure oscillations observed with the use of collocated mesh, which make the numerical scheme more unstable.

The equations are then discretized in terms of physical fluxes through the control volume faces, using the Green-Ostrogradski theorem. It has to be noted that this formulation of the problem allow to keep the conservation properties. The problem consists now in

constructing the values of the variables on the control volume faces where they are not defined. It is so necessary to have an interpolation scheme, which can differ depending on the considered terms of the equations (convective or diffusive). The approximation of the solution is made through piecewise-linear functions between the mesh grid points and its neighbors.

A second order Centered scheme is devoted to the approximation of the viscous and the augmented Lagrangian terms, whereas several schemes can be chosen among a second order Hybrid Centered scheme, an Upwind scheme or a second order Centered scheme for the non-linear convective term, depending on the problem to be dealt with. These numerical schemes are summarized hereafter, all the details being found in (Patankar, 1990):

- the second-order Centered scheme, or central-difference scheme, evaluates the values of the considered variable at $i + \frac{1}{2}$ from a Taylor-Series formulation truncated at an order 1. It is similar to calculating a geometrical average value with the two neighboring values of the considered point. This scheme can be unstable

- the Upwind scheme consists in replacing the unknown value at $i + \frac{1}{2}$ by the one which can be found at the upstream point of the flow. This one-order scheme implies a non-negligible numerical dissipation, but remains adapted to the flows where the convective terms are preponderant

- the Hybrid scheme is composed with several interpolation schemes. Its principle is to choose a numerical scheme to be the most adapted to the local characteristics of the flow. To do so, a non-dimensional number is introduced and allow to locally evaluate the ratio between the convective and the diffusive terms. This non-dimensional number is called the Peclet number (Pe) and is defined on a finite spatial interval $[X_{i+1}, X_i]$ as $Pe = \dfrac{\rho u \left(X_{i+1} - X_i\right)}{\Gamma}$, where u is the local velocity. Then, the Hybrid scheme is defined as :

$$\begin{aligned} -2 \leq Pe \leq 2 \quad &\Rightarrow \quad \text{Centered scheme} \\ Pe > 2 \quad &\Rightarrow \quad \text{Upwind scheme} \\ Pe < -2 \quad &\Rightarrow \quad \text{Upwind scheme} \end{aligned} \tag{2.8}$$

2.2.6 Numerical resolution of the linear system

The use of implicit discretization for the approximation of the system of equations (Eq. 2.7) induces the determination of the inverse of a matrix. The matrices are rather big, proportional to the number of mesh grid points. Moreover, the matrices resulting from the previous discretizations are nonsymmetric. The usual iterative methods (Jacobi, Gauss-Seidel, etc.) are rather low in converging.

The linear algebra problem is then solved numerically with an iterative Bi-CGSTAB (Bi-Conjugate Gradient Stabilized) algorithm (Vorst, 1992), preconditioned under a Modified and Incomplete LU (MILU) algorithm of Gustafsson (1978) to speed up the convergence and improve the resolution of big linear systems.

2.3 Numerical methods for the description of free surface flows

The methods dedicated to the treatment of non-miscible two-phase flow interfaces can be divided in two main categories: interface tracking (Lagrangian approach) and interface capturing (Eulerian approach).

2.3.1 Interface tracking

The most representative methods of this category are the original Marker-And-Cell (MAC) method (Harlow and Welsh, 1995), the line segment method (Chan and Street, 1970) and the Front-Tacking method (Unverdi and Tryggvason, 1992).

Harlow and Welsh (1995) introduced the original MAC method, where massless markers are initially distributed over all rectangular computational cells occupied by fluids. During computations, the dynamic free surface boundary condition is applied at the center of free surface cells, which are defined as cells with at least one marker inside and is adjacent to at least one cell without marker. At the end of a computational cycle for each time step, all markers are moved in accordance with the velocity at their locations $\mathbf{X}(x_0, t + \Delta t) = \mathbf{X}(x_0, t) + \mathbf{u}\Delta t$, where $\mathbf{X}(x_0, t)$ is the position vector of the massless marker originally located at x_0.

(Chan and Street, 1970) first developed the idea of improving the MAC method by placing massless markers only on the free surface, instead of the entire flow region. Some other methods were proposed with the same basic idea (Unverdi and Tryggvason, 1992; Shin and Juric, 2002).

Other methods, very similar to the previous one, were introduced by Takikawa et al. (1997), the Simplified Marker-And-Cell (SMAC) method, and Chen et al. (1991), the Surface Marker (SM) method.

These methods are very accurate to take into account the forces acting on the interface, such as surface tension. However, they become difficult to implement in three dimensions and are very time consuming. Moreover, they cannot handle merging or tearing of interfaces and the free surface shape is not clearly defined. They then suffer from their need to the dynamical addition of extra markers to maintain the resolution on rapidly changing free surface.

2.3.2 Interface capturing

Because of the limitations of the previous methods, other free surface treatment techniques have been developed.

Hirt and Nichols (1981) first proposed the Volume Of Fluid (VOF) method. Its principle is very simple. For each medium, a phase function C, or "color" function, is used to locate the different fluids and solids standing $C = 0$ in the outer media, $C = 1$ in the considered medium. This function C is a fractional volume of fluid parameter, indicating the rate of presence of each medium in a given computational cell. The color function is advected depending on the fluid velocity. Its evolution is described thanks to a kinematic equation (Eq. 2.9):

$$\frac{\partial C}{\partial t} + \mathbf{u}.\nabla C = 0 \tag{2.9}$$

In this way, the multiphase problem is represented by an equivalent fluid admitting variable local properties.

This color function allows to locate the materials and the evolutions of the physical characteristics are solved according to the advection equation on the VOF function (Eqs. 2.14 and 2.9). The challenge in this approach is to solve the Navier-Stokes equations in their multi-material formulation (Scardovelli and Zaleski, 1999) in the presence of discontinuous densities and viscosities. The Eulerian approach has been widely used over the last 10 years for its easy programming in three dimensions and its potential application to interface distortion or rupture.

Thanks to this method and according to the definition of the color function C, the surface tension can be expressed only as a function of the color function C. The surface

tension is a force acting when free surface deformations occur. It is proportional to the free surface curvature κ. For a free surface area unity, according to the surface tension coefficient σ, the surface curvature κ, the presence function gradient at the interface and the jump in color function $[C]$, the surface tension volume force is expressed as follows (Eq. 2.10):

$$F_{ST} = \sigma \kappa n_i \tag{2.10}$$

with n_i being the unit normal to the interface.

As the surface tension force F_{ST} is acting as a pressure on the interface, a volume, in the divergence sense, modelling is suitable on a fixed curvilinear grid. Indeed, the volume of fluid distribution is accurately calculated by means of the generalized fluid model whereas the free surface location, whose precision is dependent on the grid spacing, is not able to ensure a precise geometrical calculation of κ. Following the work of Brackbill et al. (1992), the unit normal to the interface can be assumed to be $n_i = \overrightarrow{\nabla} C = \dfrac{\overrightarrow{\nabla} C}{\| \nabla C \|}$. Then, using the general surface curvature definition $\kappa = -(\nabla . n_i)$, the surface tension volume force is rewritten in a divergence form as a differential expression of the presence function C (Eq. 2.11):

$$F_{ST} = \sigma \overrightarrow{\nabla} C \nabla . \left(\frac{\overrightarrow{\nabla} C}{\| \nabla C \|} \right) \tag{2.11}$$

This volume force is finally added to the momentum equation (Eq. 2.4).

The problem is now to find an accurate solution to equation (2.9), which has to be discretized by classical VOF algorithms detailed hereafter.

Donor-Acceptor method

Hirt and Nichols (1981) first proposed the Donor-Acceptor method, where equation (2.9) is discretized by a finite difference scheme. The color function C is determined by reconstructing in a particular cell the free surface orientation, being either horizontal or vertical depending on the volume fraction value in the cell and its neighboring cells.

This reconstruction method is referred to as Simple Linear Interface Calculation (SLIC). It is only first-order accurate and the method suffers from its simple approximation of free surface orientation.

Piecewise Linear Interface Construction

Youngs (1982) corrected the inaccuracy of the previous Donor-Acceptor method by introducing a more precise way to reconstruct the free surface (PLIC-VOF).

The interface is now defined by its slope and intercepts in each surface cell. The slope is calculated thanks to the color function C gradients and the intercepts are determined by conservation of volume fraction in each cells. The problem is now based on reconstructing the sloping interface.

Some improvements or derived methods can be found in the literature, such as the Defined Donating Region (DDR-VOF) algorithm, developed by Harvie and Fletcher (2001), or the Semi-Lagrangian VOF (SL-VOF) method introduced in two-dimension by Guignard (2001); Guignard et al. (2001) and generalized in three-dimension by Biausser (2003).

However, this method still suffers from some limitations. It is very difficult to implement in three dimensions and calculations can be very time consuming.

This method has been computed in Aquilon by Abadie (1998) in two dimensions, Breil (2001) extended it in three dimensions. Some numerical methods are under development to increase the PLIC-VOF method accuracy (Vincent and Caltagirone, 2004).

Level set method

It is a recent technique dedicated to interface tracking, introduced by Osher and Sethian (1988) and refined by Sussman et al. (1994).

A level set function ϕ is defined as the normal distance function from the interface with its original value set to zero at the interface. This function is advected in place of the color function C thanks to the same equation $\frac{\partial \phi}{\partial t} + \mathbf{u} \cdot \nabla \phi = 0$. The free surface is located where ϕ is zero. ϕ is a smooth function, so it is easy to compute and induces less numerical diffusion (see Sethian (1996) and Osher and Fedkiw (2001) for complete reviews).

Total Variation Diminishing schemes

This method belongs to the VOF methods, as it is still based on the color function C advected in the flow. There is no explicit interface reconstruction, the interface between a medium and the entire domain is repaired by the discontinuity of C between 0 and 1. In practice, $C = 0.5$ is used to characterize this surface.

Numerical schemes are implemented to discretized the advection equation (2.17). The problem is to find accurate schemes to avoid numerical dispersive effects. An Upwind scheme will give too much dissipation and the discontinuity will lower. Higher-ordered

schemes will give rise to numerical oscillations due to the high discontinuity of the free surface.

The use of Total Variation Diminishing (TVD) schemes (Yee, 1987) allows to track accurately the interface by reducing the numerical oscillations and decreases the numerical diffusion of the discontinuity in the three neighboring cells of the interface. Moreover, its implementation in three dimensions is very straightforward (Vincent, 1999).

In Aquilon, the interface tracking is then achieved by a Lax-Wendroff TVD scheme, which is able to handle with interface reconnections (Vincent and Caltagirone, 2000).

2.3.3 Calculation of the two-phase flow characteristics

For a free surface flow, the evolutions of the characteristics (viscosity, density) have to be estimated using μ_0, ρ_0 (gas characteristics), μ_1, ρ_1 (liquid characteristics) and C.

Once the color function is known in the whole numerical domain, according to the advection equation on the VOF function (Eqs. 2.9), we are able to locate each medium. The physical characteristics are then updated, as functions of space, time and color function.

Two methods can be used for updating the viscosities and densities, assuming a continuous or discontinuous variation of the physical characteristics.

First, the densities and viscosities can be calculated through a linear (Eqs. 2.12) or a harmonic (Eqs. 2.13) continuous averaging:

$$\begin{cases} \rho = \rho_1 + (\rho_2 - \rho_1)\ C \\ \mu = \mu_1 + (\mu_2 - \mu_1)\ C \end{cases} \tag{2.12}$$

$$\begin{cases} \rho = \dfrac{\rho_1 \rho_2}{(1-C)\rho_1 + C\rho_2} \\ \\ \mu = \dfrac{\mu_1 \mu_2}{(1-C)\mu_1 + C\mu_2} \end{cases} \tag{2.13}$$

This first method introduces intermediate values for the viscosity and density under the action of a possible artificial diffusion of the color function and physical characteristics spreading over few mesh grid cells. The accuracy of both methods is shown to be highly

dependent to the mesh grid resolution (see section 2.5).

To avoid these discrepancies, we can estimate the values of the viscosity and density in a discontinuous way (Eq. 2.14), where we use the location of the interface ($C = 0.5$) to determine the values of the viscosity and density. No average calculation is needed in this method, giving thus very accurate results (see section 2.5).

$$\begin{cases} \rho = \rho_0 \text{ and } \mu = \mu_0 \text{ if } C \geq 0.5 \\ \rho = \rho_1 \text{ and } \mu = \mu_1 \text{ else} \end{cases} \tag{2.14}$$

We show in section (2.5) the influence of each method of calculation on the accuracy of the results, through the example of a two-dimensional two-phase Poiseuille flow.

2.4 Governing equations system for two-phase flows

To summarize, let $\mathbf{u}$ be the velocity field, C the volume of fluid function, p the pressure, $\mathbf{g}$ the gravity vector, t the time, σ the surface tension coefficient, k the average curvature of interface, $\mathbf{n}_i$ its normal, δ_i a Dirac function indicating the interface being considered as a jump in terms of physical properties, K the permeability coefficient, ρ the density and μ the dynamic viscosity, where ρ_0, ρ_1, μ_0 and μ_1 are the densities and the viscosities in the respective considered media, the conservation equation system which describes the entire hydrodynamic and geometrical processes involved in the motion of multi-phase media now reads:

$$\nabla \cdot \mathbf{u} = 0 \tag{2.15}$$

$$\begin{aligned} \rho \left(\frac{\partial \mathbf{u}}{\partial t} + (\mathbf{u} \cdot \nabla)\mathbf{u} \right) + \mathbf{B}_{\mathbf{u}}(\mathbf{u}^{n+1} - \mathbf{u}_\infty) &= \rho \mathbf{g} - \nabla p \\ &+ \nabla \cdot [\mu(\nabla \mathbf{u} + \nabla^T \mathbf{u})] \\ &+ \sigma k \mathbf{n}_i \delta_i - \frac{\mu}{K} \mathbf{u} \end{aligned} \tag{2.16}$$

$$\frac{\partial C}{\partial t} + \mathbf{u} \cdot \nabla C = 0 \tag{2.17}$$

$$\begin{cases} \rho = \rho_0 \text{ and } \mu = \mu_0 \text{ if } C \geq 0.5 \\ \rho = \rho_1 \text{ and } \mu = \mu_1 \text{ else} \end{cases} \tag{2.18}$$

in the numerical domain and $-\dfrac{\partial \mathbf{u}}{\partial \mathbf{n}} = \mathbf{B_u}(\mathbf{u} - \mathbf{u}_\infty)$ on the lateral boundaries, $\mathbf{B_u}$ being a matrix (see section 2.2.1).

2.5 Validation: two-dimensional two-phase Poiseuille flow

We give in appendix B the analytical solution for the problem of a two-dimensional laminar two-phase Poiseuille flow. The solution is valid in the case of a horizontal stratification of two incompressible non-miscible viscous fluids flowing between two horizontal parallel fixed walls. The motion is driven by a pressure gradient imposed between the two right and left lateral boundaries of the canal. The two fluids are initially at rest. Then, the flow tends to a laminar state.

On one hand, this test-case allows us to validate our numerical model for the modelling of two-phase flow configurations and, on the other hand, to estimate the significance of the choice for the physical properties method of calculation (continuous or discontinuous - see section 2.3.3).

In our configuration, the interface between the gas and the liquid is located in the middle of the channel, which is $H = 0.02\ m$ high and $L = 1\ m$ long. The imposed pressure gradient is $\Delta p = 1\ Pa$. We have based our convergence study on the variation in the number of mesh grid points along the height of the channel. For each case, we have calculated the difference between the analytical solution (see section B) and the computed velocity profile, as $e_{max} = max\|u_{analytical} - u_{numerical}\|/u_{analytical}$.

We consider that we have reached a stationary state when the flow is divergence free and the flow characteristics do not vary anymore to a 10^{-15} level. We keep the same numerical parameters for all simulations to do pertinent comparisons.

We start with a one-phase configuration ($\mu_2/\mu_1 = 1$ and $\rho_2/\rho_1 = 1$), the numerical domain being discretized into 4×32 Cartesian grids. Figure (2.1) shows that, whatever the method of calculation for the densities and viscosities, the velocity profiles are merged with the analytical solution, to a 10^{-15} computer error.

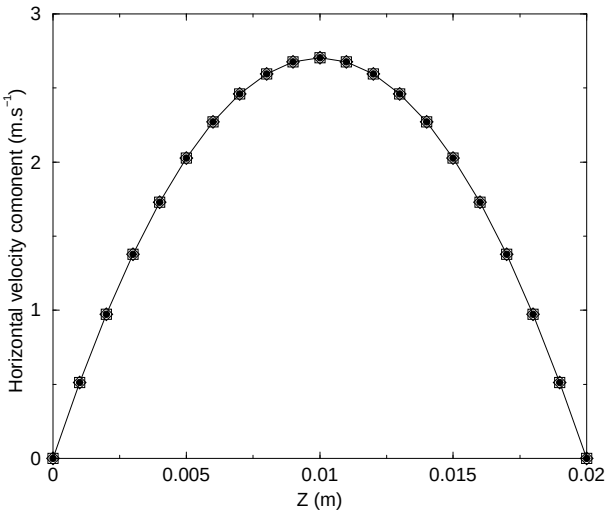

Figure 2.1: Horizontal velocity component profiles are plotted against the channel height for a $\mu_2/\mu_1 = 1$ and $\rho_2/\rho_1 = 1$ configuration. Line: analytical solution (see section B); $\diamond$: equation (2.14); $\square$: equation (2.12); $\bullet$: equation (2.13).

We have then simulated a two-phase configuration, with $\mu_1 = 5.10^{-4}$ and $\mu_2 = 1.85\ .10^{-5}$ ($\rho_2/\rho_1 = 1$). We present in figures (2.2 a) and (2.2 b) the comparison between the analytical solution for the horizontal velocity profile as a function of the channel height and our numerical results with continuous average calculations of the viscosity (Eqs. 2.12 and 2.13). For each case, continuous linear and harmonic averaging calculations, we show the evolution of the solutions depending on the mesh grid resolution.

As shown by Benkenida and Magnaudet (2000), depending on the method of calculation, the interface can be shifted from its real position ($C = 0.5$). Due to the continuous linear averaging, the most viscous fluid becomes preponderant (Fig. 2.2 a), whereas a continuous harmonic averaging tends to impose the lowest viscous fluid in the control volume (Vincent, 1999). Anyway, it is clear in figures (2.2) that the continuous harmonic averaging gives much better results than the continuous linear averaging. Moreover, both methods show a mesh grid resolution dependency, the finer the mesh grid is, the better the solution becomes. We show in figure (2.3) the comparison between the analytical solution for the horizontal velocity profile as a function of the channel height and our numerical results with a discontinuous determination of the viscosity (Eqs. 2.14) for a 4×32 mesh grid resolution. It can be seen that the black spots showing the numerical results for the horizontal velocity are merged with the solid line presenting the analytical solution, to a 10^{-15} computer error. We find no mesh grid resolution dependency as the same accuracy is found for a 4×16 or a 4×256 mesh grid.

It is then the latest method (Eq. 2.14) which will be used in this study.

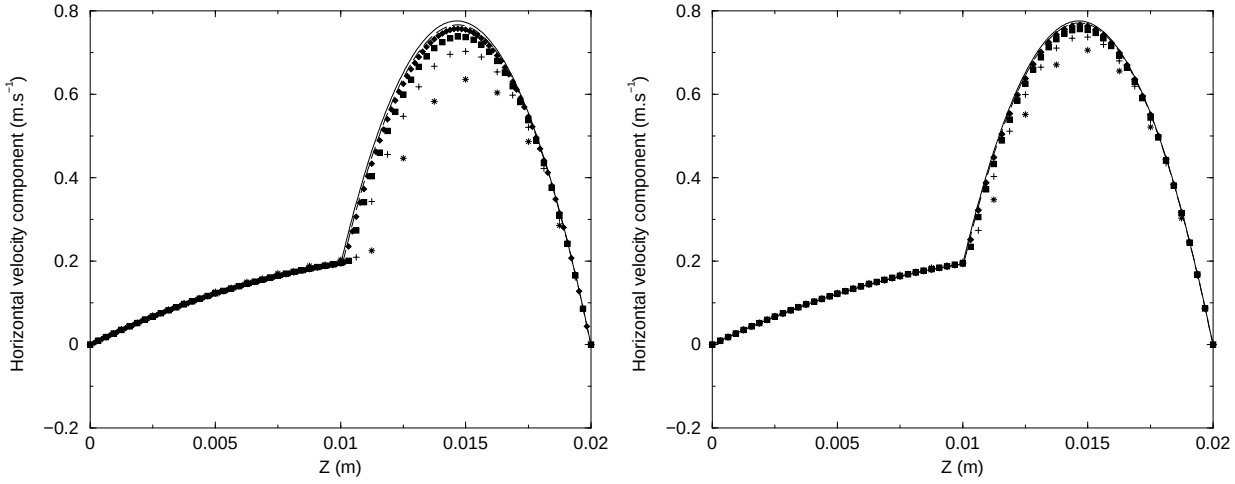

(a) Continuous linear averaging

(b) Continuous harmonic averaging

Figure 2.2: Horizontal velocity component profiles are plotted against the channel height for a $\mu_1 = 5.10^{-4}$ and $\mu_2 = 1.85\ .10^{-5}$ configuration. Line: analytical solution; $*$: 4×16; $+$: 4×32; ■: 4×64; ♦: 4×128; dashed-line: 4×256.

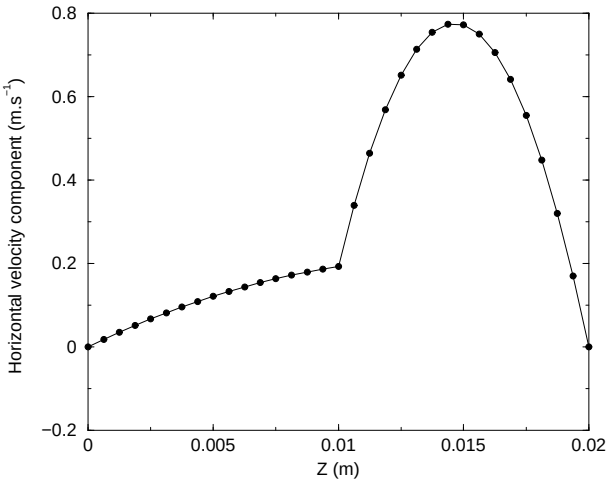

Figure 2.3: Horizontal velocity component profiles are plotted against the channel height for a $\mu_1 = 5.10^{-4}$ and $\mu_2 = 1.85\ .10^{-5}$ configuration. Solid line: analytical solution; •: equation (2.14).

Summary and conclusion

A detailed description of the numerical methods dedicated to the resolution of the governing equations (see section 2.4) for modelling of a two-phase flow has been presented in the present chapter.

An original augmented Lagrangian method is proposed and illustrated for the numerical simulation of multi-phase flows. The linear algebra problem is solved numerically with an iterative Bi-CGSTAB (Bi-Conjugate Gradient Stabilised) algorithm, preconditioned under a Modified and Incomplete LU (MILU) algorithm.

A Finite-Volume method on a staggered mesh is implemented to discretize the Navier-Stokes equations through a second-order Euler scheme, or GEAR scheme, on the time derivatives. A second-order Centered scheme, a first-order Upwind scheme or a second-order Hybrid Centered scheme can be devoted to the non-linear convective term, whereas a second-order Centered scheme is chosen for the approximation of the viscous and the augmented Lagrangian terms.

The interface tracking is achieved by Volume Of Fluid methods (PLIC-VOF or Lax-Wendroff TVD scheme), which are both able to handle accurately with interface reconnections in the modelling of three-dimensional two-phase flows.

The numerical tool has been carefully validated with the simulation of two-dimensional two-phase Poiseuille flows. The numerical results for the horizontal velocity are found to be in an excellent agreement with the analytical solution, to a 10^{-15} computer error. We find no mesh grid resolution dependency for the accuracy of the numerical results.

No turbulence model is used at this point, the governing equations being directly solved. The following section introduces the Large Eddy Simulation method which has been implemented in Aquilon during this study.

Chapter 3

Large Eddy Simulation - LES

Introduction

A Navier-Stokes solver and numerical methods for two-phase flow problems have been presented and validated in the previous chapter. An appropriate numerical model for the wave breaking problem should be able to describe accurately the phenomena occurring at all the scales of the problem. The contribution of the present work has then consisted in implementing in Aquilon the Large Eddy Simulation (LES) method. Large Eddy Simulation is not only used to simulate standard and academic flows, but is now very generally implemented to study complex engineering-like applications. The originality of this work is to apply this technique to turbulent two-phase flows.

The objective of this chapter is to present the concepts and the subgrid-scale turbulence models that has been implemented and validated using Aquilon during this study:

- the concept of turbulent viscosity is considered to remove energy from the resolved scales, mimicking the drain associated with the energy cascade
- the Smagorinsky Model, the Turbulent Kinetic Energy Model and the Mixed-Scale Model, have been implemented to model the subgrid energy dissipation
- a dynamic procedure has been added to improve the subgrid-scale models performance
- the numerical code is validated with the three-dimensional channel flow
- the filtered system of equations governing the one-phase flow is extended to a two-phase flow configuration

3.1 Position of the problem

Numerical resolution of the Navier-Stokes equations (see section 2.4) applied to unstationary turbulent two-phase flow problems should take into account the dynamics existing at all the temporal and spatial scales. This requires a very fine spatial and temporal discretizations of the governing equations, respectively smaller than the characteristic length and time associated with the smallest dynamically active scale in the flow.

The numerical resolution of the Navier-Stokes equations for unstationary problems has been well improved thanks to the rapid increasing of the computing skills.

In general, three main distinct approaches exist for turbulence modelling:

- The Direct Numerical Simulation (DNS) is the most straightforward method. The governing equations are solved without any modelling simplification or assumptions. All the scales of the flow are supposed to be resolved thanks to a sufficiently fine mesh grid. The numerical schemes are also assumed to be the less dispersive and dissipative possibly. The only numerical errors are then those introduced by the numerical approximation. Given the large number of discretizations points needed to simulate directly a turbulent flow (proportional to the 9/4 power of the Reynolds number Re), DNS has been limited to low Re numbers and simple geometries.

- The Reynolds Averaged Navier-Stokes Equations (RANS) describe the evolution of mean quantities. The method is based on the splitting of the velocity field into a time averaged part and a fluctuating component. The RANS equations are found by applying the Reynolds' averaging to the Navier-Stokes equations. The effect of turbulence appears in the Reynolds stress term that has to be modelled to close the system of equations. The most used RANS models are the $k-\epsilon$ model, the RNG model, the v^2-f model or the $k-l$ model (Glockner, 2000).

- Large Eddy Simulation (LES) is an intermediate method, which allow to reach unstationary information to a lower computational cost. This kind of simulation only solves the large scales which drive the flow dynamics, whereas the small scales are modelled thanks to a so-called *subgrid-scale model* (SGS). Simulations can be run with coarser mesh grids which cannot take into account the small dissipative scales of the flow. The separation between the resolved and the modelled scales is mathematically formalized by applying a convolution filter to the Navier-Stokes equations, which introduces the notion of *cut-off length*.

3.2 Formulation of the one-phase model

The selection between the large and small scales, which is the basic idea of this technique of LES, implies the definition of these two categories subjected to the determination of a reference length, the cut-off length:

- are called the large scales, or resolved scales, those which characteristic length are greater than the cut-off length
- are called the small scales, or subgrid scales, the others.

These latest will be taken into account through a subgrid-scale model.

The basic idea of the LES is then to deliberately separate the large scales from the rest of the flow, this being achieved thanks to a filtering technique detailed hereafter.

Thus, the largest eddies which contain the energy of the flow are completely solved. The extra terms, called subgrid terms, appearing during the filtering process of the governing equations and representing the interactions between small and large eddies, are modelled by introducing closure assumptions for the filtered system of equations.

3.2.1 The filtering operation

The filtering of a given space-time variable $f(x,t)$ is obtained in real space by applying a convolution product between the function f to be filtered and the defined filter function $G(x,t)$ (Eq. 3.1):

$$\overline{f(x,t)} = \int_{-\infty}^{+\infty} \int_{-\infty}^{+\infty} f(y,t')G(x-y,t-t')dydt' \tag{3.1}$$

The cut-off scales associated to the filter function $G(x,t)$ in space and time are respectively $\overline{\Delta}$ and $\overline{\tau}$. The non-resolved part of the variable $f(x,t)$, related to the subgrid scales, denoted $f'(x,t)$, is then defined in the physical domain as (Eq. 3.1):

$$f'(x,t) = f(x,t) - \overline{f(x,t)} \tag{3.2}$$

The choice of the spatial filter is intrinsically linked to the method of simulation which is used. The Finite-Volume method in physical space is generally associated to a top-hat filter, *i.e.* the value in the center of the control volume is the result of an integration over the elementary mesh grid of discretization. As a consequence, all the large eddies, which

size is strictly greater than the mesh grid $\overline{\Delta}$, called cut-off length, are calculated thanks to the governing equations in every mesh grid points.

Among the classical filters used for LES in real space, the top-hat filter is defined as (Eq. 3.3):

$$G(x) = \begin{cases} 1/\overline{\Delta} \text{ if } |x| \leq \overline{\Delta}/2 \\ 0 \text{ otherwise} \end{cases} \tag{3.3}$$

in a mono-dimensional case.

Applying a low-pass frequency filter to the governing equations, the filtering operation introduces exclusively the effect from the smallest eddies, which are not resolved due to the mesh grid size, to the larger eddies.

3.2.2 Classical filtered one-phase Navier-Stokes equations

The governing equations of the large eddy simulation in real space are obtained by filtering the system of equations (2.1):

$$\nabla \cdot \overline{\mathbf{u}} = 0 \tag{3.4}$$

$$\begin{aligned} \rho \left(\frac{\partial \overline{\mathbf{u}}}{\partial t} + (\overline{\mathbf{u}} \cdot \nabla)\overline{\mathbf{u}} \right) &= \rho \mathbf{g} - \nabla \overline{p} \\ &+ \nabla \cdot [\mu(\nabla \overline{\mathbf{u}} + \nabla^T \overline{\mathbf{u}})] - \frac{\mu}{K} \overline{\mathbf{u}} - \nabla \cdot \tau \end{aligned} \tag{3.5}$$

where $\overline{p}$ and $\overline{\mathbf{u}}$ are, respectively, the filtered pressure and velocity fields, which are the new unknowns of the problem.

The effect of the small scales appears in the momentum equation (Eq. 3.5) through the subgrid-scale tensor τ, which has to be expressed as a function of the filtered variable $\overline{\mathbf{u}}$ and a subgrid-scale velocity, defined as the decomposition $\mathbf{u}' = \mathbf{u} - \overline{\mathbf{u}}$. So, we introduce the subgrid-scale stress term τ, defined as (Eq. 3.6):

$$\tau = \overline{\mathbf{u}} \otimes \overline{\mathbf{u}} - \overline{\mathbf{u} \otimes \mathbf{u}} \tag{3.6}$$

These equations govern the evolution of the large energy-carrying scales of motion, for a one-phase problem. The information coming from the small scales being lost, their effect is gathered in this subgrid-scale stress term τ, which contains the interactions between resolved and subgrid scales.

This subgrid-scale stress term has now to be modelled.

3.2.3 Physical subgrid-scale models

As already detailed previously, the main role of the subgrid-scale model is to remove energy from the resolved scales. Thus, most subgrid-scale models are eddy-viscosity models, the differences between the models found in the literature lying in the formulation of this eddy-viscosity. In most cases, the equilibrium assumption is made to simplify the problem: the small scales are in equilibrium, and dissipate entirely and instantaneously all the energy they receive from the resolved ones. So the forward energy cascade mechanism to the subgrid scales is modelled explicitly using the hypothesis stating that the energy transfer mechanism from the resolved to the subgrid scales is analogous to the molecular mechanisms represented by the diffusion term, in which the viscosity ν appears.

So the energy cascade mechanism will be modelled by a term having a mathematical formulation similar to that of molecular diffusion, in which the molecular viscosity μ in equation (3.5) is completed with an eddy viscosity, or subgrid viscosity, denoted μ_T. We then have (Eq. 3.7):

$$\rho\left(\frac{\partial\overline{\mathbf{u}}}{\partial t}+(\overline{\mathbf{u}}\cdot\nabla)\overline{\mathbf{u}}\right) = \rho\mathbf{g}-\nabla\overline{p^*}+\nabla\cdot[(\mu+\mu_T)(\nabla\overline{\mathbf{u}}+\nabla^T\overline{\mathbf{u}})]-\frac{\mu}{K}\overline{\mathbf{u}} \tag{3.7}$$

Assuming a linear relationship between the deviatoric part of the subgrid tensor τ^D and the resolved deformation rate tensor $\overline{S}$, the unknown term τ has then been replaced with (Eq. 3.8):

$$\tau^D=\tau-\frac{1}{3}\mathbf{Tr}(\tau)Id=-2\mu_T\overline{S} \tag{3.8}$$

with $\overline{S}=\frac{1}{2}(\nabla\overline{\mathbf{u}}+\nabla^T\overline{\mathbf{u}})$. The isotropic part of the subgrid stress tensor being injected in the pressure term, which is now called the modified pressure and denoted $p*=\overline{p}+\frac{1}{3}\tau_{kk}$, where $\tau_{kk}=\mathbf{Tr}(\tau)$.

The eddy viscosity $\nu_T = \frac{\mu_T}{\rho}$ has now to be modelled, as a function of the resolved variables. In the following, the cut-off length $\overline{\Delta}$ is chosen to be calculated as the cube root of the cell volume (Eq. 3.9):

$$\overline{\Delta} = (\Delta x \Delta y \Delta z)^{\frac{1}{3}} \tag{3.9}$$

where Δx, Δy and Δz are the sizes of the mesh grids in the respective directions X, Y and Z (Deardorff, 1970).

Smagorinsky model

The eddy viscosity, based on the resolved scales, is defined as (Eq. 3.10):

$$\nu_T(\mathbf{x}, t) = \left(C_s \overline{\Delta}\right)^2 |\overline{S}| \tag{3.10}$$

where $|\overline{S}| = \sqrt{\left(2\overline{S}_{ij}\ \overline{S}_{ij}\right)}$ and C_s is the Smagorinsky constant (Smagorinsky, 1963), which takes values between 0.18 and 0.23 in the case of homogeneous isotropic turbulent flows. It must be decreased to 0.1 in the case of shear, near solid boundaries, or transitional flows (*e.g.* channel flow).

This constant is determined thanks to the following relation (Eq. 3.11):

$$C_s = \frac{1}{\pi}\left(\frac{3C_k}{2}\right)^{-\frac{3}{4}} \tag{3.11}$$

in the case of an infinite Kolmogorov energy cascade $E(k) = C_k \epsilon^{\frac{2}{3}} k^{-\frac{5}{3}}$, in isotropic turbulence of kinetic energy spectrum $E(k)$ (Lilly, 1967). We then have $C_s \simeq 0.18$ for $C_k = 1.4$, which is the usual value admitted for the Kolmogorov constant C_k.

The main problem of this model is its simplicity: it affects the flow as soon as the resolved velocity field contains spatial variations. This model is unable to describe the transition between a laminar to a turbulent state of a flow. Even worst, a turbulent flow can be relaminarized due to the eddy viscosity calculation. The eddy viscosity does not vanish near solid walls, this causing the destruction of the coherent flow structures due to a too high dissipation rate. Subsequently, the model is often corrected with the Van Driest damping law (Eq. 3.12):

$$\nu_T = \nu_T(1 - exp\ (-z^+/A)) \tag{3.12}$$

where A is a constant taken to be equal to 25. z^+ is the distance from the solid boundaries in wall units, $z^+ = \frac{z u_\tau}{\nu}$, with u_τ being the wall shear velocity (see section 3.3.2).

Turbulent Kinetic Energy model (TKE)

The eddy viscosity ν_T is determined as a function of the cut-off length $\overline{\Delta}$ and the kinetic energy of the subgrid modes q^2_{SGS} (Bardina et al., 1980). This subgrid kinetic energy is supposed to be equal to the kinetic energy at cut-off q_c^2, evaluated in real space as (Eq. 3.13):

$$q^2_{SGS}(\mathbf{x},t) \equiv q_c^2(\mathbf{x},t) = \frac{1}{2}\,\overline{\mathbf{u}(\mathbf{x},t)}'\,\overline{\mathbf{u}(\mathbf{x},t)}' \tag{3.13}$$

where the *test field* velocity ($\overline{\mathbf{u}}'$) can be evaluated thanks to an explicit *test filter* applied to the resolved scales, $\widetilde{(.)}$ (Eq. 3.14):

$$(\overline{\mathbf{u}}') = \overline{\mathbf{u}} - \widetilde{\overline{\mathbf{u}}} \tag{3.14}$$

The test filter is associated with the cut-off length $\widetilde{\overline{\Delta}} > \overline{\Delta}$. This test field velocity represents the high frequency part of the resolved velocity field. So:

$$\nu_T(\mathbf{x},t) = C_{TKE}\,\overline{\Delta}\,(q^2_{SGS}(\mathbf{x},t))^{\frac{1}{2}} \tag{3.15}$$

The constant C_{TKE} is generally taken to be equal to 0.2.

The Mixed Scale model

The Mixed Scale model (Sagaut, 1998) is derived by taking a weighted geometric average of the two previously detailed models. This model then exhibits a triple dependency on the large and small structures of the resolved field as a function of the cut-off length. The eddy viscosity is defined as (Eq. 3.16):

$$\begin{aligned} &\nu_T = {\nu_{T(Sm)}}^{\alpha}\,{\nu_{T(TKE)}}^{1-\alpha} \\ &\nu_T(\mathbf{x},t) = C_M \overline{\Delta}^{1+\alpha}\left(|\overline{S}|\right)^{\frac{\alpha}{2}}(q^2_{SGS}(\mathbf{x},t))^{\frac{1-\alpha}{2}} \end{aligned} \tag{3.16}$$

with:

- C_M is a constant evaluated from the values of the constants from the Smagorinsky and TKE models, such that $C_M = (C_s)^{2\alpha}(C_{TKE})^{1-\alpha}$. In the following, the constant will be chosen as $C_M = 0.06$.

- a new parameter α which value varies between 0 and 1. Generally, and in the following, α is taken to be equal to 0.5. If $\alpha = 0$, we get the TKE model, whereas if $\alpha = 1$, we find the Smagorinsky model.

The use of this model does not require any complementary wall model, as the Smagorinsky model does, because the eddy viscosity vanishes when the kinetic energy at cut-off tends to zero. So does it near solid walls.

3.2.4 Improvement of subgrid-scale models

Some work has been produced to improve the simulation results by adapting the subgrid models better to the local state of the flow. We choose to implement some of these techniques.

Structural sensor

In order to improve the previously detailed subgrid-scale models, we can use a sensor based on local information of the flow (David, 1993). This sensor, or selection function, is related to the local angular fluctuations of the vorticity ω.

This sensor locally checks if the flow is of fully turbulent developed type. The selection criterion is based on an estimation of the angle θ between the instantaneous vorticity vector ω and the local average $\tilde{\omega}$, which is determined by applying a test filter to the instantaneous vorticity vector. The threshold angle θ_0 has been identified to be around the value of 20 (David, 1993).

The angle θ is given by (Eq. 3.17):

$$\theta(\mathbf{x}) = \arcsin\left(\frac{\| \tilde{\omega}(\mathbf{x}) \otimes \omega(\mathbf{x}) \|}{\| \tilde{\omega}(\mathbf{x}) \| \cdot \| \omega(\mathbf{x}) \|}\right) \tag{3.17}$$

A function is then developed to modulate the subgrid-scale model when the angle θ is less than the threshold angle θ_0 (Eq. 3.18):

$$f_{\theta_0}(\theta) = \begin{cases} 1 \text{ if } \theta \geq \theta_0 \\ r(\theta)^n \text{ otherwise} \end{cases} \tag{3.18}$$

where n is in practice taken to be equal to 2. r is the function defined as $r(\theta) = \dfrac{\tan^2(\theta/2)}{\tan^2(\theta_0/2)}$ (Sagaut, 1998).

The selection function is used as a multiplicative factor of the eddy viscosity, calculated through a chosen subgrid-scale model. This leads to what is called a selective model (Eq. 3.19):

$$\nu_T^{slc} = \nu_T(\mathbf{x}, t) f_{\theta_0}(\theta(\mathbf{x})) \tag{3.19}$$

where the constant that appears in the subgrid-scale model has to be multiplied by a factor 1.65, evaluated on the basis of isotropic homogeneous turbulence simulations, in order to keep the same average eddy viscosity value over the whole domain.

Dynamic procedure to compute the constants

Another technique of better adapting subgrid-scale models to the local state of the flow, Germano et al. (1991) developed an algorithm which can be used for any subgrid-scale models. It consists in computing automatically the constant at each point in space and at each time step, the constant being now denoted $C_d = C_d(\mathbf{x}, t)$.

A test filter is used, still denoted $\widetilde{(\cdot)}$. Coarser than the previous one, denoted $\overline{(\cdot)}$, its characteristics length $\widetilde{\overline{\Delta}}$ is greater than the characteristic length $\overline{\Delta}$ associated to the implicit filter.

Rewriting equation (3.8)under a symbolic form, two tensors, τ and T, are respectively associated to the first and second filtering levels, such that (Eq. 3.20):

$$\begin{aligned} \tau_{ij}^d &= C_d f_{ij}(\overline{\Delta}, \overline{u}) \\ T_{ij}^d &= C_d f_{ij}(\widetilde{\overline{\Delta}}, \widetilde{\overline{u}}) \end{aligned} \tag{3.20}$$

under the assumption that the two subgrid tensors can be modelled by the same subgrid-scale model $f_{ij} = -2\mu_T \overline{S}$ with the same constant C_d, for both filtering levels.

This approach is based on the Germano identity (Germano, 1992), which states that the subgrid tensors corresponding to two different levels of filtering can be related through an exact relation. This can be formulated as (Eq. 3.21):

$$\begin{aligned} L_{ij} &= T_{ij} - \widetilde{\tau_{ij}} \\ L_{ij} &= \widetilde{\overline{\mathbf{u}} \otimes \overline{\mathbf{u}}} - \widetilde{\overline{\mathbf{u}}} \otimes \widetilde{\overline{\mathbf{u}}} \end{aligned} \tag{3.21}$$

where K is a tensor determined directly, as $\overline{\mathbf{u}}$ is a resolved field of the problem and the test filter is known.

Equation (3.21) can be written as (Eq. 3.22)

$$L_{ij} = C_d f_{ij}(\widetilde{\overline{\Delta}}, \widetilde{\overline{u_i}}, \widetilde{\overline{u_j}}) - C_d \widetilde{f_{ij}}(\overline{\Delta}, \overline{u_i}, \overline{u_j}) \tag{3.22}$$

If we assume that the constant does not vary over the test filter length, (Lilly, 1992) proposes calculating the constant C_d by a least-squares method. To do so, we introduce the residual E_{ij} (Eq. 3.23):

$$\begin{aligned} E_{ij} &= L_{ij} - \tfrac{1}{3} L_{ij} \delta_{ij} - C_d M_{ij} \\ M_{ij} &= f_{ij}(\widetilde{\overline{\Delta}}, \widetilde{\overline{u_i}}, \widetilde{\overline{u_j}}) - \widetilde{f_{ij}}(\overline{\Delta}, \overline{u_i}, \overline{u_j}) \end{aligned} \tag{3.23}$$

This definition is made of six independent equations, which gives six values for the constant C_d. To obtain a unique value of the constant, the constant C_d is a solution of the problem formulated as follows (Eq. 3.24):

$$\frac{\partial E_{ij} E_{ij}}{\partial C_d} = 0 \tag{3.24}$$

A unique value is obtained for the dynamic constant C_d through the relation (Eq. 3.25) :

$$C_d = \frac{L_{ij}\ M_{ij}}{M_{kl}\ M_{kl}} \tag{3.25}$$

This technique gives the following properties:

- the technique does not modify the subgrid-scale models, but only adjust locally the constant

- the constant C_d can cancel out in some region of the flow
- it is not bounded.

Some of these properties are interesting, but in order to solve some numerical instability problem, a treatment has to be done to the calculation of the constant to guaranty the good numerical behavior of the model.

Some treatments are proposed:

- averaging the constant in space (Germano et al., 1991)
- averaging in space and time (Zang et al., 1993)
- bounding the constant and the eddy viscosity Zang et al. (1993)
- combining these treatments (Zang et al. (1993)).

The averaging procedures, denoted $< . >$, can be defined in two non-equivalent ways (Zhao and Voke, 1996): by averaging the numerator and denominator separately, or by averaging the constant itself (Eqs. 3.26 and 3.27):

$$C_d = \frac{< L_{ij}\ M_{ij} >}{< M_{kl}\ M_{kl} >} \tag{3.26}$$

or

$$C_d =< C_d >= \left\langle \frac{L_{ij}\ M_{ij}}{M_{kl}\ M_{kl}} \right\rangle \tag{3.27}$$

Bounding the constant and the eddy viscosity is used to guaranty that the following conditions will be verified:

- $\nu + \nu_{sm} \geq 0$ (dissipation positive or zero)
- $C_d \leq C_{max}$ (upper bound).

Practically, C_{max} is of the order of the theoretical value of the Smagorinky constant $C_{max} \simeq 0.2^2$.

3.2.5 Explicit discrete filtering

The subgrid-scale models used in the framework of the implementation and validation study of the LES method in Aquilon imply two levels of filtering:

- the first level is a frequency filtering, denoted $\overline{(\cdot)}$ (see section 3.2.1), which associated characteristic length is $\overline{\Delta}$
- the second level is an explicit discrete filtering, called test filtering, denoted $\widetilde{(\cdot)}$, which associated characteristic length is $\widetilde{\overline{\Delta}}$.

Some subgrid-scale models and improvement techniques detailed previously need the definition of the latest level of filtering:

- the Turbulent Kinetic Energy and Mixed Scale models (see sections 3.2.3 and 3.2.3)
- the structural sensor (see section 3.2.4)
- the dynamic determination of the constant (see section 3.2.4).

As already mentioned through the previous sections, the associated characteristic length of the test filter is defined as $\widetilde{\overline{\Delta}} > \overline{\Delta}$. We choose $\widetilde{\overline{\Delta}} = 2\overline{\Delta}$, because it is the value which is the most used and seems to give the best results (Calmet, 1995; Zhao and Voke, 1996; Sergent, 2000; Sagaut et al., 1999; Montreuil, 2000; Sagaut et al., 2002).

It has been shown that the results were very sensitive to the definition of this explicit discrete filter (Sagaut and Grohens, 1999).

All the variables to be filtered are located on the middle of the computational cells. The explicit discrete filter is a linear combination of the neighboring values (Sagaut, 1998; Sagaut and Grohens, 1999). A three-dimensional test filter results from the tensorial product of the following mono-dimensional three-points filter (Eq. 3.28):

$$\widetilde{\overline{f_i}} = \frac{1}{6}(\overline{f}_{i+1} + 4\overline{f_i} + \overline{f}_{i-1}) \tag{3.28}$$

this weighted average being obtained by applying the Simpson rule to compute the average of the resolved variable $\overline{f}$ over the control cell surrounding the i^{th} point.

This formula is valid for a uniform cartesian mesh grid, but most of the authors apply it to non-uniform mesh grids, considering the error as negligible. We do so, keeping in mind this approximation in the following.

3.3 Simulation of the turbulent three-dimensional incompressible plane channel flow

The channel flow test-case is a very well documented configuration in literature and represents a reference in terms of turbulent shear flow near a solid wall. This case study will allow us to validate the subgrid-scale models and the associated numerical techniques implemented in Aquilon. We will compare and discuss our numerical results with respect to the published works of Moin and Kim (1982); Kim et al. (1987); Deschamps (1988); Calmet (1995); Sagaut et al. (1999); Montreuil (2000); Sagaut et al. (2002).

3.3.1 Computational domain and grid spacing

The choice of the geometrical characteristics of the numerical domain is ruled by some criteria.

First of all, the spatial resolution must be fine enough not to loose too much information of the flow, the basic idea of the LES method being to assume that the large resolved structures of the flow are mainly responsible for the turbulent transport. The point is to identify and localize accurately which are these structures and their representative sizes. Whatever the Reynolds number, there is a near wall area where the viscous effects are preponderant, the viscous sublayer. We can define non-dimensional quantities, indicated with the superscript $(.^+)$, scaled by the wall variables:

- wall unit: $\mathbf{x}^+ = \dfrac{\mathbf{x}u_\tau}{\nu}$
- time unit: $t^+ = \dfrac{tu_\tau^2}{\nu}$
- non-dimensional velocity: $\mathbf{u}^+ = \dfrac{\mathbf{u}}{u_\tau}$

The viscous sublayer goes from $z^+ = 0$ (wall position) to $z^+ = 5$. As Kline et al. (1967), we have chosen a non-uniform mesh grid size in the direction normal to the walls, the first discretization point being located at $z^+ = 1$ above the wall. We chose to compare our results to those of Kim et al. (1987), who performed DNS of the flow, and Montreuil (2000), who run LES. So we used the same transformation (Eq. 3.29) to give the location of grid points in the normal direction:

$$\begin{cases} z_j = \dfrac{1}{a}\tanh[\xi_j \arg\tanh(a)] \\ \text{with } \xi_j = -1 + 2(j+1)/(N_z - 1) \text{ and } \quad j = 1, ..., N_z \end{cases} \tag{3.29}$$

where a is an adjustable parameter ($0 < a < 1$) which controls the distribution of grid points near the walls. The larger the value of a is, the more grid points will be near the walls. In our case, we use $a = 0.98346$ in order to have five points distributed in the viscous sublayer.

In the case of a flow near a solid wall, turbulence originates in the vicinity of the walls. Kline et al. (1967) numerically observed the occurrence of organized structures of high- and low-speed, called *streaks*, in this area. They are the unique characteristics of the wall-layer flow. These streaks are formed with a series of thin filaments of fluid, alternately fast and slow, stretched in the flow direction (streamwise) and finely spaced in the transverse direction of the mean flow (spanwise). They have a mean length corresponding to a thousand of wall units and a mean spacing corresponding to a hundred of wall units. These structures have been numerically and experimentally studied (Jeong et al., 1997; Zhou et al., 1999; Adrian et al., 2000; Tomkins and Adrian, 2003).

The turbulent flow between two parallel infinite planes being homogeneous in the streamwise and spanwise directions of the flow, periodic conditions are imposed with respect to these directions.

The computational domain must be large enough to contain the largest structures of the flow. The artificial periodic conditions must not influence the statistics of the solution. The selection of the size of the computational domain in the streamwise and spanwise directions is ruled by the two-point correlations measurements of Comte-Bellot (1963). This has been shown to be verified if the streamwise length is taken to be equal to $4\pi\delta$ and the spanwise length $\pi\delta$, with δ the channel half-height. The mesh grid size is uniform with respect to these directions. The computational domain is discretized into $64 \times 64 \times 68$ grid points.

3.3.2 Definitions

Space and time-averaging

LES or DNS gives unstationary solutions for the velocity and pressure fields. We will then discuss the results in terms of mean values. Moreover, in order to control the global evolution of the flow, we define a spatial statistical operator, denoted $< . >$. The directions

parallel to the walls are supposed to be homogeneous, so any characteristic variable f of the flow can be averaged with respect to these homogeneous directions:

$$< f > (z,t) = \frac{1}{L_X L_Y} \int_{-L_X/2}^{+L_X/2} \int_{-L_Y/2}^{+L_Y/2} f(x,y,z,t) dx dy \tag{3.30}$$

The space-averaged quantities will be denoted $< . >$ and the fluctuations with respect to the mean value will be denoted with a prime ($.'$). We will indicate if the variables are space-averaged (functions of space and time (z,t)) or both space and time-averaged (functions of space (z)) thanks to the following notations.

If $\overline{\mathbf{u}}$ is the resolved quantity from LES, its time-averaged value is denoted $\overline{\mathbf{U}}$ and its space-averaged value $< \overline{\mathbf{u}} >$, while the space and time-averaged value is $< \overline{\mathbf{U}} >$. The fluctuations will be denoted $\overline{\mathbf{U}}' = \overline{\mathbf{u}} - \overline{\mathbf{U}}$ and $\overline{\mathbf{u}}'' = \overline{\mathbf{u}} - < \overline{\mathbf{U}} >$ (which are different from the subgrid quantity $\mathbf{u}'$ defined in section 3.2.2).

Flow rate, bulk mean velocity and skin friction coefficient definitions

The flow rate Q is given by:

$$Q = \frac{1}{L_Z} \int_{-L_Z/2}^{+L_Z/2} < \overline{\mathbf{u}} > dz \tag{3.31}$$

The bulk mean velocity is defined as:

$$U_m = \frac{1}{L_Z} \int_{-L_Z/2}^{+L_Z/2} < \overline{\mathbf{U}} > dz \tag{3.32}$$

The skin friction coefficient is then:

$$C_f = \frac{2u_\tau^2}{U_m^2} = \frac{\tau_w}{\frac{\rho}{2} U_m^2} \tag{3.33}$$

with the wall shear stress τ_w defined as $\tau_w = \mu \left. \frac{\partial u}{\partial z} \right|_{z=0}$ and the wall shear velocity given by $u_\tau = \sqrt{\frac{\tau_w}{\rho}}$.

3.3.3 Initial conditions and flow characteristics

Three Reynolds numbers defines the flow:

1. the Reynolds number, based on the wall shear velocity u_τ and the channel half-height δ, is $Re_\tau = \dfrac{u_\tau \delta}{\nu} \simeq 180$

2. the Reynolds number, based on the mean centerline velocity U_c and the channel half-height δ, is $Re_c = \dfrac{u_\tau \delta}{\nu} \simeq 3300$

3. the Reynolds number, based on the bulk mean velocity U_m and the channel half-height δ, is $Re_m = \dfrac{U_m 2\delta}{\nu} \simeq 5600$.

We summarize the given initial data of the three-dimensional plane channel geometrical configuration:

- the computational box is $L_x = 4\pi\delta$ long, $L_y = \pi\delta$ wide and $L_z = 2\delta$ high, with δ the channel half-height,

- which gives the non-dimensional length ${L_x}^+ = 2262$, width ${L_y}^+ = 566$ and height ${L_z}^+ = 360$,

- it is discretized into $64 \times 64 \times 68$ grid points,

- the non-dimensional mesh grid sizes is $\Delta x^+ = 35$, $\Delta y^+ = 8.8$ and the first mesh grid point is located at $\Delta z^+ = 1$

We choose to initiate our velocity field, as proposed by Deschamps (1988), Calmet (1995) or Montreuil (2000), by a two-dimensional disturbance flow with finite amplitude ϵ_{2D} and a three-dimensional disturbance flow with amplitude ϵ_{3D}, taken to be respectively equal to 0.2 and 0.02, superimposed upon a laminar Poiseuille flow $U_{Poiseuille}$:

$$U_0(x, t = 0) = U_{Poiseuille}(z) + Re(0.1\ U_{2D}(z)\ e^{i\alpha x} + 0.01\ U_{3D}(z)\ e^{i(\alpha x + \beta y)}) \qquad (3.34)$$

where U_{2D} and U_{3D} are chosen such that U_0 is divergence free. The coefficients α and β are taken to be equal to $\alpha = \dfrac{1}{L_x}$ and $\beta = \dfrac{1}{L_y}$ (Montreuil, 2000).

This corresponds to a superimposition of Tollmein-Schlichting waves, the basic idea being that the disturbance should amplify. The transition from a laminar to a turbulent state is then forced.

The transition mechanisms are summarized in picture (3.1).

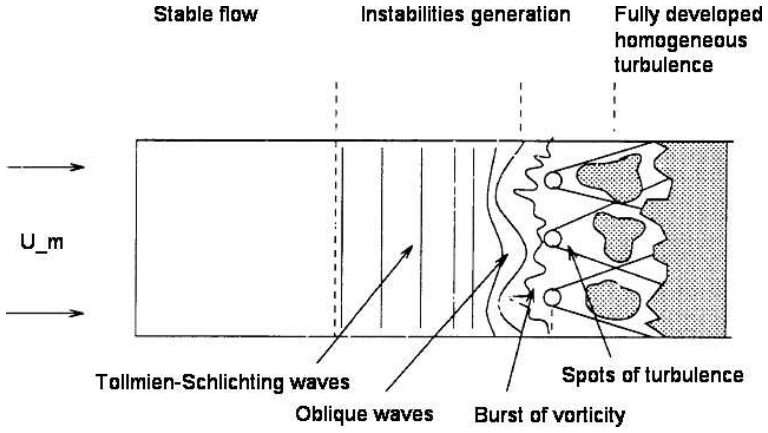

Figure 3.1: Example of the transition mechanisms from laminar to turbulent flow in a boundary layer over a flat plate (Arbez, 1998).

3.3.4 Boundary conditions

Periodic conditions are used in the directions parallel to the walls, and no-slip conditions are imposed on the velocity field at the solid walls.

Time evolution of a transitional flow may be simulated by imposing a constant mean pressure gradient equals to its initial laminar value or by imposing a constant flow rate condition. As shown by Deschamps (1988), the best solution is the latest. It has been proved that this technique has two advantages: a quicker disturbance and a better time evolution of the flow are observed. On the contrary, imposing a negative value for the constant mean pressure gradient has a more stabilizing effect, tends to relaminarize the flow and do not allow to keep a constant bulk mean velocity.

To maintain a constant flow rate Q (Eq. 3.32), the mean pressure gradient $\Delta p(t)$ has to be readjusted at each time step Δt. The following scheme (Deschamps, 1988) is implemented into the numerical procedure:

$$\Delta p^{n+1} = \Delta p^n + \alpha(Q^{n+1} - Q_0) + \beta(Q^n - Q_0) \tag{3.35}$$

where Q_0 is the initial flow rate.

3.3.5 Turbulent structures

As already explained in introduction, the large structures carrying all the flow energy are resolved by LES. We then have a picture of the structures present in the flow, as long as they are bigger than the mesh grid cell length.

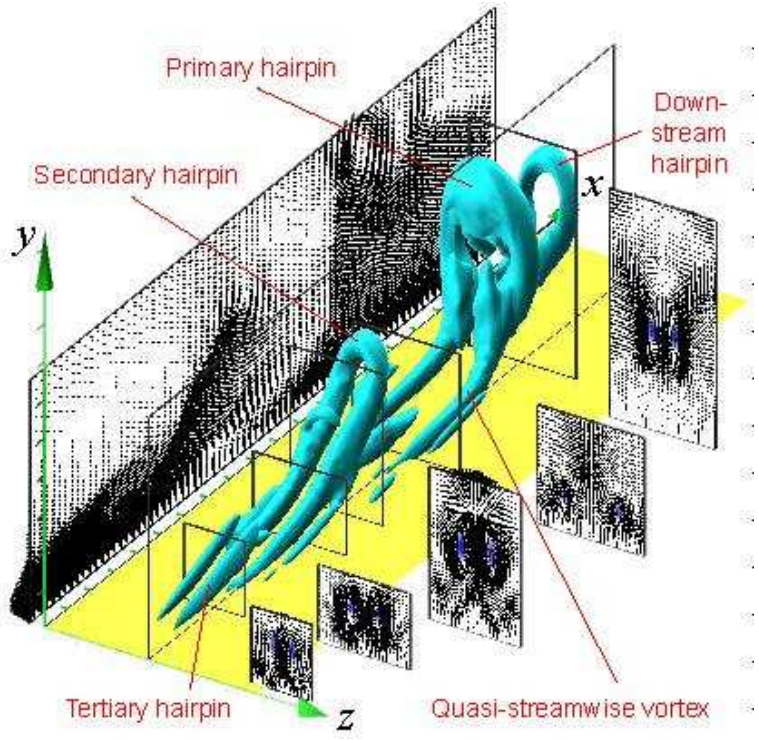

Figure 3.2: Generation of hairpin vortices (Zhou et al., 1999).

To observe these eddies, we examine the statistical information through the two-points correlations, contour plots of instantaneous velocity and vorticity fields, and the respective fluctuations.

Moin and Kim (1982) and Kim et al. (1987) show flow visualizations of turbulent boundary layers done with particle tracking. Coherent packets of low- and high-speed fluid (with respect to the mean local velocity) appears: hydrogen-bubble flow illustrates the formation of low- and high-speed streaks, showing non-parallel trajectories, distorted by the instantaneous velocity field. The flow presents a striped aspect where dark and light streaks alternate.

Kline et al. (1967) observed these organized structures and highlighted a repetitive behavior of low-speed streaks which, at first rise from the wall, oscillate and finally burst and eject fluid far away from the walls. Kline et al. (1967) qualified the whole process *bursting* or *ejection*. Low-speed packets of fluid are also brought near the walls by the main mean flow, this process being called *sweep*. These thin stretched streaks have been shown to be responsible for the generation of various forms of large eddies, *e.g.* the hairpin vortices (Fig. 3.2):

It is obvious that LES is not the most appropriate method to observe accurately these

eddied and their generation mechanisms, due to the coarse mesh grids used and the low spatial resolution. Nevertheless, this method remains very effective because it is able to give access to the overall process.

The distinctive feature of the flow patterns is this existence of highly longitudinally elongated regions of high-speed fluid located adjacent to the low-speed regions. They have been shown to be absent in the regions away from the walls.

The streaks are associated to negative or positive velocity fluctuations. To visually highlight the sweep and bursting events, the quadrant method is usually used. We examine the instantaneous velocity fluctuations field $\overline{\mathbf{u}}'' = \overline{\mathbf{u}} - < \overline{\mathbf{U}} >$, the longitudinal and normal components being:

$$\begin{aligned} \overline{u}'' &= \overline{u} - < \overline{U} > \\ \overline{w}'' &= \overline{w} - < \overline{W} > \end{aligned} \tag{3.36}$$

The quadrant method allow us to study the flow by analyzing the sign of the instantaneous velocity fluctuations, separated into four categories:

1. the first quadrant, associated with $\overline{u}'' > 0$ and $\overline{w}'' > 0$, points out an ascending rapid fluid motion

2. the second quadrant, associated with $\overline{u}'' < 0$ and $\overline{w}'' > 0$, points out the ejection away from the walls of a slow fluid motion

3. the third quadrant, associated with $\overline{u}'' < 0$ and $\overline{w}'' < 0$, points out a descending slow fluid motion

4. the fourth quadrant, associated with $\overline{u}'' > 0$ and $\overline{w}'' < 0$, points out the sweep event of a rapid fluid motion

The distance between the streaks increases as we go away from the walls, until they disappear from the flow in the core of the flow.

3.3.6 Results

For this chosen configuration, two large eddy simulations of the channel flow are run with two subgrid-scale models, the selective versions of the Smagorinsky model (SM) and the Mixed Scale Model (MS).

$$Re_\tau = \frac{u_\tau \delta}{\nu} \simeq 180 \qquad \frac{U_m}{u_{tau}} \simeq 15.63$$

$$Re_c = \frac{U_c \delta}{\nu} \simeq 3300 \qquad \frac{U_c}{u_{tau}} \simeq 18.20$$

$$Re_m = \frac{U_m 2\delta}{\nu} \simeq 5600 \qquad \frac{U_c}{U_m} \simeq 1.16$$

$$C_f = \frac{\tau_w}{\frac{\varrho}{2} U_m^2} \simeq 8.18 \times 10^{-3}$$

Table 3.1: Mean flow quantities computed by (Kim et al., 1987).

The numerical results are validated by comparing the mean values of the resolved quantities. Dean (1978) suggested the correlations of $C_f = 0.073\ Re_m^{-0.25}$ and $\frac{U_c}{U_m} = 1.28\ Re_m^{-0.0116}$. The results obtained by Kim et al. (1987) are summarized in table (3.1).

The SM and MS simulations give the results given in tables (3.2) and (3.3), respectively. It can be seen that we are in similar flow conditions than those computed by (Kim et al., 1987). Indeed, we are about 5.56% under the targeted Reynolds number based on the wall shear velocity, Re_τ, and only 0.2 % under the targeted Reynolds number based on the bulk mean velocity, Re_m. We also find that our computed Reynolds numbers, based on the mean centerline velocity, Re_c, are 5 % and 4.1 % under the DNS value for the SM and MS simulations, respectively.

We can observe that the values of the centreline velocity U_c and the skin friction velocity u_τ are underpredicted. We can also check that, as expected, the MS simulation gives improved results compared to those computed with the SM simulation. The level of calculated errors are of the same order compared to the errors obtained by Sagaut et al. (1999); Montreuil (2000); Sagaut et al. (2002), considering the SM simulation, but are slightly higher compared to the computed results from the MS simulation. Sagaut et al. (1999); Montreuil (2000); Sagaut et al. (2002) also found overpredicted values for the skin friction velocity u_τ, whereas we find underpredicted computed values.

Considering the ratio of the mean centerline velocity to the mean bulk velocity, we calculate errors of 5 % and 4.1 %, with respect to the value calculated from Dean's correlations, for the SM and MS simulations, respectively. This error suggests that the simulated mean velocity profile is slightly too flat in the center of the channel compared to

$u_\tau \simeq 6.03683 \times 10^{-2}$	$Re_\tau \simeq 170$
$U_c \simeq 1.12$	$Re_c \simeq 3136$
$U_m \simeq 0.9979$	$Re_m \simeq 5589$
$\frac{U_m}{u_{tau}} \simeq 16.53$	$\frac{U_c}{u_{tau}} \simeq 18.55$
$\frac{U_c}{U_m} \simeq 1.12$	$C_f \simeq 7.3213 \times 10^{-3}$

Table 3.2: Mean flow quantities computed with the large eddy simulation computed with the SM model.

$u_\tau \simeq 6.11674 \times 10^{-2}$	$Re_\tau \simeq 170$
$U_c \simeq 1.13$	$Re_c \simeq 3164$
$U_m \simeq 0.9979$	$Re_m \simeq 5589$
$\frac{U_m}{u_{tau}} \simeq 16.31$	$\frac{U_c}{u_{tau}} \simeq 18.47$
$\frac{U_c}{U_m} \simeq 1.13$	$C_f \simeq 7.515 \times 10^{-3}$

Table 3.3: Mean flow quantities computed with the large eddy simulation computed with the MS model.

	SM	MS
Re_τ	5.6	5.6
Re_c	5	4.1
Re_m	0.2	0.2
u_τ	5.6	4.4
C_f	13.3	11
U_m/u_{tau}	- 6.3	- 4.9
U_c/u_{tau}	- 1.2	- 0.75
U_c/U_m	5	4.1

Table 3.4: Computed relative error (in %) on the mean flow quantities, with respect with DNS data (Kim et al., 1987) and the Dean's suggested correlations (Dean, 1978) for the SM and MS simulations.

the real mean velocity profile. This is confirmed by Calmet (1995) who computed a similar level of error and observed that this discrepancy results from a too coarse grid resolution in the flow direction. This trend is confirmed if we have a look at the mean velocity profiles shown in figure (3.3), where we present the comparison between our computed mean velocity profiles normalized by the bulk mean velocity and the DNS data (Kim et al., 1987) as a function of the wall distance normalized by the channel half-height δ. However, we show in figure (3.4) the comparison between the mean velocity profiles as a function of z^+, and we can observe that the present results are in a good agreement compared with the DNS data. The near-wall behavior of the flow is generally well predicted.

We also present in figure (3.5) a comparison between our computed mean velocity profile normalized by the skin friction velocity and the DNS data (Kim et al., 1987). It can be seen that, within the sublayer ($z^+ < 5$), our numerical results are in a very good agreement with the DNS data and follow very well the linear law of the wall, given by the equation $u^+ = z^+$. Then, in the logarithmic region, we observe a discrepancy between our numerical results, the DNS data and the log law given by the equation $u^+ = 2.5\ \ln(z^+) + 5.5$ (Kim et al., 1987).

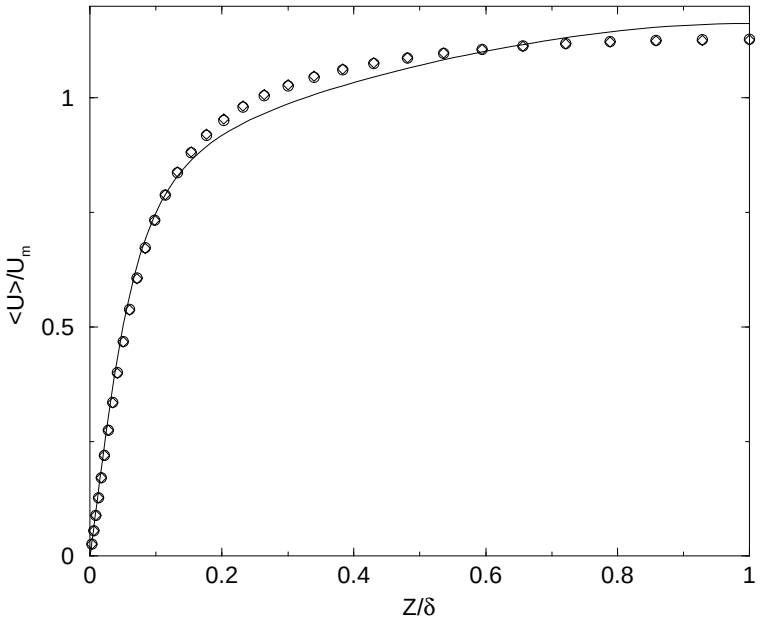

Figure 3.3: Mean velocity profile normalized by the bulk mean velocity as a function of the wall distance normalized by the channel half-height δ. Solid line: DNS (Kim et al., 1987); $\diamond$: SM; $\circ$: MS.

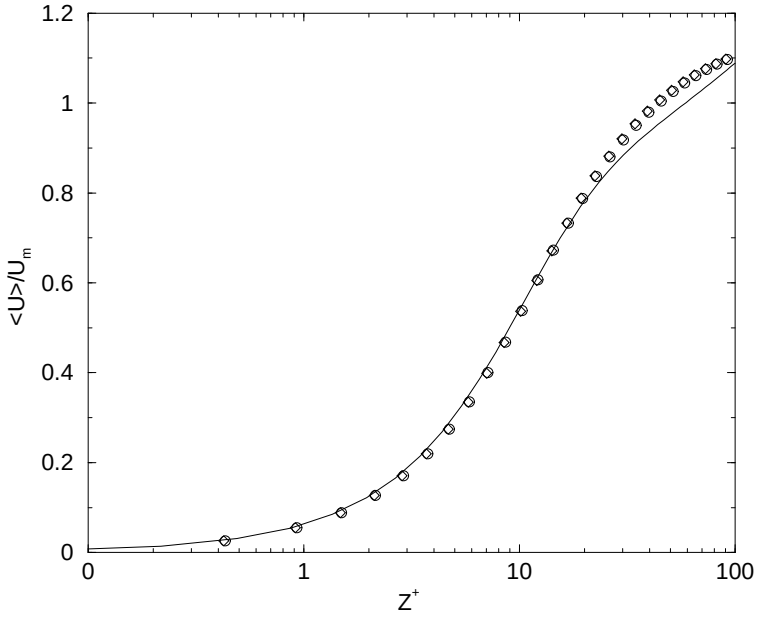

Figure 3.4: Mean velocity profile normalized by the bulk mean velocity as a function of the wall distance z^+. Solid line: DNS (Kim et al., 1987); $\diamond$: SM; $\circ$: MS.

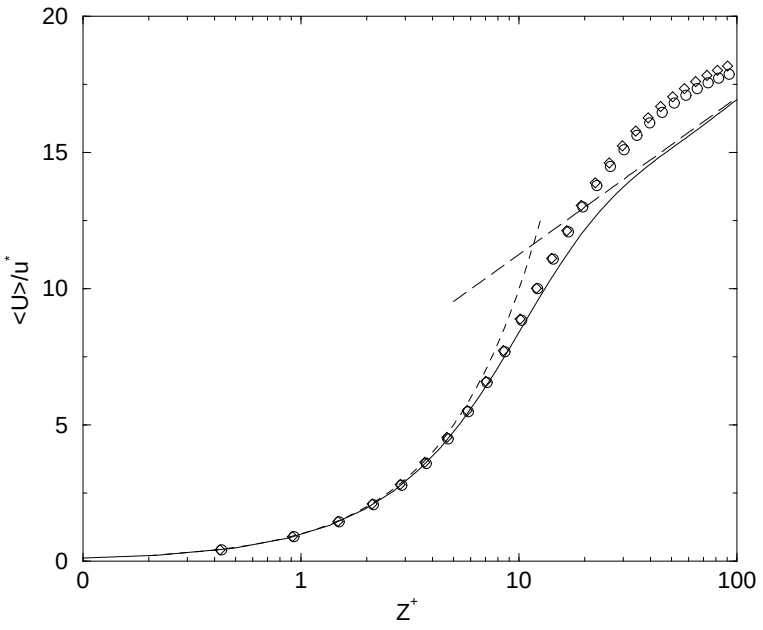

Figure 3.5: Mean velocity profile normalized by the skin friction velocity as a function of the wall distance z^+. Solid line: DNS (Kim et al., 1987); $\diamond$: SM; $\circ$: MS; dashed line: $u^+ = z^+$; long-dashed line: $u^+ = 2.5\ \ln(z^+) + 5.5$.

3.3.7 Conclusion

The selective versions of two subgrid-scale models have been implemented in the numerical tool Aquilon and validated. This test-case leads us to the conclusion that the numerical model gives acceptable results compared to those found in the literature for the description of the three-dimensional incompressible turbulent plane channel flow, with the given geometric configuration and mesh grid resolution.

However, more numerical tests are under consideration with finer mesh grid resolutions to have a clearer idea about the behavior of the discrepancies observed on the mean quantities of the flow to ensure ourselves about the ability of the numerical tool to yield reliable results for the near-wall behavior of the flow. In particular, a direct numerical simulation of the same level of accuracy than the one computed by (Kim et al., 1987) would be of great interest to evaluate our numerical tool. Some other academical test-cases, such as the backward-facing step, are also under consideration to be tested.

The dynamic versions of the subgrid-scale models is now implemented and validations will be undertaken in a near future, but will not be the subject of any development in this document.

3.4 Extension to the two-phase model

3.4.1 Mathematical formulation for a filtered multi-fluid model

We present here the work which is now undertaken to derive the full governing equations system for Large Eddy Simulation of incompressible multi-phase flows.[1] The aim of this study is to try and develop the motion equations for multi-phase flows by carrying out spatial filterings associated to both turbulence (Sagaut, 1998) and phase presence (Drew, 1983; Magnaudet, 1997)). We then formulate turbulent and interface contributions resulting from the filtering and averaging procedures, to derive a completely general formulation of the filtered equations in a conservative form.

Unfiltered equations

In a multi-phase flow consisting of k phases, let us denote the domain occupied by the k^{th} phase as $\mathcal{D}^k$. The most general formulation of conservation of mass and momentum for each phase is given by:

$$\frac{\partial \rho^k}{\partial t} + \nabla \cdot \left(\rho^k u^k\right) = 0 \tag{3.37}$$

$$\frac{\partial \rho^k u^k}{\partial t} + \nabla \cdot \left(\rho^k u^k \otimes u^k + p^k Id\right) - \rho^k g = \nabla \cdot \tau^k \tag{3.38}$$

where g is gravity, Id stands for the identity tensor, and τ^k is the deviatoric stress tensor, defined by:

$$\tau^k = \mu^k \underbrace{\left(S^k - \frac{1}{3} tr\left(S^k\right) Id\right)}_{S_D^k} \quad \text{where} \begin{cases} tr \text{ accounts for the trace of a tensor} \\ S \text{ is the deformation rate } S = \nabla u + \nabla^T u \end{cases}$$

In this work, we assume that the density of the interface is always zero. Therefore, the following so-called jump conditions can be applied (Delhaye, 1974).

The mass transfer of the k^{th} phase at the interface is defined by:

$$\dot{m}^k = \rho^k \left(u^k - W\right) \cdot n^k \tag{3.39}$$

[1] The following section is summarized from the pre-print version of the work which has been submitted by Labourasse et al. (2004).

The mass balance for all phases can then be written as:

$$\sum_k \dot{m}^k = \sum_k \left(\rho^k \left(u^k - W\right) \cdot n^k\right) = 0 \tag{3.40}$$

where W is the speed of displacement of the interface.

The balance of momentum at the interface reads:

$$\sum_k \left(u^k \dot{m}^k - n^k \cdot \left(-p^k Id + \tau^k\right)\right) = \sigma n^k \nabla_s \cdot n^k - \nabla_s \sigma \tag{3.41}$$

where ∇_s is the surface derivative operator along the interface and σ is the associated surface tension.

To work with this formalism, it is convenient to extend the definition of each phase to the whole domain (in order, for instance, to use non-conditional boundary conditions for each phase). In order to properly define these extensions, we have to introduce a definition of the interface of the k^{th} phase, as a function of position and time. The interface corresponds to a $n-1$ dimensional restriction of the n dimensional space and can then formally be defined as a function f^k of space and time as follows:

$$x \in \text{the interface} \Leftrightarrow f^k(x,t) = 0$$

$$\text{with the function } f^k \text{ chosen as } \begin{cases} x \in \text{the } k^{th} \text{ phase} & \Leftrightarrow & f^k(x,t) > 0 \\ x \notin \text{the } k^{th} \text{ phase} & \Leftrightarrow & f^k(x,t) < 0 \end{cases}$$

The sharp phase indicator χ^k can then be defined as:

$$\chi^k = h[f^k] \tag{3.42}$$

where h is the Heaviside function. This indicator has several useful properties:

$$\sum_k \chi^k = 1 \tag{3.43}$$

$$\chi^m \, \chi^n = \delta_{mn} \chi^m \tag{3.44}$$

$$\nabla \chi^k = -n^k \delta_i \tag{3.45}$$

Furthermore, χ^k follows an evolution equation (Kataoka, 1986):

$$\frac{\partial \chi^k}{\partial t} - W \cdot n^k \delta_i = 0 \tag{3.46}$$

where δ_i is defined as the Dirac function centered on the interface. Each interface is considered as the intersection surface between different subdomains $\mathcal{D}^k$. The behavior of each phase for points near the boundary of the subdomains $\mathcal{D}^k$ can be easily described using δ_i. Note that reciprocally, δ_i can be expressed as a function of χ^k and n^k:

$$\delta_i = -n^k \cdot \nabla \chi^k \tag{3.47}$$

Using the equations (3.40-3.45), the governing equations (3.37) and (3.38) for the phase-weighted variables can be written as:

$$\frac{\partial \chi^k \rho^k}{\partial t} + \nabla \cdot \left(\chi^k \rho^k u^k\right) = \rho^k \left(W - u^k\right) \cdot n^k \delta_i \tag{3.48}$$

$$\begin{aligned} \frac{\partial \chi^k \rho^k u^k}{\partial t} + \nabla \cdot \left(\chi^k \left[\rho^k u^k \otimes u^k + p^k Id - \tau^k\right]\right) - \chi^k \rho^k g \\ = \left(\rho^k u^k \otimes \left(W - u^k\right) - p^k Id + \tau^k\right) \cdot n^k \delta_i \end{aligned} \tag{3.49}$$

The jump conditions defined by equation (3.39) appears explicitly in equations (3.48) and (3.49).

Using equation (3.45), equations (3.48) and (3.49) can be written in a pure volumetric form as follows:

$$\frac{\partial \chi^k \rho^k}{\partial t} + \nabla \cdot \left(\chi^k \rho^k u^k\right) = -\rho^k \left(W - u^k\right) \cdot \nabla \chi^k \tag{3.50}$$

$$\begin{aligned} \frac{\partial \chi^k \rho^k u^k}{\partial t} + \nabla \cdot \left(\chi^k \left[\rho^k u^k \otimes u^k + p^k Id - \tau^k\right]\right) - \chi^k \rho^k g \\ = - \left(\rho^k u^k \otimes \left(W - u^k\right) - p^k Id + \tau^k\right) \cdot \nabla \chi^k \end{aligned} \tag{3.51}$$

The system of governing equations defined by equations (3.50) and (3.51) has to be closed owing to thermodynamic relations. The dynamic viscosity μ can be classically assumed as a function of temperature only.

The exact one-fluid formulation

A one-fluid formulation can be obtained by introducing the exact one-fluid variable that is defined as the sum of the phase indicator weighted phases:

$$\phi = \sum_k \chi_k \phi_k \tag{3.52}$$

Summing equations (3.50) and (3.51) on all the phases of the flow, the so-called one-fluid mass and momentum conservation equations are written as:

$$\frac{\partial \rho}{\partial t} + \nabla \cdot (\rho u) = \sum_k \rho^k \left(W - u^k\right) \cdot \nabla \chi^k \tag{3.53}$$

$$\begin{aligned} \frac{\partial \rho u}{\partial t} + \nabla \cdot (\rho u \otimes u + pId - \tau) \quad & -\rho g \\ = \sum_k (\rho^k u^k \otimes \left(W - u^k\right) \quad & -p^k Id + \tau^k) \cdot \nabla \chi^k \end{aligned} \tag{3.54}$$

Using respectively mass jump condition (3.40) and momentum jump condition (3.41), each previous equation becomes:

$$\frac{\partial \rho}{\partial t} + \nabla \cdot (\rho u) = 0 \tag{3.55}$$

$$\frac{\partial \rho u}{\partial t} + \nabla \cdot (\rho u u + pId - \tau) - \rho g = \nabla_s \cdot n^k \sigma n^k \delta_i - \nabla_s \sigma \delta_i \tag{3.56}$$

The transport equation for χ does not give further information, since the equality $\sum_k \left(n^k \delta_i\right) = 0$ is obvious.

The one-fluid formulation has been introduced by Kataoka (1986). It allows the implementation of classical one-phase numerical tools for solving multi-phase flow problems. Nevertheless, we should be cautious when performing simplifications.

Filtering operation

The filtering process detailed in section 3.2 is applied to the previous set of equations, the filtered velocity field being then given by $\overline{u(x,t)} = G \star u$, where G is the filter kernel (see section 3.2.1). The properties of the filtering have been used to obtain a general filtered

formalism. We assume that G commutes with the spatial and time derivation, as it is widely assumed in single-phase LES (Sagaut, 1998). We will assume the same for multi-phase flows, even if such assumption has to be verified (theoretically, the commutation error depends more on the topology of the mesh than on the characteristics of the flow).

The operator is applied to the set of equations (3.48) and (3.49).

Clearly, the filtering of the phase indicator function is of great importance. We set:

$$\alpha^k = \overline{\chi^k} \tag{3.57}$$

It is worth noting that α^k is a "smooth" indicator function and no longer satisfies property (3.44). That is $\alpha^l \alpha^m \neq 0$ because α varies continuously from 0 to 1. However, property (3.43) is always valid, such that $\sum_k \alpha^k = 1$.

The resolved normal vector can be defined as:

$$\begin{cases} \widehat{n^k} = & -\frac{\nabla \alpha^k}{\left|\left|\nabla \alpha^k\right|\right|} & \text{if } \left|\left|\nabla \alpha^k\right|\right| \neq 0 \\ \widehat{n^k} = & 0 & \text{otherwise} \end{cases} \tag{3.58}$$

A formal definition for the "resolved filtered Dirac function" $\widehat{\delta_i}$ is given as $\widehat{\delta_i} = \left|\left|\widehat{n^k}\right|\right|$. Furthermore, following Favre et al. (1976), the "phase-weighted" filtering of the variable ϕ^k is defined as:

$$\alpha^k \widetilde{\phi^k} = \overline{\chi^k \phi^k} \tag{3.59}$$

Under this assumption, the filtered set of equations for multi-phase flow reads:

$$\frac{\partial \alpha^k \widetilde{\rho^k}}{\partial t} + \nabla \cdot \left(\alpha^k \widetilde{\rho^k u^k} \right) = \overline{\rho^k \left(W - u^k\right) \cdot n^k \delta_i} \tag{3.60}$$

$$\begin{aligned} \frac{\partial \alpha^k \widetilde{\rho^k u^k}}{\partial t} + \nabla \cdot \left(\alpha^k \rho^k \widetilde{u^k \otimes u^k} + \alpha^k \widetilde{p^k Id} - \alpha^k \widetilde{\tau^k} \right) & -\alpha^k \widetilde{\rho^k} g \\ = \overline{\left(\rho^k u^k \otimes \left(W - u^k\right) - p^k Id + \tau^k\right) \cdot n^k \delta_i} & \end{aligned} \tag{3.61}$$

The evolution of the phase indicator function has to be added to these three classical equations:

$$\frac{\partial \alpha^k}{\partial t} = \overline{W \cdot n^k \delta_i} \tag{3.62}$$

The non-linear terms have to be modelled as none of them can be directly computed. On the left-hand side of the equation, phase-weighted non-linear terms are introduced, while on the right-hand side, we retrieve filtered interfacial terms. For the multi-fluid formulation (that is a set of equation for each phase), it is more convenient to define $\widetilde{\phi}$ in the following way:

$$\beta^k \widetilde{\phi^k} = \overline{\chi^k \rho^k \phi^k}, \quad \text{where } \beta^k = \overline{\chi^k \rho^k} \tag{3.63}$$

With this formulation, non-linear terms are avoided in the time derivatives. This leads to the following set of equations:

$$\frac{\partial \beta^k}{\partial t} + \nabla \cdot \left(\beta^k \widetilde{u^k} \right) = \overline{\rho^k \left(W - u^k \right) \cdot n^k \delta_i} \tag{3.64}$$

$$\begin{aligned} \frac{\partial \beta^k \widetilde{u^k}}{\partial t} + \nabla \cdot \left(\beta^k \widetilde{u^k \otimes u^k} + \overline{\chi^k p^k} Id - \overline{\chi^k \tau^k} \right) - \beta^k g \\ = \overline{\left(\rho^k u^k \otimes \left(W - u^k \right) - p^k Id + \tau^k \right) \cdot n^k \delta_i} \end{aligned} \tag{3.65}$$

To build a one-fluid filtered formulation, let us define $\overline{\phi}$ as the filtering of the one-fluid variable proposed in equation (3.52):

$$\overline{\phi} = \overline{\sum_k \chi^k \phi^k} \tag{3.66}$$

Using this definition and summing the evolution equations over all the phases, we obtain:

$$\frac{\partial \overline{\rho}}{\partial t} + \nabla \cdot \left(\overline{\rho u} \right) = \overline{\sum_k \left(\rho^k \left(W - u^k \right) \cdot n^k \delta_i \right)} \tag{3.67}$$

$$\begin{aligned} \frac{\partial \overline{\rho u}}{\partial t} + \nabla \cdot \left(\overline{\rho u \otimes u} + \overline{p} Id - \overline{\tau} \right) \quad - \overline{\rho} g \\ = \overline{\sum_k \left(\rho^k u^k \otimes \left(W - u^k \right) - p^k Id + \tau^k \right) \cdot n^k \delta_i} \end{aligned} \tag{3.68}$$

The quantities arising in the right-hand side of equations (3.67) and (3.68) are the overlined counterparts of the jump-condition quantities defined in equations (3.40) and (3.41). Expressions (3.40) and (3.41) can then be used to replace the right-hand-side quantities of the previous equation. It is more convenient, from now, to use as unknown the so-called "Favre average" (Favre et al., 1976) for the velocity field. In this case, a new definition for the filtering of u is employed:

$$\widetilde{u} = \frac{\overline{\rho u}}{\overline{\rho}} \tag{3.69}$$

Closure

The closure of the system is very complicated, giving the thematic of the filtering for multi-phase flows all its interest. The closure terms, which can be evaluated, can be classified into two categories as follows (Labourasse et al., 2004):

- the "classical" subgrid terms, which account for the effects of subgrid scale correlations on the resolved flow, and which arise in the equations from the non-linearities, are common to those found in single-phase turbulence studies, as detailed in section 3.2. Therefore, the modelling work already done on this field (Sagaut, 1998) can be partly used. Nevertheless, all new modelling must tend to classical modelling in the single-phase areas

- the pure interfacial subgrid terms, which take into account the subgrid contribution of the interface characteristics to the flow evolution. In the set of equations (3.67) and (3.68), these terms appear in the right-hand side and can be replaced using the jump conditions given by equations (3.40) and (3.41).

In the present study, isothermal flows are only considered as a preliminary stage. So the subgrid error committed by using thermodynamical and physical laws to represent a mixed phase volume of fluid is not taken into account. Moreover, we focus on the one-fluid model, so all the non-linear terms of the system of equations (3.67) and (3.68) will be written using the resolved variables:

$$\tau_{\phi\psi} = \overline{\phi\psi} - \overline{\phi}\,\overline{\psi} \tag{3.70}$$

where $\tau_{\phi\psi}$ is the subgrid contribution of non-linearity to the filtered evolution equations, and has to be closed using the resolved quantities. From now, the subscripts l and r

are respectively related to left and right-hand-side terms in equations (3.67) and (3.68). Moreover, when this is necessary, the subscript f is added when using the filtering process (Filter2) for the equations (3.82) and (3.83).

Considering the left-hand-side of the equations (3.67) and (3.68), the following terms have to be modelled:

$$\tau_{l\rho u} = \overline{\rho u} - \overline{\rho}\,\overline{u} \tag{3.71}$$

$$\tau_{l\rho uu} = \overline{\rho u \otimes u} - \overline{\rho}\,\overline{u} \otimes \overline{u} \tag{3.72}$$

$$\tau_{l\mu S} = \overline{\tau} - \overline{\mu}\overline{S_D} \tag{3.73}$$

The use of the filtering variable $\widetilde{u}$ allows us to avoid the subgrid scale term into the time derivative. So, no more subgrid terms appear in the right-hand-side of the conservation equation. The new non-linear terms that have to be taken into account owing to the non-linear terms in left-hand-side of the equation are:

$$\tau_{fl\rho uu} = \overline{\rho u \otimes u} - \overline{\rho}\,\widetilde{u} \otimes \widetilde{u} \tag{3.74}$$

$$\tau_{fl\mu S} = \overline{\tau} - \overline{\mu}\overline{S_D} \tag{3.75}$$

In the right-hand-side of the equation, the expression of the subgrid terms does not change.

As observerved by Labourasse et al. (2004), we can note that:

- these subgrid terms are formally not different from those that can be found in filtering a single-phase flow (see section 3.2). However, the order of magnitude of each of them can be non-negligible in the case of multi-phase flows. Indeed, in the case of the term $\tau_{l\mu S}$, for instance, μ can vary sharply through the interface, since it depends on the phases that are considered
- the terms (3.71), (3.72) and (3.73) can be decomposed to make the different phases appear. For instance, let us decompose $\tau_{l\rho u}$ into k phases:

$$\begin{aligned}
\tau_{l\rho u} &= \sum_k \left(\overline{\chi^k \rho^k u^k}\right) - \sum_k \left(\overline{\chi^k \rho^k}\right) \sum_k \left(\overline{\chi^k u^k}\right) \\
&= \sum_k \left(\overline{\chi^k \rho^k u^k} - \overline{\chi^k \rho^k}\;\overline{\chi^k u^k}\right) - \sum_{k \neq l} \left(\alpha^k \widetilde{\rho^k} \alpha^l \widetilde{u^l}\right) \\
&= \sum_k \tau_{l\rho}^k - \sum_{k \neq l} \left(\alpha^k \widetilde{\rho^k} \alpha^l \widetilde{u^l}\right)
\end{aligned} \tag{3.76}$$

the first term on the right-hand side of equation (3.76) being the sum of the classical subgrid terms that exist in each single-phase flow, The second term being a sum of cross terms, which is a peculiar feature of multi-phase flows.

- the time derivatives of the subgrid terms $\tau_{l\rho}$ appear in the momentum equation. This system is then unusable for direct implementation. To avoid these terms, it is possible to sum over k equations (3.64) and (3.65) instead of equations (3.67) and (3.68). This will result into different subgrid-scale terms that has to be modelled. These terms disappear when the filter is applied to conservation equations in non conservative form

- the use of $\overline{\mu}$, for instance, makes difficult the closure of the equation by the classical thermodynamic laws. It may be more convenient to write for example the resolved dynamic viscosity $\widehat{\mu} = \mu\left(\overline{T}\right)$.

For the right-hand side of the equations, two strategies can be used. The first one consists in a direct filtering of the system of equations (3.67) and (3.68). This will lead to a system in which all phase quantities remain on the right-hand side. The second possibility, detailed hereafter, is to replace the right-hand side of the system of equations (3.67) and (3.68) by the filtered quantities coming from the jump conditions (3.40) and (3.41).

The exact jump conditions given by equations (3.40) and (3.41) is then used to derive a new system of filtered equations. Note that the commutation error between the filter and the surface derivatives cannot be generally assumed to be zero. The generalized surface gradient and divergence are then defined as follows:

$$\nabla_s\varphi = (Id - n\otimes n)\cdot\nabla\varphi \iff \widehat{\nabla_s}\varphi = (Id - \widehat{n}\otimes\widehat{n})\cdot\nabla\varphi \tag{3.77}$$

$$\nabla_s\cdot\psi = (Id - n\otimes n) : \nabla\psi \iff \widehat{\nabla_s}\cdot\psi = (Id - \widehat{n}\otimes\widehat{n}) : \nabla\psi \tag{3.78}$$

Then, the error committed in commuting the filter and the surface derivative will introduce new subgrid scale error terms that have to be calculated.

The right-hand-side subgrid contributions are:

$$\tau_{r\rho} = 0 \tag{3.79}$$

$$\tau_{rnn} = -\overline{\sigma n\nabla_s\cdot n\delta_i} + \overline{\sigma}\widehat{n}\widehat{\nabla_s}\cdot\widehat{n} \tag{3.80}$$

$$\tau_{r\sigma} = \overline{\nabla_s\sigma} - \widehat{\nabla_s}\overline{\sigma} \tag{3.81}$$

no contribution appearing from the right-hand side for the mass conservation equation.

This strategy leads to a simpler set of equations, than the first detailed by Labourasse et al. (2004):

$$\frac{\partial \overline{\rho}}{\partial t} + \nabla \cdot (\overline{\rho}\ \widetilde{u}) = 0 \tag{3.82}$$

$$\begin{aligned} \frac{\partial \overline{\rho}\ \widetilde{u}}{\partial t} + \nabla \cdot (\overline{\rho}\ \widetilde{u} \otimes \widetilde{u} + \overline{p} Id - 2\overline{\mu S_D} \quad & + \tau_{fl\rho uu} + \tau_{l\mu S}) - \overline{\rho} g \\ & = \overline{\sigma \widehat{n}} \widehat{\nabla_s} \widehat{n} - \widehat{\nabla_s} \overline{\sigma} + \tau_{rnn} + \tau_{r\sigma} \end{aligned} \tag{3.83}$$

using the Favre-filtered variable $\widetilde{u}$.

This formulation is employed for performing the applications shown by Labourasse et al. (2004).

As explained in section 2.3, the numerical simulations are run with a Piecewise Linear Interface Construction (VOF-PLIC) method of Youngs (1982) using the Continuum Surface Force (CSF) method (Brackbill et al., 1992) for the treatment of the surface tension. Without phase change, this equation degenerates into:

$$\frac{\partial \alpha^k}{\partial t} + u \cdot \nabla \alpha^k = 0 \tag{3.84}$$

Filtering this equation, a new subgrid term appears:

$$\tau_C = \overline{u \cdot \nabla \alpha^k} - \overline{u} \cdot \nabla \overline{\alpha^k} \tag{3.85}$$

Conclusion

The complete study (Labourasse et al., 2004), valid for both RANS or LES approaches, is a preliminary step towards complete modelling of the interaction between interface and turbulence. The governing equations for under-resolved systems, written here before, and the specific exhibited multi-phase terms are discussed. Case studies are carried out to conclude about the magnitude of the subgrid tensors appearing in the previous analytical developments.

The work is illustrated with two two-dimensional academic test cases mimicking the turbulence-interface interaction. The test cases of vortices impacting on a bubble and the phase inversion in a closed square box are simulated and commented. *A priori* tests have

been conducted to provide information on the order of magnitude of the subgrid terms that arise with under-resolved calculation, the relative importance of these terms being carefully compared.

Labourasse et al. (2004) has shown the interface to be considered in a sense as a deformable wall, as a phenomenological analysis of the evolution of the kinetic energy highlights the importance of the interfacial terms in the turbulent behavior: the interface absorbs part of the turbulent high-frequency energy and releases it at a lower frequency due to the interface oscillations.

The work consisting in filtering the results of DNS, in order to evaluate the magnitude of the new subgrid terms, brings these two main conclusions:

- the most important term remains the inertia term as in single-phase flows. However its behavior is clearly different close to the interface and can no longer be modelled with a viscosity assumption. The other terms are weaker, but not negligible compared to the diffusion term

- when considering flows driven by capillarity and viscosity mechanisms, the conclusions have to be moderated. The classical subgrid acceleration remains the dominant term, but the terms corresponding to the viscosity jump, and the capillary forces are almost of the same order.

Some more work still has to be done to get clear and general conclusions about this innovative study. This implies very challenging new modelling processes beyond the scope of the work proposed by (Labourasse et al., 2004). Moreover, the influences of the numerical methods used to describe the two-phase flow and to discretize the governing equations have to be investigated accurately.

As no closure models are proposed to evaluate the new subgrid terms, a simpler one-fluid model for LES has to be used, with the assumption that the subgrid terms found earlier are considered to be negligible.

3.4.2 Simpler one-fluid model for LES

A much simpler and more tractable one-fluid model for LES can be derived by filtering the system of equations (2.15 and 2.4):

$$\begin{cases} \nabla \cdot \overline{\mathbf{u}} = 0 \\ \rho \left(\dfrac{\partial \overline{\mathbf{u}}}{\partial t} + (\overline{\mathbf{u}} \cdot \nabla)\overline{\mathbf{u}} \right) & = \rho \mathbf{g} - \nabla \overline{p^*} + \nabla \cdot [(\mu + \mu_T)(\nabla \overline{\mathbf{u}} \ + \ \nabla^T \overline{\mathbf{u}})] \\ & \quad + \sigma \ k \ \mathbf{n}_i \ \delta_i - \dfrac{\mu}{K} \ \overline{\mathbf{u}} \end{cases} \tag{3.86}$$

and injecting the resolved velocity field $\overline{\mathbf{u}}$ in equation (2.17). So the color function evolution is now governed by:

$$\frac{\partial C}{\partial t} + \overline{\mathbf{u}} \cdot \nabla C = 0 \tag{3.87}$$

with

$$\begin{cases} \rho = \rho_0 \text{ and } \mu = \mu_0 \text{ if } C \geq 0.5 \\ \rho = \rho_1 \text{ and } \mu = \mu_1 \text{ else} \end{cases} \tag{3.88}$$

This is the classical system of equations which is exclusively used in the literature to run LES of two-phase flows. No assumption is made about the neglected tensors found in the previous section (3.4.1), the one-phase system of equations is used with a non-filtered advection equation.

This being the simpler way of modelling two-phase flows with LES method, and no closure being proposed at this time for all the tensors found in section (3.4.1), we used the latest system of equations to study the breaking waves problem.

Summary and conclusion

We give in this chapter the detailed description of the mathematical formulation for the classical filtered one-phase Navier-Stokes equations. Some subgrid-scale models are introduced for the modelling of the subgrid stress tensor.

These subgrid-scale models have been implemented and validated in Aquilon. The academic three-dimensional incompressible turbulent plane channel flow test-case is detailed.

An introduction to the full filtered multi-fluid model is presented for the Large Eddy Simulation of multi-phase flows, this work being now undertaken intensively. Large efforts still have to be done to propose modelling solutions for the subgrid tensors found by filtering the complete system of equations.

The classical set of filtered governing equations for the two-phase flow problem is finally given.

Chapter 4

Validation and exploitation of the numerical model

Introduction

The breaking wave problem is a very complex phenomenon. The numerical methods have been introduced and validated separately in the previous sections. In the present chapter, the numerical model is utilized to study various wave configurations. It should be mentioned that the test cases include solitary waves, that involve interesting phenomena (see appendix C) and is served by a large number of investigators. Comparisons have been made between the present numerical results and the numerical and experimental results available in the literature for these test cases. The usefulness of LES for modelling two-phase flow configurations, as compared to DNS, is shown. Good agreement with the literature data demonstrates the accuracy and the capability of the present numerical model.

The physical configurations investigated in the present chapter are, from the simpler to the most complicated in terms of breaking and splashing occurrence:

- the breaking of a dam on a wet bottom
- the propagation of solitary waves
- the original configuration of the interactions between solitary waves
- the propagation of solitary waves over various submerged obstacles
- the breaking of solitary waves over sloping beaches

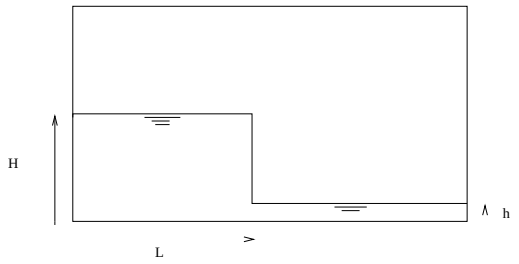

Figure 4.1: Sketch of the initial condition for the dam-break problem.

4.1 Breaking of a dam on a wet bottom

The interest of the dam-break problem is the existence of numerous experimental and theoretical studies which can be used to validate the direct numerical simulation approach for solving air-water free surface flows. The usual configuration found in the literature is the breaking of a dam on a dry bottom. However, a more complex case, in terms of breaking and splashing occurrence, has been studied experimentally by Stansby et al. (1998) for the breaking of a dam on a wet bottom. This situation is extremely interesting as it puts the stress on strong free surface deformations, turbulent flow behavior and dynamic interactions between air and water. The objective in this section is to tackle with this dam-break case to evaluate and validate the numerical methods for a three-dimensional configuration. The present results are compared with with those published by Stansby et al. (1998).

4.1.1 The physical model

As presented in figure (4.1), we consider an idealized three-dimensional dam separating an upstream column of quiescent water of height H and length L, from a downstream region of water of height h. With respect to the work of Stansby et al. (1998) and the dimensions of the experimental flume, the values of H, L and h are 0.1 m, 0.01 m and 0.6 m, respectively. We spread the 2D initial condition along the transverse axis. The computational domain is 1.2 m long, 0.2 m high and 0.4 m wide. The mesh is then $600 \times 100 \times 10$ points. The time step is fixed equal to 2.10^{-4} s to ensure a Courant-Friedrichs-Levy condition less than 1, necessary for the explicit advection of the free surface.

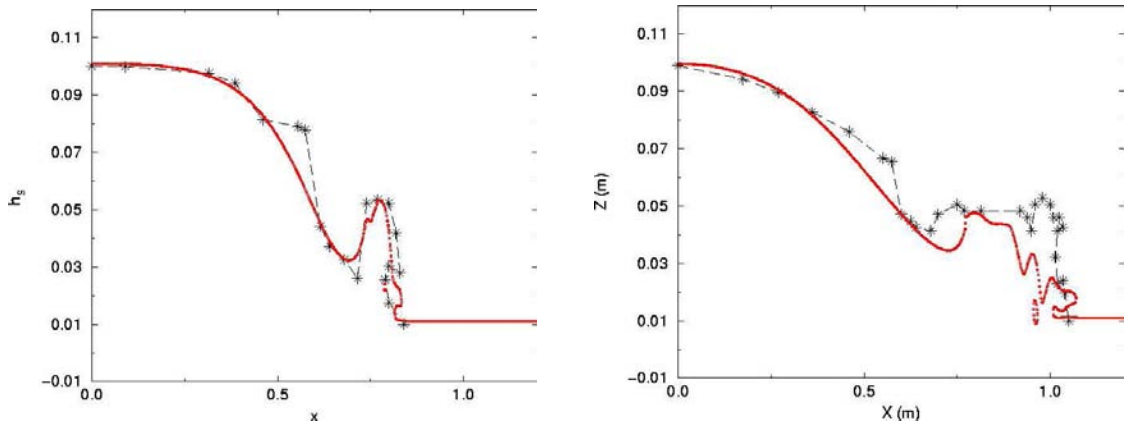

a. t = 0.24 s b. t = 0.40 s

Figure 4.2: Comparison between experimental free surface profiles (∗) and three-dimensional numerical results (solid line).

4.1.2 Comparisons between numerical and experimental results

Water columns of constant depths are initially considered on both sides of the dam, the water being assumed to be at rest. At $t = 0$ s, the dam is suddenly destroyed or removed. Then the flow motion is driven by gravity. Upstream, a rarefaction wave propagates, growing wider and wider during time. A shock wave, or bore, is developed on the downstream side, the water pushing down from above acts somewhat like a piston being pushed downstream with an acceleration (Stoker, 1957). A vertical jet (a *mushroom-like jet*, as called in Stansby et al. (1998)) then occurs. This phenomenon can be compared with what happens during the breaking of waves.

The free surface profiles are compared with those from Stansby et al. (1998) at the same instants (Figs. 4.2). The free surface profiles are taken from the middle slice of the 3D numerical simulation results. A good agreement can be seen in the numerical results, in terms of jet occurrence amplitude and splash-ups behavior.

In figure (4.2 a), we can see that the splash rises as high as the one measured experimentally. The bore propagates at the same speed (Fig. 4.2 b) with the same height and width. The differences observed may come from the fact that Stansby et al. (1998) drawn their free surface profiles from blurred pictures showing a large amount of foam. This is not very accurate and gives a rough idea of the interface location. The velocity fields of water and air regions are shown separately for easy and clear inspection in figure (4.3).

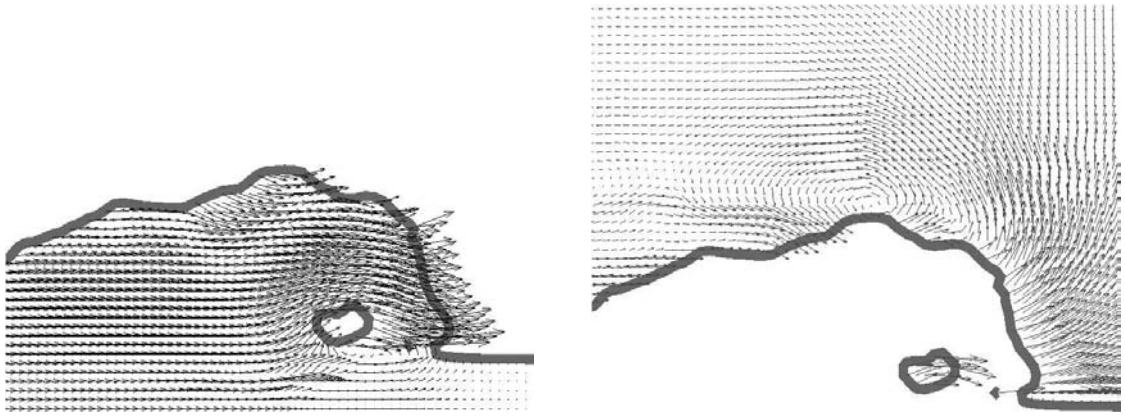

(a) Water (b) Air

Figure 4.3: Velocity field in both media. $t = 0.24\ s$, $C = 0.5$.

The interface is located using the value of $C = 0.5$. It is obvious that the dam-break flow has a fully 3D chaotic behavior. It can be observed that the free surface is distorted due to the interactions with the large eddies in the air. A gas pocket has been observed to be entrapped and is advected in the water.

4.1.3 Conclusions and perspectives

We have found a very good agreement in both profiles and characteristic times for the simulation of the breaking of a dam on a wet bottom, compared to some experimental data. A more detailed investigation of the ability of the numerical model to tackle with the dam-break configuration has been presented by Vincent (1999). The numerical model gives very satisfactory results for this three-dimensional turbulent two-phase problem.

4.2 A solitary wave propagating in a constant water depth

Solitary waves are known for having some interesting properties: indeed, such a wave has a symmetrical form with a single hump and propagates with a uniform velocity without changing form. When simulating two-phase flows, it is important to evaluate the general accuracy of the numerical methods and numerical schemes used by checking for example the balance of mass and energy in the computing domain. Thus, the results of the different solitary wave theories can be used to compute the initial kinematic properties and simulate the waves propagation in constant depths over horizontal beds in periodic

Test-case	ϵ	$d(m)$	H (m)
1	0.11	0.3020	0.03322
2	0.19	0.4046	0.076874
3	0.29	0.2040	0.05916
4	0.70	0.3020	0.2114

Table 4.1: Values of the parameters describing the experiments by Lee et al. (1982), with $\epsilon = H/d$.

domains. The precision of the simulation is assessed by comparing the free surface shapes and velocities to the theoretical values. As our final interest is the complete description of the flow induced by breaking waves over sloping beaches, we need to insure ourselves that the incoming wave will keep its integrity and its characteristics all along its propagation over the varying bathymetry.

In order to verify both the accuracy of the numerical schemes when solving the wave problem and the conservation laws of mass and energy in the computational domain, we model a solitary wave propagating in a constant depth of water over a flat bottom. We use the first-order solitary wave theory for the initial wave shape and wave velocity (see appendix C).

4.2.1 Comparisons between numerical and analytical results

The propagation of solitary waves are simulated in four different configurations, according to the parameters of table (4.1), detailed in appendix C: water particle velocities for various depths and wave profiles are plotted along the time (Lee et al., 1982).

As described in appendix C, the solitary wave is completely defined for a given depth of water, d, and relative amplitude, ϵ. Therefore, it is possible to compare the computed evolution of the wave profiles and velocities during the non-dimensional time $t\sqrt{g/d}$, at various depths, z, to the results of the experiments and to the analytical solutions for the four values of ϵ.

The chosen numerical configuration is to consider an initial solitary wave computed from a chosen analytical theory, any of those presented in appendix C giving good results, except the already mentioned low order solution (Eq. C.8). We will only show the results obtained for test-case 1, with $d = 0.3020\ m$ and $\epsilon = H/d = 0.11$, which gives a crest

ordinate $z = 0.33522\ m$. The initial wave celerity is $c = 1.8134\ m.s^{-1}$, calculated from the first-order theory (Eq. C.3). The crest is located in the middle of the numerical domain at the beginning of the calculation, periodic boundary conditions are imposed in the flow direction. All calculations are made with the densities and the viscosities of air and water ($\rho_a = 1.1768\ kg.m^{-3}$ and $\rho_w = 1000\ kg.m^{-3}$, $\mu_a = 1.85\ \times 10^{-5}\ kg.m^{-1}.s^{-1}$ and $\mu_w = 1.10^{-3}\ kg.m^{-1}.s^{-1}$), and the surface tension ($\sigma = 0.075 N.m^{-1}$). The numerical domain is 10 m long and 0.6 m high. It is discretized into 300×150 regular Cartesian grids. It is obvious that a sufficient number of grid points may be chosen in order to have enough accuracy in the free surface description. We impose a symmetry condition at the lower boundary and a free condition at the upper boundary. The time step is constant and equals $\Delta t = 1.10^{-2}\ s$, which gives 45 s of propagation simulated as we run 4500 iterations.

The analytical models are non dissipative. Therefore, the conservation of mass and energy may be checked during the numerical simulation, the kinetic energy, the potential energy and the total energy being:

$$\begin{aligned} E_k &= \frac{1}{2}\int\int \rho u^2\ dxdy \\ E_p &= \int\int \rho z\ dxdy \\ E_t &= E_k + E_p \end{aligned} \tag{4.1}$$

The integrations are calculated over the whole domain, in the liquid part ($C \neq 0$). We take the bottom $z = 0\ m$ as the reference level for the calculation of the potential energy. We also define zero potential energy corresponding to a non-perturbed surface. We normalize the values of the energies by the respective initial values and we observe that they were well preserved all along the 4500 iterations of the simulations. We did not evaluate the energy dissipation, but it could have been interesting to run simulations until the waves would have been completely damped. The tests aimed only at checking the accuracy of the conservation of mass and energy for a time scale which we will later on consider.

As a matter of fact, an easy check to do is to consider the celerity of the initial wave, estimate the theoretical distance it has to propagate during the time of the simulation and compare it to the final position of the wave crest. We want to carefully check that the solitary wave maintains its original shape as it propagates. We then also calculate the differences between the theoretical and numerical crest ordinates. We also take the opportunity to compare the VOF-PLIC and TVD schemes and the influence of the use of

Schemes	VOF-PLIC		TVD	
Surface tension	With σ	Without σ	With σ	Without σ
z_{fin} (m)	0.33054	0.33054	0.3339	0.3339
Error (m)	-4.68×10^{-3}	-4.68×10^{-3}	-1.32×10^{-3}	-1.32×10^{-3}
Error (%)	-1.4 %	-1.4 %	-4.10^{-1} %	-4.10^{-1} %
x_{fin} (m)	80.85	80.89	81.13	81.17
Error (m)	0.753	0.713	0.473	0.433
Error (%)	0.92 %	0.87 %	0.58 %	0.53 %

Table 4.2: Numerical errors calculated for the solitary wave coordinates (test-case 1).

Schemes	VOF-PLIC		TVD	
Surface tension	With σ	Without σ	With σ	Without σ
$volume_{fin}$ (m^2)	3.109	3.110	3.114	3.114
Error (m^2)	-6.9×10^{-3}	$-6 .10^{-3}$	$-2 .10^{-3}$	$-2 .10^{-3}$
Error (%)	-2.2×10^{-1} %	$-2 .10^{-1}$%	-6.42×10^{-2}%	-6.42×10^{-2}%

Table 4.3: Numerical errors calculated for the mass conservation (test-case 1).

the surface tension σ.

As already mentioned, the calculation domain is periodic in the flow direction, so the wave propagates towards the right side of the domain. During the 4500 iterations, the waves must reach 81.603 m, which has been verified as the wave passed eight times by its initial position (Tab. 4.2). It has been observed that the wave maintains its original shape as it propagates without major distortion. We also checked that the mass was preserved during the computation. Indeed, the amplitude of the solitary wave is approximately constant, as summarized in the following tables (Tabs. 4.2 and 4.3) where we report the numerical errors calculated with the results obtained at the 4500^{th} iteration. The initial crest ordinate and volume are respectively $z_{ini} = 0.33522$ m and $vol_{ini} = 3.116$ m^2, the theoretical final crest abscissa being $x_{fin} = 81.603$ m.

Taking the surface tension into account for the translation of a solitary wave problem has no critical effect on the propagation in time, which could be expected as the curvature

of the free surface is very weak due to the small amplitude of the solitary wave. The TVD scheme gives the best results in terms of free surface description and mass conservation, as we can observe a smoother interface, the small perturbations propagating at the free surface being erased by the numerical dissipation of the scheme. The VOF method, coupled or not with the surface tension, tends to keep, and sometimes amplify, these perturbations coming from the interaction between the gas and the fluid. A rough interface initialization can enhance the occurrence of interface perturbations. The results are anyway very good and could be improved by using a smaller time step, which has been checked by using a time step in order to verify the stability criterion (Courant-Friedrichs-Levy) less than one for the interface algorithm.

4.2.2 Conclusions and perspectives

We have found that the numerical model gives very satisfactory results for this simple propagation problem. We have then checked the ability of the numerical tool to conserve both the mass and energy along the simulation. We have also shown the consequences of each VOF-PLIC and TVD methods on the description of the free surface, in terms of interface locations. The modelling of the surface tension is also tested.

4.3 Interactions between solitary waves

Another major interest, that can be found in solitary waves, is in the types of interaction that can happen between solitary waves, especially the direct, head-on collision between two waves travelling in opposite directions. Maxworthy (1976) carried out two kind of wave interaction experiments. After studying the reflexion occurring when a single wave hits a vertical end wall, Maxworthy compared the case of two waves interacting directly. Three main features were outlined from these experiments. Fisrt, it has been shown that the waves reach a maximum amplitude greater than the sum of the initial wave amplitudes. Moreover, experimental results showed that a collision has some consequences on the waves (in both wave-wave interactions or end-wall reflexions) such as spatial phase shifts and the shedding of secondary weaker waves following the first.

Su and Mirie (1980) developed analytical solutions for calculating the effects of the collision, up to the third order of accuracy. They showed that the waves emerging from the collision preserve their original identities to the third-order of accuracy. They stressed on the fact that the collision does leave imprints on the colliding waves with spatial phase shift and shedding of secondary waves. They also calculated analytically the maximum run-up amplitude reached during the collision of the two solitary waves, as a function of

both propagating wave amplitudes.

The subscripts R and L refers to the right- and left-going waves, respectively, heading towards each other. For two head-on colliding solitary waves with their maximum heights defined as ϵ_R and ϵ_L, the maximum run-up η_m is defined by:

$$\eta_m = \epsilon_R + \epsilon_L + \frac{\epsilon_R\ \epsilon_L}{2} + \frac{3}{8}\epsilon_R\ \epsilon_L(\epsilon_R + \epsilon_L) \tag{4.2}$$

If we consider two identical solitary waves $\epsilon_R = \epsilon_L = \epsilon$, then:

$$\eta_m = 2\ \epsilon + \frac{\epsilon^2}{2} + \frac{3}{4}\epsilon^3 \tag{4.3}$$

However, we will not go any further in the details dealing with the spatial phase shift as both cited authors (Maxworthy, 1976; Su and Mirie, 1980) showed discrepancies in the comparison between the experimental and the analytical results. The basic idea of this section being to show the ability to reproduce numerically the previously described characteristics and to compare our results to those published in order to validate our model, we choose not to talk about this particular point, even if it is a question that would be of interest for us to tackle in the future.

4.3.1 Solitary waves colliding a vertical end-wall

As a first test, a solitary wave hitting a vertical end wall has been simulated with the parameters defined by Maxworthy (1976), who considered that, since the system of two head-on colliding waves of equal amplitude is symmetric about the mid-plane, it can be modelled by a single wave hitting a vertical wall. The water depth is $d = 0.0668\ m$, the amplitude is $\epsilon = 0.31$, which gives a dimensional amplitude $H = 0.020708\ m$ and a maximum waveheight located at $z = 0.087508\ m$. The initial wave celerity is $c = 0.93\ m.s^{-1}$, the experimental celerity measured by Maxworthy (1976) being $c = 0.9255\ m.s^{-1}$. During the interaction between the wave and the wall, we could observe that large vertical accelerations were developed until the wave reached its maximum amplitude. At the instant when the vertical velocity vanishes, the kinetic energy is nil and the potential energy reaches its maximum magnitude, the wave seems to be at rest and then it starts to fall down to propagate towards the other end of the numerical domain. As pointed out by Maxworthy (1976), the wave is then steeper than the incoming wave and propagates faster until it recovers its original shape.

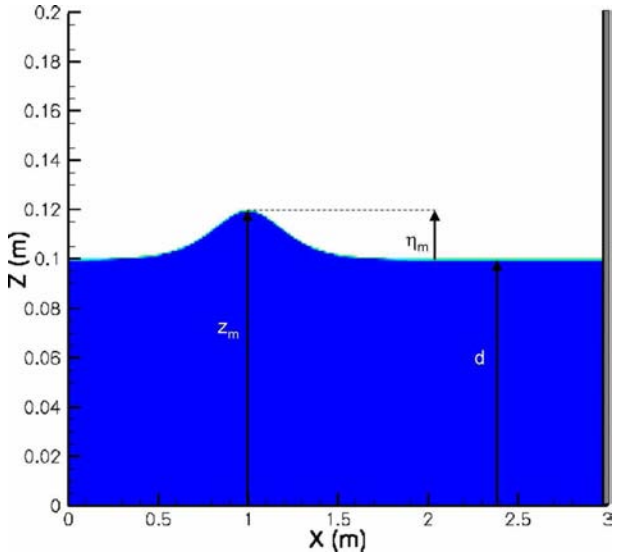

Figure 4.4: Initial conditions for the end-wall collision test-case. $t = 0\ s.$ $\epsilon = 0.2$, $C > 0.5$.

A systematical study has then been done, the water depth being $d = 0.1\ m$, the amplitudes varying from $\epsilon = 0.1$ to $\epsilon = 0.6$. The crests are located at $x_{crest} = 1\ m$ at the beginning of the calculation. All calculations are made with the densities and the viscosities of air and water ($\rho_a = 1.1768\ kg.m^{-3}$ and $\rho_w = 1000\ kg.m^{-3}$, $\mu_a = 1.85 \times 10^{-5}\ kg.m^{-1}.s^{-1}$ and $\mu_w = 1.10^{-3}\ kg.m^{-1}.s^{-1}$). The numerical domain is 3 m long and 0.2 m high. It is discretized into 600×200 regular Cartesian grids. We impose a symmetry condition at the lower boundary and a free condition at the upper boundary. The simulation time step is chosen to verify the stability criterion (Courant-Friedrichs-Levy) less than one for the interface algorithm. We illustrate hereafter (Figs. 4.4, 4.5 and 4.6) the different steps of the collision for the case $\epsilon = 0.2$, which gives a dimensional amplitude $H = 0.02\ m$ and a maximum waveheight located at $z = 0.12\ m$. The initial wave celerity is $c = 1.085\ m.s^{-1}$. We can see the wave propagating towards the right boundary of the domain (Figs. 4.6 a to c) to reach its maximum run-up $z_m = 0.14058\ m$ ($\eta_m/d = 0.4058$) (Fig. 4.5) at $t = 1.80\ s$, to be compared with the predicted value $z_m = 0.140206\ m$ ($\eta_m/d = 0.40206$) (which gives an error of 0.3 %). The profile shown in figure (4.5) seems to be a propagating wave cut in half.

We show hereafter (Fig. 4.7) the plot of our numerical results compared to those found in literature. We could then observe a very good agreement between our numerical results and those, experimental, numerical and analytical, compiled in Su and Mirie (1980). The general trend is followed with a reasonable accuracy. The discrepancies come from the fact

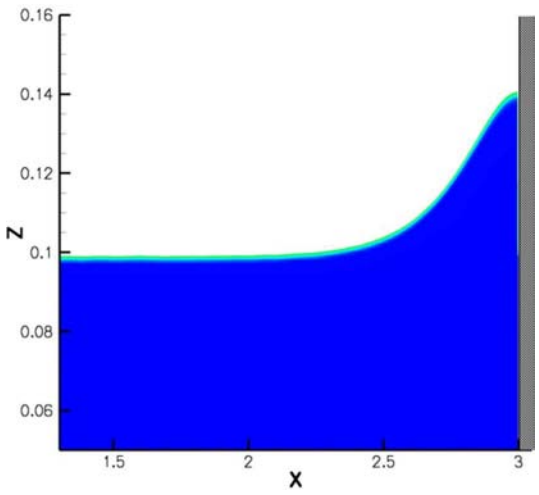

Figure 4.5: Maximum run-up for the collision at $t = 1.80\ s$. $\epsilon = 0.2$, $C\ >\ 0.5$.

that the analytical developments from Su and Mirie (1980) were performed for head-on colliding waves, without taking into account the friction effects when waves interact with walls. It agrees very well anyway with the published results of wave-wall reflexions (Chan and Street, 1970; Maxworthy, 1976). This systematical study confirms that the shedding of secondary waves is enhanced at higher amplitudes. This point has been discussed by Maxworthy (1976).

4.3.2 Head-on collisions between two solitary waves

We are now interested with the next configuration studied by Maxworthy (1976) and Su and Mirie (1980), which is the case of two head-on colliding solitary waves. We simulate two solitary waves with different amplitudes propagating towards each other in a 20 m long and 0.6 m high periodic domain, in order to see these waves colliding several times. This configuration will allow us to put in evidence the imprints left on each wave after each collision: the phase shift phenomenon, i.e. the delay in time during their interaction, and the shedding of secondary waves. The numerical domain is discretized into 1000×150 regular Cartesian grids. A symmetry boundary condition in the lower limit and a free boundary condition in the upper limit are imposed. The same stability criterion (Courant-Friedrichs-Levy) is chosen to ensure a good time step. We run 3250 iterations, which gives 27 s of propagation. The same values for the densities and viscosities have been used in our calculation. As defined previously, the subscripts L and R will hereafter denote respectively the left- and right-going waves.

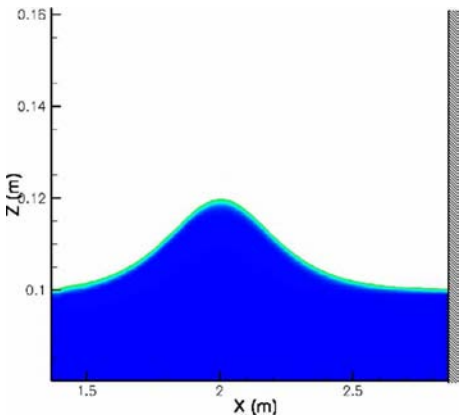

(a) $t = 0.92\ s$

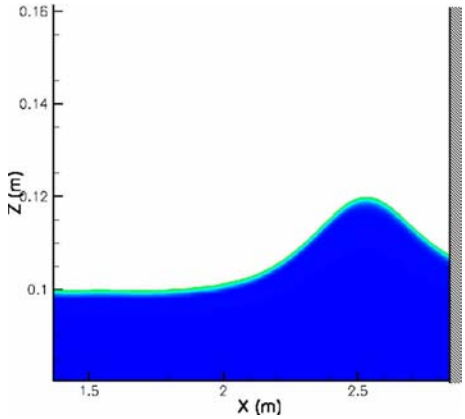

(b) $t = 1.41\ s$

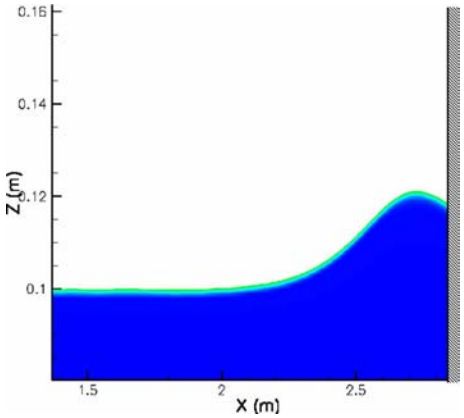

(c) $t = 1.58\ s$

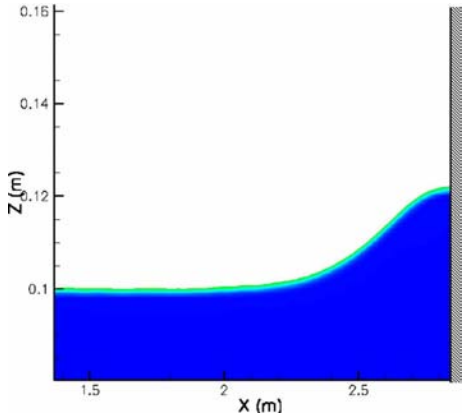

(d) $t = 2.09\ s$

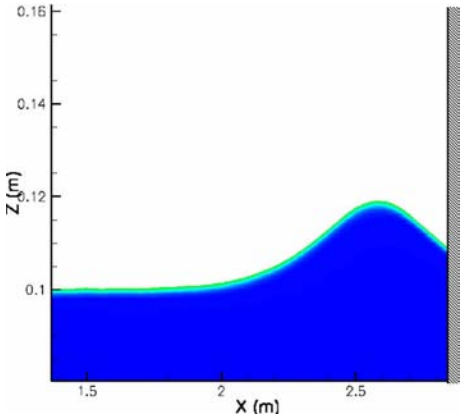

(e) $t = 2.27\ s$

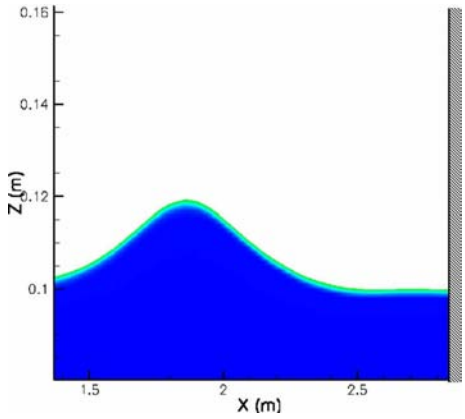

(f) $t = 2.93\ s$

Figure 4.6: Details of the end-wall collision at various instants. $\epsilon = 0.2$, $C > 0.5$.

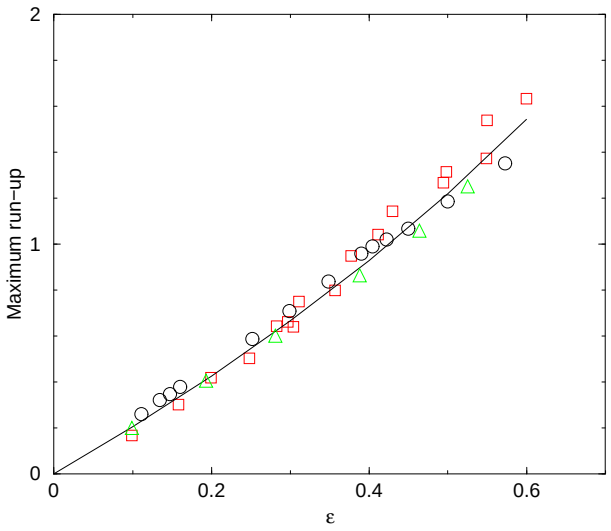

Figure 4.7: Maximum wave run-up, η_m/d, plotted versus wave non-dimensional amplitude, ϵ. Black line: $3^r d$ order analytical results from Su and Mirie (1980) (Eq. 4.3); ○: Maxworthy (1976) (black); △: numerical results (green); □: Chan and Street (1970) (red).

The wave crests are initialized far apart from each other at $x_R = 5\ m$ and $x_L = 15\ m$ (Fig. 4.8). The water depth is $d = 0.302\ m$, the waveheights are $\epsilon_R = 0.11$ and $\epsilon_L = 0.33$, which give the dimensional amplitudes $H_R = 0.03322\ m$ and $H_L = 0.1\ m$, so the crests ordinates are located at $z_R = 0.33522\ m$ and $z_L = 0.402\ m$. The initial wave celerities are $c_R = 1.8134\ m.s^{-1}$ and $c_L = 1.9859\ m.s^{-1}$ (Eq. C.3). From equation (4.2), the maximum theoretical run-up is $\eta_m = 0.1349\ m$, which gives a maximum ordinate $z_m = 0.4369\ m$. They are assumed to meet for the first time at $t = 2.7\ s$ and $x_{1^{st}collision} = 9.8\ m$. During the 3250 iterations, the waves will propagate and collide each other four times.

We measured that the abscissa of the first collision is $x_{1^{st}collision} = 9.778\ m$, which agrees with the theoretical value $x = 9.8\ m$, as shown in figure (4.9). We illustrate in figures (4.10) the first collision in details. Both waves propagate towards each other and seem to merge into a unique wave, which amplitude is higher than the sum of both incoming waves (Fig. 4.9). The profile looks like a single wave. Then both waves split apart to recover their original characteristics. But it can be observed in figure (4.11) that the left-going wave seems to be slightly distorted, which is consistent with the discussions of Maxworthy (1976) and Su and Mirie (1980). The left-going wave looks unsymmetrical and appears to propagate with a slightly higher celerity than its initial one. The wave will reorganize itself to recover its initial characteristics and will collide the right-going

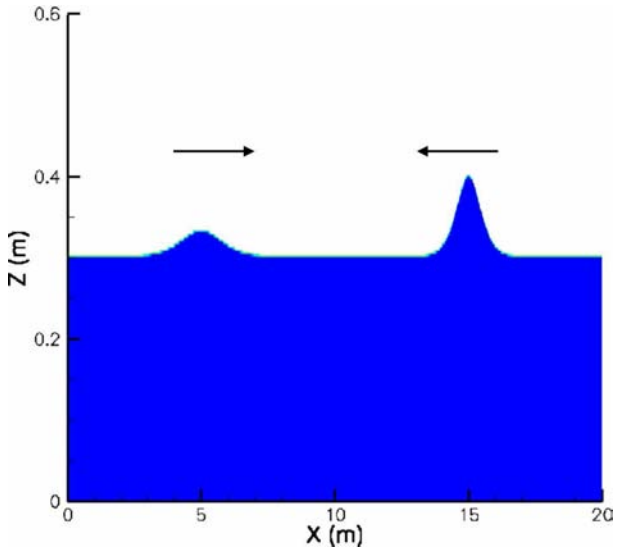

Figure 4.8: Initial condition for the head-on collisions test-case. $t = 0\ s$, $\epsilon_R = 0.11$ and $\epsilon_L = 0.33$, $C > 0.5$.

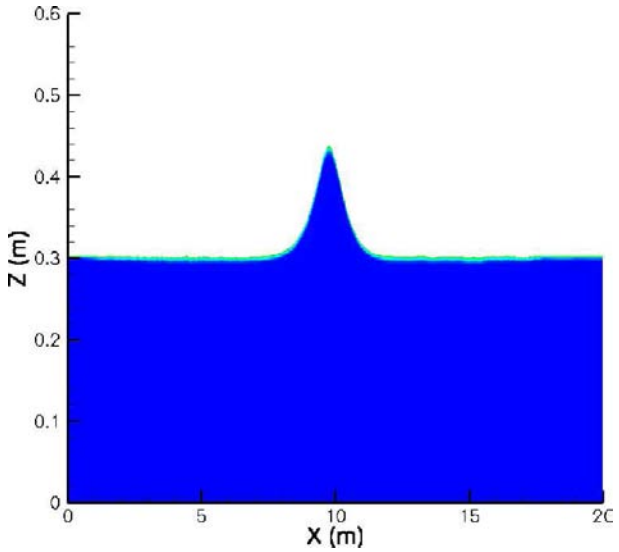

Figure 4.9: Maximum run-up for the first collision at $t = 2.7\ s$ and $x_{1^{st}collision} = 9.778\ m$. $C > 0.5$.

Collisions	z_m (m) (th.)	z_m (m) (num.)	Error (m)	Error %
1^{rst}	0.4369	0.4372	3.10^{-4}	7.10^{-2} %
2^{nd}	0.4279	0.4301	2.10^{-3}	5.10^{-1} %
3^{rd}	0.4229	0.4247	2.10^{-3}	4.10^{-1} %
4^{th}	0.4215	0.4233	2.10^{-3}	4.10^{-1} %

Table 4.4: Maximum run-up ordinates reached for each collision.

wave another time. We can clearly see a weak wave following it, propagating in the same direction. These observations are not so easy to do with the right-going wave because of its low amplitude. The waves collide four times, thus giving a general impression of spasmodic movement because of the left-going wave which is subjected to accelerations and decelerations between each collision and the slow motion of the two waves coming together.

During the 3250 iterations (27 s of propagation), the right-going wave should propagate along 48.96 m and the left-going wave should propagate along 53.62 m. These theoretical distances correspond to the abscissae the waves should have reached in the case they would not have been interacting. We checked that the waves passed more than two times by their initial position propagating without major distortion. However, we recorded that the right-going wave propagated along 48.3 m and the left-going wave along 52.2 m, which correspond, respectively, a translation of 0.66 m and 1.42 m, as compared to the respective values for the distance of propagation, simply estimated with the initial celerities and the time of simulation. This difference is due to the time delay during their interaction and also possibly due to the numerical dissipation of our simulation.

The right-going wave loses 1.10^{-3} m after each collision, the amplitude at the end being $z = 0.334$ m (so a total loss of 1.22×10^{-3} m or 3.6×10^{-1} %). The left-going wave loses 8.10^{-3} m after the first collision, then loses 3.10^{-3} m on average, the amplitude at the end being $z = 0.384$ m (so a total loss of 1.6×10^{-2} m or 4 %). These successive losses in amplitudes put in evidence the fact that each collision gives birth to secondary waves travelling in the same direction of the wave which they come from. As evoked previously, the higher the wave is, the higher the secondary shed wave will be, which is confirmed by the fact that the right-going wave loses less amplitude than the left-going one. The numerical error has been evaluated for the mass and found to be less than 4.8×10^{-2} %, the initial volume being $vol_{ini} = 6.271$ m^2. Table (4.4) is a summary of each calculated maximum amplitudes, considering the loss of amplitude for each wave after each collision.

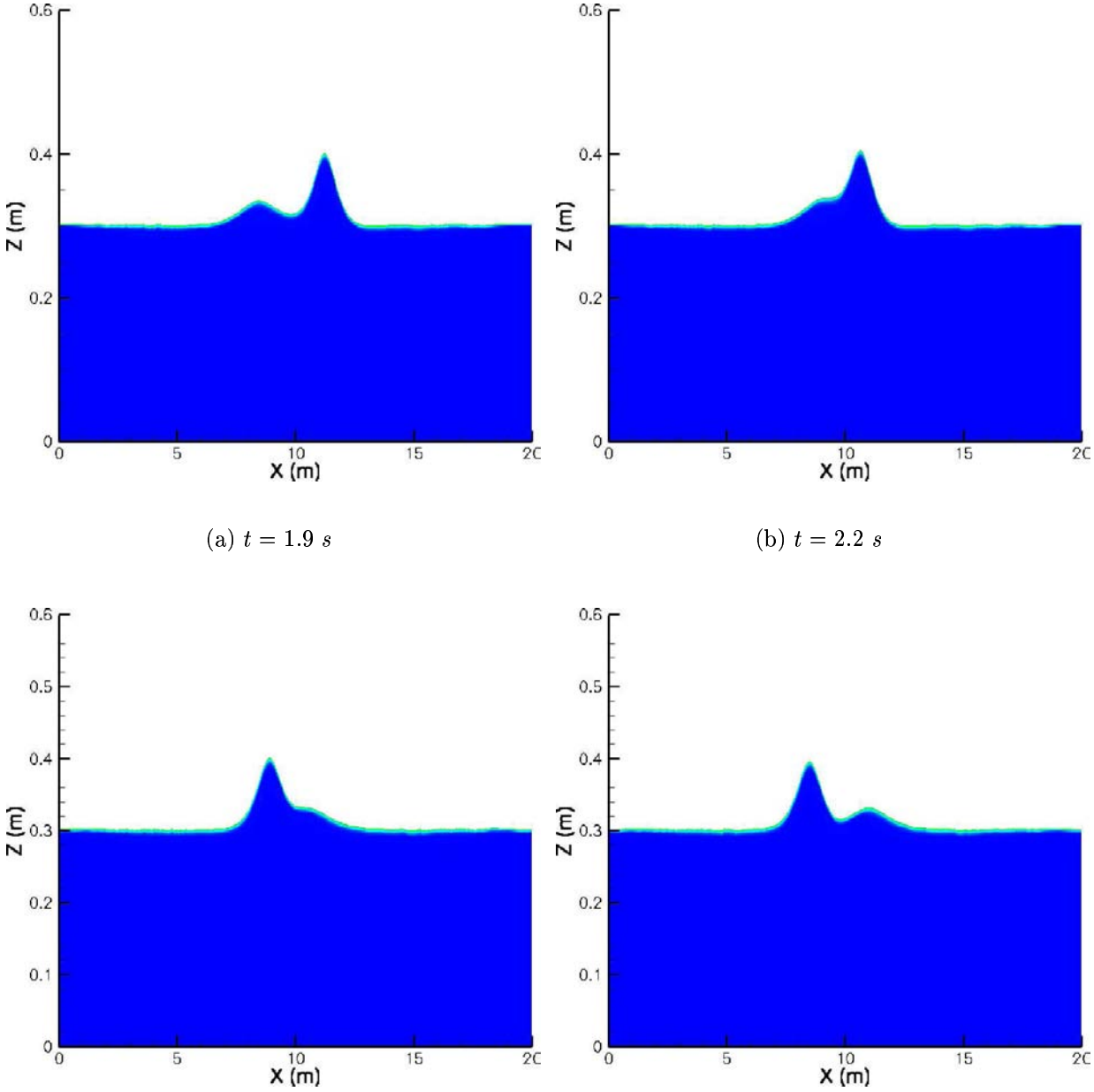

(a) $t = 1.9\ s$

(b) $t = 2.2\ s$

(c) $t = 3.2\ s$

(d) $t = 3.4\ s$

Figure 4.10: Details of the first collision at various instants. $C > 0.5$.

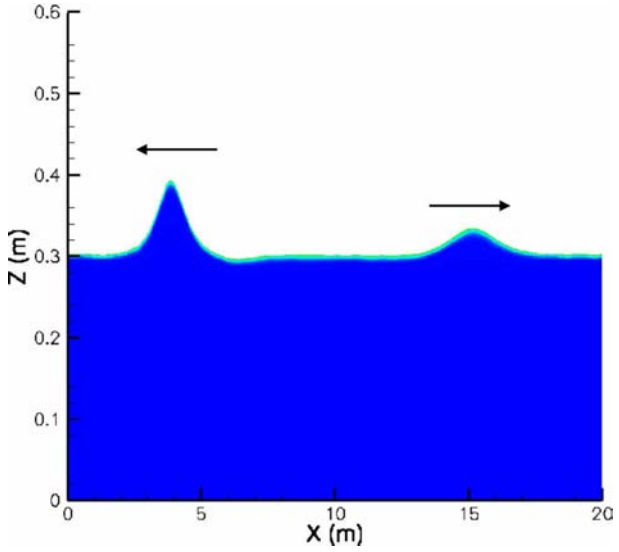

Figure 4.11: End of the first collision. $t = 5.7\ s$, $C > 0.5$.

We also performed all the calculations with the VOF-PLIC method and we obtained results showing the same order of differences with TVD results than presented in section (4.2).

4.3.3 Conclusions and perspectives

We can conclude from the presented results agree with the observations made by Maxworthy (1976) and Su and Mirie (1980). The collisions induce imprints to the waves, the waves propagating faster after each collision. We can also conclude that our numerical model is able to take accurately into account highly complex nonlinear effects such as solitary waves interactions. From this point, we choose to use the TVD scheme in the following of our work.

It could have been interesting to study the case of two solitary waves propagating in the same direction, with the possibility of one wave catching the other up and passing it by (overtaking collision), but we choose to concentrate on the case of two interacting waves with opposite velocity fields, for which experimental and analytical results are available. It would be another great interest to have a close inspection on the phase shift phenomenon as the refereed authors did not agree in their results. A systematical study of the configuration with two solitary waves of same amplitudes colliding would also be of great interest in order to discuss with the results found in the literature. Indeed, Maxworthy (1976) left the discussion open about the opportunity to do the analogy

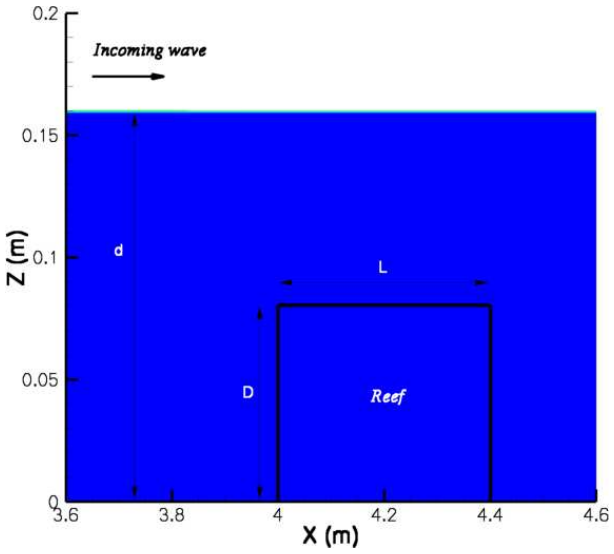

Figure 4.12: Initial conditions for the propagation of a solitary wave over a submerged rectangular reef. $t = 0\ s$, $C > 0.5$.

between two solitary waves of same amplitudes interacting directly and the wave-reflexion case. A discussion on the new results could clarify that particular point.

4.4 Solitary wave propagating over a submerged obstacle

The interactions between a solitary wave and a submerged reef have been investigated experimentally and numerically by Chang et al. (2001). The height of the rectangular obstacle is $D = 0.08m$ and its length is $L = 0.4\ m$. The mean water depth is $d = 0.16\ m$. This is a two-dimensional simulation. The numerical domain is 7 m long and 0.23 m high, and it is discretized into 1000×170 nonuniform grids, in order to have the same Δx_{min} and Δz_{min} as Chang et al. (2001) in the vicinity of the submerged obstacle ($1.10^{-3}\ m$). Chang et al. (2001) studied different solitary wave heights, but reported in details only a representative case with $H = 0.0288\ m$ ($H/d = 0.18$). We choose to simulate the case using the characteristics of air and water.

The velocity field and the free surface profile are initially calculated with the theoretical first order solitary wave solution (see appendix C.1.1), as proposed by Chang et al. (2001). The initial wave celerity is $c = 1.36\ m.s^{-1}$. The incident solitary wave is initialized in the numerical domain, the crest of the wave being set at $x = 2\ m$, the upstream corner of the rectangular obstacle being located at $x = 4\ m$. The solitary wave propagates

towards the right side of the numerical domain.

Chang et al. (2001) compared the profiles of the wave in time, and showed some visualizations of velocity and vorticity fields between the experimental measurements and the numerical results. The main features of the interactions are observed in the vicinity of the obstacle: vortices are generated at the corners of the reef as the wave propagates and passes by the reef. The evolutions of the weatherside and leeside vortices are recorded and analyzed. Chang et al. (2001) used a numerical model based on the Reynolds Averaged Navier-Stokes (RANS) equations with a $k-\epsilon$ turbulence model (results not shown here). We solved directly the full Navier-Stokes equations using the numerical model presented in the previous section (this simulation will be referred to as DNS, as no model is added - see section (2.4)) and we did large eddy simulation (LES - see section (3.4.2)). In order to be able to compare our results with those from Chang et al. (2001). We remind that these two simulations were done with the same criteria concerning the grid spacing and the number of grid points.

4.4.1 Comparisons with experimental results

We compare our numerical simulations to the experimental results published by Chang et al. (2001). As the wave propagates, two main vortices are generated, one on the weatherside and one on the leeside of the obstacle, the size of the latest one being greater than the first one (Figs. 4.13 and 4.14).

The first vortex is generated on the weatherside of the obstacle, as the wave approaches (Fig. 4.13 a). The vortex is confined by the near presence of the free surface above and the obstacle below. Its shape is flattened and stretched in the downstream direction. Then the eye of the vortex moves slowly in the flow direction, along the side of the obstacle (Fig. 4.13 b), towards the right side of the numerical domain, and rises as the wave crest passes by (Figs. 4.13 c and d). Once the wave has moved away, the shape of the vortex becomes circular and its size increases (Figs. 4.13 e and f).

As the solitary wave is propagating to the downstream corner of the rectangular obstacle, the flow above it is more or less unidirectional and is almost uniform in the vertical direction. A vortex starts to form behind the obstacle (Fig. 4.14 a), on the leeside, and, as the wave moves towards and passes by the corner of the obstacle, the size of the vortex increases just as the horizontal velocity above the obstacle (Fig. 4.14 b). This structure is confined by the presence of the free surface and the large amount of water above it.

So, unlike the weatherside vortex which is packed between the obstacle and the free surface, the vortex is free to grow in size and its shape is circular. As the wave propagates, the vortex moves slowly away from the corner and towards the bottom of the numerical domain (Figs. 4.14 c and d). The vortex is constrained to move deeper by the amount of water increasing above it. As the wave propagates farther away from the reef, the velocity above the obstacle vanishes and the eye of the vortex rises suddenly and drifts slowly downstream (Figs. 4.14 e and f).

We plot (Fig. 4.15) the trajectories of the eyes of both main structures observed. We can see in figure (4.15 b) that we have a very good agreement between our numerical results and the experimental measurements concerning the leeside vortex. The trajectories are identical, the lines being superposed, and match very well with the experimental data.

Both vortices show very similar trajectories (Fig. 4.15). The differences come from the kind of interaction which occurs with the obstacle. The vortices move towards the main flow direction, then suddenly rises to the surface as the wave passes by: it can be checked in figures (4.15) that the lines are broken and heading straight to the top. They are then sucked in the wave's wake. They first follow the wave before being animated with a kind of yo-yo motion, *i.e.* moves slowly up and down interacting turn after turn with the free surface and the upper side of the reef, as they are free from any interaction with the wave.

However, it can be seen in figure (Fig. 4.15 a) that the trajectory of the weatherside vortex is very well reproduced by the LES simulation, the dark line following the green circles showing the experimental results from Chang et al. (2001). The DNS simulation shows a great discrepancy: the trajectory of the weatherside vortex seems, at the beginning, to follow the right tendency, but then diverge away from the experimental trajectory.

In order to investigate and to show where the difference comes from between our numerical simulations, we show (Fig. 4.16) two pictures of the weatherside vortex at $t = 2\ s$. We checked that the maximum solitary wave height was at $x = 4.649\ m$ in both DNS and LES simulations, which is very close to $x = 4.856\ m$ as expected theoretically (the discrepancy coming from the presence of the submerged reef and the energy loss). On the left picture, corresponding to the LES simulation, the main structure can be easily seen, above the top left corner of the obstacle. The vortex is moving downstream and starts rising as the solitary wave propagates and passes by the corner (located at $x = 4\ m$). Some structures are generated near the corner of the reef (here, two structures can be seen at this instant) during the propagation of the wave, the main vortex moving downstream along the reef. These are smaller and constrained by the main vortex (acting

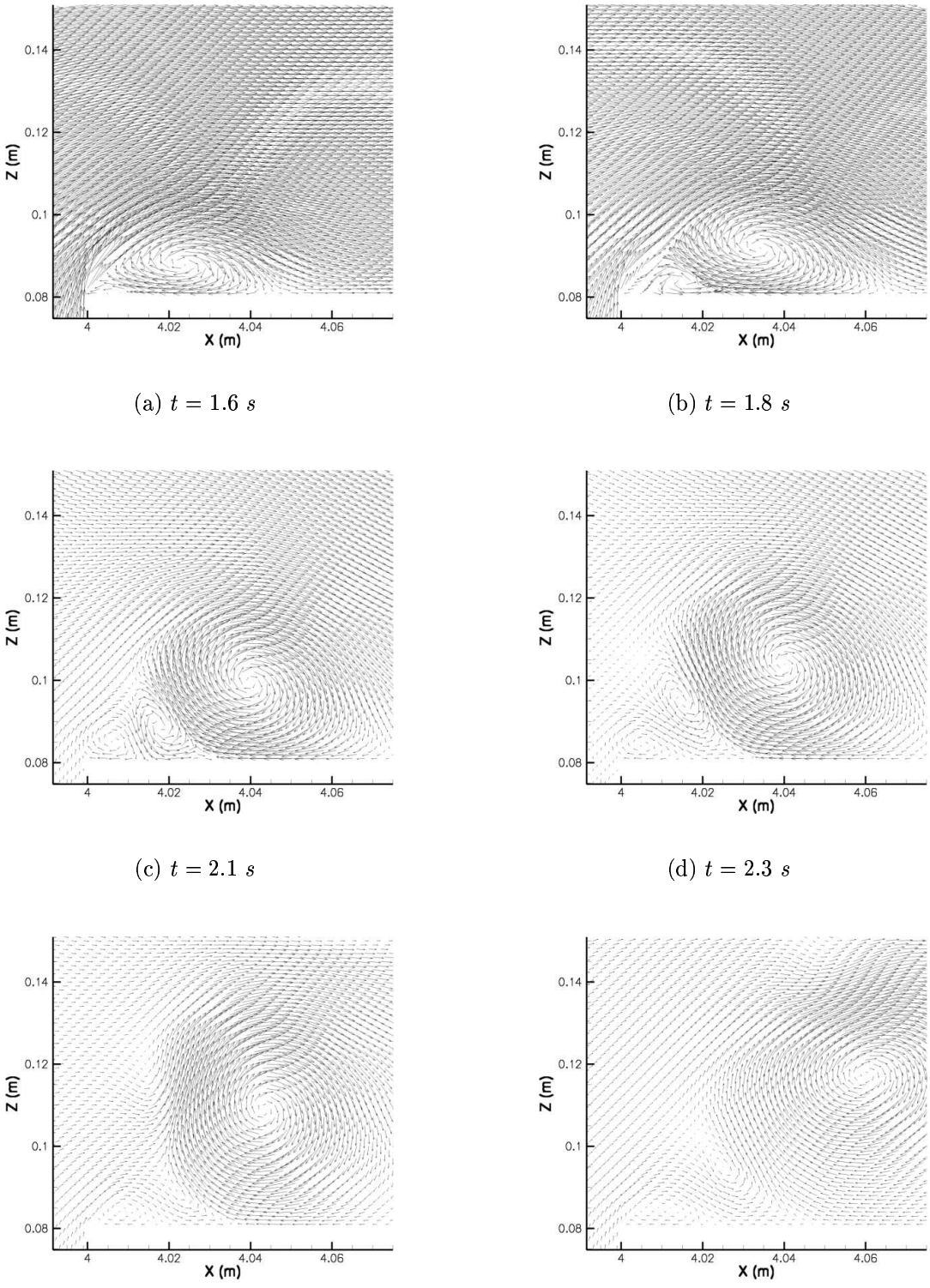

(a) $t = 1.6\ s$

(b) $t = 1.8\ s$

(c) $t = 2.1\ s$

(d) $t = 2.3\ s$

(e) $t = 2.5\ s$

(f) $t = 2.8\ s$

Figure 4.13: Evolution of the weatherside vortex in the vicinity of the upstream corner of the reef. One vector over three are shown.

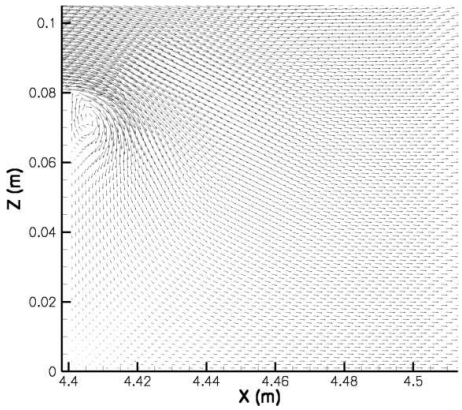

(a) $t = 1.6\ s$

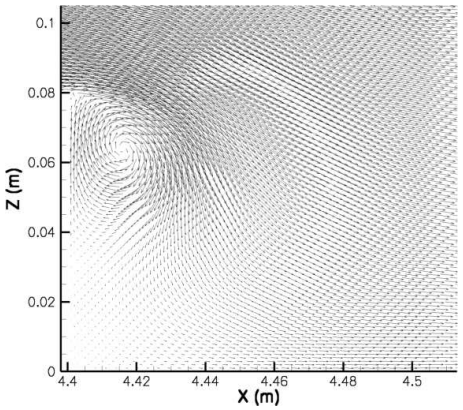

(b) $t = 1.8\ s$

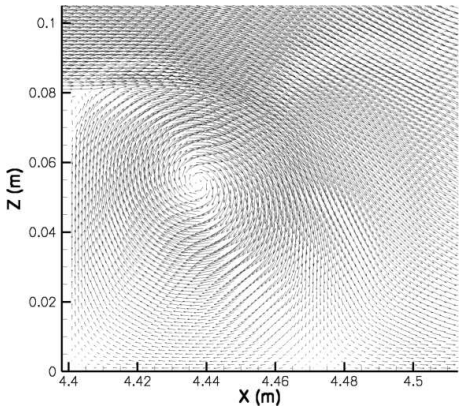

(c) $t = 2.1\ s$

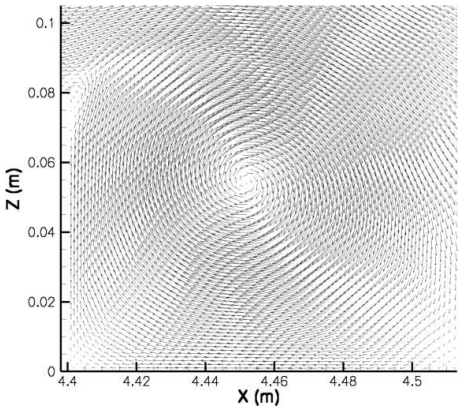

(d) $t = 2.4\ s$

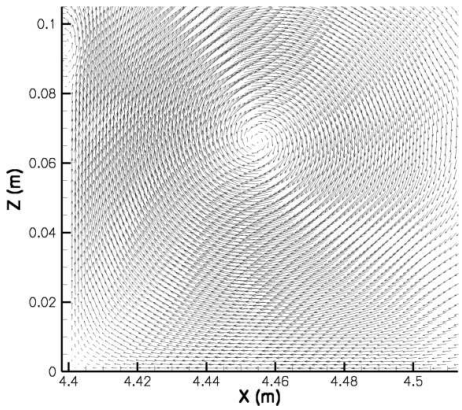

(e) $t = 2.48s$

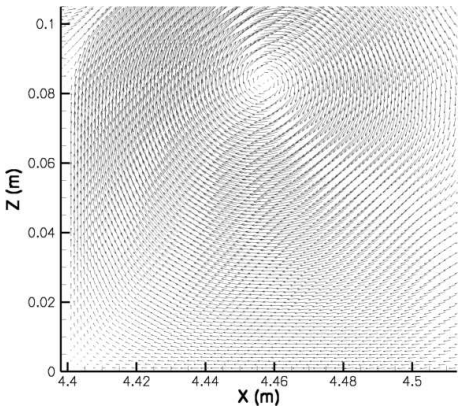

(f) $t = 3.3\ s$

Figure 4.14: Evolution of the leeside vortex in the vicinity of the downstream corner of the submerged reef. One vector over three are shown.

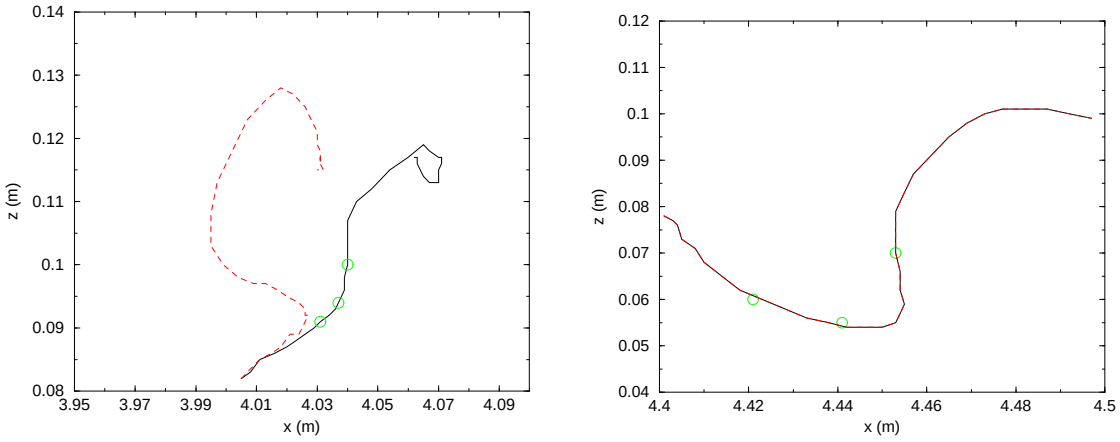

(a) Weatherside vortex (b) Leeside vortex

Figure 4.15: Trajectories of the eye of the weatherside (a) and leeside (b) vortices. Green ∘: experimental data (Chang et al., 2001); black line: present LES simulation; red dashed line: present DNS simulation.

as a solid wall), the obstacle and the large amount of water increasing above them. These small vortices push the main vortex downstream.

In the same way, the figure (4.16 b) corresponding to the DNS simulation shows the main structure, but no other structure appears in the flow, near the corner. The vortex grows in size as the wave propagates. Once it passed by the reef, the vortex rises and then moves upstream, away from the obstacle.

This seems to be due to the fact that, in the LES simulation, some energy is extracted from the main vortex thanks to the turbulent viscosity. The smaller structures have then a chance to appear. This is missing in the DNS simulation, which then should not be called DNS, because the energy cascade is not well simulated. In the latter simulation, the main vortex grows and grows in size, no energy dissipation occurring, and no other vortices develop to block the main vortex to move upstream. The trajectories of the leeside vortices simulated by LES or DNS do not show any difference for the main reason that, except at the time of its generation, this structure does not interact with the reef. Once it appears, it keeps growing in size and moves away from the wall in the flow, as the wave comes and moves towards the right end of the numerical domain. So the energy dissipation process is less important in this situation. This is confirmed by Chang et al. (2001) who measured the turbulence level around the two main vortices and shown that the intensity was found to be smaller around the leeside vortex.

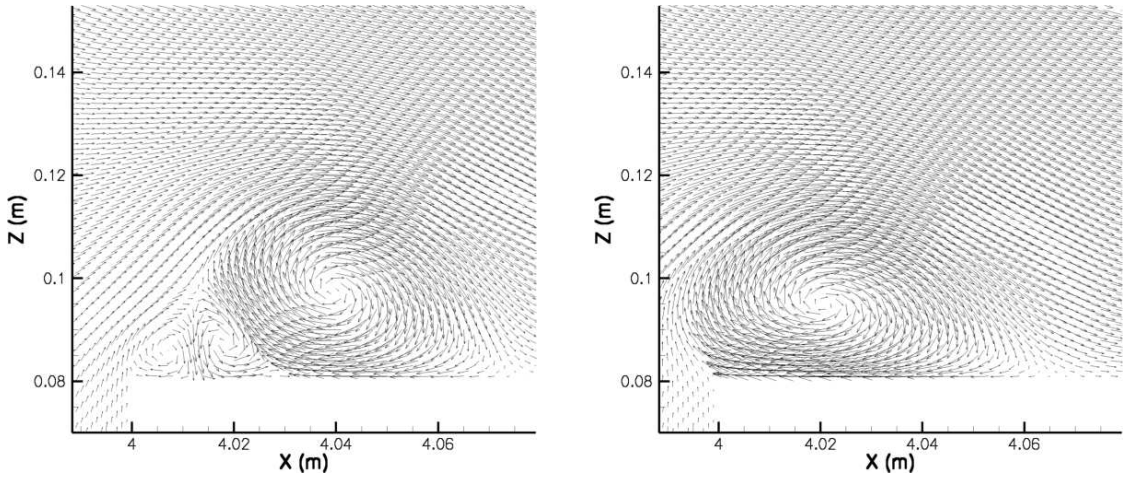

(a) LES (b) DNS

Figure 4.16: Comparison at $t = 2\ s$ between: (a) LES and (b) DNS. One vector over three are shown.

We then tried to get closer to what could be called a "real" DNS by refining the mesh size of the grid in the vicinity of the reef upstream corner. We do not pay anymore attention to the leeside vortex, as we already obtained very satisfactory results. The numerical domain is reduced to 2.5 m long and 0.2 m high to zoom in the area of the upstream corner we are interested in. It is now discretized into 1100×570 nonuniform grids, the grid spacing being $\Delta x_{min} = \Delta z_{min} \simeq 1.10^{-4}\ m$. This should, hopefully, describe more accurately the behavior of the turbulent vortex, in a DNS point of view, and reproduce the experimental results. Nevertheless, the goal of this investigation is not to answer whether or not it is possible to simulate turbulence in two dimensions in a convincing way. The results we obtained show that, by refining the mesh size of the grid, more vortices were simulated. The main vortex first behaves as expected, as shown in figure (4.17), where the red dashed line stands for the DNS main vortex trajectory and the black line recalls the LES main vortex trajectory. Then it disappears as it merges with another vortex which follows and rolls over it. Its trajectory is shown in figure (4.17) with the red long dashed line. The simulation has been stopped and we do not have more information about the evolution of this secondary vortex.

The main vortex evolution has been clearly improved, compared to the wrong behavior we obtained with the previous DNS simulation. But it seems that the more we will refine the mesh grid size, the more vortices will be observed, without simulating in a satisfactory way the turbulent energy cascade. However, the end is grid independent results that

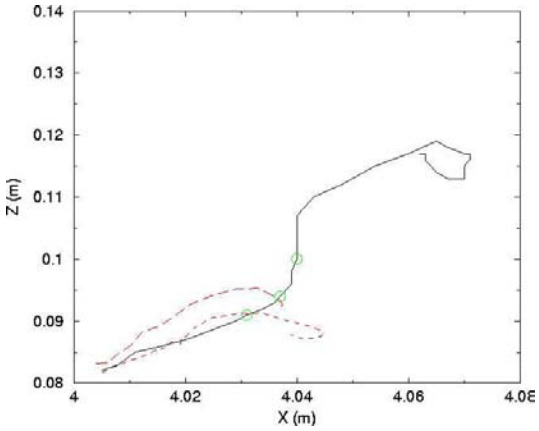

Figure 4.17: Trajectories of the eye of the weatherside vortices. Green ∘: Chang et al. (2001); black line: LES; red dashed line: DNS main vortex; red long dashed line: DNS secondary vortex.

are ideally expected using DNS when the grid captures all the turbulence phenomena. Obtaining an accurate numerical solution using DNS simulation is costly in terms of numerical resources.

We also checked that our results were in agreement in terms of free surface profiles, compared with those shown by Chang et al. (2001). We observe that, at some point after the obstacle, the free surface profile shows a distortion revealing the presence of the submerged reef. This phenomenon will be investigated further in details in the next test case of study.

4.4.2 Conclusions and perspectives

This test-case is very similar to the academic one of a turbulent flow around an obstacle. The results lead us to the conclusion that, even if it is a two-dimensional simulation exercise, we must take into account a turbulence model if the purpose of our work is to improve the understanding of turbulence induced by breaking waves. It is also interesting to show that it is possible to produce good results with a two-dimensional simulation of a three-dimensional phenomenon, but a great care should be taken while interpreting the results obtained using DNS. Three-dimensional simulation of such a problem is too time consuming to be carried out at that time, but would be interesting to be considered for comparison. It would also be of great interest to have a look to the erosion matters. If we consider that the submerged reef is surrounded with sand or any friable material, a great amount of it could be put into suspension if we look at the amplitude of the velocity field

near the downstream face of the reef for example (Fig. 4.14). This could cause erosion, or accretion, into some areas or even damage the reef itself.

4.5 Solitary wave propagating and breaking over a submerged obstacle

The aim of this section is to go further in the complexity and to come closer to our main concern, the breaking waves, in order to validate our numerical model more accurately. The reference case is taken from the work presented by Yasuda et al. (1997). The propagation and the overturning of a solitary wave on a submerged reef, consisting in a rectangular step-like obstacle, is investigated (Fig. 4.18). This test-case will allow us to put in evidence the behavior of the wave propagating over a shallower obstacle, compared to the previous case (4.4). We solve directly the full Navier-Stokes equations using the numerical model presented in the previous section (this simulation will be referred to as DNS, as no model is added - see section (2.4)) and we did large eddy simulation (LES - see section (3.4.2)) in order to point out the effect of LES on the free surface behavior when it is strongly disturbed.

The height of the obstacle is $D = 0.263\ m$ ($D/d = 0.848$) and the mean water depth is $d = 0.31\ m$. The initial amplitude and celerity are $H = 0.1314\ m$ ($H/d = 0.424$) and $c = 2.072\ m.s^{-1}$ (Eq. C.10), respectively. The velocity field and the free surface profile are initially calculated with the theoretical third order solitary wave solution (see appendix C.1.2). The numerical domain is 8 m long and 0.6 m high, discretized into 1200×200 nonuniform grids in the x-direction, with $\Delta x_{min} \simeq 4.10^{-3}\ m$ in the vicinity of the submerged obstacle. A uniform grid spacing $\Delta z_{min} \simeq 3.10^{-3}\ m$ is used. The incident solitary wave is initialized in the numerical domain and the crest of the wave is set at $x = 2\ m$. The reef face is located at $x = 4\ m$. The solitary wave propagates towards the right side of the numerical domain.

Yasuda et al. (1997) used a fully nonlinear potential theory model to study the internal velocity and acceleration fields and their relationship to breaker type. They checked the accuracy of their numerical model with some experimental data. Four capacitance wave gauges recorded the free surface elevations at different locations in the canal. The first gauge was placed upstream of the reef face to check the incident waveheight. The second gauge was located above the upstream corner of the reef. The last two gauges measured the free surface at 0.515 m and 1.020 m away from the tip of the obstacle.

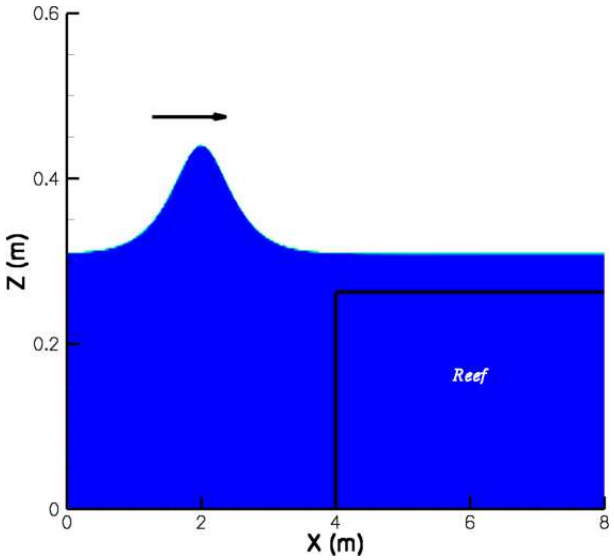

Figure 4.18: Initial conditions for the propagation and the breaking of a solitary wave over a submerged rectangular reef. $t = 0\ s$, $C > 0.5$.

4.5.1 Comparisons with experimental results

With respect to the positions of the three last gauges (referred to as P2, P3 and P4 by Yasuda et al. (1997)), we give the values of the non-dimensional numerical amplitudes ($\eta/d = (z_m - d)/d$) compared to the experimental ones, as well as the percentage of error (Tab. 4.5). As we already verified closely the accuracy of the propagation of a solitary wave over a flat bottom (see section 4.2), we do not pay attention to the results from the first gauge given by Yasuda et al. (1997).

We can then check that our numerical model accurately reproduces the propagation and the interaction between the solitary wave and the obstacle. As shown in figure (4.19), we plot and compare the non-dimensional free surface elevations versus the non-dimensional time, with respect to the positions of the three gauges P2, P3 and P4. We can note that our numerical model gives very satisfactory results, as the black lines plotted in figure (4.19) are almost superposed with the red circles corresponding to the experimental data from Yasuda et al. (1997). As we do not have any information about the starting time of the experiments from Yasuda et al. (1997), we shifted our results until the maxima of abscissa were in agreement with the experimental data. We can then compare the behavior of the wave in time, in terms of free surface deformations as it interacts with the reef.

First, the wave propagates over a flat bottom without any change of form. As it comes

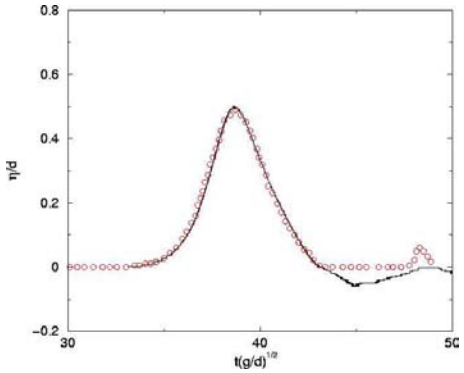

(a) P2

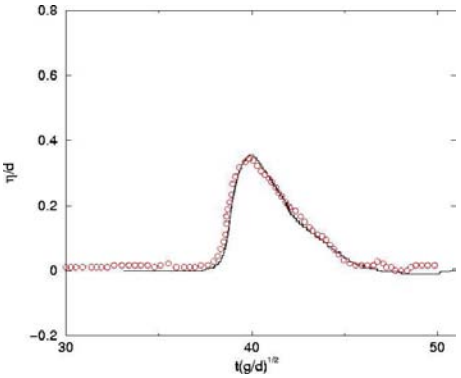

(b) P3

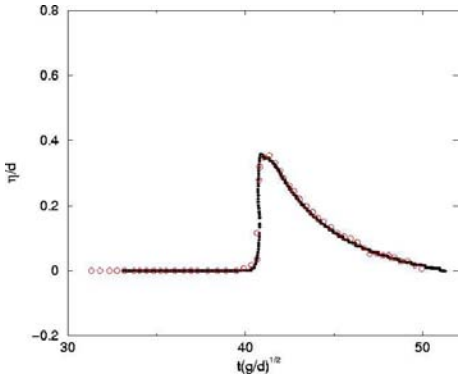

(c) P4

Figure 4.19: Comparisons of the non-dimensional free surface elevations, η/d, plotted versus the non-dimensional time, $t\sqrt{g/d}$, recorded at each location P2, P3 and P4. Black line: present numerical results; red $\circ$: experimental results (Yasuda et al., 1997).

Gauges	Numerical	Experimental	Error (%)
P2	0.5004	0.505	0.9
P3	0.348	0.3444	1.0
P4	0.3577	0.3536	1.2

Table 4.5: Present numerical maximum non-dimensional free surface elevations, η/d, compared to the experimental measurements (Yasuda et al., 1997).

in the neighborhood of the obstacle, the depth of water over the reef is abruptly reduced, which leads the wave profile to be dramatically transformed (Fig. 4.20). The wave is then forced to reorganize itself. As recorded by the gauge standing over the reef's upstream corner (Fig. 4.19), the free surface elevation rises from the initial value $H/d = 0.424$ to $\eta/d = 0.4977$ (Tab. 4.5). The wave loses its symmetrical aspect (Figs. 4.20 a) and starts steepening till the front face of the crest becomes vertical (Fig. 4.21.a). We have then a plunging breaking wave (Fig. 4.21.b).

A jet of liquid is about to be projected from the crest of the wave. However, the shape of the tongue of water thrown from the crest is slightly different from what is shown in Yasuda et al. (1997) (Fig. 4.21 b). It free-falls down forward into a characteristic overturning motion. It can be observed that several gas pockets are entrapped.

In order to compare our results with the work of Yasuda et al. (1997), we use the same non-dimensional values. Yasuda's reef face is located at $x/d = 32$, our reef being at $x/d \simeq 12.9$. So, we show in figures (4.21 (a) and (b)) our free surface profiles translated to the same reference, with η/d the non-dimensional free surface elevation. At first glance, the figures are not to our advantage and seem completely wrong. It can be seen that our computed propagating wave is late at both compared instants.

But if we consider the abscissa of the vertical front face of the wave (Fig. 4.21 a), the error between our numerical results and the experimental data is only $\simeq 1.5$ %.

At the jet fall initiation instant (Fig. 4.21 b), if we consider again the abscissa of the vertical face of the wave, under the overhanging jet, the calculated error between the numerical results and the experimental data is $\simeq 1.2$ %. Although we can observe that the computed jet looks "thicker" than the experimental one, it is approximately of the same length. Unfortunately, no more experimental pictures were presented by Yasuda et al. (1997), so we have no information about the abscissa of the jet impact or the splash-up behavior. If we consider that we are going further in complexity, we can be satisfied with those results, as the errors calculated at this stage are of the same order of magnitude as those calculated so far (see sections 4.2 and 4.3).

As already done in the previous section (4.4), we take the opportunity to compare our numerical model with the provided experimental results. We now investigate the influence of LES on the free surface description.

At the stage of the steepening of the wave, no clear difference appears between DNS and LES simulations (Fig. 4.21 a). On the contrary, discrepancies start to occur when the jet is generated (Fig. 4.21 b). It is confirmed when we look at various instants presented in figures (4.22).

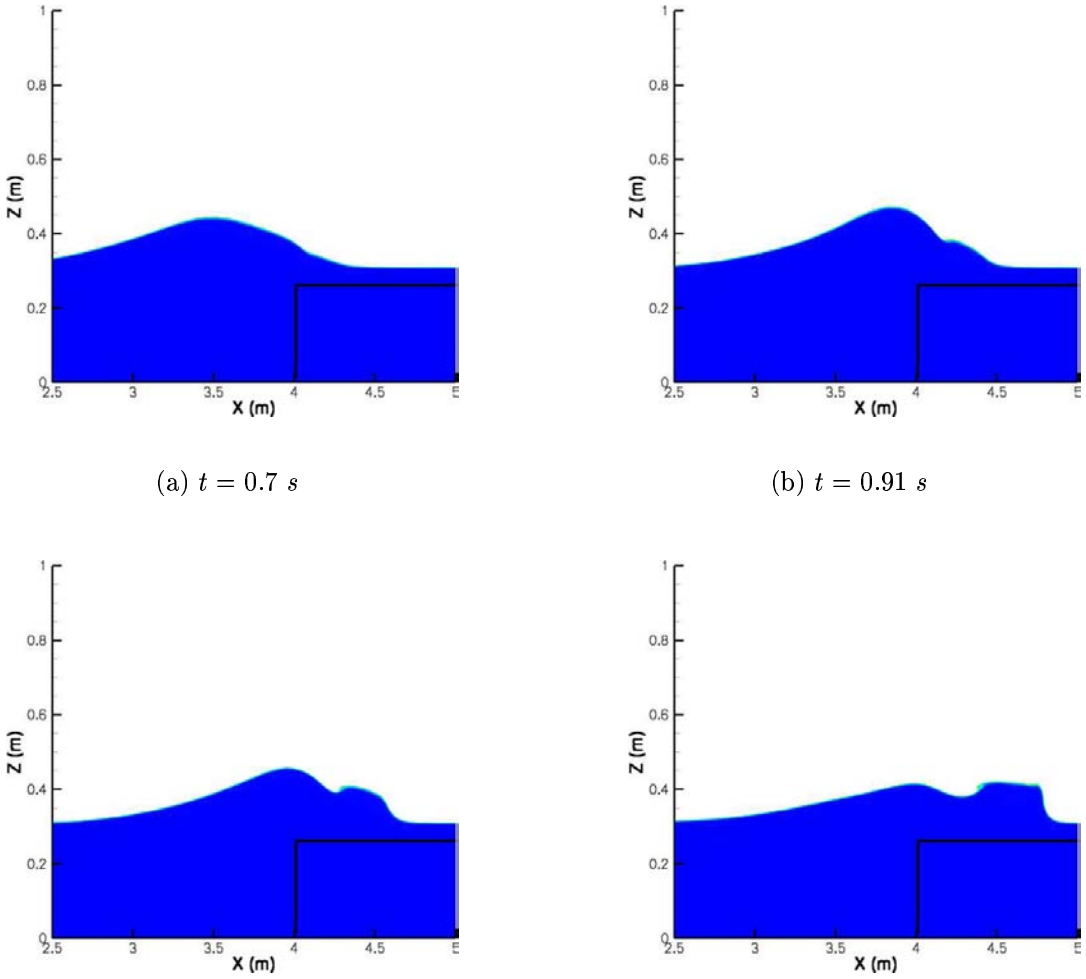

(a) $t = 0.7\ s$

(b) $t = 0.91\ s$

(c) $t = 1.1\ s$

(d) $t = 1.2\ s$

Figure 4.20: Solitary wave propagating and steepening over the submerged reef. The straight black line stands for the reef. $C > 0.5$.

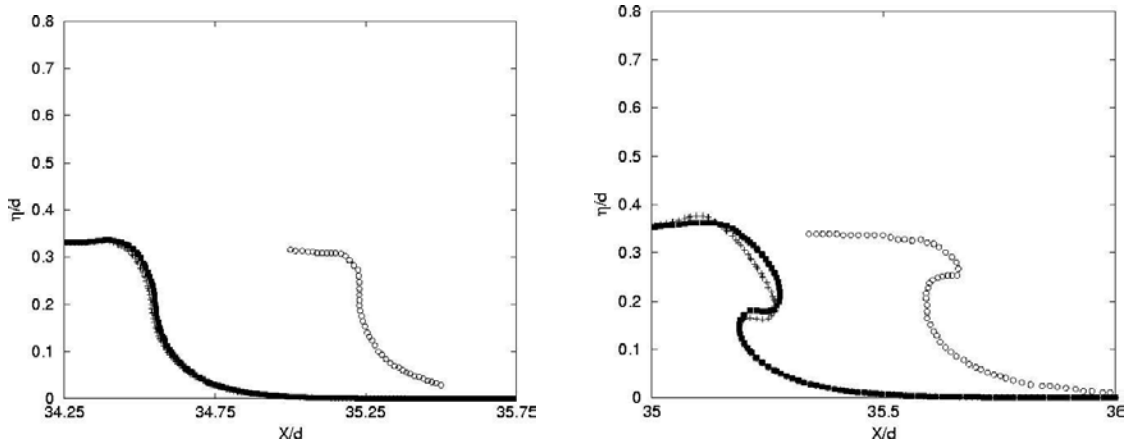

(a) Breaking point (b) Jet fall initiation

Figure 4.21: Comparison of the free surface profiles prior to the jet ejection (a) and at the jet initiation (b). Black ■: present LES ($C = 0.5$); black +: present DNS; black ∘: experimental results (Yasuda et al., 1997).

The most striking difference is in the sizes of the gas pockets entrained in the water. Not only the shape and the size of the jet are affected by the addition of a turbulent viscosity (Fig. 4.22 a and b), but also the general dynamics of the flow. The crest of the wave is rounder in the DNS simulation, rather than flat in the LES simulation. The occurrence of this small bump can be explained by a perturbation in the air which interacts with the free surface, this being absent in the LES simulation, certainly erased by the turbulent viscosity.

The jet is ejected farther in the LES simulation, so this implies that it also impacts differently: in the DNS simulation, the jet free-falls earlier and touches down a non-vertical part of the water, whereas it impacts hard on a flat surface in the LES simulation. More gas is entrapped and entrained by the jet. The splash-up generated by the first impact rises higher and, in its turn, entraps a larger amount of gas. The flow is then more dynamical and intense in the LES simulation because these larger structures will try to rise to the surface and dislocate in smaller gas pockets feeding the flow with turbulence.

The reason why this difference between the jet generations occurs is not so clear. After a close inspection of the velocity field at an early stage of the process (Fig. 4.23), we could see that the free surface profiles are still identical at this time. The velocity fields are very similar for both simulations, but we can notice some small changes in the DNS simulation.

Some imperfections arise in the horizontal velocity component in the wave, compared

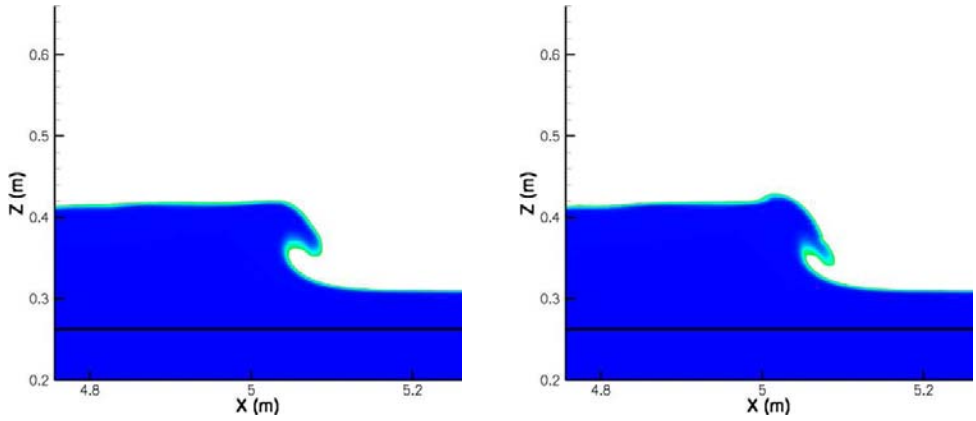

(a) $t = 1.4\ s$

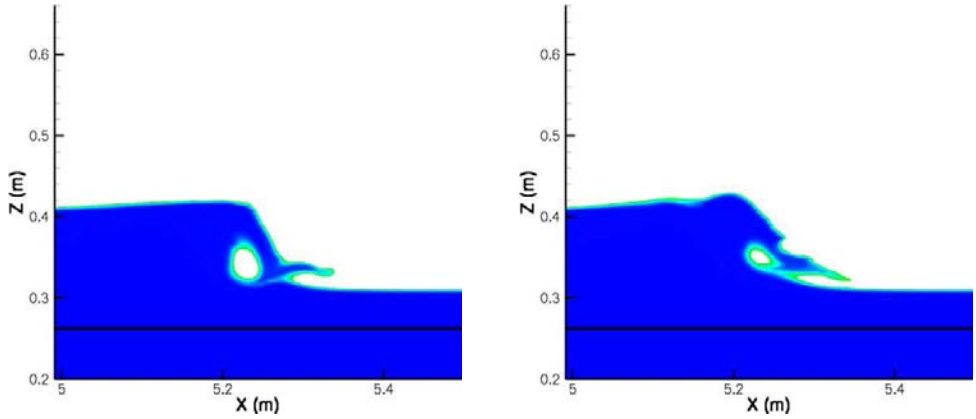

(b) $t = 1.5\ s$

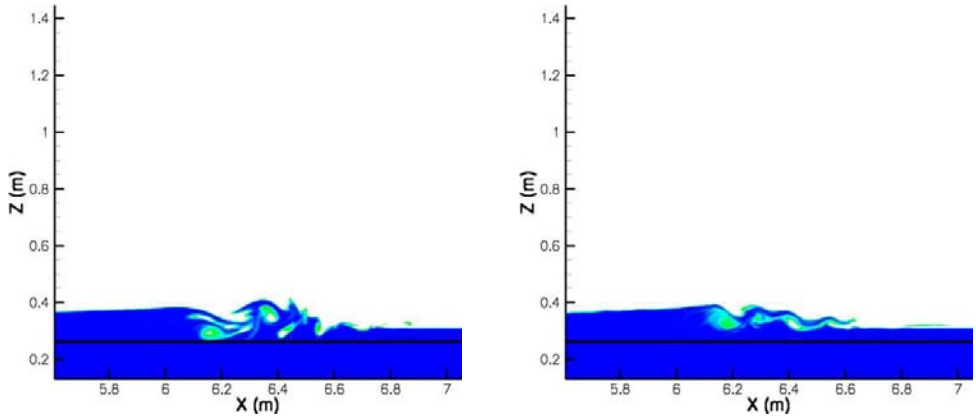

(c) $t = 2.2\ s$

Figure 4.22: Comparison between LES (left column) and DNS (right column) simulations. The straight black line stands for the reef upper face. $C > 0.5$.

to the LES one (Fig. 4.23 a and b). The vertical component slightly differs in the air (Fig. 4.23 c and d), at the top of the crest. But, above all, its positive magnitude is less important on the forward face of the overturning wave and its negative magnitude is more important in the tip of the jet, which tends to make the jet being ejected weakly and pointing downward. These defects seem to lead to the change in shape and behavior of the free-falling jet in the DNS simulation. Moreover, it can be observed in figures (4.22 c) that the resulting flow can be affected and be very different. The observed imperfections seem to be due to some numerical oscillations, which are not damped by the Hybrid Centered-Upwind scheme.

So the turbulent viscosity would appear to regularize the velocity field in both fluids. This has been confirmed with a numerical test. It appears that the same DNS simulation, obtained by using the diffusive Upwind scheme instead of the Hybrid Centered-Upwind scheme, leaded to more acceptable results. This simulation will be referred to as the UPWIND simulation or results. We observed that the imperfections, shown in figures (4.23 c and d), are erased. The UPWIND results seem then more comparable with the LES results, shown in figures (4.22). Discrepancies still remain (Fig. 4.24) in the free surface profiles between the UPWIND and LES results: the UPWIND simulation gives a free surface profile in between those found from the DNS and LES simulations. The jet is ejected further from the DNS one, but a bump still persists at the crest of the breaking wave. This test would tend to illustrate that turbulent viscosity can also be useful to stabilize an accurate, but sensible, numerical scheme. Some more tests would be needed to give a clear conclusion to that point.

To ensure ourselves about the behavior of the model and to investigate some aspects of the interactions of the solitary wave and the obstacle, we performed another simulation corresponding to parameters given by Yasuda et al. (1997), who worked on some various numerical experiments, and referred to as *"ST5"*. We keep the same general configuration, as illustrated previously (Fig. 4.18). The mean water depth is still $d = 0.31\ m$, but the height of the obstacle is now $D = 0.186\ m$ ($D/d = 0.6$) and the initial amplitude is $H = 0.155\ m$ ($H/d = 0.5$). The initial celerity is $c = 2.123\ m.s^{-1}$ (Eq. C.10). The numerical domain is still 8 m long and 0.6 m high, discretized into 1200×200 nonuniform grids in the x-direction, with $\Delta x_{min} \simeq 4.10^{-3}\ m$ in the vicinity of the submerged obstacle, and a uniform grid spacing $\Delta z_{min} \simeq 3.10^{-3}\ m$. The incident solitary wave is initialized in the numerical domain and the crest of the wave is set again at $x = 2\ m$. The reef face is still located at $x = 4\ m$.

This simulation corresponds again to a plunging breaking wave, as illustrated in fig-

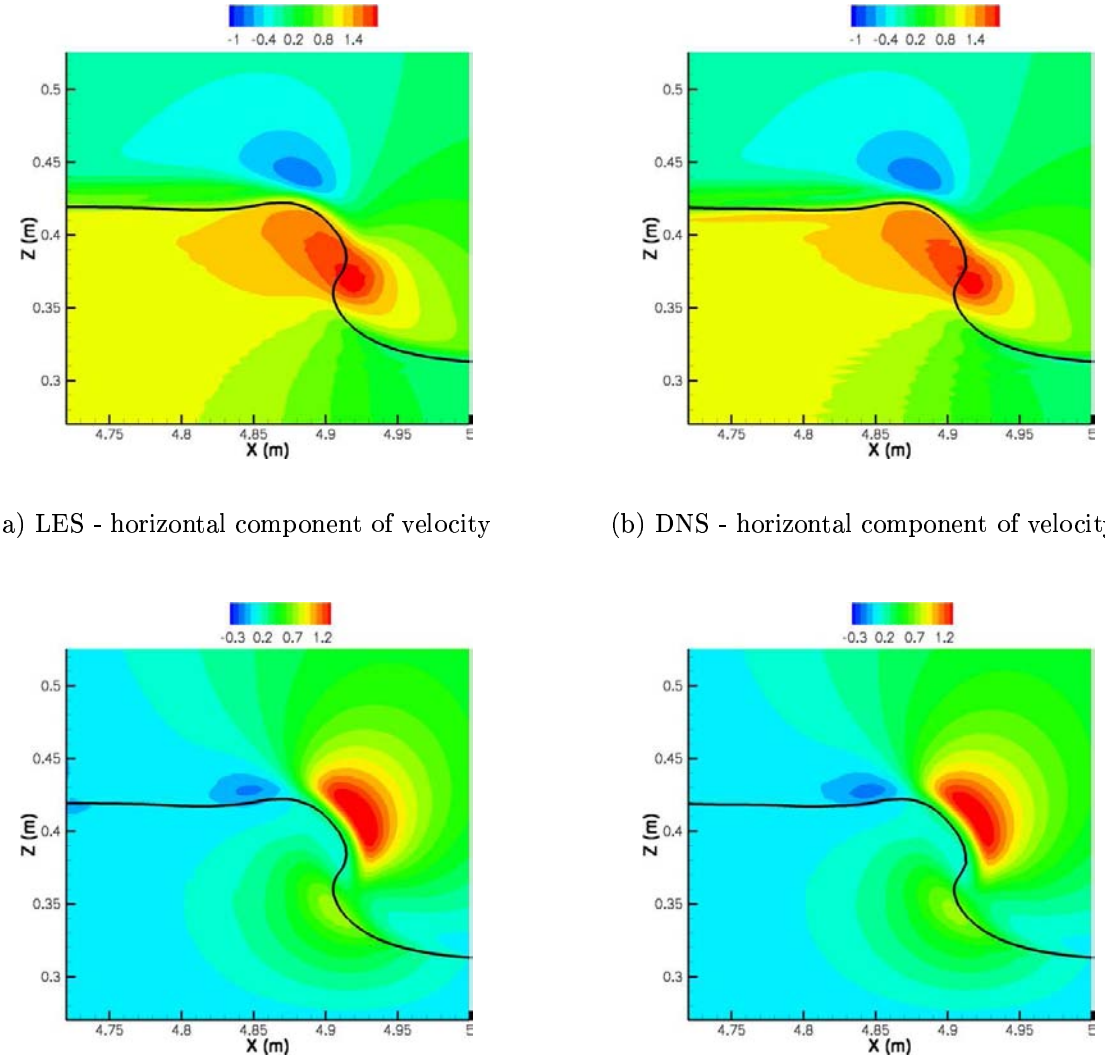

(a) LES - horizontal component of velocity

(b) DNS - horizontal component of velocity

(c) LES - vertical component of velocity

(d) DNS - vertical component of velocity

Figure 4.23: Comparison between the Cartesian velocity components in both media from the LES (left column) and DNS (right column) simulations at $t = 1.3\ s$. The black line stands for $C = 0.5$.

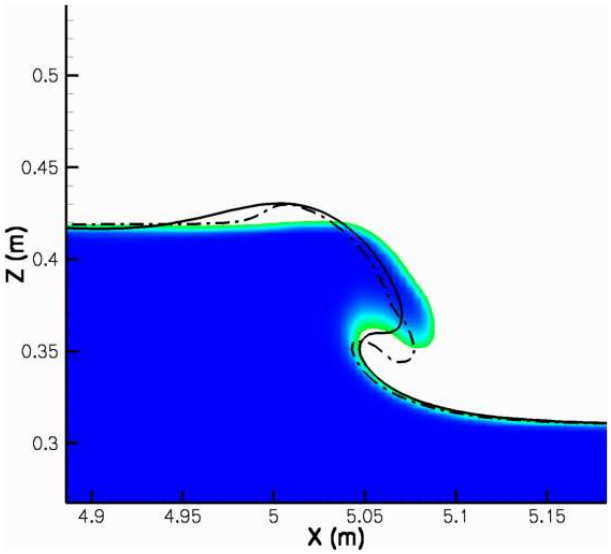

Figure 4.24: Comparison between the free surface profiles, at $t = 1.4\ s$. The black solid line stands for the UPWIND simulation, the dash-dotted black line stands for the DNS simulation. The color function $C > 0.5$ shows the LES result.

ures (4.25). We can note that we have the same characteristically overturning motion and splash-up generation. This breaking shape visually corresponds well to what we can see on shorelines. The crest of the steepening wave rises much higher than its original amplitude. The free surface profiles are again very similar with those shown by Yasuda et al. (1997). We can see in figure (4.25 b) the jet ejection from the crest of the steepening wave (Figs. 4.25 a). It develops into a nice and long tongue of water (Figs. 4.25 c and d) which hits the forward face of the overturning wave (Fig. 4.25 e).

As the wave propagates towards the reef, we can observe the occurrence of a weather-side vortex at the upstream corner of the obstacle, as shown in the previous section (see section 4.4). This structure behaves differently, their motions depending on the proximity of the free surface. To illustrate and discuss about this particular feature of the flow, we gather in table (4.6) the initial parameters of the simulations we performed. The one called *"Chang"* refers to the simulation detailed in the previous section (see section 4.4), *"ST"* refers to the first configuration we shown in this section, *"ST5"* being the last simulation we presented (Figs. 4.25). We introduce the relative depth $d' = \eta - D$, which is the initial depth of water above the submerged obstacle. It will increase and decrease along the propagation of the wave over the reef, but it gives an idea of the variety of the heights of the columns of water in which the weatherside vortices develops and

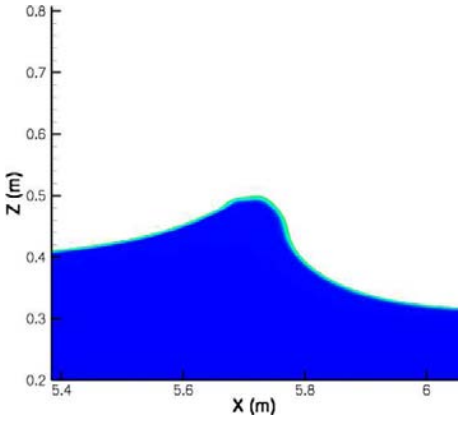

(a) $t = 1.7\ s$

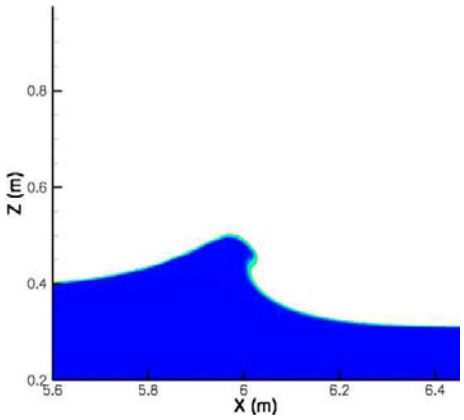

(b) $t = 1.8\ s$

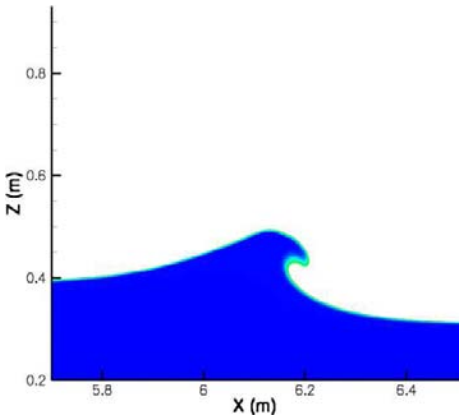

(c) $t = 1.9\ s$

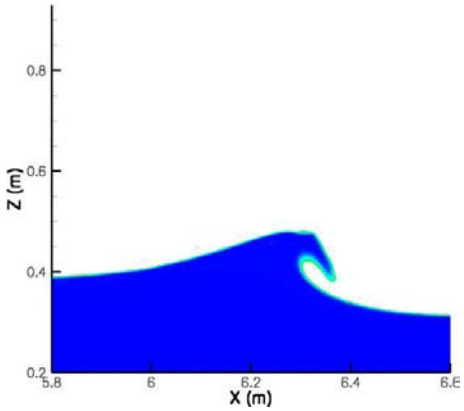

(d) $t = 2.0\ s$

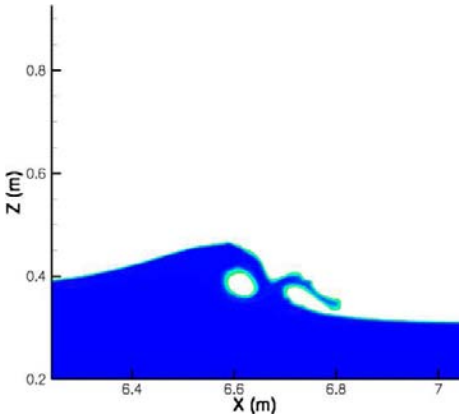

(e) $t = 2.2\ s$

Figure 4.25: Details of the solitary wave breaking process - *"ST5"* simulation. $H/d = 0.5$, $D/d = 0.6$ - $C > 0.5$.

moves in the cases we simulated. We plot in figure (Fig. 4.27) the trajectories of both weathersides vortices observed in *"ST5"* and *"ST"* simulations. Unfortunately, Yasuda et al. (1997) did not show any visualizations of this feature of the flow, as it was not their interest, so we do not have any possibility to confront our numerical results to any experimental data. Thanks to the experience from the previous section (see section 4.4), we can assume the results we obtained are not so far from what could be seen experimentally.

As a matter of fact, we can notice that both lines plotted in figure (4.27) express that the vortices behave similarly. These two vortices propagates along the obstacle face as the wave propagates towards the right side of the numerical domain. They are both constrained by the increasing amount of water above the reef. Their shapes are flattened and their motions in the flow direction are slower than what we showed in section (4.4), the relative depths of water being more important. They stay very close due to the near presence of the reef. The vortex observed from the *"ST"* simulation never rises to the surface, as shown by the dot-dashed line plotted in figure (4.27). It moves suddenly downstream when the incoming wave passes by the reef corner, but stays at the same distance from the reef upper face and seems to retreat. This is due to the fact that, once the waves propagates over the reef, the incoming wave separates in two humps. One keeps propagating towards the right side of the domain, as shown in figures (4.20 c and d), and steepens before breaking, as already discussed previously. The other hump stands over the upstream corner and feeds the propagating one, as its amplitude decreases more or less regularly along the time (Fig. 4.19 a). This process is very similar to a hydraulic jump: a depression is created, a large amount of water flows downstream, which forces the vortex to retreat. This is illustrated in figure (4.19 a), where the non-dimensional free surface elevations, η/d, plotted versus the non-dimensional time, shows the depression above the upstream corner, and in figure (4.26). The free surface comes even closer to the obstacle, crushing the vortex until it disappears.

The vortex observed from the *"ST5"* simulation shows a different behavior. We can see that the "broken" black dashed line expresses a very chaotic motion influenced by the wave propagation. First, both generation and propagation of the vortex are very similar to what we detailed for the vortex from the *"ST"* simulation. The difference is that this vortex rises slightly and grows in size before changing completely its direction: the wave just passed by the upstream corner. But this time, the depression noticed behind the steepening wave forces the vortex to move downstream, parallel to the reef upper face. The vortex has more space to move as the relative depth of water is more important. Then it suddenly rushes upstream again, rising to the surface. The vortex is then influenced by the breaking, or what we could call a "back splashing", of the free surface

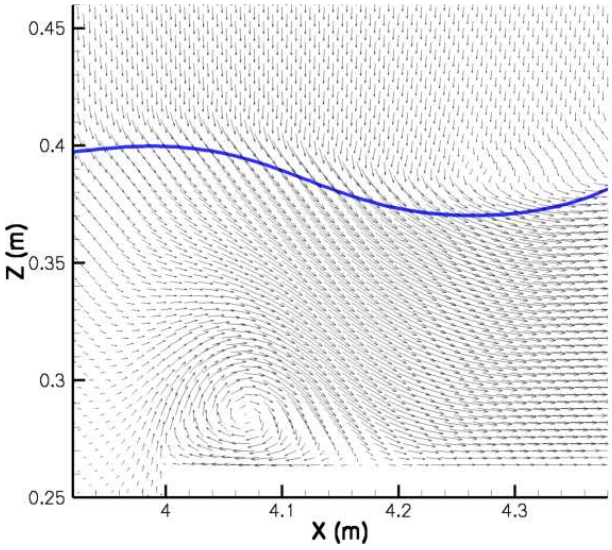

Figure 4.26: Zoom in of the weatherside vortex for the *"ST"* simulation, at $t = 1.3\ s$. Only one vector over three are shown in both media. The blue line stands for $C = 0.5$.

which pushes it back the same way it came. It is moving pairing with a counter-rotating pocket of gas entrapped in the water. This pair of counter-rotative vortices is moving fast towards the upstream corner of the reef and separates as the pocket of air hits the reef and the vortex rises again to the surface, as shown by the curved part of the black dashed line.

It can be noticed that, as shown in figure (4.26), the flow in the air follows the free surface while its level decreases due to the depression (Fig. 4.28 a). When the rear of the steepening wave comes to splash above the weatherside vortex, the air above it is violently entrained (Fig. 4.28 b) and thrown away by a tongue of water resulting from the splash. A rotating pocket of air is enveloped and entrained in the water. The flow in the air is very chaotic due to the strong interface deformations.

The behavior detailed in section (4.4) is in between what we described, the relative depth of water of the *"Chang"* simulation being itself bounded by the relative depths of water of both *"ST"* and *"ST5"* simulations. A major difference comes from the fact that the wave propagates over the reef and does not break over it. As there is no depression behind the propagating wave, the weatherside vortex is free to move in a constant relative depth of water once the wave passes by it, diffusing its momentum in a quietening down column of water. More vortices were generated in that case because the main structure drifted downstream. This does not happen to appear in both *"ST"* and *"ST5"* simulations,

Simulations	Chang	ST	ST5
Depth (d (m))	0.16	0.31	0.31
Amplitude (H (m))	0.0288	0.1314	0.155
Reef height (D (m))	0.08	0.263	0.186
Initial relative depth ($d^{'}$ (m))	0.08	0.047	0.124

Table 4.6: Initial parameters for the solitary wave propagation simulations.

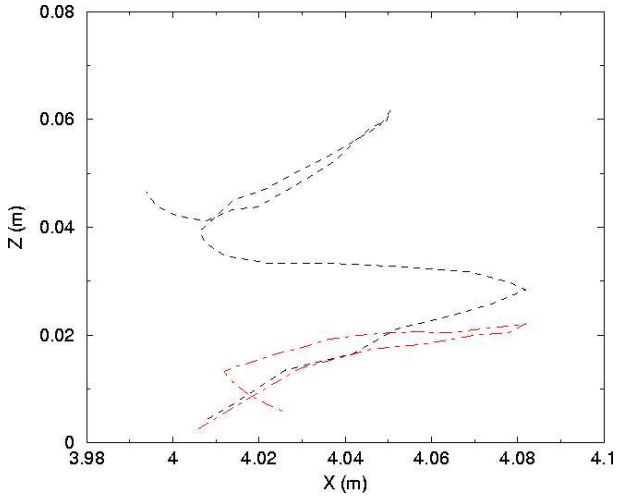

Figure 4.27: Comparison of the weatherside vortices trajectories. Black dashed line: *"ST5"* simulation; red dot-dashed line: *"ST"* simulation.

due to the stronger interactions between the generated vortices and the free surface and the wave breaking occurrence.

4.5.2 Conclusions and perspectives

This test-case leads us to the conclusion that the numerical model gives accurate results for the breaking of a solitary wave over a rectangular submerged obstacle. Numerical results match very well with the provided experimental and numerical data from Yasuda et al. (1997). However, it has been shown that a great care has to be taken in the choice of the numerical methods. A wrong interpretation can be given on the basis of some results dramatically affected by numerical imperfections.

Another great interest would be to go further in the investigation of the fission phenomenon: when solitary waves propagate from deep water into shallower water, the in-

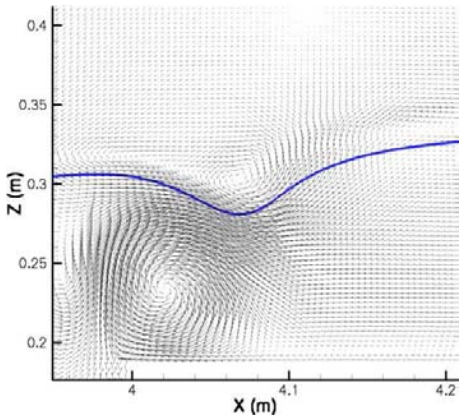

(a) $t = 1.8\ s$

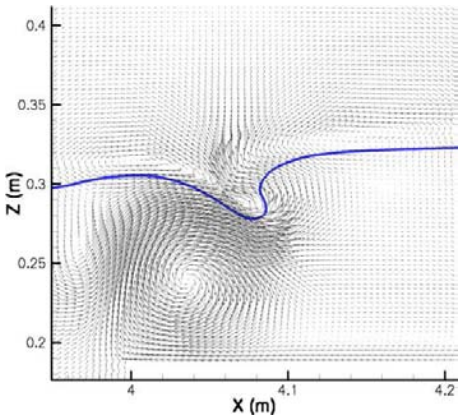

(b) $t = 1.9\ s$

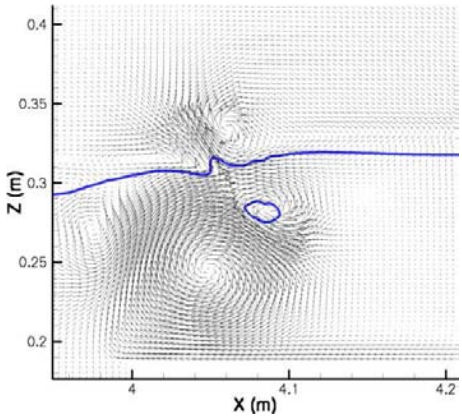

(c) $t = 2.0\ s$

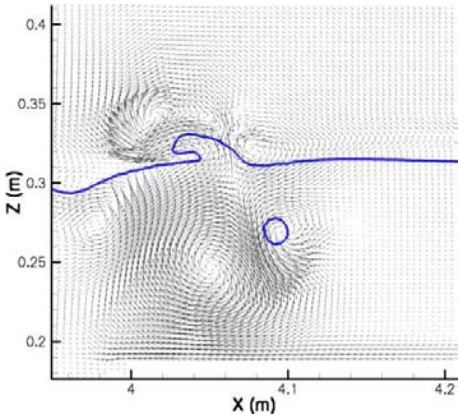

(d) $t = 2.1\ s$

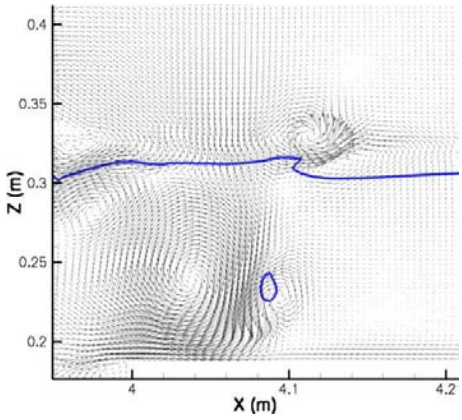

(e) $t = 2.2s$

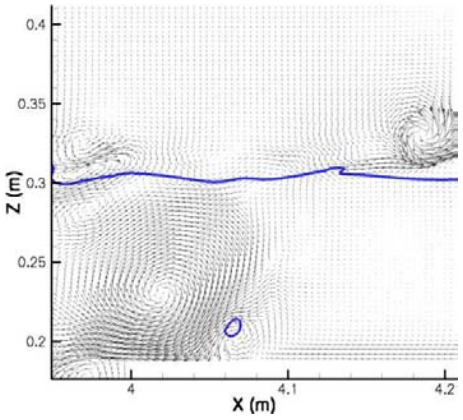

(f) $t = 2.3\ s$

Figure 4.28: Evolution of the weatherside vortex (*"ST5"* simulation) and "back-splashing". The velocity field is shown in both media. Blue line stands for $C = 0.5$.

coming waves disintegrate into two or more solitons. This has already been explained analytically (Whitam, 1974) and more closely studied and illustrated numerically and experimentally (Seabra-Santos et al., 1997; Liu and Cheng, 2001), for breaking and non-breaking cases. Given the initial conditions (*i.e.* the mean water depth, the amplitude of the incoming solitary wave and the height of the obstacle), the amplitude and the number of the transmitted waves can be predicted, as well as the amplitude of the reflected wave. The free surface shape can also be described at any time. This process can be observed in figure (4.20), where the initial wave separates into two humps. It would then have been of a great interest to validate our numerical model by checking the accuracy of the description of this phenomenon.

4.6 Solitary wave shoaling and breaking over a sloping beach

The shoaling and breaking of solitary waves over a sloping beach is studied to investigate the ability of our numerical model to reproduce properly the breaking phenomenon induced by a bathymetric variation, smoother than in previous cases (see section 4.5), where the bottom topology changed abruptly due to a submerged obstacle. The first two test-case references are taken from Grilli et al. (1997), who developed a fully nonlinear potential flow model based on a Boundary Element Method (BEM). The shoaling and breaking of solitary waves over a wide range of slopes between 1/100 to 1/8 have been numerically experimented. In the following, we will consider a 1/15 slope with various initial wave amplitudes in order to generate a plunging and a surging breaking waves. We will then inspect another plunging breaking case (Biausser, 2003).

Some experimental data are provided in the next section to investigate more precisely our numerical method, with the help of some data initialization supplied by a fully nonlinear potential flow model based on a Boundary Element Method (BEM) (Grilli et al., 2004).

4.6.1 Comparisons with numerical results

Comparisons with BEM results

The slope of the beach is 1/15. The mean water depth is $d = 0.7\ m$ and the initial amplitude is $H = 0.21\ m$ ($H/d = 0.3$), which gives the initial celerity $c = 2.981\ m.s^{-1}$ (Eq. C.10). The numerical domain is 20 m long and 1.2 m high, discretized into 1200×200

Simulations	H'_b	x'_b	h'_b	t'_b
Grilli et al. (1997)	0.395	12.75	0.15	11.43
Aquilon - LES	0.401	13	0.13	12
Error (%)	1.52	1.96	13	5

Table 4.7: Data for the solitary wave breaking simulations. Plunging breaking case.

nonuniform grids in the x-direction, with $\Delta x_{min} \simeq 9\ .10^{-3}\ m$ in the vicinity of the breaking point, and a uniform grid spacing $\Delta z_{min} \simeq 6\ .10^{-3}\ m$. The incident solitary wave is initialized in the numerical domain, the crest of the wave being set at $x = 4\ m$, the beach slope starting at $x = 8\ m$.

We present in table (4.7) the comparisons between the results coming from our LES simulation and the values published by Grilli et al. (1997). The subscript b denotes that these quantities are considered at the breaking point, *i.e.* where the wave front face has a vertical tangent. h'_b is the non-dimensional water depth at x'_b, calculated as $h'_b = 1 - x'_b \times s$, s being the slope of the beach. t' is considered to be set at 0 when the incident wave crest passes by the toe of the beach slope. The superscript $'$ denotes dimensionless variables, lengths and times being respectively divided by the initial water depth d and $\sqrt{d/g}$.

It can be deduced from our values that the wave breaks later than what is expected from the results from Grilli et al. (1997). The wave crest is then higher and breaks further in a shallower water depth. Nevertheless, the jet impacts at $x = 10\ m$, which gives $x' = 14.29$ to be compared with the abscissa $x' \simeq 14.25$ read on the pictures presented by Grilli et al. (1997). This delay in the breaking process has already been pointed out by Biausser (2003), who used comparable numerical methods than ours. The figures presented (Figs. 4.30) are to be compared to the profiles published by Grilli et al. (1997). The first striking feature is the rounder shape of the impinging jet than those coming from the BEM results. The jet appears to be smaller in size in our LES simulation and seems to be ejected less farther, as it falls down. The amount of air entrapped under the jet will then be smaller than what is expected from the BEM simulation. The overall flow seems less dynamical.

The spatial distribution of the velocity field at the crest of the wave and the magnitudes of the velocity components turn out to be responsible for the difference in the shapes of the ejected jets. This is confirmed by the figure (4.29) which shows the velocity

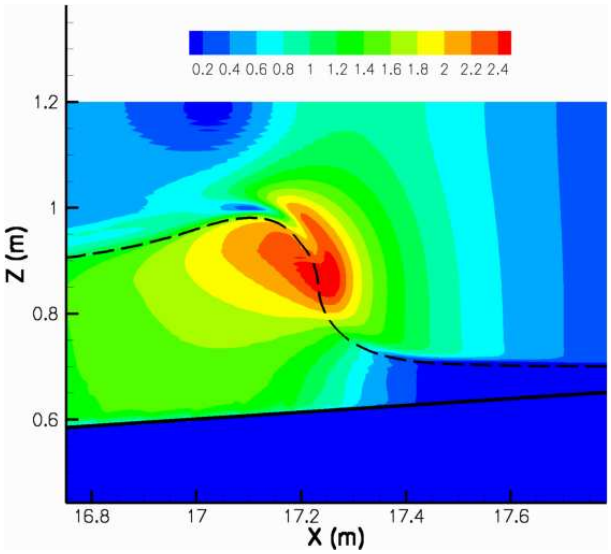

Figure 4.29: Velocity modulus at $t = 4.8\ s$, $H/d = 0.3$. The black line stands for the beach profile (1/15). The black dashed line stands for $C = 0.5$.

modulus in both air and water. Actually, it can be seen that the maximum of the velocity modulus is located on the upper face of the wave, as this region is usually observed at the crest of the wave (Figs. 4.35). The maximum horizontal velocity component is $u \simeq 2.4\ m.s^{-1}$ whereas the maximum vertical velocity component is $v \simeq 1\ m.s^{-1}$. Then, the jet of water is ejected with less intensity towards the vertical direction and will fall down more rapidly, as already pointed out in section (4.5).

The magnitudes of the velocity modulus shown in the air (Fig. 4.29) point out the dynamics of the flow. The air is pushed by the front face of the wave (large values) and a vortex is observed in the air above the crest of the wave (large / low values). The flow follows the rear of the wave, as it propagates (low values).

Both numerical and viscous dissipation are responsible for these discrepancies. Our results are anyway considered as fairly good as the overall breaking process is very well reproduced. The bottom topology variation induces the breaking of the wave with a general good agreement.

We also consider the case of a surging breaking case. Surging breakers are very different from plunging breakers, in the sense that there is no overturning motion and no jet ejection. Surging waves do not break in the traditional sense. The wave front becomes vertical and the wave runs up the slope without breaking. The breaker surges up the beach face as a wall of water with the wave crest and base travelling at the same speed.

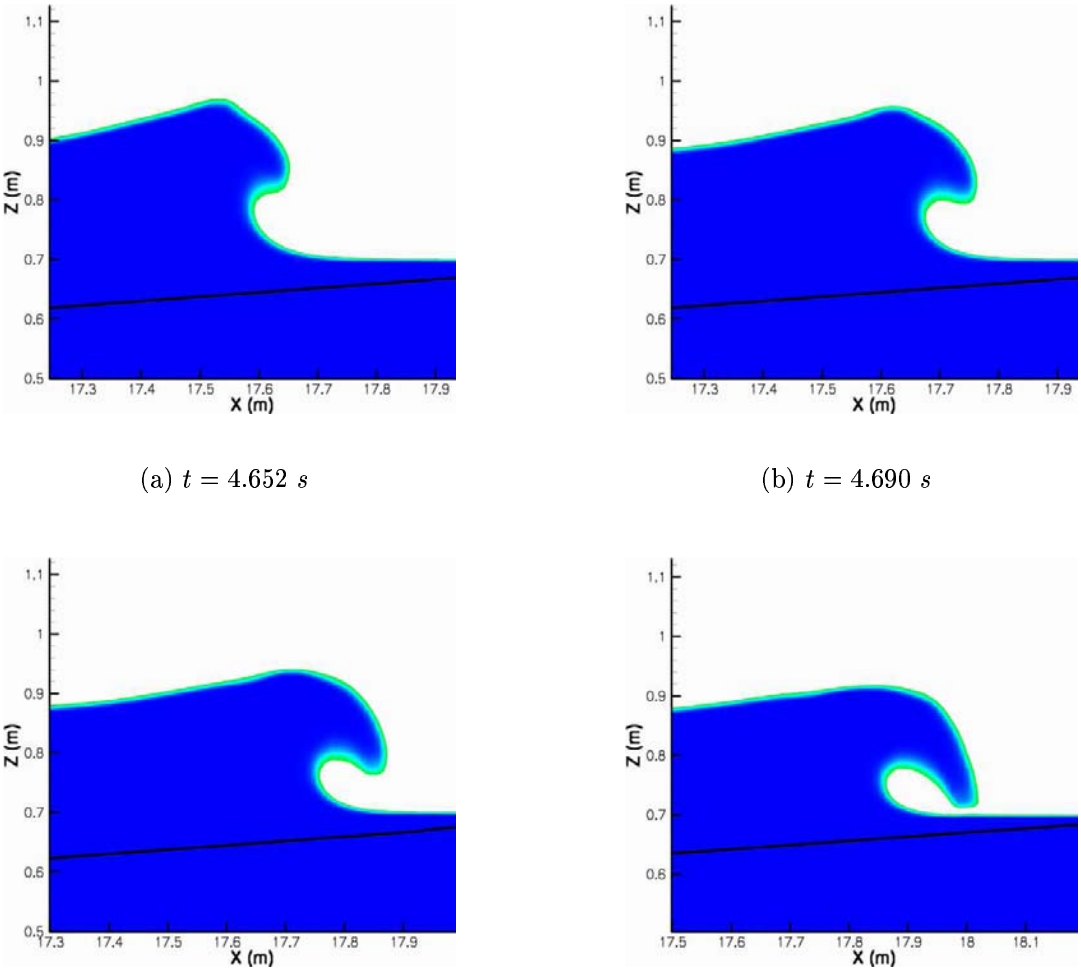

(a) $t = 4.652\ s$

(b) $t = 4.690\ s$

(c) $t = 4.729\ s$

(d) $t = 4.780\ s$

Figure 4.30: Details of the solitary wave plunging breaking process. The black line stands for the beach profile (1/15). $H/d = 0.3$, $C > 0.5$.

Simulations	H'_b	x'_b	t'_b
Grilli et al. (1997)	0.111	14.75	16.20
Aquilon - LES	0.112	14.87	16.32
Error (%)	0.9	0.82	0.75

Table 4.8: Data for the solitary wave breaking simulations. Surging breaking case.

Surging breakers are usually found on beaches with very steep slopes. So we will evaluate the capability of our numerical method to describe accurately the interactions between the wave and the beach in terms of shoaling and free surface deformation occurrence, and we will thus try to have a clear idea of where the observed discrepancies come from.

The slope of the beach is still 1/15. The mean water depth is still $d = 0.7\ m$ and the initial amplitude is $H = 0.07\ m$ ($H/d = 0.1$), which gives the initial celerity $c = 2.747\ m.s^{-1}$ (Eq. C.10). The numerical domain is 19 m long and 1 m high, discretized into 1200×200 nonuniform grids in the x-direction, with $\Delta x_{min} \simeq 9\ .10^{-3}\ m$ in the vicinity of the breaking point, and a uniform grid spacing $\Delta z_{min} \simeq 5\ .10^{-3}\ m$. The crest of the wave is set at $x = 5\ m$, the beach slope starting at $x = 8\ m$. We present in table (4.8) the comparisons between the results coming from our LES simulation and the values published by Grilli et al. (1997), the subscript b denotes again that these quantities are considered at the breaking point. We do not show any picture of this case.

This time again, the wave breaks later when compared to the results from Grilli et al. (1997) (Tab. 4.8), but the error is far much lower than the one calculated in the plunging breaking case (Tab. 4.7). This implies that the abscissa x'_b is also much closer to the value found by Grilli et al. (1997). The difference between the plunging and surging breaking cases is that, in the latter one, the flow in the breaking zone is mainly unidirectional so there is almost no vertical velocity component involved in the surging process. The better results obtained in the surging breaking case highlight the conclusions drawn previously, where the numerical and viscous dissipation are pointed out to be responsible for the discrepancies. It has already been clearly observed and detailed (see section 4.5) that the vertical velocity component is very sensible to numerical oscillations and dissipation and important in the overturning process. As this vertical velocity component is initially low in magnitude (see section C.2), the numerical dissipation process can tend to reduce its intensity, affecting then the breaking process. Previously, the waveheight H'_b was proved

to be overpredicted due to the delay in breaking and to the occurrence of a small bump at the crest (Figs. 4.30). It is still overpredicted in the surging configuration, but the calculated error is much lower due to the fact that, this time, we observe a flat crest as the velocity field in the flow is directed horizontally.

So the surging breaking case, which is more favorable, illustrates the accuracy of our numerical model to predict the main stages of the breaking process (shoaling and steepening of the wave), but still shows that our numerical methods suffer from numerical and viscous dissipation. Even if the BEM method does not take the air into account, it has been shown to be very accurate to simulate the breaking of solitary waves on sloping beaches (Grilli et al., 1997), so we know that in our method, where both fluids are considered, the air should not be responsible for the discrepancies.

Comparisons with Navier-Stokes results

In order to evaluate more precisely our numerical methods in this configuration, we compare our results with some published work using the same schemes (Biausser, 2003). The slope of the beach is again 1/15. The mean water depth is now $d = 1\ m$ and the initial amplitude is $H = 0.5\ m$ ($H/d = 0.5$), which gives the initial celerity $c = 3.813\ m.s^{-1}$ (Eq. C.10). As previously, both velocity field and free surface profile are initially calculated with the theoretical third order solitary wave solution (appendix C.1.2). The numerical domain is 34 m long and 2 m high, which corresponds to the numerical domain used by Biausser (2003). It is discretized into 1300×200 nonuniform grids in the x-direction, with $\Delta x_{min} \simeq 1.4\ 10^{-2}\ m$ in the breaking zone ($20 - 34\ m$), and a uniform grid spacing $\Delta z_{min} \simeq 1.10^{-2}\ m$. The crest of the wave is set at $x = 9\ m$, the beach slope starting at $x = 14\ m$ as chosen by Biausser (2003).

We compare our results to those obtained numerically by Biausser (2003), who used a numerical tool very similar to the one we use. The air is not considered and the viscosity of the water is set to zero, so the configuration considered by Biausser (2003) is a one-phase flow solved with the Euler equations. So we first choose not to consider the turbulent viscosity for the following results in order to compare the numerical dissipation of our schemes ("DNS"). From the pictures shown by Biausser (2003), we can observe the occurrence of a plunging jet, impacting at $x \simeq 28\ m$ at $t > 4\ s$. It can be seen in the pictures we present (Figs. 4.32), that we are in agreement with the results shown by Biausser (2003). A plunging breaker is developing (Fig. 4.31) at $t > 4\ s$ and the wave breaks in a very thin film of water. There is almost no more water depth and the successive splash-ups

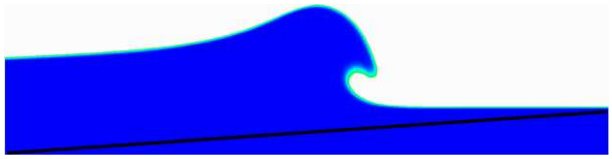

Figure 4.31: Solitary wave developing into a plunging breaker at $t = 4.8\ s$ ("DNS" simulation). The black line stands for the beach profile (1/15). $H/d = 0.5$, $C > 0.5$.

rebounds on the beach, which would induce a large erosion of this upper part of the beach.

As we have no further information about the time at which occur the breaking processes, we will not go through detailed comparisons, the abscissae being the only relevant details that we can consider. The wave front steepens at $x \simeq 26\ m$ and the jet ejection is initiated at $x \simeq 26.5\ m$ (Figs. 4.32 a and b), which is very similar to the results shown by Biausser (2003). The only discrepancy appearing is that the jet impacts a little before $x \simeq 28\ m$ ($x = 27.7\ m$). As both numerical tools are based on the Navier-Stokes equations and use more or less the same numerical schemes, the results should then be subjected to the same order of numerical dissipation. This leads us to conclude that the discrepancy should be due to the fact that we consider two viscous fluids, air and water, the energy dissipation being then increased. This highlights the conclusions we draw in the previous section (4.6.1), where both numerical and viscous dissipation are responsible for the discrepancies between the results.

Nevertheless, it is highly important to take both fluids into account as the entrainment of the air in the water during the breaking processes is responsible for a large amount of the generation of turbulence. Biausser (2003) shows many pictures were all the entrapped gas pockets disappear once they are caught, due to the fact that they do not consider the air. Moreover, the gas pockets have a great effect on the wave energy dissipation and on the free surface deformations.

We now run a test with a finer mesh grid and, as in the previous section (4.5), we do LES simulation of the same solitary wave configuration. In order to save some mesh points, we reduce the length of the numerical domain (30 m long). The numerical domain is now discretized into 1200×200 nonuniform grids in the x-direction, with $\Delta x_{min} \simeq 1.10^{-2}\ m$ in the breaking zone ($20 - 30\ m$), and a uniform grid spacing $\Delta z_{min} \simeq 1.10^{-2}\ m$. The crest of the wave is set at $x = 9\ m$, the beach slope starting at $x = 14\ m$ as chosen by Biausser (2003).

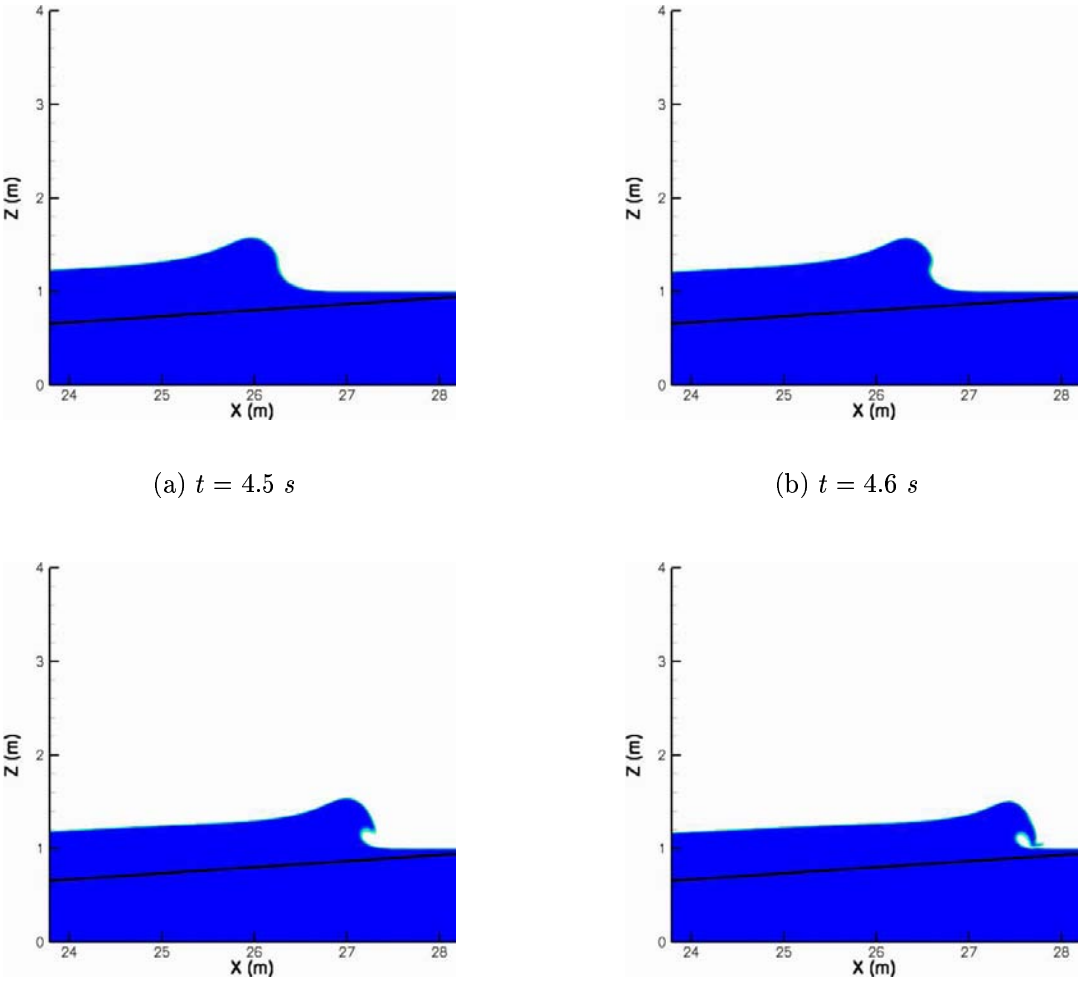

(a) $t = 4.5\ s$

(b) $t = 4.6\ s$

(c) $t = 4.8\ s$

(d) $t = 4.9\ s$

Figure 4.32: Details of the solitary wave breaking process ("DNS" simulation). The black line stands for the beach profile (1/15). $H/d = 0.5$, $C > 0.5$.

A significant change can be observed in the shape of the ejected jet. The breaking of the wave starts slightly earlier in space and time ($x = 25.8\ m$ at $t = 4.33\ s$) than in the DNS simulation ($x = 26.3\ m$ at $t = 4.5\ s$). The jet impacts at $x = 27.5\ m$ at $t = 4.7\ s$, to be compared with the values obtained with the DNS simulation, $x = 27.7\ m$ at $t = 4.9\ s$ (Figs. 4.32). This seems quantitatively very similar, but the most striking result is in both the shape and size of the jet. The tongue of water touches down at more or less the same abscissa, but it is far bigger in the LES result and thrown further horizontally. It then envelopes a bigger gas pocket. Moreover, its size being increased, the strength of the impact is thus influenced. Similar observations have been highlighted in section (4.5). The discrepancies quantified can be expected, as the addition of the turbulent viscosity tends to expend to a slender extent the energy of the shoaling wave.

This point is anyway very important. Turbulent viscosity, being a positive quantity, has many non-negligible effects (see sections 4.5 and 4.6.1). It regularizes and erases numerical imperfections brought by false DNS, in the same manner than a dissipative numerical scheme, but based on physical assumptions and models. However, it may seem abusive to use turbulent viscosity when the flow is not turbulent, except in the air, where a vortex is located above the crest of the propagating and then breaking wave, and at the bottom, where friction occurs.

4.6.2 Comparisons with experimental results

This section deals with the validation of our numerical model, used for simulating shoaling and breaking solitary waves on slopes, based on experiments performed at the Ecole Supérieure d'Ingénieurs de Marseille (ESIM) laboratory. This work has been carried out in the framework of the national program *P.A.T.O.M.* ("Programme Atmosphère et Océan à Multi-échelles") of the CNRS[1].

The aim of this collaboration study is twofold. The first interest is to validate some numerical tools based on the two-phase Navier-Stokes equations, compared to the experimental measurements and numerical simulations run with a model based on the potential theory.

Then, we want to evaluate the numerical methods and schemes used to discretize the Navier-Stokes equations, as most laboratories implied in this benchmark develop or utilize numerical tools involving different technics.

The first results are presented hereafter, as the study is still undertaken.

[1]I truly thank Pr. S. T. Grilli, R. Gilbert, O. Kimmoun and H. Branger for authorizing me to use their material in this section.

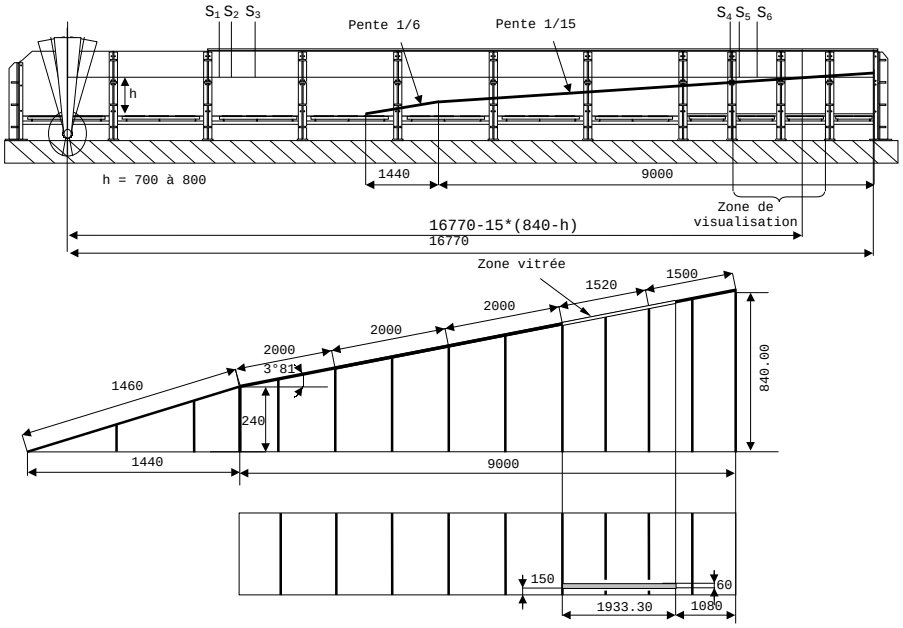

Figure 4.33: Experimental wave tank. With permission (Kimmoun et al., 2004).

Kimmoun et al. (2004) reported on experiments. Waves were generated using a flap wavemaker whose axis of rotation was located below the tank bottom (Fig. 4.33). Experiments were run over a range of water depths and for two different wave sizes, referred to as type 2 for a larger solitary wave ($H = 0.1\ m$ in $d = 0.74\ m$, which gives $H/d = 0.135$), and type 7 for a smaller solitary wave ($H = 0.16\ m$ in $d = 0.76\ m$, which gives $H/d = 0.211$). Experimental data includes wave elevation measured at 6 wave gauges, visualizations of breaking wave shapes around the location of the shallower probe over the slope, and flow velocities measured in the breaking wave area using a Particle Image Velocimetry (PIV) method.

A fully nonlinear potential flow model based on a Boundary Element Method (BEM) developed at the University of Rhode Island (Grilli et al., 2001), is used to generate and propagate solitary waves over a slope, up to overturning, in a set-up closely reproducing the laboratory tank geometry and wavemaker system. Then, our numerical model is initialized based on the BEM solutions and used for modelling breaking solitary waves in a finely discretized region encompassing the top of the slope and the surf-zone (Figs. 4.42 and 4.35), so we can compare our results to the experimental visualizations provided.

This coupling method between BEM and VOF simulations has already been used

Cases	Crest abscissa (m)	Crest ordinate (m)	Time (s)
7-72-1	2.98	0.10	4.14
7-72-2	10.0	0.11	6.99
7-72-3	13.9	0.14	8.75
2-76-1	3.03	0.17	4.19
2-76-2	10.0	0.18	6.82
2-76-3	13.5	0.24	8.19

Table 4.9: Data for the solitary wave breaking simulations. Time and crest positions for each considered data set.

(Guignard, 2001; Guignard et al., 2001; Biausser, 2003). The BEM method has been proved to be very accurate for computing the propagation, shoaling and steepening processes, but it does not allow to simulate the jet impacts. The VOF method has the advantage to be able to handle with interface reconnections, but is less precise to simulate all the process leading to the breaking of the wave. So we can take benefits of each method efficiency and qualities where it is the more adapted.

In the following, for simplicity, the slope has been revised to a single 1/15 slope rather than the compound slope with a 1/6 toe. For each solitary wave (types 2 and 7), three sets of data are given (Tab. 4.9). Two corresponds to the times when the waves are somewhere above the slope of the beach, shoaling and running up (Fig. 4.41 and 4.42), and the other corresponds to the time when both waves are steepening and the jet is about to be projected (Figs. 4.35).

In this section, we only discuss about the last configuration, for each solitary wave (types 2 and 7).

The Navier-Stokes numerical domains are discretized such that the grid spacings are $\Delta x_{min} \simeq 2.10^{-3}\ m$ and $\Delta z_{min} \simeq 2.10^{-3}\ m$ for the cases 7-72-3 and 2-76-3 (1800×200 mesh grid points). The heights of the numerical domain have been chosen to be far enough from the wave crests. The widths of the numerical domains are chosen such that the waves dynamics are well preserved, the waves velocities being still large only 1 m away from the crests.

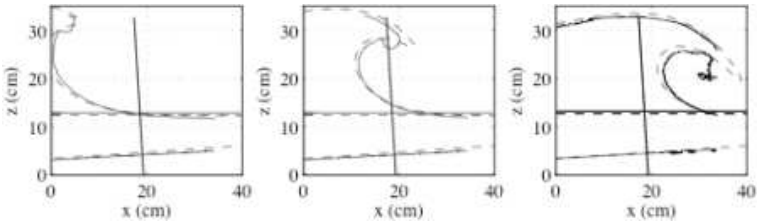

(a) Case 2-76-3

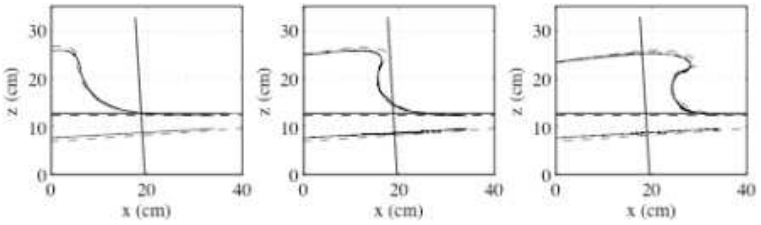

(b) Case 7-72-3

Figure 4.34: Comparisons between free surface profiles. Line: experimental visualizations ; dashed line: BEM results.

The $z = 0\ m$ position in the BEM simulations refers to the level of water after initial paddle pullback, and before the impulse. This differs from $z = 0\ m$ of the physical experiments which is at the still water level with a vertical paddle before pullback. That is why for the type $2 - 76\ cm$ depth wave, the bottom coordinates are at $-74.7\ cm$, and for the type $7 - 72\ cm$ depth wave, the bottom coordinates are at $-71.2\ cm$. The cases (type 2-76, and type 7-72) were chosen, commented on by Grilli et al. (2004), because they had the most detailed visualization from the physical experiment.

The results obtained with the BEM simulations have shown a very good agreement with experimental measurements, as shown in figures (4.34). We will then consider that these numerical results are precise enough to correspond to the experimental conditions and can be considered as accurate initial conditions for the Navier-Stokes simulations (Figs. 4.35). The results obtained will then in turn be relevantly comparable to the experimental measurements.

Figures (4.36) and (4.38) show both solitary waves breaking process. The results have been translated such that the bottom coordinates is $z = 0\ m$.

Before any further comparison, an important detail has to be commented. An undesirable feature appears in both cases, as seen in figures (4.36) and (4.38): an initial backward jet takes place at the crest. This spurious effect could be expected to happen. This is due to the fact that the free surface is strongly distorted, due to a high shear region

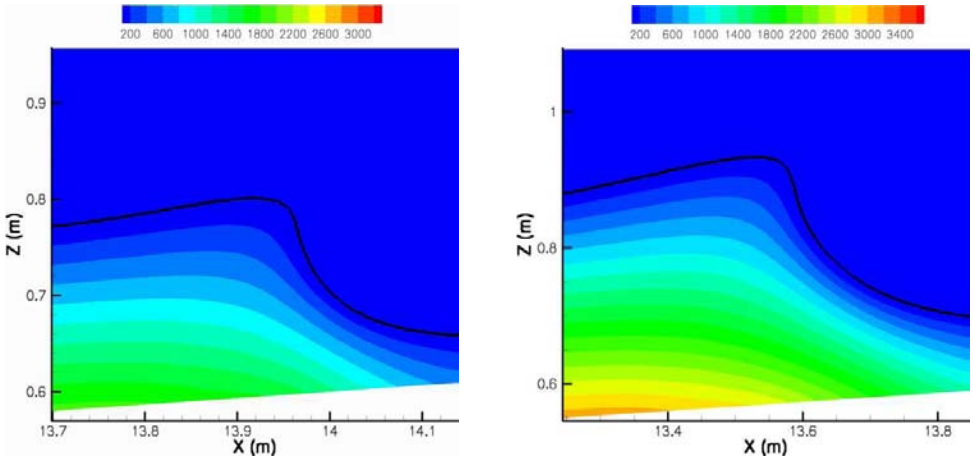

(a) Pressure

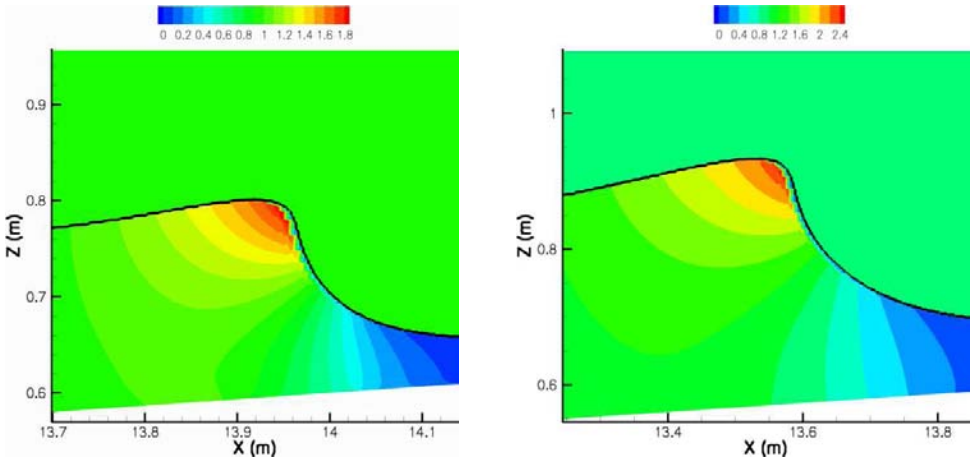

(b) Horizontal velocity

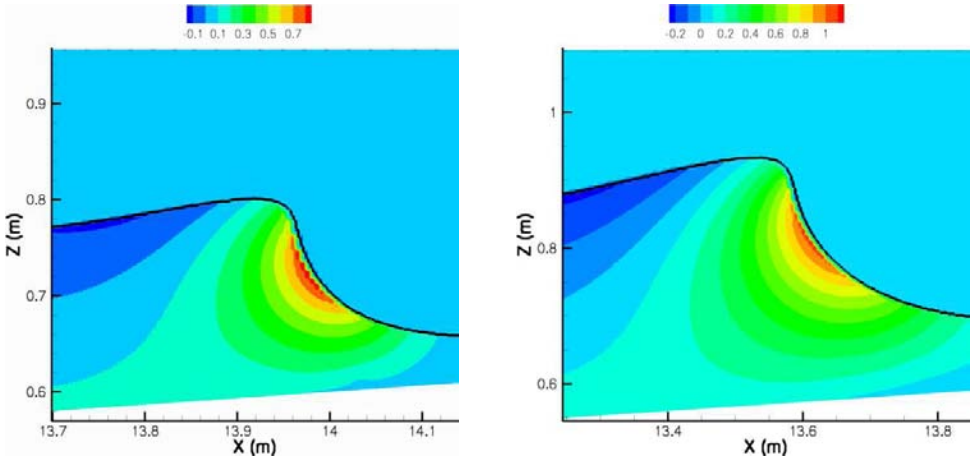

(c) Vertical velocity

Figure 4.35: Initial conditions computed from BEM model on the Eulerian grid, just before breaking. Left column: case 7-72-3; right column: case 2-76-3. The black line stands for $C = 0.5$.

at the interface generated by the starting wave crest motion surrounded by a medium at rest. It is also due to the fact our numerical code is maybe initialized too late in the breaking process: at this stage of the breaking process, there should be vorticity in the air. Indeed, in previous simulations, we checked there was a vortex following the crest. It could be part of some discrepancies when we compare the results. However, it is not really significant but has to be remembered, especially if EOLE runs without taking the air into account.

We will discuss qualitatively the numerical results compared to the experimental pictures (Figs. 4.37 and 4.39).

If we consider the case 7-72-3, we show in figures (4.37) sequences of pictures taken during the experimental wave breaking process, each window of measurement being spaced 15 *cm* apart. The wave steepening, the overturning and the jet impact can be observed. Some discrepancies can be highlighted at the stage of the jet ejection, as already pointed out previously. The shape and the general behavior of the "numerical" jet is influenced by the delay due to the discussed initialization problem. Nevertheless, it looks very similar to the "experimental" jet, once the jet is ejected. The main discrepancy can be checked in pictures (4.36), when the steepened wave seems to crush against the air at rest. A certain amount of energy is surely lost at this initial stage to transmit momentum to the air (Figs 4.40). The high horizontal velocities area, which is supposed to be located at the very top of the crest (Figs. 4.35), is found to be spread in the upper part of the wave, as the jet is projected. It seems that some time is necessary for the flow in both media to stabilize itself such that the air and the water are in a well balanced dynamics, so the jet is not ejected as fast as it should be observed.

The "numerical" jet is thus not ejected from the very top of the crest (Figs. 4.36 b and c), as the "experimental" jet (Fig. 4.37 a). The numerical jet appears to envelop a smaller amount of air as it starts falling to impact.

The "experimental" jet is measured to impact about 30 to 35 *cm* away from the abscissa where the front face of the shoaling solitary wave has been first observed to be vertical (Figs. 4.37). This is in a general good agreement with the numerical results, the jet being found to impact about 40 *cm* away from the initial condition (Fig. 4.36 e). The discrepancy comes from the delay in the jet ejection.

If we now consider the case 2-76-3, the same descriptions and conclusions can be drawn for this case as previously. The "experimental" jet has been measured to impact about 60 *cm* away from the the abscissa where the front face of the shoaling solitary wave has been observed to be vertical (Figs. 4.39).

The discrepancies are more important with the "numerical" jet being found to impact about 80 *cm* away from the initial condition (Fig. 4.36 e). This comes again from the delay in the jet ejection. The considered wave is much larger than in the previous case, so the initial steepened wave has much energy at this stage of the breaking process but, in turn, its vertical face offers a much larger surface to the air to resist.

The shape of the "numerical" jet has a similar thin aspect as it free-falls down (Fig. 4.36 d), as observed in the experimental visualizations (Figs. 4.39).

A much detailed study would be necessary to confirm the conclusions, but these uncertainties lead us to consider earlier times to initialize our simulations (Figs. 4.42 and 4.41). The grid spacings are $\Delta x_{min} \simeq 5.10^{-3}\ m$ and $\Delta z_{min} \simeq 2.10^{-3}\ m$ in the breaking zone (3000×200 mesh grid points).

Figure (4.42) shows the initial pressure and velocity fields of the larger solitary wave at an initial time when the free surface profile is unsymmetrical, the wave having already started the process of steepening as it shoals on the sloping beach. Figure (4.41) shows another example with the smaller solitary wave at an earlier initial time, the wave still shoaling on a flat bottom and approaching to the sloping beach.

4.6.3 Conclusions and perspectives

This study is still undertaken and the present results are the first deliveries introducing the future work of comparisons. More quantitative comparisons with the experimental measurements will be done in order to validate more precisely our numerical model. We will pay a careful attention to the general behavior of the splash-up and air entrainment at the impact.

Comparisons with other Navier-Stokes numerical results will also allow us to evaluate our numerical technics and confirm the first conclusions we gave.

However, this study will be limited to two-dimensional simulations, due to the large number of mesh grid points already required for the two-dimensional simulations (360000 points for the smallest configuration and 600000 points for the largest). Increasing the sizes of the numerical domains by adding a third transverse dimension is not conceivable due to the important CPU time augmentation.

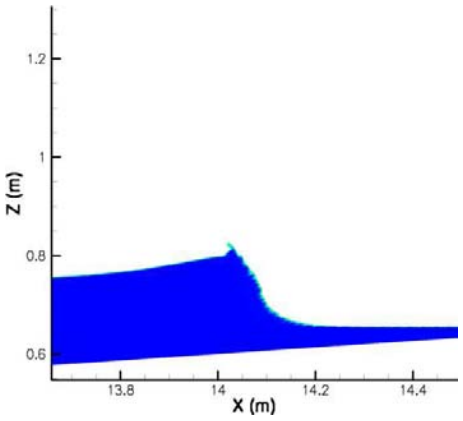

(a) $t = 6.2 \times 10^{-2}\ s$

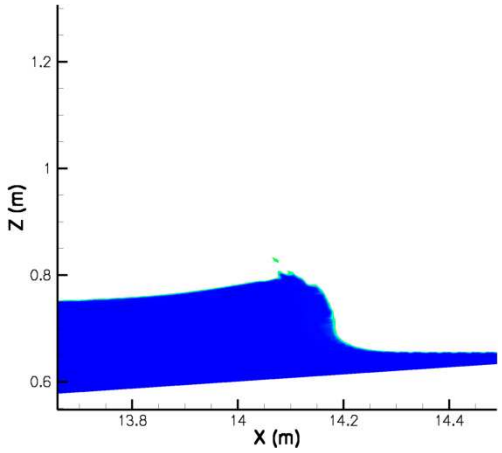

(b) $t = 0.11\ s$

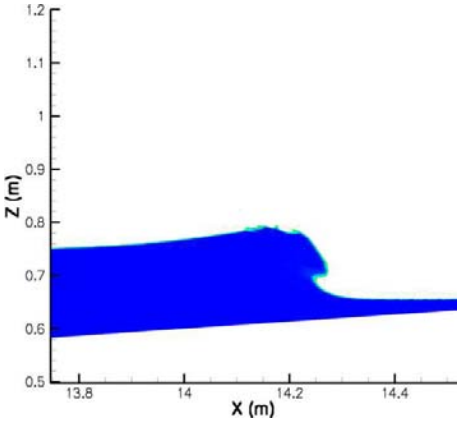

(c) $t = 0.15\ s$

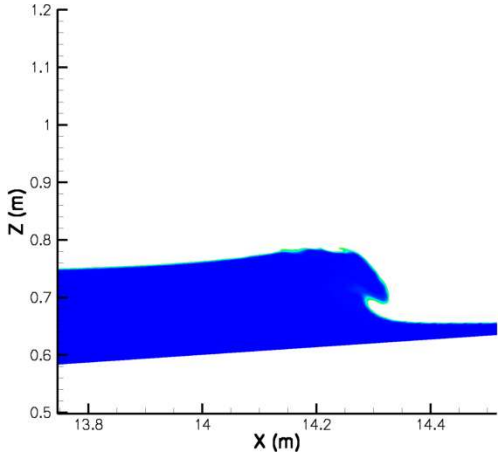

(d) $t = 0.20\ s$

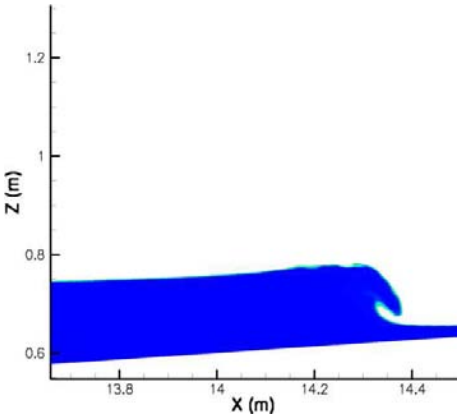

(e) $t = 0.20\ s$

Figure 4.36: Details of the solitary wave breaking process. Case 7-72-3. $C > 0.5$.

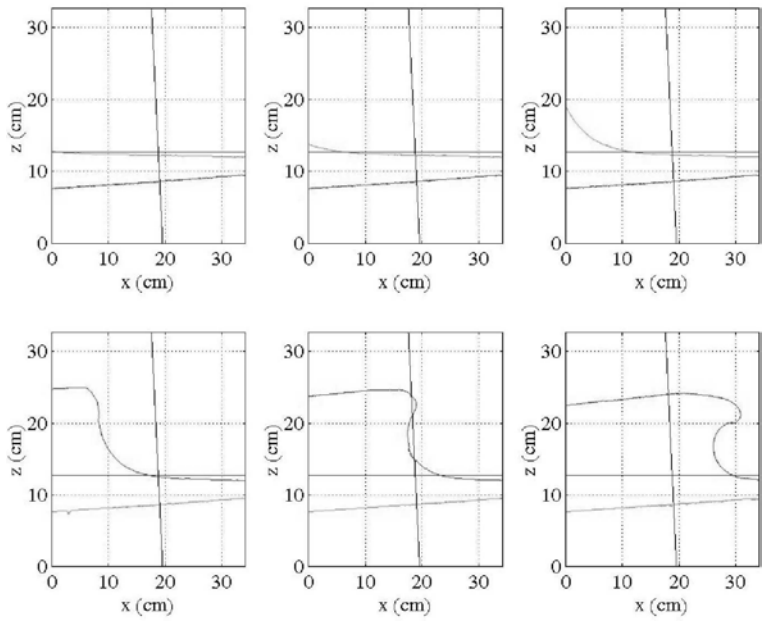

(a)

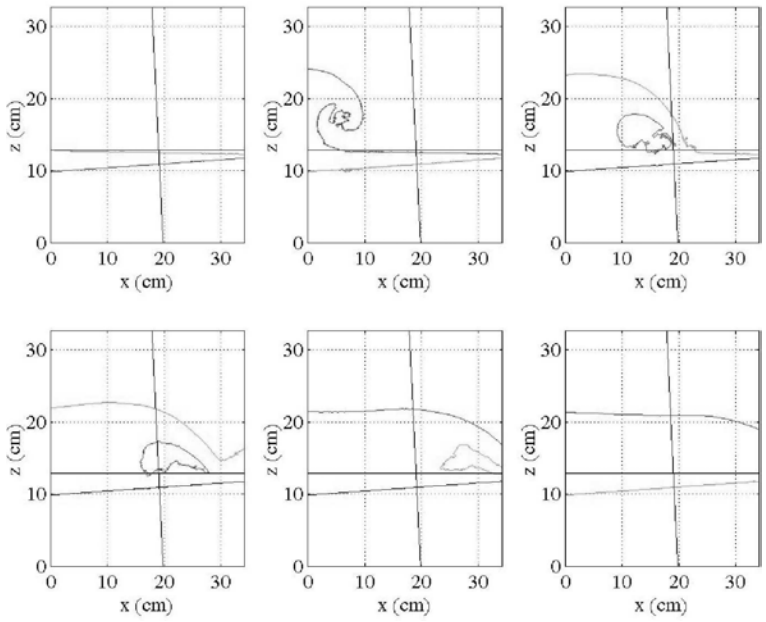

(b)

Figure 4.37: Experimental measurements of the breaking process. Case 7-72-3. Each window of measurement is spaced 15 *cm* apart. With permission (Kimmoun et al., 2004).

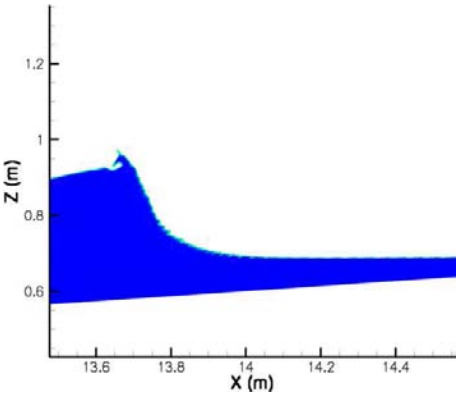

(a) $t = 6.2 \times 10^{-2}\ s$

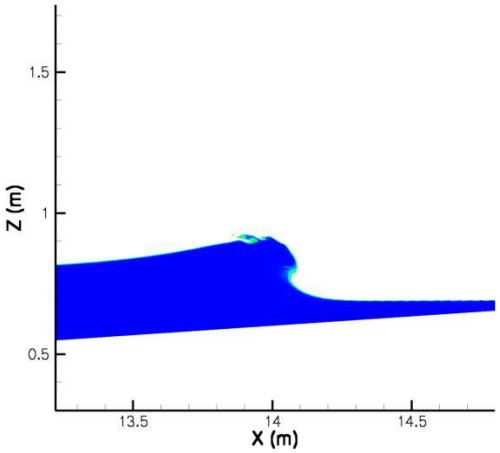

(b) $t = 0.2\ s$

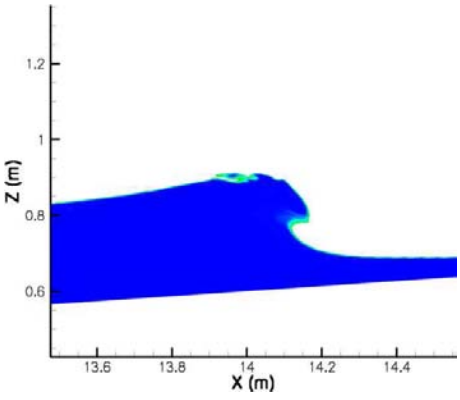

(c) $t = 0.22\ s$

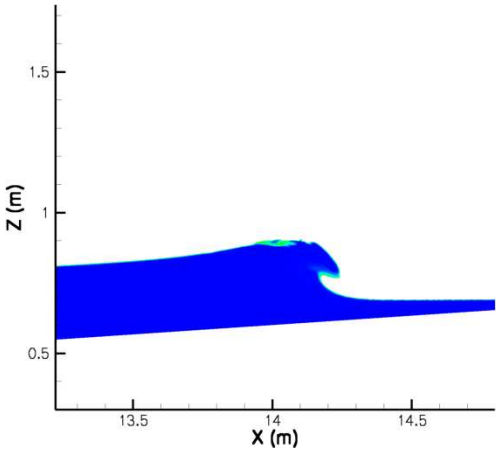

(d) $t = 0.25\ s$

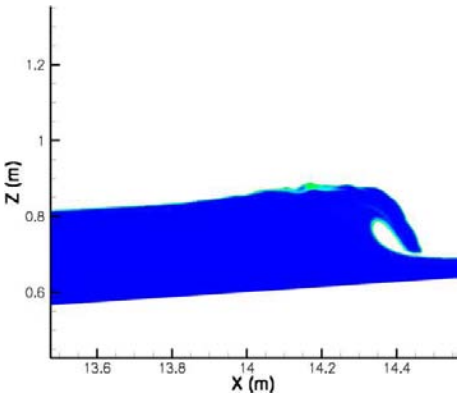

(e) $t = 0.33\ s$

Figure 4.38: Details of the solitary wave breaking process. Case 2-76-3. $C > 0.5$.

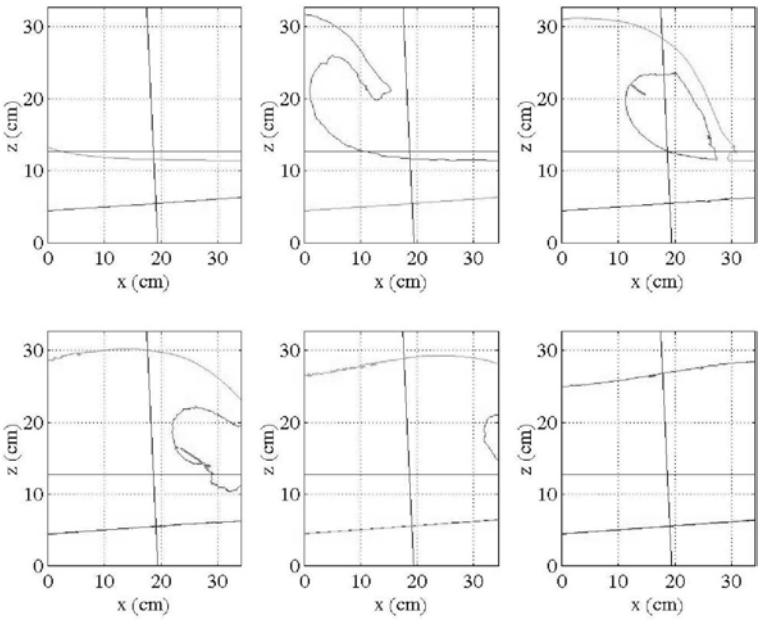

(a)

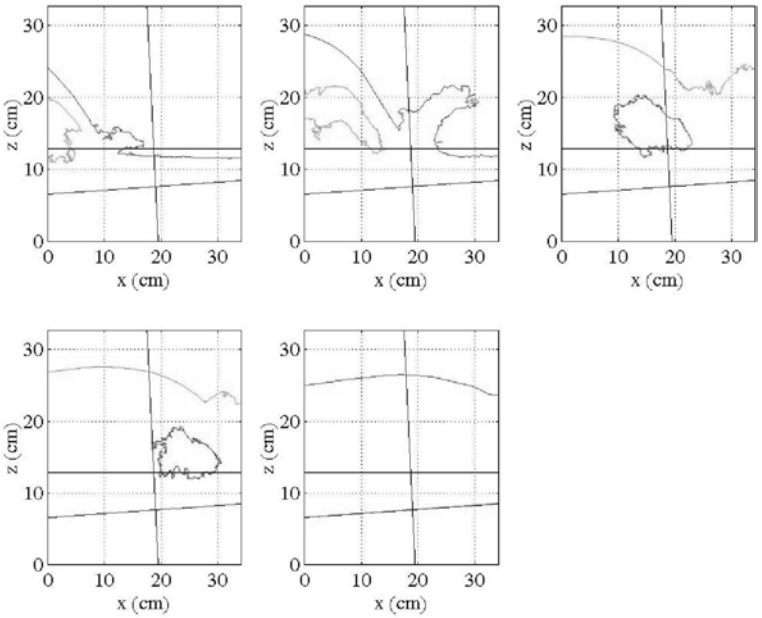

(b)

Figure 4.39: Experimental measurements of the breaking process. Case 2-76-3. Each window of measurement is spaced 15 *cm* apart. With permission (Kimmoun et al., 2004).

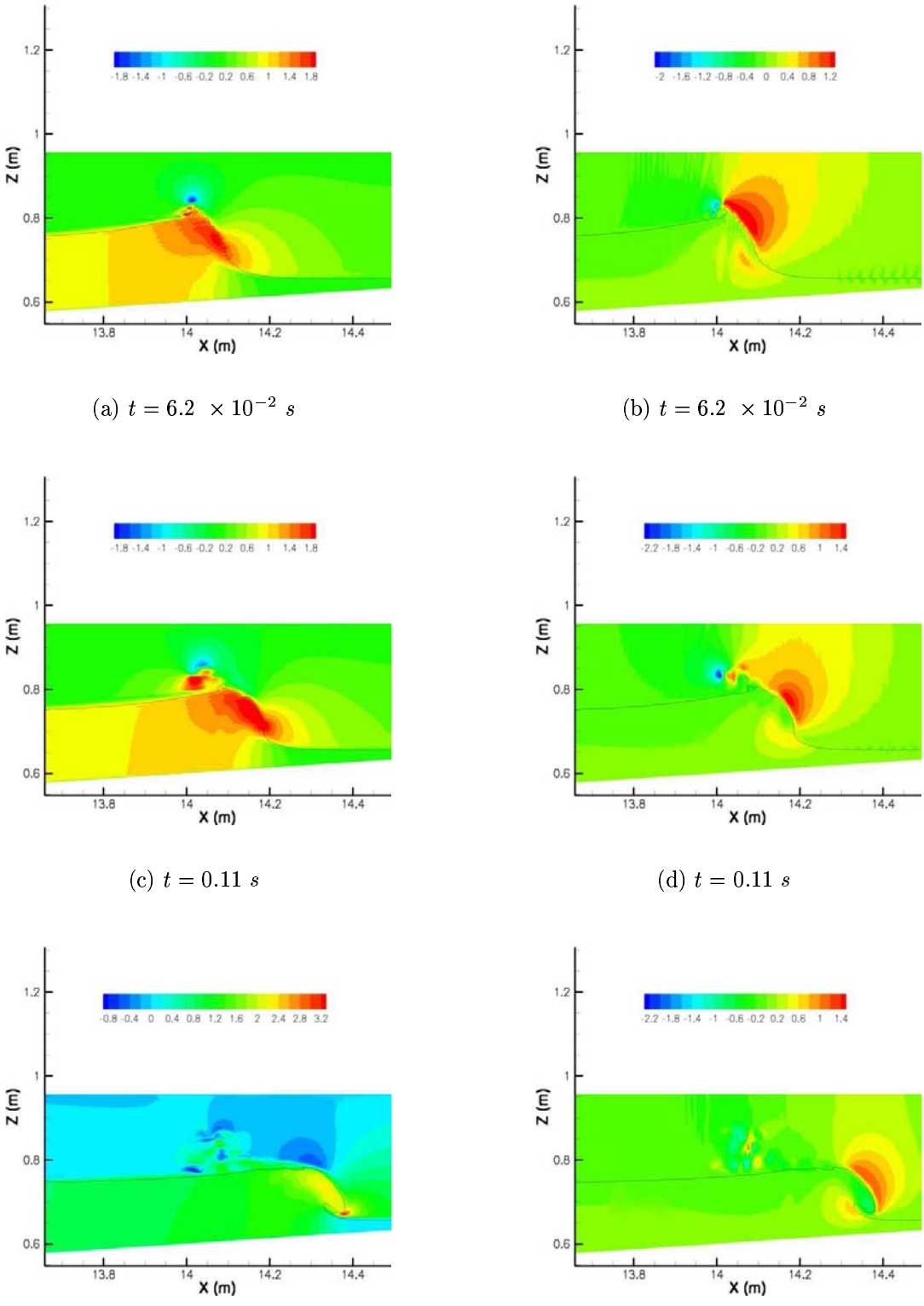

(a) $t = 6.2 \times 10^{-2}\ s$

(b) $t = 6.2 \times 10^{-2}\ s$

(c) $t = 0.11\ s$

(d) $t = 0.11\ s$

(e) $t = 0.2\ s$

(f) $t = 0.2\ s$

Figure 4.40: Details of the solitary wave breaking process - case 7-72-3. Left column: horizontal velocity component; right column: vertical velocity component. The black line stands for $C = 0.5$.

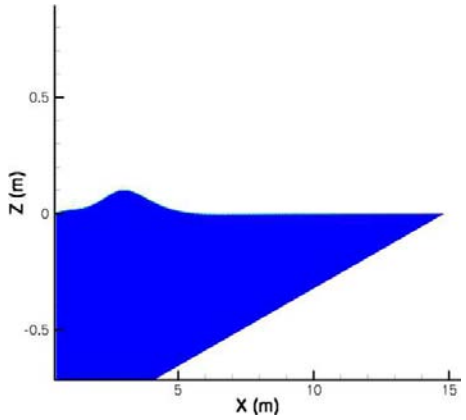

Figure 4.41: Initial conditions from BEM model, solitary wave shoaling and approaching the sloping beach - case 7-72-1. $C > 0.5$.

Summary and conclusion

We give in this section a detailed study of the abilities of our numerical tool to describe highly nonlinear and complex flows. The solitary waves are of great interest for such a kind of investigation.

The Large Eddy Simulation of many two-phase flows is studied, involving simple propagation configurations to complicated breaking cases. The effects of solitary waves interactions are successfully described, compared to analytical and numerical results. Some plunging breaking cases are validated, compared to experimental and numerical works.

The limitations of our methods are pointed out, some more efforts still have to be put into the development of more accurate numerical schemes. Specific grid generation techniques and parallel algorithms will soon be available in Aquilon and will therefore allow us to simulate three-dimensional configurations for the breaking of waves on sloping beaches. The progresses in applied mathematics and computer architectures offer the possibility of considering the three-dimensional Navier-Stokes equations to study the breaking phenomenon.

We proved our results to reach a promising level of accuracy. However, the presented numerical studies are mostly limited to two-dimensional configurations, due to the large number of mesh grid points required to discretize the numerical domains. Moreover, many presented breaking configurations do not involve air entrainment as the main feature. To study more in details the air entrainment process under three-dimensional plunging breakers, we choose a more simple configuration, unstable periodic sinusoidal waves of large amplitude in periodical domains.

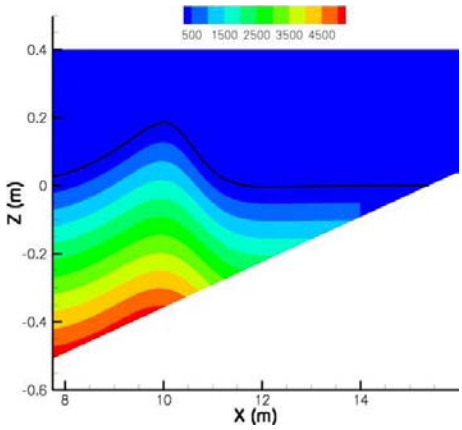

(a) Pressure

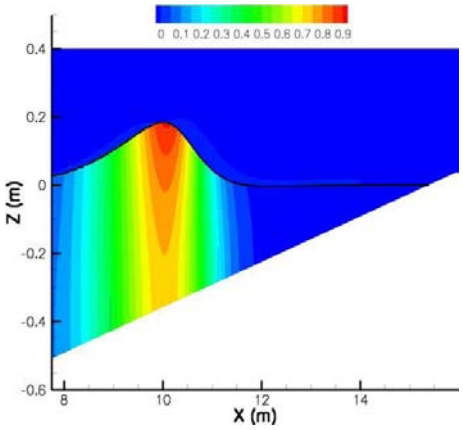

(b) Horizontal velocity

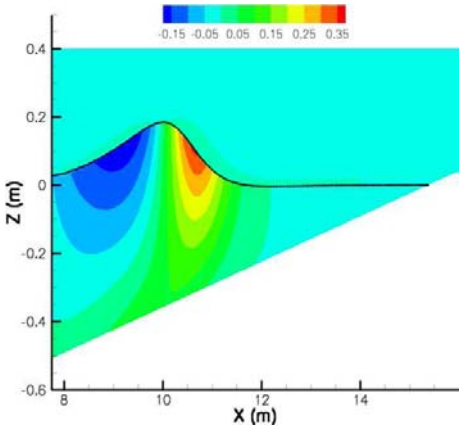

(c) Vertical velocity

Figure 4.42: Initial conditions from BEM model, solitary wave shoaling above the sloping beach - case 2-76-2. The black line stands for $C = 0.5$.

Chapter 5

Application to plunging breaking waves over a flat bottom

Introduction

The breaking wave problem is a very powerful and fascinating phenomenon. We have introduced and validated the numerical methods through many test-cases involving solitary waves. However, it has been shown that one of the limitation of the study of the breaking wave problem is the need for a high mesh grid resolution, in order to reach an acceptable level of accuracy in the description of the processes.

We choose to use initial conditions corresponding to unstable periodic sinusoidal waves of large amplitude. This study involves smaller numerical domains, which make possible three-dimensional configurations to be simulated. In this chapter, a great care is taken to describe the air entrainment process and its influence on the wave energy dissipation.

The scope of this section is to present, though some examples, detailed two- and three-dimensional descriptions of:

- the overturning motion and the general flow motion observed during the breaking of a wave
- the resulting splash-up phenomenon
- the vortices generated by the plunging crest and the series of successive splash-ups
- the energy dissipation occurring during the plunging breaking process

5.1 Two-dimensional plunging wave breaking simulations

5.1.1 Initial conditions of the case study

As already reported by Cokelet (1979), Vinje and Brevig (1981), Abadie (1998), Abadie et al. (1998), Chen et al. (1999), Abadie (2001), we use initial conditions corresponding to unstable periodic sinusoidal waves of large amplitude, the initial quantities being calculated from the linear theory. Such a wave cannot remain steady as the initial velocity field in water is not stable with the initial wave profile. As it is not a steadily travelling wave and it is steeper than an irrotational steady wave, these initial conditions lead to breaking waves. The overturning motion is therefore controlled by the initial steepness and the dispersion parameter, which makes this approach interesting as we are then able to study any breaker type by only varying these two parameters introduced latter on.

The calculation domain is periodic in the flow direction (one wavelength long), with a symmetry boundary condition in the lower limit, and a free boundary condition in the upper limit. As a periodic condition is imposed in the flow direction, the wave moving out of the domain on the right side will re-enter on the left side (Fig. 5.1). The reference variables of the initial incident wave are:

- the celerity c $(m.s^{-1})$;
- the period T (s);
- the wavelength L (m);
- the depth d (m);
- the waveheight H (m);
- the densities and viscosities of air and water media ($kg.m^{-3}$ and $kg.m^{-1}.s^{-1}$);

the flow motion being driven by the Reynolds number, $Re = \rho cL/\mu_w$, the Froude number, $Fr = c/\sqrt{gL}$, the density ratio, ρ_a/ρ_w, the viscosity ratio, μ_a/μ_w, the initial steepness, H/L, and the dispersion parameter, d/L. The last two dimensionless numbers are respectively representative of the non linearity degree of the wave and the influence of the bottom on oscillatory movement. The dispersion parameter allows us to determine if we are in deep, shallow or intermediate water:

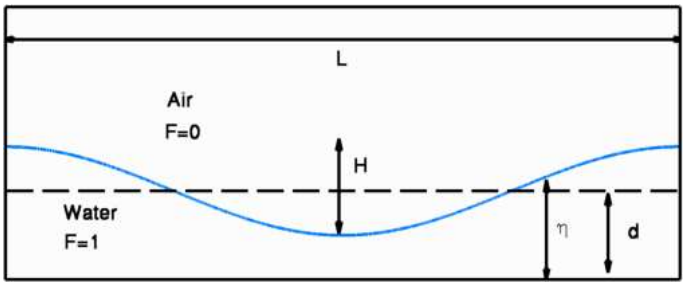

Figure 5.1: Sketch of the initial condition for the unstable periodic sinusoidal wave of large amplitude.

- $\frac{d}{L} > 0,5$: deep water ;
- $\frac{d}{L} < 0,04$: intermediate water ;
- $0,04 < \frac{d}{L} < 0,5$: shallow water.

We remind that the viscosities and densities ratios are constant in our numerical work, $\mu_a/\mu_w = 1.85 \times 10^{-2}$ and $\rho_a/\rho_w = 1.1768 \times 10^{-3}$. The initial quantities are given by:

$$\begin{aligned} \eta_0 &= \frac{H}{2} \cos kx + d \\ u_0 &= \frac{\omega H}{2} \frac{\cosh kz}{\sinh kd} \cos kx \\ v_0 &= \frac{\omega H}{2} \frac{\sinh kz}{\sinh kd} \sin kx \\ p_0 &= \rho g (z_{int} - z) \end{aligned} \tag{5.1}$$

where η_0 is the initial free-surface shape, x and z are respectively the horizontal and vertical coordinates, u_0 and v_0 are the initial velocity components, p_0 is the initial pressure filed, z_{int} is the height of the interface, $k = 2\pi/L$ is the wave number and $\omega = 2\pi/T$ is the angular frequency.

The main difference with the previous work is in the initial conditions or the assumptions employed. Indeed, many authors studied numerically plunging breakers, with artificial initial conditions, under the assumption of an inviscid flow (Longuet-Higgins

and Cokelet, 1976; Cokelet, 1979; Peregrine et al., 1980; Vinje and Brevig, 1981; Longuet-Higgins, 1982; New et al., 1985; Dommermuth et al., 1988; Skyner, 1996). Moreover, some published works have been done with the Navier-Stokes equations (Abadie, 1998; Abadie et al., 1998; Chen et al., 1999; Yasuda et al., 1999; Abadie, 2001; Guignard, 2001; Guignard et al., 2001; Biausser, 2003), but the density and viscosity ratios used in the simulations were not the real ones we use. Abadie (1998) showed that adding an artificial viscosity was useful to erase numerical perturbations observed in the vicinity of the free surface. In the work presented hereafter, the real density and viscosity ratios are used for all simulations, as few authors did (Sakai et al., 1986; Takikawa et al., 1997; Lin and Liu, 1998a,b; Bradford, 2000; Iafrati et al., 2001; Watanabe and Saeki, 2002; Iafrati and Campana, 2003).

We can then study accurately the breaking phenomenon in a smaller numerical domain, as it is periodical in the flow direction, compared to simulations involving a shoaling wave breaking over a sloping beach (see section 4) which are very demanding in terms of grid mesh points. Nevertheless, the method we use corresponding to an unstable sinusoidal wave is an artificial way of leading a wave to the breaking process, compared to the usual shoaling process and change in water depth. However, it has already been shown that there is a certain similarity with what can be observed in real conditions. As the method we use is an artificial way of reproducing the breaking of a wave, it has to have some limitations somewhere. It will be discussed later on, but the main restriction in the descriptions comes from the fact that the numerical domain is periodical in the flow direction. This configuration is similar to simulating an infinity of waves breaking in the same time, which does not happen in reality. Moreover, waves break where some other waves broke. In our case, waves will break in a "turbulence free" area.

The initial conditions of unstable periodic sinusoidal waves of large amplitudes allow us to generate a wide range of breaker types, from weak plunging to collapsing breakers (Galvin, 1968). The most realistic configuration is the plunging one. Table (5.1) shows the range of values for the initial steepness, H/L, and the dispersion parameter, d/L, that have been simulated in the present study. All simulations have been carried out for a constant wavelength.

What we call a weak plunging breaker is the limit between the plunging breaker and the spilling breaker we reached. A small jet is ejected from the crest of the breaking wave and impacts in the very upper part of the face of the wave. Spilling breaking waves involve a much more complex combination between the wave propagation and the vorticity

	d/L			
H/L	0.1	0.13	0.17	0.2
0.06	WP	NB	NB	NB
0.07	WP	WP	NB	NB
0.08	PL	WP	WP	NB
0.09	PL	PL	WP	WP
0.1	PL	PL	PL	WP
0.11	PL	PL	PL	PL
0.12	PL	PL	PL	PL
0.13	CO	PL	PL	PL
0.14	CO	CO	PL	PL
0.15	CO	CO	CO	PL
0.16	CO	CO	CO	CO
0.17	CO	CO	CO	CO
0.18	CO	CO	CO	CO

Table 5.1: Values of the initial steepnesses, H/L, and dispersion parameters, d/L, for a constant wavelength. NB: non-breaking wave; WP: weak plunging breaker; PL: plunging breaker; CO: collapsing breaker.

generation based on perturbations appearing on the steepening face of the wave (Duncan et al., 1999). A collapsing breaker occurs when a wave explodes more than it breaks in the conventional sense. The wave is so big and unstable that, as it steepens, no jet is ejected but the whole face splashes in its lower part. Our method has then been shown to be appropriate to describe accurately plunging breaking waves. A precise description of the whole breaking process will be carried out, including some characteristic phenomena such as splash-ups generation and entrainment of gas in the water. The results are shown only for some examples taken from simulations run in the range of values presented in table (5.1).

Grid convergence analysis is quite difficult and questionable for this kind of flow characterized with unsteady free-surface breaking. We also remind that we generate artificially the breaking of the wave, so we are not able to do comparisons with experimental data, except qualitatively. But some tests have been realized to ensure ourselves about the effect of the mesh grid size. We did two-dimensional simulations with regular cartesian grids of, 125×50, 250×100, 500×200 and 1000×400 points. It is obvious that the finer the grid will be, the more precise the free surface will be described. In order to be reasonable about time calculations, we choose to run simulations with 250×100 ($\Delta x = \Delta z = 4 \times 4.10^{-4}\ m$) and 500×200 ($\Delta x = \Delta z = 2.10^{-4}\ m$) mesh grid points, in order to be able to describe correctly the plunging breaking phenomenon, and, above all, to be able to extend our observations to three-dimensional configurations.

5.1.2 Overturning motion and general flow description

The first configuration we simulated was carried out with $H/L = 0.13$ and $d/L = 0.13$ in order to compare free surface profiles, velocity and acceleration fields, this case referring to Vinje and Brevig (1981). The Reynolds number of the flow is $Re \simeq 32\ 400$, based on the definition given previously. Keeping a constant mesh grid resolution, we checked that for any value of the wavelength L greater than 10 cm, the wave breaking process was not affected by capillary effects. Figure (5.2) shows a comparison of the velocity fields at $t = 0.28\ s$. The overturning motion and surface profiles are compared in figures (5.3).

Three main features of the overturning motion are detailed and illustrated hereafter (see section 1.1.2):

- high particle velocities in the impinging jet;
- high particle accelerations under the curl;

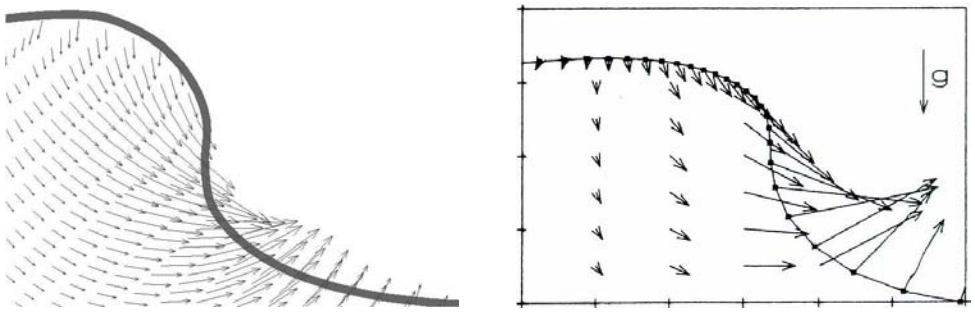

(a) Lagrangian acceleration field

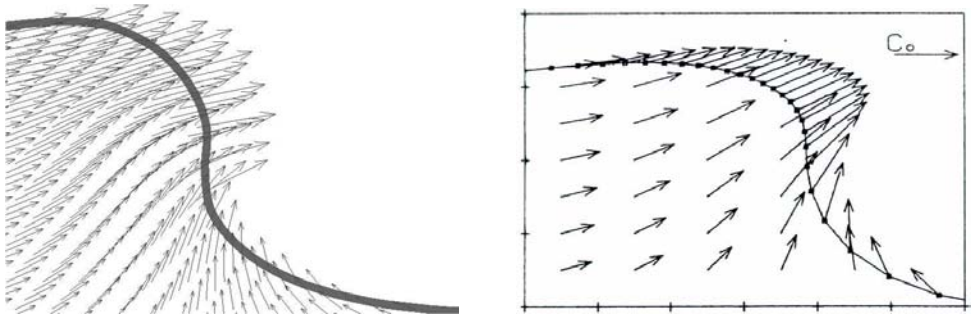

(b) Velocity field

Figure 5.2: Qualitative comparison between our numerical results (left column) and the results published by Vinje and Brevig (1981) at $t = 0.28\ T\ s$. The blue line stands for $C = 0.5$. We only show one vector over four in the water.

- low particle accelerations on the rear of the wave.

At the initial time of the simulation, the water velocity field in the wave is obtained from the linear theory and the air is at rest. The wave propagates towards the right side of the domain and the free-surface shape becomes more and more asymmetric, particularly in the region of the crest (Fig. 5.3, $t = 0.17\ T\ s$). An increase of the crest elevation occurs as the trough depth decreases. The front face of the crest steepens and becomes vertical. At the instant $t = 0.28\ T\ s$ (Fig. 5.2), a good agreement is found between our simulation and the Boundary Integral Element Method computation of Vinje and Brevig (1981). Note that for a better comparison with the figures shown by Vinje and Brevig (1981), we choose to present only one over four vectors in water, the interface being chosen to be located at $C = 0.5$.

Vinje and Brevig (1981) found that the maximum acceleration magnitude, at $t =$

0.28 T s, is located on the face of the wave and is about 2.4 g. This value is compared with maximum acceleration magnitude of 2.3 g obtained in the present simulation, the initial wave period being $T \simeq 0.308$ s. They also indicated that the horizontal velocities at the wave crest are slightly larger than the phase velocity. The initial wave celerity is $c = 0.324$ $m.s^{-1}$. The present computed maximum horizontal velocity is about $u = 0.351$ $m.s^{-1}$.

Once the front face of the crest steepens and becomes vertical, a jet of liquid is about to be projected from the crest of the wave. Then the tongue of water thrown from the crest develops and free falls down forward developing a characteristic overturning motion (Fig. 5.3).

The surface profiles shown in figures (5.3) have been chosen to correspond to those presented in Vinje and Brevig (1981). A general good agreement can be observed between the present simulation and the results of Vinje and Brevig (1981) up to the time where the front face of the wave steepens (Fig. 5.3 $t = 0.30$ T s). As already discussed (Abadie, 1998; Chen et al., 1999; Lubin et al., 2003b), some differences are clearly seen between results taken from BEM and Navier-Stokes simulations. These differences can be observed by comparison in figures (5.3). The most striking one is that plunging jet profiles from Vinje and Brevig (1981) look like sharpened hooked blades, whereas profiles shown in figures (5.3) look like rounded finger tip. This feature has already been observed by Abadie (1998) and Chen et al. (1999) (Figs. 1.16). The jet and crest of the wave look bigger, with a fatter aspect than the BEM ones. At $t = 0.17$ T s (Fig. 5.3 c), the height of the wave, predicted in the present simulation, is slightly higher than Vinje and Brevig's results. They also show a jet formed at the top of the crest, projected straight forward along an horizontal axis, whereas the jet shown in figures (5.3 c) is formed in the upper half of the face of the steepened wave and has a curled aspect. The volume of gas entrapped by the jet seems to be smaller, even if the distance of the impact is approximately the same. In addition to size and shape considerations, the other discrepancy lies in the time evolution, the present results showing a jet impacting earlier than the jet shown by Vinje and Brevig (1981). This has been observed to happen in many configurations detailed in sections (4.5), (4.6.1), (4.6.1) and (4.6.2).

Above mentioned differences may be attributed as due to the BEM calculations, which are based on potential flow theory that ignores the effects of water viscosity. BEM results have been shown to be very accurate compared to the experimental measurements, up to the point where the overturning jet is about to touch the wave trough in front. However, further computations using BEM method beyond this point are not possible. This limitation of BEM calls for other approaches for studying the consequent breaking processes.

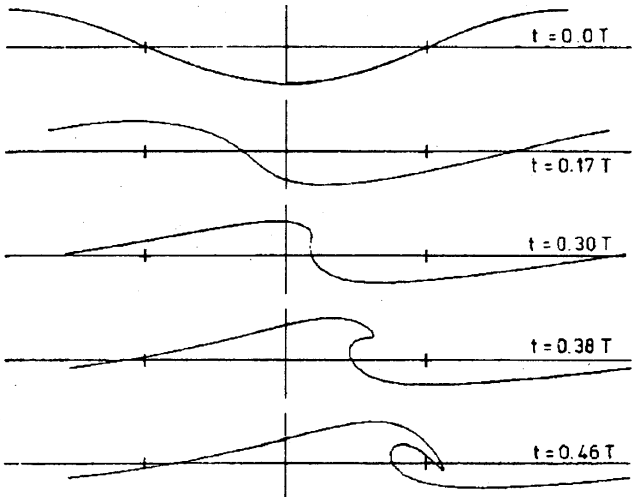

(a) Vinje and Brevig (1981)

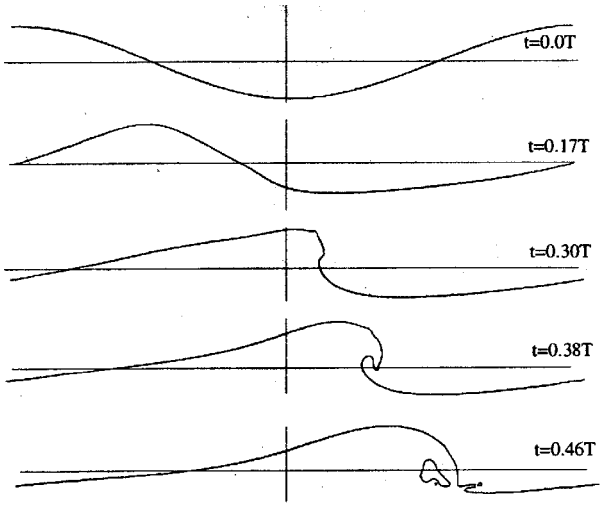

(b) Abadie (1998)

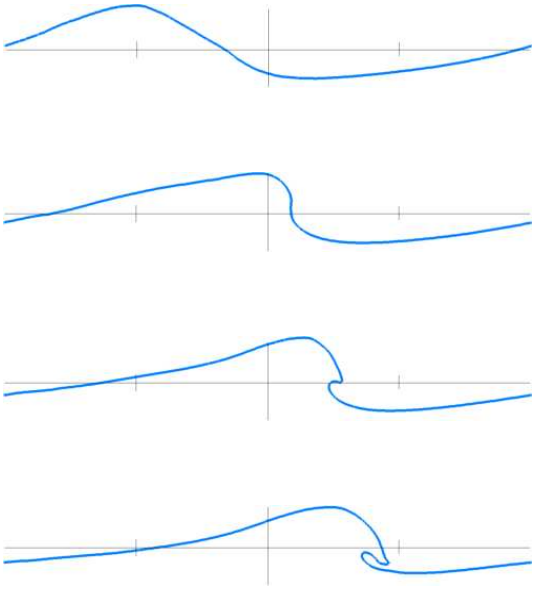

(c) Present study, $C = 0.5$

Figure 5.3: Overturning motion comparison between the BEM results from Vinje and Brevig (1981) (a), the Navier-Stokes simulations from Abadie (1998) (b) and the present simulation (c). $\frac{H}{L} = 0.13$, $\frac{d}{L} = 0.13$.

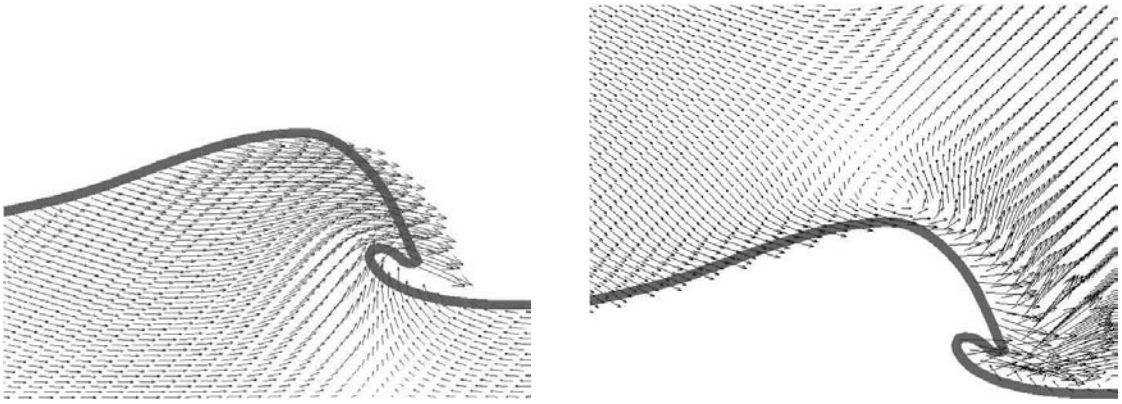

a. Water b. Air

Figure 5.4: Velocity field in both media. Only one vector over three is shown in each medium. $t = 0.39\ T\ s$, $C = 0.5$.

At $t = 0\ s$, the initial velocity and pressure fields are located in the water, the air being at rest. A strong flow dynamics is then generated in the air, as the wave starts its sudden motion towards the right side of the numerical domain. A regular velocity field is predicted in both media (Fig. 5.4). A depression is created in the air and a low acceleration region is observed in the water, on the rear of the wave. On the contrary, a large amount of air is pushed forward by the moving wave and the jet of water (Fig. 5.4 b). A vortex above the crest is generated and follows the wave during its motion. Moreover, as the jet is ejected, more or less abruptly, turbulence is generated in the air.

The maximum of acceleration is located on the under side of the overhanging jet and is directed out of the fluid, towards the air. The jet is about to impact the undisturbed surface. As expected, a high velocity region is found in the impinging jet. The plunging jet closes over the air to form a tube around which there is a considerable circulation. The pressure in the gas pocket increases and the air is trying to escape.

The breaking of the waves comes very rapidly in the case of a plunging breaker, while it occurs more slowly in the spilling case. We observed that the starting time is less than one wave period (the beginning of the breaking process is usually chosen when the wave front is almost vertical). This is confirmed by the work of New et al. (1985).

The jet entrains a pocket of gas and hits the forward face of the wave, forcing up a second jet, a splash-up. In Vinje and Brevig's case, a unique resulting splash, rising higher than the initial waveheight, forms a pair of counter-rotative vortices and a small vortex in front of these structures. Different breaking configurations and behaviors are shown later on by varying the dispersion parameter. It is important to be able to describe accurately the splash-up mechanism as it is responsible for a large amount of gas to be entrapped and entrained in the water, this, in turn, playing a great role in the wave energy dissipation.

5.1.3 Splash-up phenomenon

As detailed in section (1.1.2), Peregrine et al. (1980) first discussed about splashes in waterfalls and breaking waves. Peregrine (1983) then presented three assumptions about the splash-up generation (Fig. 1.8). The first hypothesis was shown to be very unlikely by some pictures. Peregrine (1983) then wandered if the splash-up could fall back onto the initiating jet and a part of the jet return under the tube.

Abadie et al. (1998) identified that the water in the splash-up originated from the forward face of the wave. But, Abadie et al. (1998) argued that the viscosities in both media has been increased by adding an artificial viscosity, the ratio being still $\mu_a/\mu_w = 1.85 \times 10^{-2}$, to reduce the Reynolds number ($Re = 10^4$) and damp some numerical oscillations. This is indeed a great difference with the present work where simulations are carried out with the viscosities and densities of air and water at high Reynolds numbers. In his observations, nevertheless, it appears that the water comes from a mixing between the initial impinging jet and the previously undisturbed forward face of the wave. It seems very likely this is what happens in real conditions (Peregrine, 1983), this being confirmed by Bonmarin (1989).

To discuss more precisely that point, we show three examples of splash-ups generations presented in figures (5.6), (5.7) and (5.8). The characteristics of the flows are summarized in table (5.2). Calculations have been carried out for a constant wavelength, so the initial waveheights, water depths and wave celerities increase, so does the initial Reynolds numbers, whereas the wave periods decrease. We remind that the case studied by Abadie (1998) was the plunging wave from Vinje and Brevig (1981), characterized by $\frac{H}{L} = 0.13$, $\frac{d}{L} = 0.13$. We use a colored water in our initial conditions, as shown in figure (5.5), which will allow us to identify where the water in the splash-up comes from. The value of $C > 0.5$ indicates the water region.

Test-case	$\frac{H}{L} = 0.10$, $\frac{d}{L} = 0.10$	$\frac{H}{L} = 0.13$, $\frac{d}{L} = 0.13$	$\frac{H}{L} = 0.13$, $\frac{d}{L} = 0.17$
Celerity $(m.s^{-1})$	0.295	0.324	0.351
Wave period (s)	0.339	0.308	0.285
Reynolds number	29 500	32 400	35 000

Table 5.2: Characteristics of the presented plunging breaking cases.

It can be clearly seen in figures (5.6), (5.7) and (5.8), that the splash-ups are made of water from both the impinging jets and the forward faces of the waves, following one of Peregrine's hypothesis. If we can judge the strength of the wave by the height of the splash-up it generates, we could say that the first one ($\frac{H}{L} = 0.10$, $\frac{d}{L} = 0.10$) is the strongest, then the second one ($\frac{H}{L} = 0.13$, $\frac{d}{L} = 0.13$), and the weakest one ($\frac{H}{L} = 0.13$, $\frac{d}{L} = 0.17$) is the last presented. In the three cases, the jet shape can be compared to a finger tip, as the falling tongue of water interacts with the air escaping from the pocket about to be closed. This shape has certainly an influence on the fact that the upper part of the splash-up is formed with a layer of water coming from the initial jet.

In the present simulations, the jets are predicted to first rebound, whatever the position of the plunge point is or the angle between the falling crest and the front face of the wave. We could have expected that feature in the last case (Figs. 5.8), where the tongue of water impacts closer to the crest than in the other cases, the rebounds would have been predominant and more water from the impacting jet would have been found in the splash-up. But this is not the case, the splash-ups generations presented in the three cases exhibit the same general behavior: the water from the splash-ups exclusively originates from the plunging jets. Moreover, the upper thin layers of water from the plunging crest are almost the same in proportions and do not increase in quantity. The splash-ups are then generated by the large amount of water pushed by the plunging jets.

The results we present in figures (5.7) have been obtained for the case $\frac{H}{L} = 0.13$, $\frac{d}{L} = 0.13$. This configuration has been studied by Abadie et al. (1998) with different viscosities in both media, to artificially reduce the Reynolds number, than those considered in this study. We can highlight that, from his results (Fig. 5.3), the shape of the falling tongue of water does not look like a rounded finger tip, but seems to be directed a bit inward the pocket of air to be trapped. The consequence is that a thinner layer of water is rebounding with the splash-up. However, too few images have been shown to draw a clear conclusion about this point. Chen et al. (1999) obtained similar results to ours, with

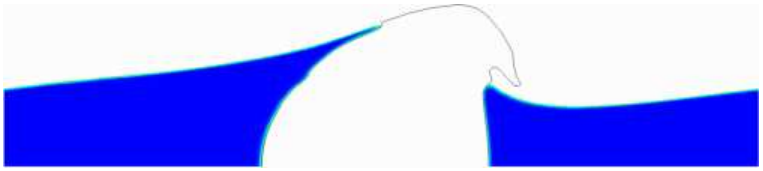

Figure 5.5: Impacting jet. $\frac{H}{L} = 0.13$, $\frac{d}{L} = 0.13$, $C = 0.5$.

greater viscosity and density ratios ($\mu_a/\mu_w = 0.4$ and $\rho_a/\rho_w = 10^{-2}$) than those we considered ($\mu_a/\mu_w = 1.85 \times 10^{-2}$ and $\rho_a/\rho_w = 1.1768 \times 10^{-3}$). Sakai et al. (1986), Takikawa et al. (1997), Lin and Liu (1998b), Iafrati et al. (2001), Watanabe and Saeki (2002), Iafrati and Campana (2003) and Biausser (2003) also showed the same kind of profiles, all these authors employing numerical tools solving the Navier-Stokes equations with various schemes and methods used to handle the interface tracking. We can anyway point out that, usually observed in pictures, the falling crest is already a mixture of air and water, the tip of the tongue being mainly composed with droplets. Miller (1976) and Bonmarin (1989) published some pictures confirming this point, the foam region of the falling jet exhibiting a round shape. We could then conclude that our results seem not to be so far from what could be observed in reality. More investigation would be of great interest to clarify this point. As Chanson and Lee (1997) recalls, the jet impact velocity and the angle between the plunging jet and the free surface of the receiving fluid are two dominant parameters for estimating the amount of entrained air and the sizes of entrained bubbles.

The most striking point is the depth of penetration of the impinging jets, from strong to weak plunging breakers (Abadie et al., 1998). It is clearly observed (Figs. 5.6, 5.7 and 5.8) that, in the three cases, the jets do not penetrate very deep. The tongues of water separates, one part of the liquid feeds the upper part of the splash-up, the other goes around the main entrapped gas pocket where a great topologically induced circulation takes place. This answers one of Peregrine's question concerning the three possible modes of splash-up generation (Fig. 1.8). As a matter of fact, it seems that the high velocities generated to the bottom are due to the spreading of the rotating vortices more than the percussion of the free falling jet.

The splash-up grows in size and can rise higher than the original wave as it is pushed by the plunging jet (Figs. 5.6 and 5.7). We show in figure (5.7) the velocity field in the splash-up. A high vertical velocity component is located in this region. As detailed previously, the liquid in the splash-up comes partly from the jet and partly from a previously

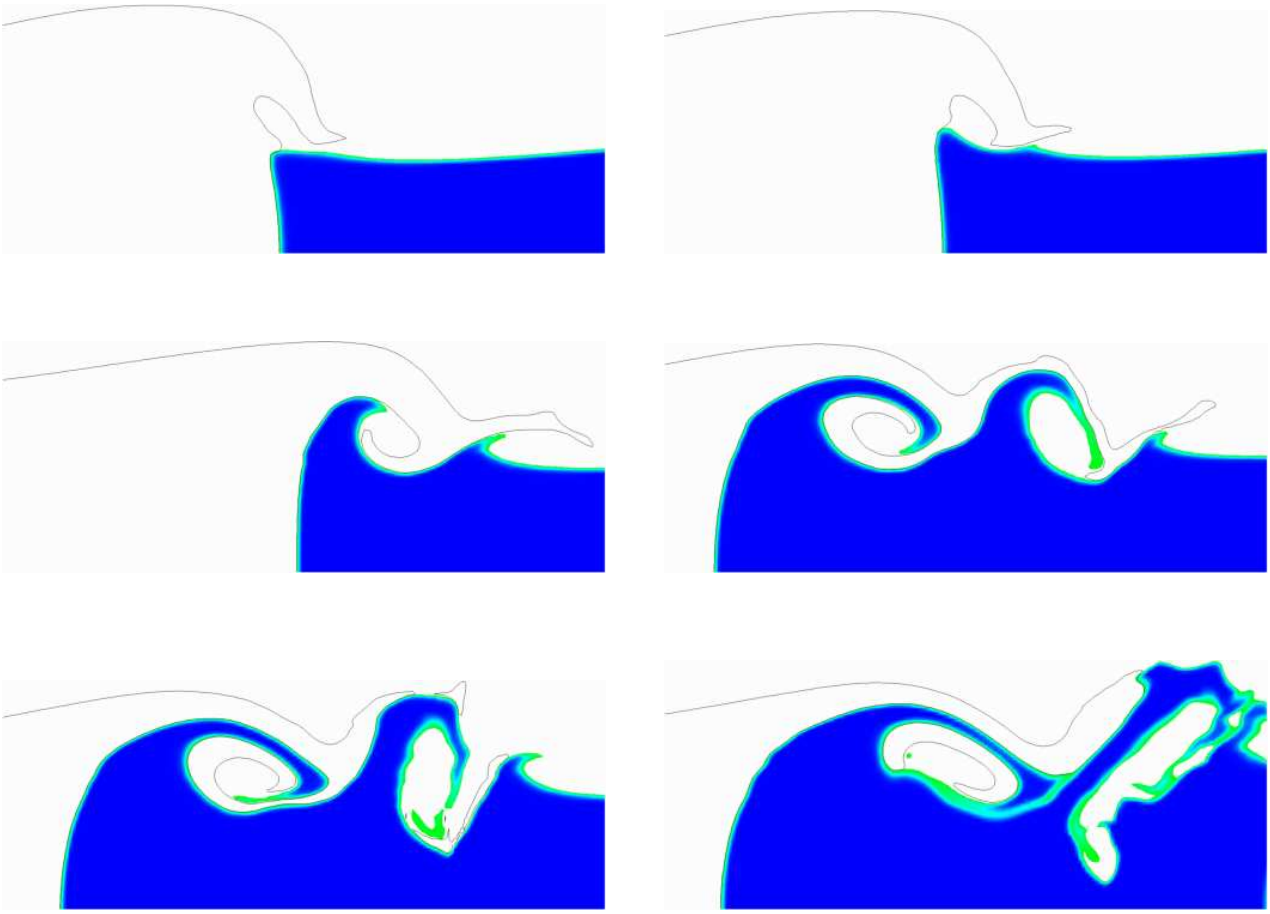

Figure 5.6: Splash-up generation. $\frac{H}{L} = 0.10$, $\frac{d}{L} = 0.10$, $C \geq 0.5$.

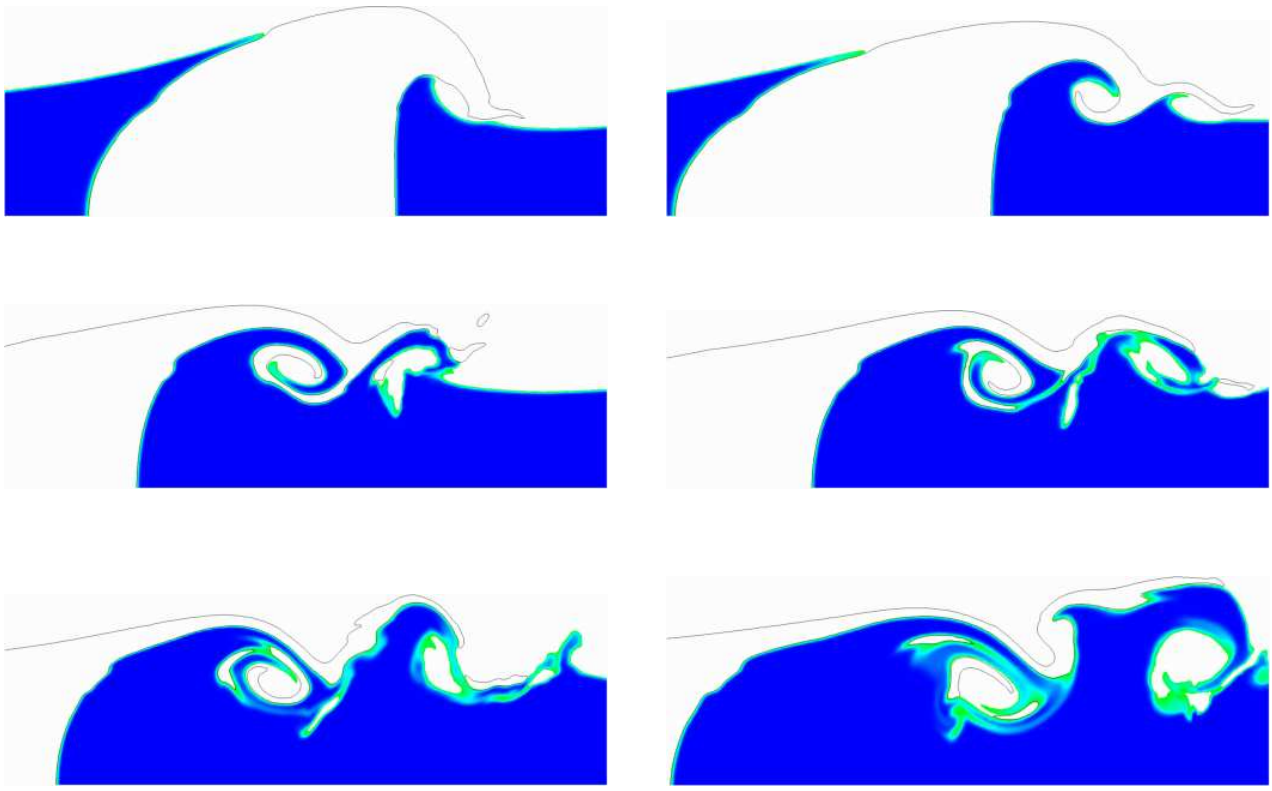

Figure 5.7: Splash-up generation. $\frac{H}{L} = 0.13$, $\frac{d}{L} = 0.13$, $C \geq 0.5$.

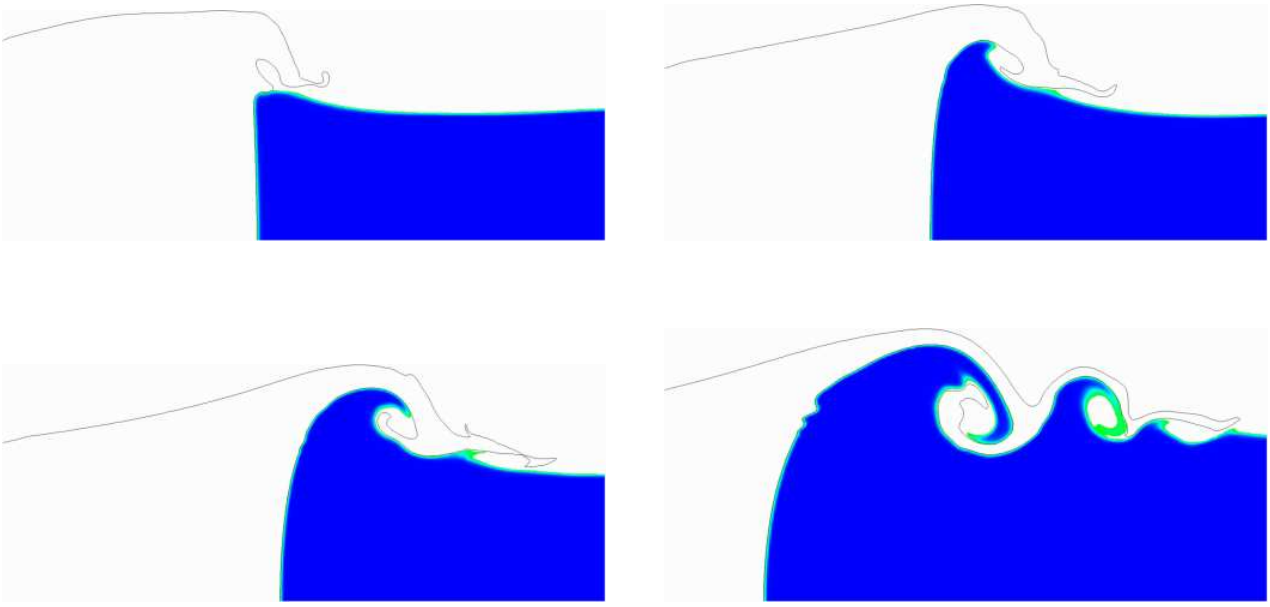

Figure 5.8: Splash-up generation. $\frac{H}{L} = 0.13$, $\frac{d}{L} = 0.17$, $C \geq 0.5$.

undisturbed liquid. A close inspection showed that in the early stage the liquid in the splash-up originates from the plunging crest, the undisturbed face acting as a solid wall. Then a large amount of liquid coming from the undisturbed liquid is pushed to develop the splash-up (Fig. 5.9). A large amount of vorticity is then generated.

The jet reconnection with the forward face of the wave gives rise to two processes which have distinct life times and behaviors depending on the initial wave strength. On one hand, gas pockets are entrapped generating a mixing of air and water and creating a strong dynamics, sometimes spread towards the bottom, as a large amount of air is entrained in the water. On the other hand, once rising at its highest level, the splash-up will generate several successive splash-ups, which are decreasing in size (Fig. 5.10). It can sometimes rise higher than the initial waveheight. The successive rebounds causes energy dissipation and air entrainment.

Depending on the splash-up configuration, several vortices will be generated. These large-scale structures are classified in two types: co- and counter-rotative vortices. The number and the size of these structures are important, because the energy dissipation process is linked to their behavior during the breaking of the wave.

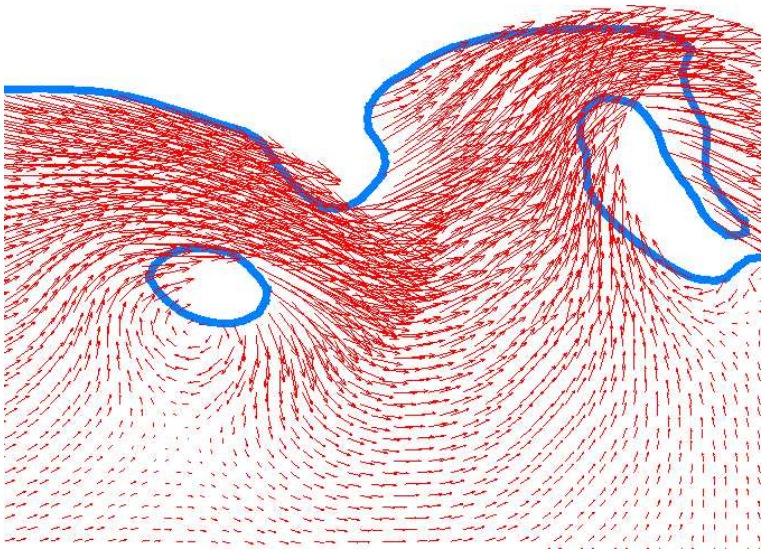

Figure 5.9: Splash-up generation. Only one vector over three is shown in the water. $\frac{H}{L} = 0.13$, $\frac{d}{L} = 0.13$, $C = 0.5$.

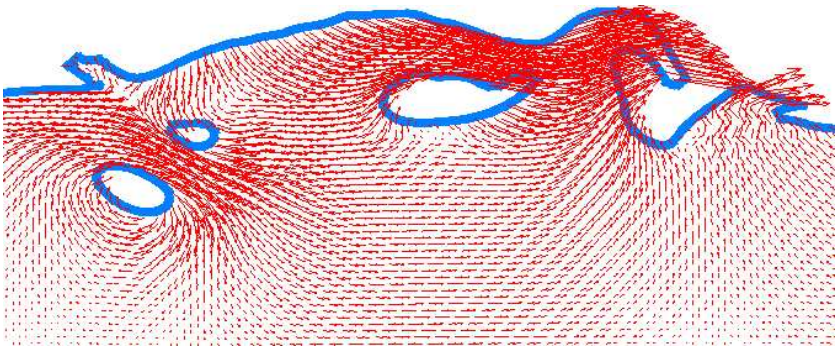

Figure 5.10: Successive splash-ups generation. Only one vector over three is shown in the water. $\frac{H}{L} = 0.13$, $\frac{d}{L} = 0.13$, $C = 0.5$.

5.1.4 Vortices occurrence

As detailed in section (1.2.1), Zhang and Sunamura (1990) classified the occurrence of the oblique and horizontal vortices. As this section is dedicated to two-dimensional simulations, the oblique vortices cannot be observed, but will be the subject of a discussion in the following section where three-dimensional simulations will be detailed.

Zhang and Sunamura (1990) subclassified the horizontal vortex into four types. Another subtype of horizontal vortices has been observed to occur in our simulations: the counter-rotative vortices (Figs. 1.10). These have been examined to be very important in the breaking process. He also showed that a condition for occurrence of visible vortices should be that the Reynolds number of the flow would be greater than $1.2\ 10^4$, which is below our Reynolds numbers (Table 5.2).

Once rising at its highest level, large-scale vortices are generated. The successive splash-ups will entrap gas pockets, smaller than the first one, and create co-rotative vortices. The initial splash-up falls down, backward on the initial impinging jet (Fig. 5.10), which creates a dipole, consisting in two counter-rotative vortices (Figs. 5.10 and 5.14). This structure transports all the momentum and the vorticity to the bottom. The flow becomes very violent and turbulent in the water.

We summarize the types of vortices we observed in table (5.3), depending on the values of the initial steepnesses, H/L, and dispersion parameters, d/L.

We can notice that the occurrence of the counter-rotative vortices coincide with plunging breakers. These structures are observed by Bonmarin (1989), as shown in figures (1.10), in the case where the splash-up rises high and expands into a mushroom-like shape, one part generating a new splash-up in the flow direction and the other part falling back on the initial plunging tongue of water. These two vortices dissipate a great amount of the wave energy, due to the high quantity of air entrapped to be entrained towards the bottom and their high speed of rotation.

Some of the co-rotative vortices can move forward and down into the interior of the wave, like a propagating bore, corresponding to the subtypes A or B from Zhang and Sunamura (1990). In some configurations, the co-rotative vortices were entrained to the bottom, or dislocated and brought to the free surface very violently, corresponding to the subtypes C or D from Zhang and Sunamura (1990). As we can imagine, a large amount of sediment would have been put in suspension.

	d/L		
H/L	0.1	0.13	0.17
0.06	$*$	NB	NB
0.07	$*$	$*$	NB
0.08	$*$	$*$	$*$
0.09	$\bullet$	$*$	$*$
0.1	$\bullet$	$\bullet$	$*$
0.11	$\bullet$	$\bullet$	$\bullet$
0.12	$\bullet$	$\bullet$	$\bullet$
0.13	$\bullet$	$\bullet$	$\bullet$
0.14	$\circ$	$\bullet$	$\bullet$
0.15	$\bullet$	$\circ$	$\bullet$
0.16	$\circ$	$\circ$	$\bullet$
0.17	$\circ$	$\bullet$	$\bullet$
0.18	$\circ$	$\bullet$	$\bullet$

Table 5.3: Types of vortices observed depending on the values of the initial steepnesses, H/L, and dispersion parameters, d/L, for a constant wavelength. NB: non-breaking wave; $*$: only co-rotative vortices; $\circ$: only counter-rotative vortices; $\bullet$: both co-rotative and counter-rotative vortices.

The dipoles of counter-rotative vortices will also behave differently depending on the strength of the initial wave.

Nevertheless, the behavior of the observed vortices depends on the three-dimensionality of the phenomenon. These are only qualitative and preliminary descriptions, a deeper analysis will be provided in the next section dedicated to three-dimensional simulations. Anyway, we observed sometimes coherent rotating structures and sometimes very chaotic: the more violent the plunging breaker is, the shorter the life time of the pockets of gas is.

According to the conclusions of Zhang and Sunamura (1990), we can expect to see oblique vortices or horizontal vortices that will change to oblique vortices if we choose configurations close to spilling breakers or plunging breakers inducing sequences of propagating horizontal vortices.

5.1.5 Energy dissipation

The wave energy dissipation processes has been investigated, according to equations 4.1. We plot in figure (5.11) the time evolutions of the normalized values (by each respective initial values) of the kinetic, potential and total energies. The results we show are in a general good agreement with the work of Chen et al. (1999), as we find that the time evolutions of the calculated energies present three distinct regimes before, during and after the breaking of the wave.

Before the ejection of the jet ($t < 0.1\ s$), the total energy decreases smoothly. The kinetic energy is transformed into potential energy, as the front face of the wave steepens and the crest height increases (Fig. 5.12 a). Then the jet is formed (Fig. 5.12 b) and ejected from the crest ($t \simeq 0.1\ s$). It starts to free-fall down: the potential energy decreases and turns into kinetic energy, which increases to an extremum value $E_c \simeq 1.11$ reached when $t \simeq 0.15\ s$ (Fig. 5.12 c).

The wave crest keeps rising: hence, the kinetic energy decreases and transforms into potential energy. This can be observed in figure (5.12 c). The wave crest exhibits a hunch back form, whereas in figure (5.12 d) the rear part of the wave presents a straight shape. The kinetic energy stops decreasing at the time when the jet touches the forward face of the wave (Fig. 5.12 d) and starts to rebound ($t \simeq 0.18\ s$). It can be observed from figure (5.11) that the potential energy decreases more rapidly and goes into kinetic energy, which reaches its maximum value at $t \simeq 0.2\ s$ ($E_c \simeq 1.12$).

From $t \simeq 0.22\ s$ (Fig. 5.12 e), the main splash-up starts to be generated: the total energy decreases rapidly, as some energy has to be spent to push the large amount of

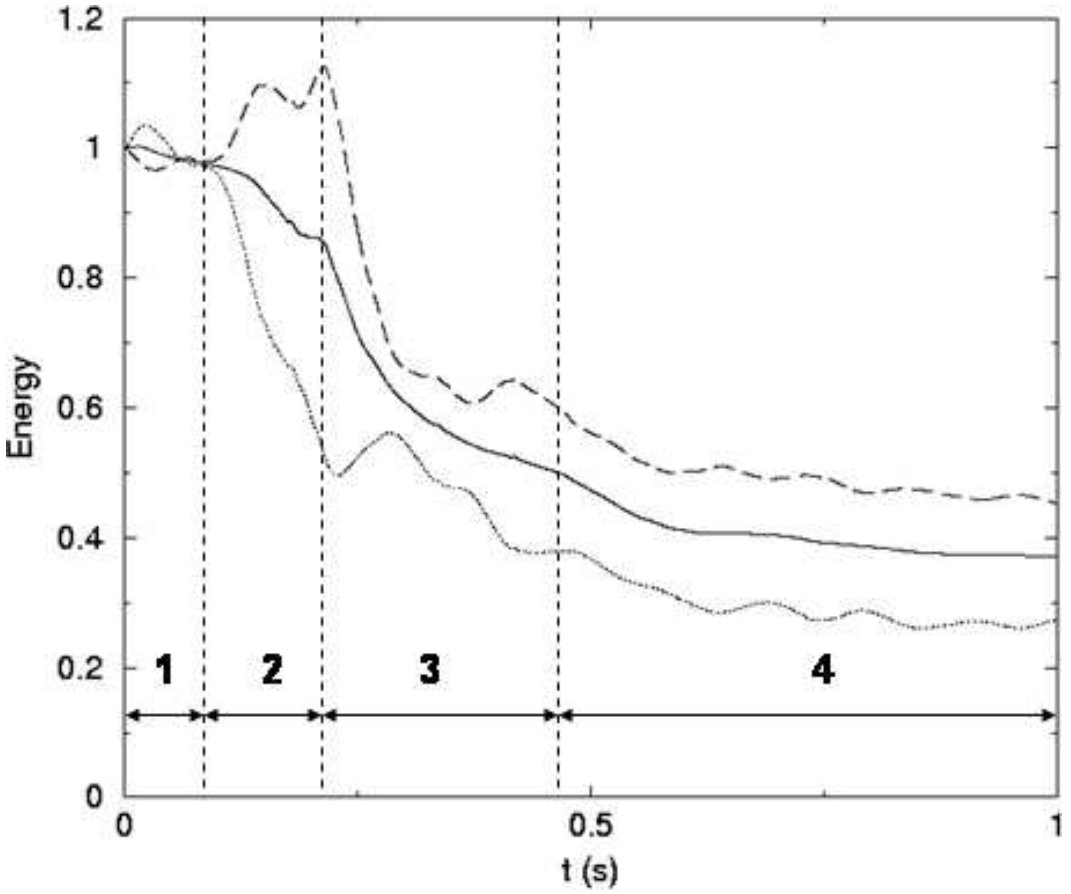

Figure 5.11: Time evolution of the non-dimensional energies. Solid line: total energy; dashed line: kinetic energy; dotted line: potential energy. $\frac{H}{L} = 0.13$, $\frac{d}{L} = 0.17$. Zone 1: steepening of the wave; zone 2: jet ejection; zone 3: jet impact and splash-ups generation; zone 4: residual flow.

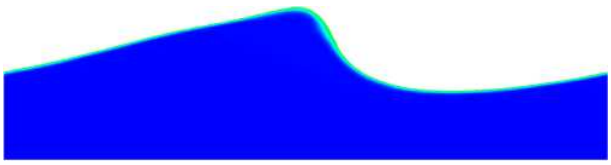

(a) $t \simeq 0.09\ s$

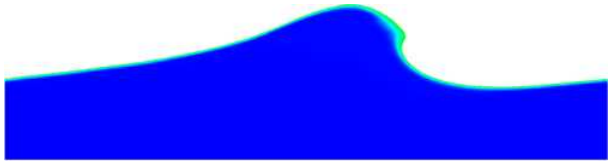

(b) $t \simeq 0.12\ s$

(c) $t \simeq 0.15\ s$

(d) $t \simeq 0.18\ s$

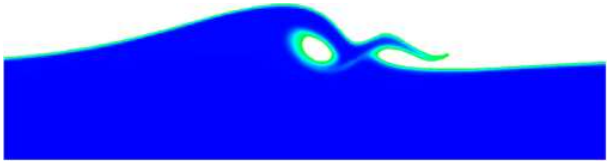

(e) $t \simeq 0.22\ s$

Figure 5.12: Two-dimensional breaking process detailed. $\frac{H}{L} = 0.13$, $\frac{d}{L} = 0.17$, $C \geq 0.5$.

water. This can be observed through the dotted line plotted in figure (5.11), which shows the time evolution of the potential energy: it stops decreasing and suddenly rises to an extremum value indicating that the main splash-up has reached its highest level. Each decreasing of the potential energy is associated with a relative increase of the kinetic energy and *vice versa*, due to the generation of the successive splash-ups. At $t \simeq 0.3\ s$, the main splash-up falls down and the two counter-rotative vortices are created. The kinetic and potential energies both keep decreasing as the large gas pockets are entrained in the water, the successive splash-ups falling down.

The total wave energy never stops decreasing, unlike the potential and kinetic energies. It first slowly decreases due to the viscosity. It also decreases because, at the beginning of the simulation, the air is set at rest, so when the wave starts propagating, some energy is dissipated to put the air into motion. Then, it can be clearly seen that it is mainly dissipated during the wave breaking process: about 40 % of the total pre-breaking wave energy is dissipated at $t \simeq 0.3\ s$. Almost 50 % of the potential energy and 65 % of the kinetic energy remain in the wave at this time. Then, the energy is dissipated slowly. At $t \simeq 1\ s$, which is about three wave periods of time, about 40 % of the total pre-breaking wave energy, 45 % of the kinetic energy and 30 % of the potential energy remain in the numerical domain. These values have to be compared with the work of Chen et al. (1999), who found that around 30 % of the kinetic energy and 5 % of the potential energy remain in the wave, more than 80 % of the total pre-breaking wave energy being dissipated at this time. The kinetic energy is shown to reach a maximum value $E_c \simeq 1.05$, which is lower than what we found. However, it has to be kept in mind that the simulation presented by Chen et al. (1999) was run with greater viscosity and density ratios ($\mu_a/\mu_w = 0.4$ and $\rho_a/\rho_w = 10^{-2}$) than those we considered ($\mu_a/\mu_w = 1.85 \times 10^{-2}$ and $\rho_a/\rho_w = 1.1768 \times 10^{-3}$), considering the breaking of a wave in deep water at a lower Reynolds number ($Re = 10^4$). The flow appears then to be damped more quickly, as it can be observed from the figures shown by Chen et al. (1999), due to the higher viscosities and densities ratios. Moreover, the deep depth configuration they considered allows the momentum to be spread in a greater quantity of water than the shallower configuration we choose.

Here can be highlighted another limitation of our method. We simulate a single wave breaking in what we could call a "turbulence free" area. Once the wave breaks, turbulence is generated and propagates in the whole domain. Fluctuations and large scale structures are free to move out of the periodic numerical domain, re-enter the domain and interact for a very long time. In reality, it should, at least, be able to spread and dissipate without

meeting any other part of the fluid put in motion. It is like holding a bottle of water horizontally and giving an impulsion to the volume of fluid, by tilting the bottom of the container to make the water splash in it. It will move back and forth, from the bottom to the neck of the bottle, for a certain long time. Similarly, after $t \simeq 0.5\ s$, the propagating vortices move out of the numerical domain on the right side to re-enter on the left side. These vortices come and interact with the two rising counter-rotative vortices (Figs. 5.24). In reality, this should not happen, as the co-rotative vortices propagate towards the shoreline, leaving behind the two counter-rotative vortices. Moreover, we choose to examine shallow water configurations. For the very low viscosities and densities of air and water: these parameters allow velocity fluctuations to last for a long time, constrained between the bottom of the numerical domain and the free surface (Sous et al., 2004).

For these reasons the water keeps waving in the numerical domain with a strongly distorted interface. This is why there is a clear change of dissipation regime, as there seems to be an inflexion point in the curve plotting the total wave energy (Fig. 5.11) at this time. More than 70 % of the total pre-breaking wave energy is finally observed to be dissipated after seven wave periods of time (Fig. 5.18).

Some similar descriptions can be given for the two other cases we choose to detail, with the same swap process between the kinetic and potential energies. The time evolutions of the normalized values of the kinetic and total energies (represented respectively by the dashed and solid lines) are plotted in figures (5.13) and (5.15). The total energy evolutions exhibit the same tendencies than previously, with three different regimes as they decrease.

The main difference between those two cases and the one described before lies in the jet impact and the following splash-up generation, which can be translated through the respective kinetic energy time evolutions. Indeed, in figures (5.13) and (5.15), the dashed lines shows only one maximum each, instead of the two peaks observed in figure (5.11).

In the case where $\frac{H}{L} = 0.10$, $\frac{d}{L} = 0.10$, the jet is ejected at $t \simeq 0.1\ s$ (Fig. 5.14 a). The kinetic energy increases subsequently until the jet touches down the forward face of the wave at the time $t \simeq 0.17\ s$ (Fig. 5.14 b). The potential energy appears to decrease more dramatically than in the previous example, this being due to the lower ordinate of the plunging point, the free surface being almost horizontal. More than 90 % of the potential energy is gone into kinetic energy or dissipated at $t \simeq 0.19\ s$. Previously, the tongue of water touched down the front face of the wave at a higher ordinate, the front face of the wave presenting a slight slope. The water depth in which the jet impacts is then shallower. The jet rebounds and the kinetic energy keeps on increasing until it reaches a maximum value $E_c \simeq 1.25$ at $t \simeq 0.19\ s$, corresponding to the beginning of the splash-up

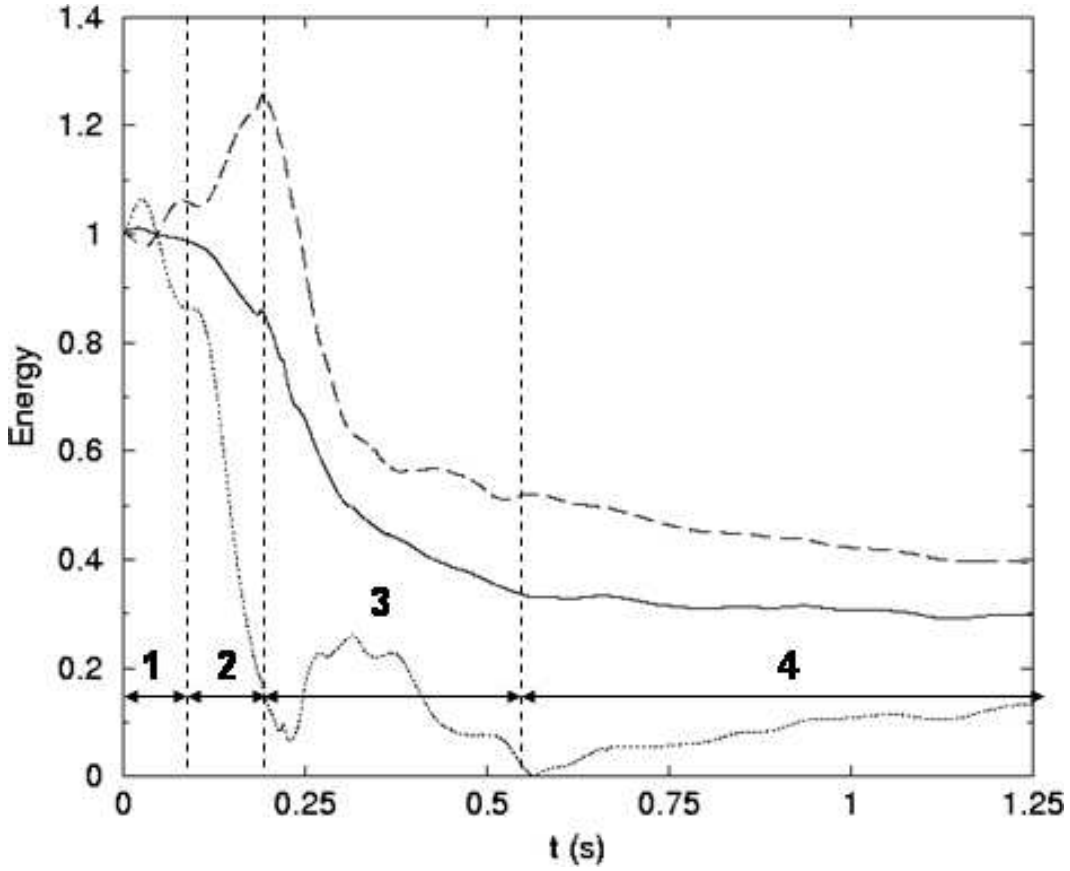

Figure 5.13: Time evolution of the non-dimensional energies. Solid line: total energy; dashed line: kinetic energy; dotted line: potential energy. $\frac{H}{L} = 0.10$, $\frac{d}{L} = 0.10$. Zone 1: steepening of the wave; zone 2: jet ejection; zone 3: jet impact and splash-ups generation; zone 4: residual flow.

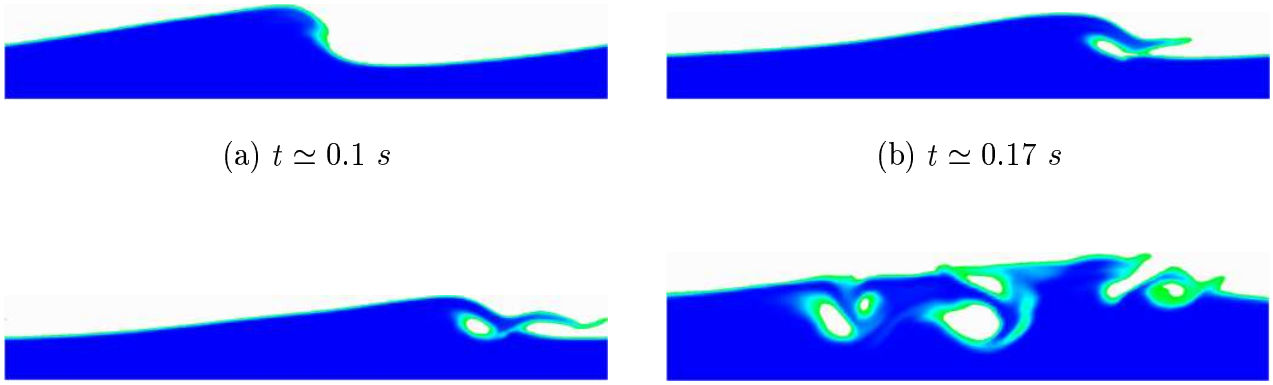

(a) $t \simeq 0.1\ s$ (b) $t \simeq 0.17\ s$

(c) $t \simeq 0.19\ s$ (d) $t \simeq 0.35\ s$

Figure 5.14: Two-dimensional breaking process detailed. $\frac{H}{L} = 0.10$, $\frac{d}{L} = 0.10$, $C \geq 0.5$.

generation (Fig. 5.14 c). Then, the kinetic energy is transferred into potential energy, leading to a fast diminution in magnitude, as the generated splash-up rises higher than the original waveheight. This fast kinetic energy diminishing translates the strength of the wave, as the impact looks spectacular when such a high splash-up is observed. The dotted line plotted in figure (5.13) showing the time evolution of the potential energy exhibits a plateau for a certain time, which indicates that the successive splash-ups rise high.

At $t \simeq 0.3\ s$, when the successive splash-ups fall down and the entrapped gas pockets rise rapidly to the surface (Fig. 5.14 d), the kinetic energy decreases more slowly, as the whole water domain is now rough. About 50 % of the total pre-breaking wave energy is dissipated at $t \simeq 0.3\ s$. Almost 20 % of the potential energy and 60 % of the kinetic energy remain in the wave at this time. Then, the energy is dissipated slowly. At $t \simeq 1.25\ s$, which is about three and a half wave periods of time, about 30 % of the total pre-breaking wave energy, 40 % of the kinetic energy and no potential energy remain in the numerical domain, the potential energy vanishing from $t \simeq 0.5\ s$. Then, the water keeps waving in the periodical numerical domain, as explained before.

In a same manner, for the case where $\frac{H}{L} = 0.13$, $\frac{d}{L} = 0.13$, the jet is ejected at $t \simeq 0.09\ s$ (Fig. 5.16 a). Again, the kinetic energy is observed to increase until the jet touches down the forward face of the wave at the time $t \simeq 0.15\ s$ (Fig. 5.16 b). The kinetic energy increases until it reaches a maximum value $E_c \simeq 1.22$ at $t \simeq 0.19\ s$, corresponding to the beginning of the splash-up generation (Fig. 5.16 c). Again, the potential energy appears to decrease more dramatically than in the first example we present: this time,

less potential energy is lost, as around 60 % of it is gone into kinetic energy or dissipated at $t \simeq 0.19\ s$. Then, the kinetic energy is again transferred into potential energy, the same fast diminution in magnitude being observed, as the generated splash-up rises higher than the original waveheight.

It appears more clearly through this example that each decreasing of the potential energy is associated with a relative increase of the kinetic energy and *vice versa*, as, this time, the dotted line showing the time evolution of the potential energy (Fig. 5.15) passes over the dashed line presenting the time evolution of the kinetic energy. This is due to the very high level reached by the splash-ups.

About 40 % of the total pre-breaking wave energy is dissipated at $t \simeq 0.3\ s$. Almost 40% of the potential energy and 55 % of the kinetic energy remain in the wave at this time. Then, the energy is dissipated slowly. At $t \simeq 1.5\ s$, which is almost five wave periods of time, about 35 % of the total pre-breaking wave energy, 40 % of the kinetic energy and 30 % of the potential energy remain in the numerical domain. The maximum kinetic energy magnitude is lower for this case than the previous one because the wave crest rises higher, hence the potential energy is this time slightly greater.

It can also be highlighted that, in the three cases detailed previously, the maximum of the total pre-breaking wave energy is dissipated during the splash-ups occurrence, an average value of 40% of the total pre-breaking wave energy being estimated from the numerical results. This observation is in a very good agreement with the results of Lamarre and Melville (1991) who measured experimentally that up to 50% of the wave energy is spent in entraining air and resisting against buoyancy forces, the turbulent behavior of the entrained and rising bubbles increasing this dissipation process.

As shown by Chen et al. (1999), it is observed that the curve of the time evolution of the total energy presents three distinct slopes indicating different wave energy decay regimes.

During the wave propagation, steepening and breaking process, the wave total energy follows an exponential decay, with two different decay rates before the jet ejection and before the jet impact.

The main observation we make is the dependence of the decay of the total energy is found to be different from the observation from Chen et al. (1999). They highlighted a t^{-1} dependence, whereas we find a general $t^{-0.3}$ dependence from the times of the generation of the splash-ups. We present in figure (5.17) an example of comparison between the time evolution of the calculated total wave energy and a fit function proportional to $t^{-0.31}$ for the $\frac{H}{L} = 0.13$ and $\frac{d}{L} = 0.17$ configuration.

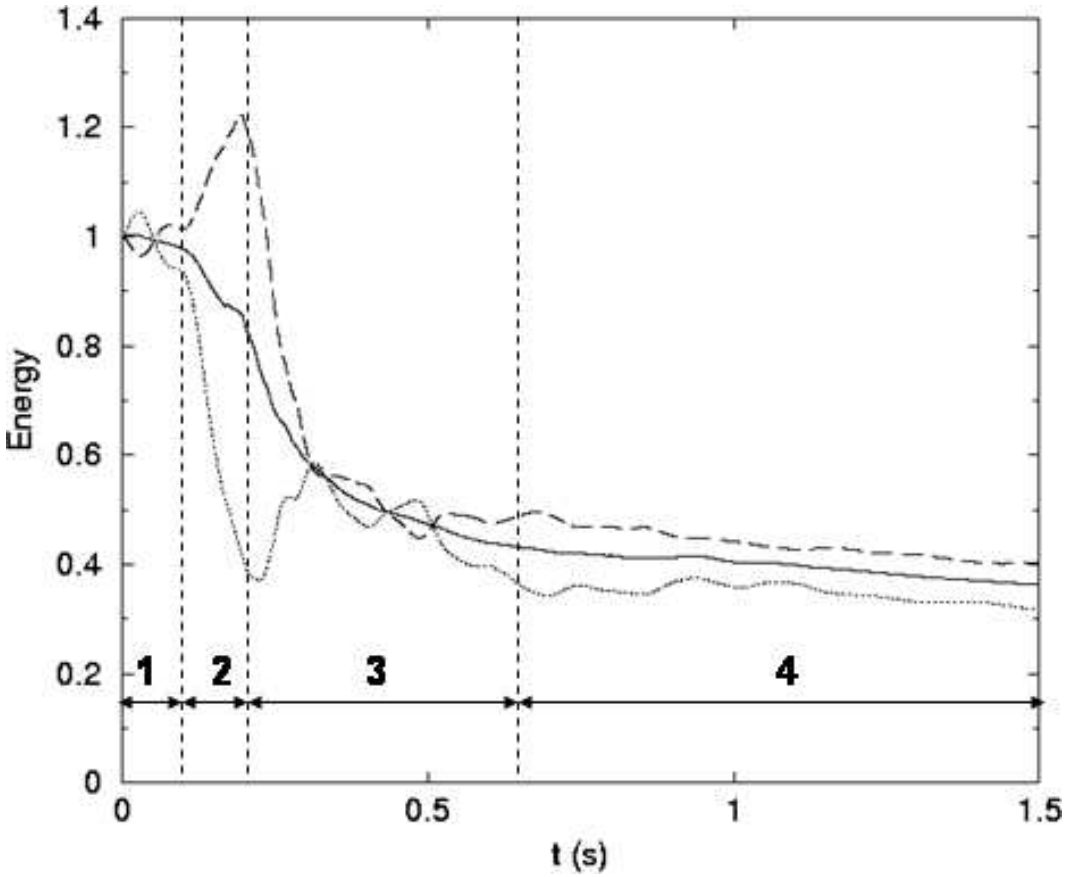

Figure 5.15: Time evolution of the non-dimensional energies. Solid line: total energy; dashed line: kinetic energy; dotted line: potential energy. $\frac{H}{L} = 0.13$, $\frac{d}{L} = 0.13$. Zone 1: steepening of the wave; zone 2: jet ejection; zone 3: jet impact and splash-ups generation; zone 4: residual flow.

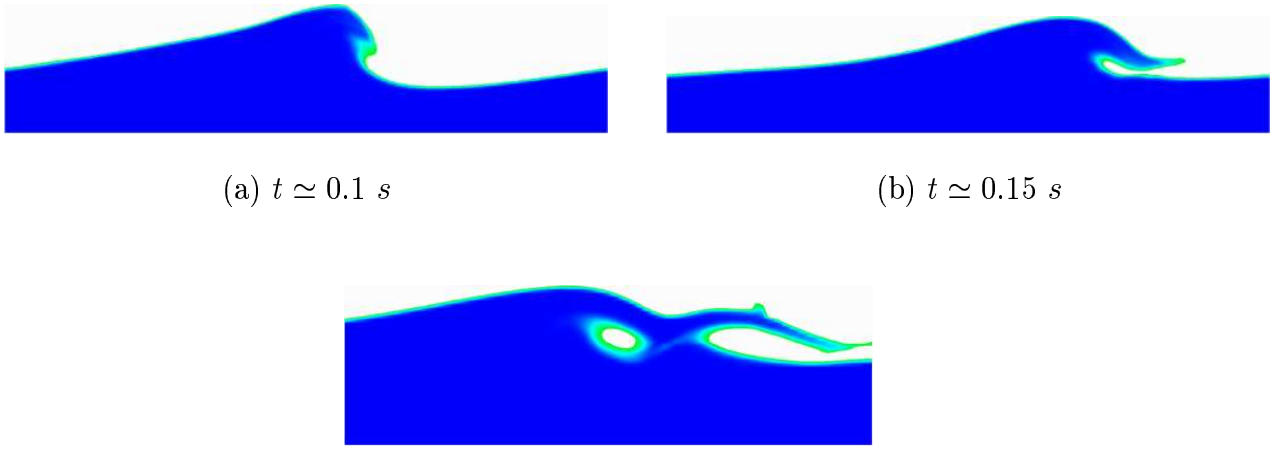

(a) $t \simeq 0.1\ s$ (b) $t \simeq 0.15\ s$

(c) $t \simeq 0.19\ s$

Figure 5.16: Two-dimensional breaking process detailed. $\frac{H}{L} = 0.13$, $\frac{d}{L} = 0.13$, $C \geq 0.5$.

These proposed fit curves appear to be well adapted to represent the decay of energy from the times when the gas pockets have disappeared to the residual flow remaining after few wave periods of time.

However, a discrepancy can be observed for the $\frac{H}{L} = 0.13$ and $\frac{d}{L} = 0.17$ configuration, which is explained by the interaction between the co-rotative vortices, re-entering the periodical domain, and the counter-rotative vortices. The flow is thus not established and stationary, turbulence being still generated. This process is absent in the $\frac{H}{L} = 0.10$ and $\frac{d}{L} = 0.10$ configuration. The fit curve is anyway very well adapted to represent the decay of the total energy of the residual flow from $t = 5\ s$.

We show in table (5.4) some other examples which have been simulated and the dependence of the decay of the total wave energy with time. More simulations would be needed to investigate this point more into details to be able to draw a general conclusion.

The main explanation for the discrepancy between our observations and the results of Chen et al. (1999) is the higher values of the viscosities they used for the computation, as already pointed out. Moreover, we will discuss about the importance of two-dimensionality of our simulations.

We compared the time evolutions of the kinetic and total energies, depending on if we calculated the turbulent viscosity in the whole domain or only in both media, without considering the region of numerical diffusion for the color function. A third simulation

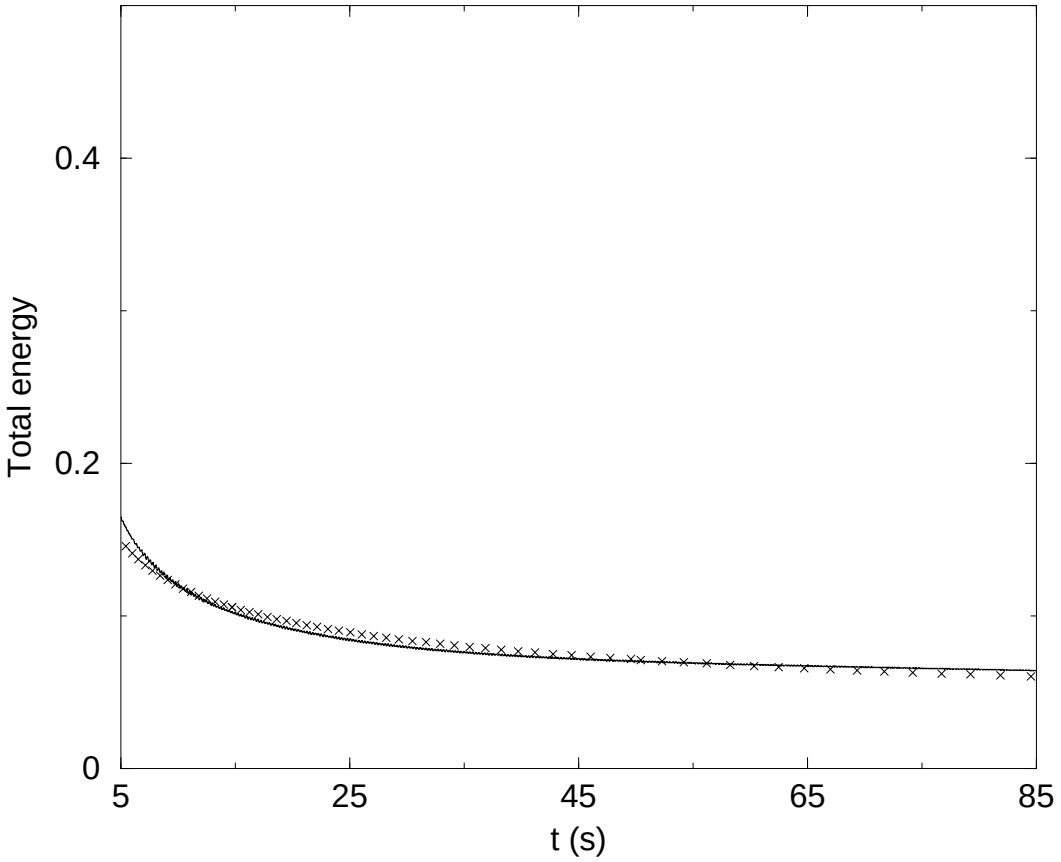

Figure 5.17: Time evolution of the non-dimensional energy. Solid line: calculated total energy; ; +: fit function given by $E = At^{-0.31}$. $\frac{H}{L} = 0.13$, $\frac{d}{L} = 0.17$.

	d/L		
H/L	0.1	0.13	0.17
0.09	t^{-24}	NC	NC
0.1	t^{-35}	NC	NC
0.12	NC	t^{-34}	t^{-35}
0.13	NC	t^{-25}	t^{-31}

Table 5.4: Decay of the total wave energy dependence. NC stands for *Not Computed*.

has been run without considering any turbulent viscosity (pseudo-DNS - see chapter 4).

It has to be kept in mind that we show two-dimensional configurations. All the descriptions have to be discussed taking this point into account.

So, this can be summarized as follows:

- Test 1: ν_t is calculated in the whole numerical domain
- Test 2: $\nu_t = 0$, if $0 < C < 1$
- Test 3: ν_t is not taken into account, using DNS

We show the comparison between the time evolutions of each calculated energies for the previously defined tests: the kinetic (Fig. 5.19), the potential (Fig. 5.20) and the total energies (Fig. 5.18).

We can notice that no clear difference can be seen before $t \simeq 0.3\ s$, whatever the energy. This corresponds to the time when the main splash-up falls down and the large-scale structures are generated. The flow cannot be qualified as turbulent before this time, so it could be expected to find similar results whatever the test. Even at the times of the impact and the splash-up generation, which are previous from $t \simeq 0.3\ s$, the lines showing the time evolutions of the non-dimensional energies seem almost joint. The two-dimensionality plays a role in this particular point, as we will show later on.

The instant $t \simeq 0.3\ s$ corresponds to the falling down of the main splash-up, creating the two counter-rotative vortices, and the beginning of the generation of the successive splash-ups, entrapping the co-rotative vortices. The flow becomes violent and turbulence is generated by the entrainment of the large gas pockets in the wave.

The main observation is that the energy dissipation is slightly underpredicted in Test 3, where we do not consider any turbulent viscosity, compared to the other results. The total energy dissipation is slightly more important in Test 1 than in Test 2. The discrepancies appear more clearly from $t \simeq 0.5\ s$, when, as already explained, the whole domain has been put into turbulent motion: the vortices have been propagating in the entire domain and turbulence has spread from the free surface to the bottom. The greater energy dissipation is obtained by calculating the turbulent viscosity in the diffusion region (Test 1), where the interface is considered to be located ($C = 0.5$). These general observations confirm that voiding ν_t, which is characterized by the fact that it is a positive quantity, slightly increases quantitatively the decay of the energies, although it does not speed up the process.

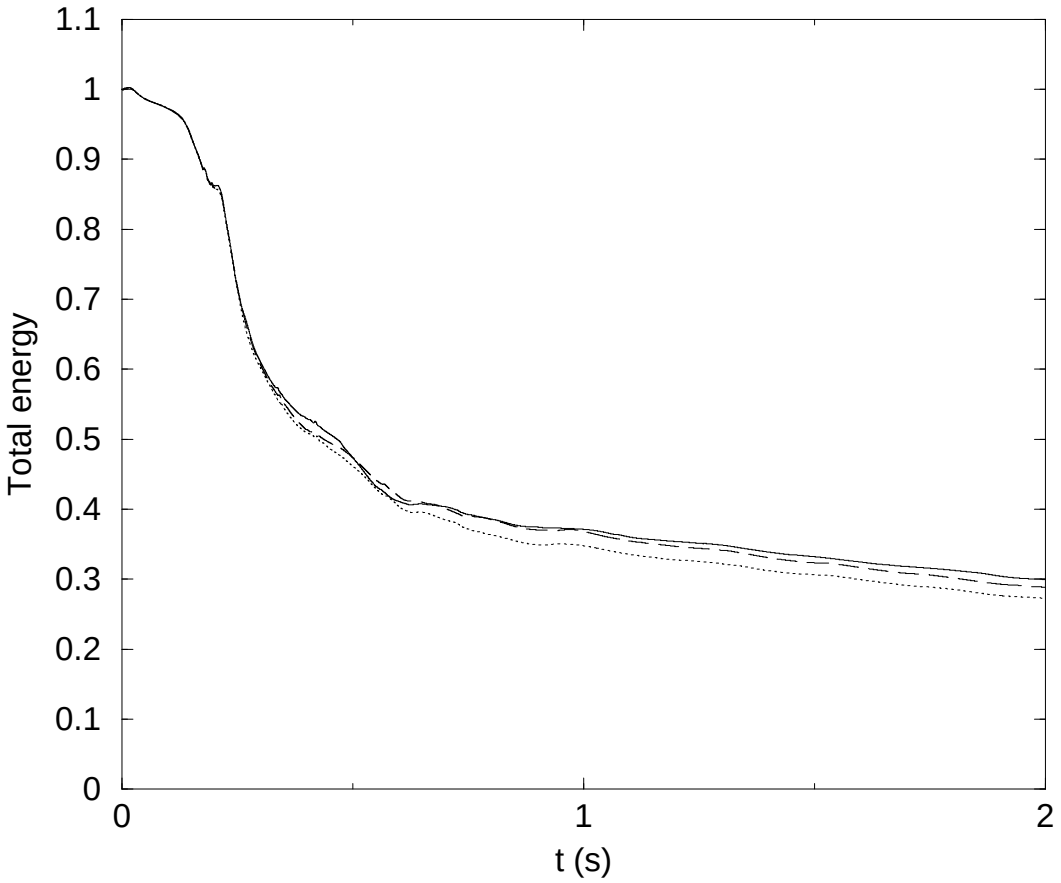

Figure 5.18: Time evolution of the total energy comparison. $\frac{H}{L} = 0.13$, $\frac{d}{L} = 0.17$. Dotted line: test 1; dashed line: test 2; solid line: test 3.

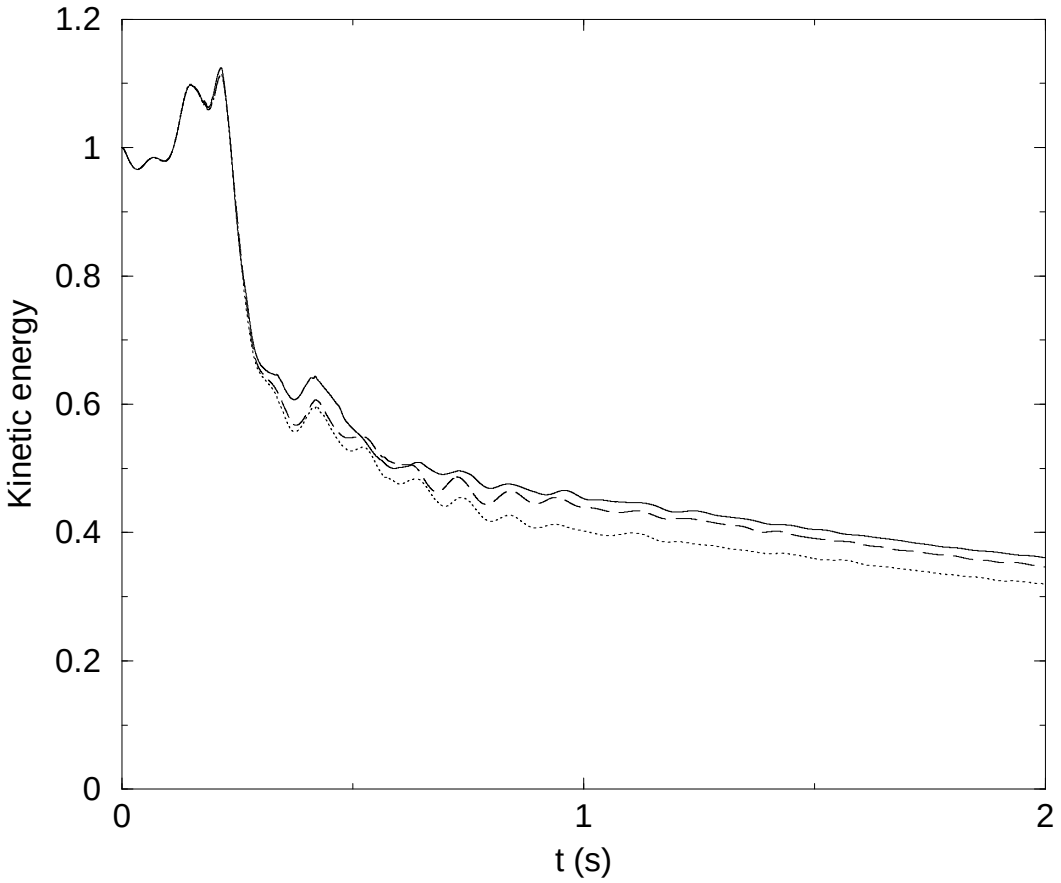

Figure 5.19: Time evolution of the kinetic energy comparison. $\frac{H}{L} = 0.13$, $\frac{d}{L} = 0.17$. Dotted line: test 1; dashed line: test 2; solid line: test 3.

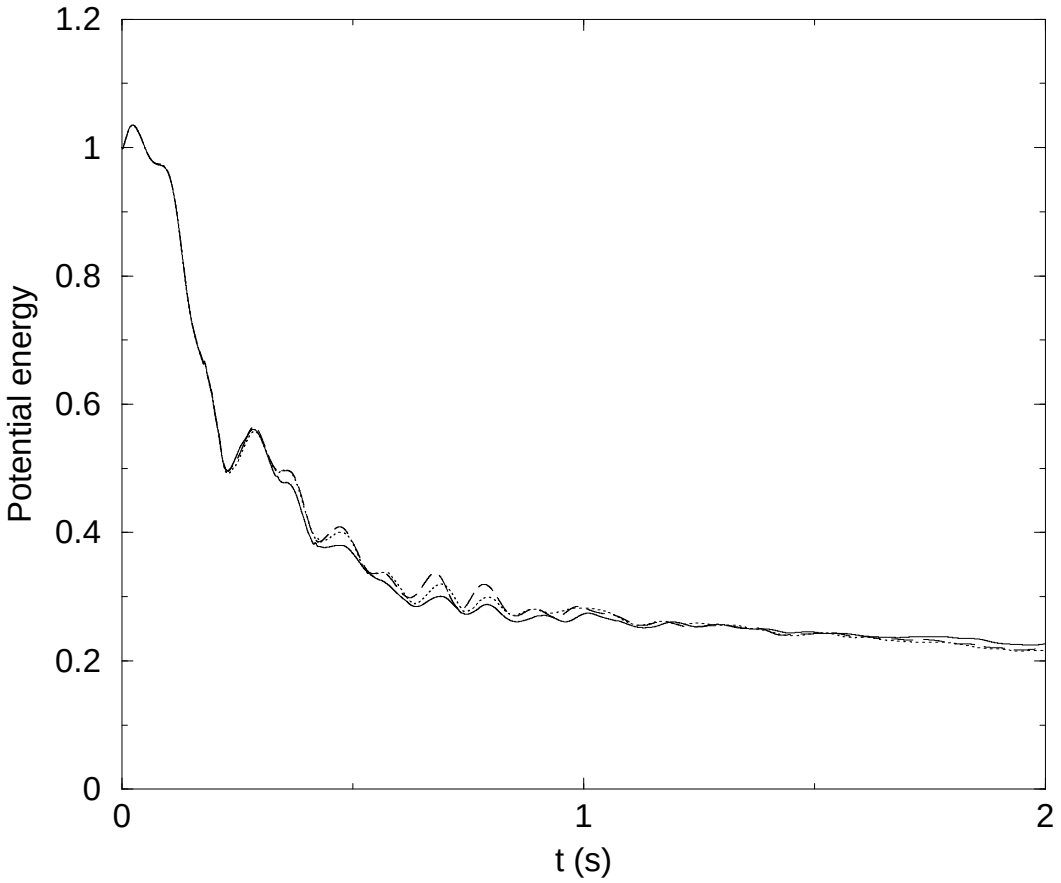

Figure 5.20: Time evolution of the potential energy comparison. $\frac{H}{L} = 0.13$, $\frac{d}{L} = 0.17$. Dotted line: test 1; dashed line: test 2; solid line: test 3.

The observed discrepancies appear differently, depending on the considered energy. The potential energy is apparently affected only when the free surface is distorted and shows some irregularities, as shown in figure (5.20) where some slight variations in magnitude can be observed at the peak values. Indeed, from $t \simeq 0.5\ s$, the splash-ups have all disappeared and the remaining potential energy is due to the waving water in the numerical domain. However, the lines plotted in figure (5.19) merges from the time $t \simeq 1\ s$ and show the same time evolution for the non-dimensional potential energy. So, the discrepancies observed in the time evolutions of the non-dimensional total energies (Fig. 5.18) must be found in the velocity field behavior.

Indeed, the clearer effect of the test can be seen in figure (5.19), where we show the time evolution of the non-dimensional kinetic energy. As we already said, each decreasing of the potential energy is associated with a relative increase of the kinetic energy and *vice versa*. So, when the kinetic energy is affected by the turbulent viscosity, the potential energy, in turn, will gain or lose some intensity. The kinetic energy is quantitatively more dissipated in Test 1 than in Test 2, which has repercussions in the dissipation of the total energy of the wave.

However, results from Test 2 are rather close from those obtained in Test 3, even if some discrepancies appear as time goes on. This would tend to show that we gained some accuracy in the description of the energy dissipation, but the overall breaking process is well described in Test 3.

The observations between the results obtained through Test 1 and 2 show that a non-negligible amount of velocity fluctuations is contained in the numerical diffusion region of the free surface. Turbulence is associated with high velocity fluctuations and the interface is the region where all turbulence tends to concentrate due to the low penetration of the air in the wave or the rising of the two counter-rotative vortices, in this particular example. This tends to prove that it could be wise not to calculate the turbulent viscosity ν_t in this numerical diffusion region ($0 < C < 1$), but we should improve the accuracy of the free surface description to reduce this area of numerical diffusion. Moreover, turbulent viscosity has been noted to increase the numerical diffusion of the color function: this, in consequence, implies that the large scale structures corresponding to pockets of air entrained in the water are disappearing more quickly. It has been detailed before that this process of air entrainment was crucial for the dissipation of the wave energy.

Nevertheless, the time evolutions follow the same tendency, whatever the test, concerning the time evolutions of the non-dimensional total and kinetic energies.

5.1.6 Conclusions and perspectives

It is very important to be able to reproduce correctly the splash-up phenomenon, because it plays a great role in the air entrainment, this process, in its turn, will participate in the whole energy dissipation. Chanson and Lee (1997) confirms that the air bubble entrainment is directly related to the plunging jet impact characteristics.

Nevertheless, two-dimensional simulations have a limited range of validity. The vortices will behave differently in three-dimensional configurations. This implies that the whole energy dissipation process description will differ from the observations detailed previously. For this reason, it is important to simulate three-dimensional breaking waves in order to take properly into account the complex turbulent processes, highly dissipative in three-dimensions.

Nevertheless, the whole flow description remains valid from the initial conditions to the beginning of the splash-ups generation. The following details are very promising and are a necessary step before evolving towards a complete three-dimensional study of the complex phenomenon of the breaking of a wave.

5.2 Three-dimensional plunging wave breaking simulations

5.2.1 Preliminary considerations of the case study

Very few three-dimensional numerical studies can be found in the literature (Christensen, 1996; Watanabe and Saeki, 1999; Christensen and Deigaard, 2001; Lubin et al., 2002, 2003a). As indicated in section 1, Zhao and Tanimoto (1998) presented the first LES tests in two dimensions, with very encouraging results. Christensen (1996), Watanabe and Saeki (1999) and Christensen and Deigaard (2001) started three-dimensional studies.

In the previous section (5.1), we validated the breaking process (Lubin et al., 2003b), which is in accordance with the general observations found in the literature. We then proceed to the study of another plunging breaking wave by the same method.

Three-dimensional direct numerical simulations (DNS) are first realized with the two-dimensional initial (x,z) solution spread in the y-direction, in order to evaluate the ability of the numerical tool to simulate accurately this type of flow in a three-dimensional configuration. The large eddy simulation of the breaking wave problem will be studied next and compared to the present results.

We choose to simulate and present a plunging breaker with $H/L = 0.13$ and $d/L = 0.17$.

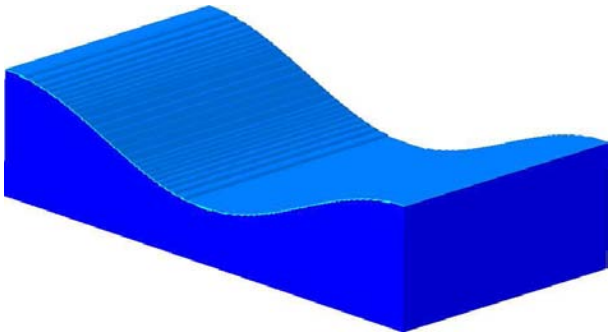

Figure 5.21: Three-dimensional simulation of a plunging breaker. Initial conditions. $\frac{H}{L} = 0.13$, $\frac{d}{L} = 0.17$, $t = 0$ s, $C \geq 0.5$.

We present the initial condition with $C \geq 0.5$, without the velocity field vectors, in order to see the water medium (Fig. 5.21). The interface is located at $C = 0.5$. We recall that the Navier-Stokes equations are solved both in air and water.

During our first simulations, we observed that the velocity field does not develop spontaneously any three-dimensional flow structures (Figs. 5.22). We did not see any difference with two-dimensional simulations carried out for the same parameters. We can observe that our results are perfectly symmetrical along the y-axis, so no fully three-dimensional structures developed (Lubin et al., 2003b).

As a matter of fact, it seems obvious to conclude that we will not be able to study turbulence induced by breaking waves if no perturbation is introduced one way or another in this already unsteady wave. It seems natural to consider any physical parameter we can control in our problem, a perturbation coming from a numerical scheme would not be acceptable as it would be hard to evaluate and so to rely on. That is why we naturally consider a change of water depth as we initialize our flow equations. The free surface is kept uniform in shape and the velocity field (Eqs. 5.2) has the information of a variation of water depth resulting from the introduced perturbed bottom $d^* = d + \epsilon$, where ϵ is a small perturbation quantity chosen to vary linearly, for example, along the y-axis. This numerical perturbation leads to an unsymmetrical flow with respect to the long-shore axis.

$$u_0 = \frac{\omega H}{2} \frac{\cosh kz}{\sinh kd^*} \cos kx, \quad v_0 = \frac{\omega H}{2} \frac{\sinh kz}{\sinh kd^*} \sin kx \tag{5.2}$$

with ω being the angular frequency and k the wave number.

To illustrate this point, two simulations are carried out with the same parameters. The first one is done as previously presented and the second one is run with a long-shore

depth perturbation introduced in the initial velocity field. We then compare the different structures we get in the flow. We use a regular Cartesian grid of $250 \times 100 \times 25$ points, giving a mesh grid resolution of $\Delta x = \Delta z = 4.10^{-4}\ m$. The time step is approximately $0.1\ ms$. As a periodic condition is imposed in the direction of wave propagation, the wave moves out of the domain on the right side to re-enter on the left side.

We checked that there appeared no difference before the jet impact between the two simulations. The distance of the impact is the same, as shown in figures (5.22 a) and (5.24 a). The perturbation does not influence the overturning motion. Before plunging, the flow remains two-dimensional. The splash-up generated rises as high as the initial waveheight. A second jet is then generated and this process is observed to repeat, each successive splash-up being weaker than the preceding one. The perturbation starts to grow when the jet has impacted the forward face of the wave.

We can then observe fully three-dimensional large-scale structures that can be noticed, for example, by examining the two counter-rotative vortices showed in different vertical slices (Fig. 5.26), the interface being located with $C = 0.5$. These vortices are observed to be twisting along the y-axis. We show the velocity field in both media at the instant $t = 0.40\ s$ (Fig. 5.26) in three slices to show that the two counter-rotative vortices distorted and separating. These two rotating structures match together to form a pair with a high velocity directed towards the bottom of the wave. The two counter-rotative vortices are separating as one of them is stretching and rising to the surface, due to the buoyancy effect. The air entrapped in the biggest pocket is rising on one side of the domain as it is still sinking and rotating at the other side (Fig. 5.25 d). The tube is then twisting along the y-axis, whereas in the non-perturbed case, the tube stays straight as it is dragged to the bottom (Fig. 5.23 d). We can see in figures (5.27) that we can see through the tube of air entrapped in the volume.

The next step is to compare large eddy simulation results obtained for the same three-dimensional configuration (Figs. 5.28). We have first checked that no difference appeared before the impact of the jet, as expected. Being a positive quantity, the turbulent viscosity is only dissipative, as it is supposed to reproduce the effects of turbulence. The coupling with a subgrid scale model is expected to lead then to some foreseeable results. For example, the interface could be slightly smothered, all the small perturbations near the free surface being erased, or the flow turbulent motion to be damped more quickly.

We can notice that the breaking of the wave shows no difference in the main features as the generation of the splash-ups, rising more or less at the same heights, the number of co- and counter-rotative vortices, being the same, *i.e.* two counter-rotative vortices and

three co-rotative vortices in the case where $\frac{H}{L} = 0.13$, $\frac{d}{L} = 0.17$.

However, surprisingly, the interface appears to be much more vigorously agitated, compared with the DNS simulation (Figs. 5.24 and 5.25). The main difference is found in the behavior of the co- and counter-rotative vortices generated in the flow. While in the DNS simulation, we could see a turbulent flow composed with large spinning and propagating parallel tubes of gas finally exploding to the surface after some time, we can see in the LES simulation a turbulent "chaotic" flow composed of gas pockets concentrated in the middle of the numerical domain. The gas pockets disappear rapidly but put volumes of water into rotation. The broken wave looks more agitated, fluctuated and disordered, but the flow still looks like it develops into a propagating turbulent bore.

We can see that the main entrapped gas pockets are rising in the middle of the domain, as they were previously observed to be present along the transverse axis of the numerical domains (Figs. 5.24 and 5.25). The two counter-rotative vortices are still found to separate, but the main pocket of air explodes to the free surface in the middle of the numerical domain (Fig. 5.29). In figure (5.30), we present three slices showing the velocity field in both air and water media showing the main gas pocket once it has pierced the free surface: the velocity field in the air proves the violent spray of gas ejected from the rising pocket.

The energy of the wave is also found to be expended slightly quicker in the sense that the co-rotative vortices have a shorter life time than what we observed during the simulation done without turbulence model. Numerical diffusion of the color function could also be responsible for this aspect. These preliminary observations are found to be very satisfactory and very promising.

5.2.2 Free surface and vortex analysis

We present in figures (5.31), (5.32), (5.33) and (5.34) two examples of three-dimensional large eddy simulations. These next two configurations can give an excellent description of the violent behavior of two plunging breakers. We choose the previous two-dimensional configurations, $\frac{H}{L} = 0.13$, $\frac{d}{L} = 0.13$ (Figs. 5.31 and 5.32), and $\frac{H}{L} = 0.10$, $\frac{d}{L} = 0.10$ (Figs. 5.33 and 5.34).

The same flow description can be made from the three-dimensional results as from the previous two-dimensional configurations.

The two main mechanisms for the production of turbulence and vortices are the topologically induced vorticity and the type of flow generated by the impacting jet on the forward face of the wave. When the jet is projected from the steepening crest of the wave,

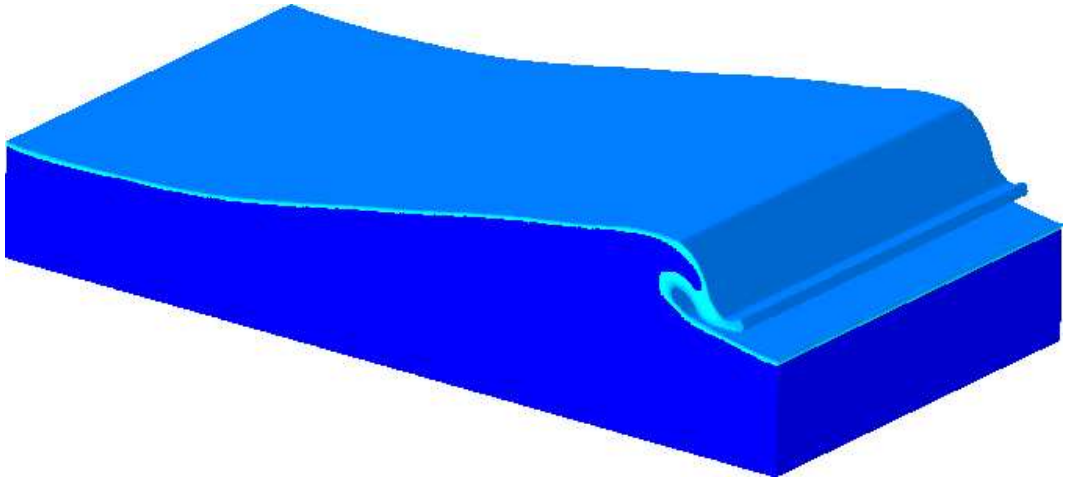

(a) $t = 0.18\ s$

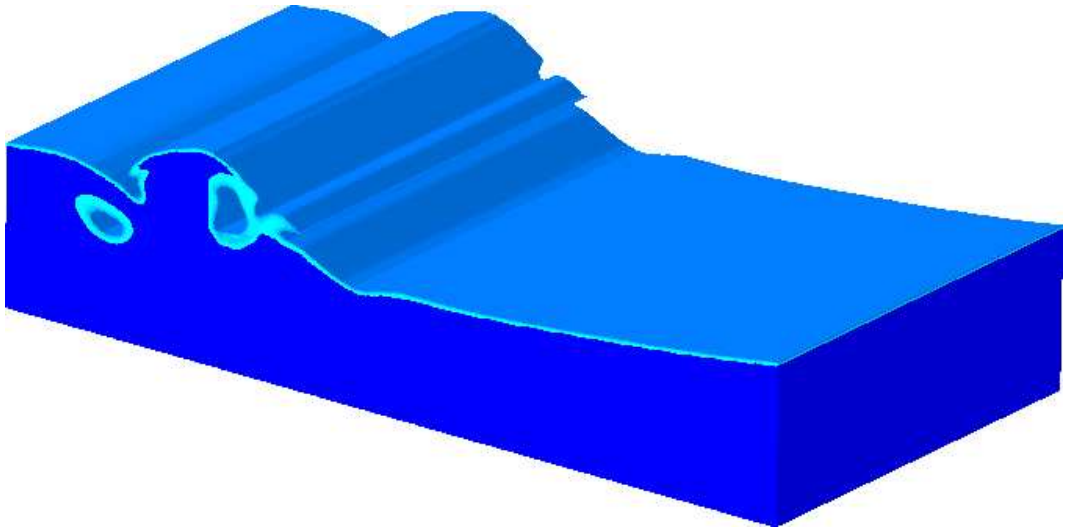

(b) $t = 0.28\ s$

Figure 5.22: Three-dimensional direct numerical simulation of a plunging breaker, without perturbation. $\frac{H}{L} = 0.13$, $\frac{d}{L} = 0.17$, $C \geq 0.5$.

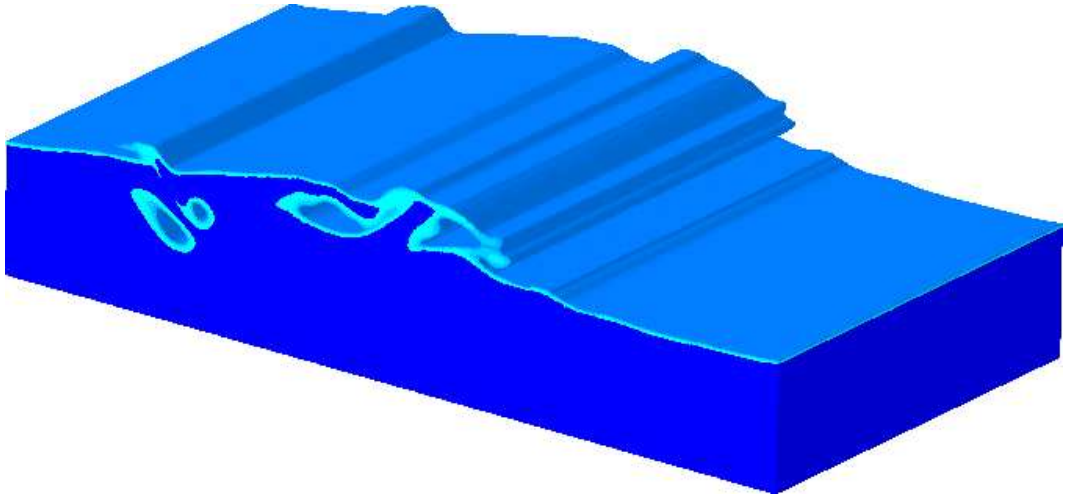

(c) $t = 0.35\ s$

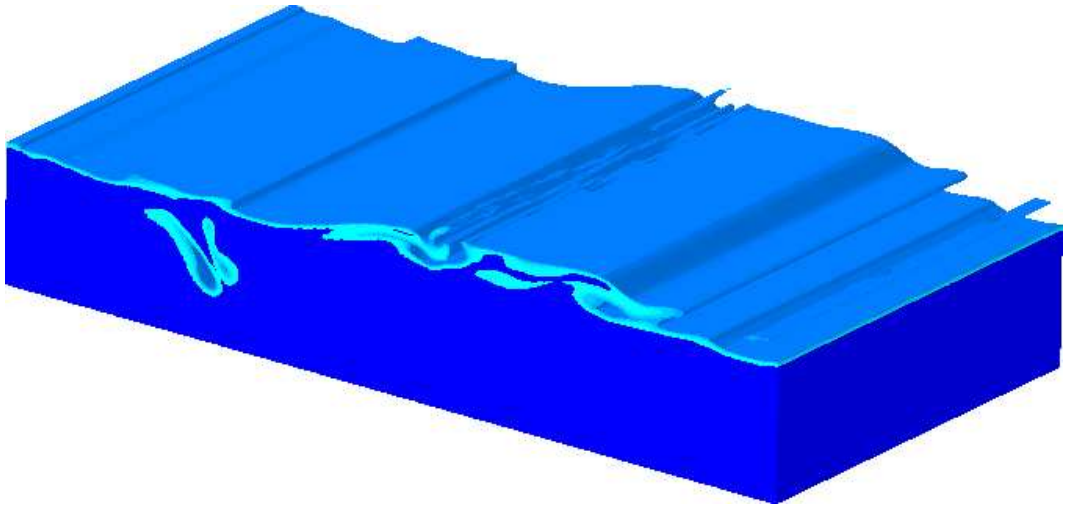

(d) $t = 0.42\ s$

Figure 5.23: See caption in figure (5.22). $\frac{H}{L} = 0.13$, $\frac{d}{L} = 0.17$, $C \geq 0.5$.

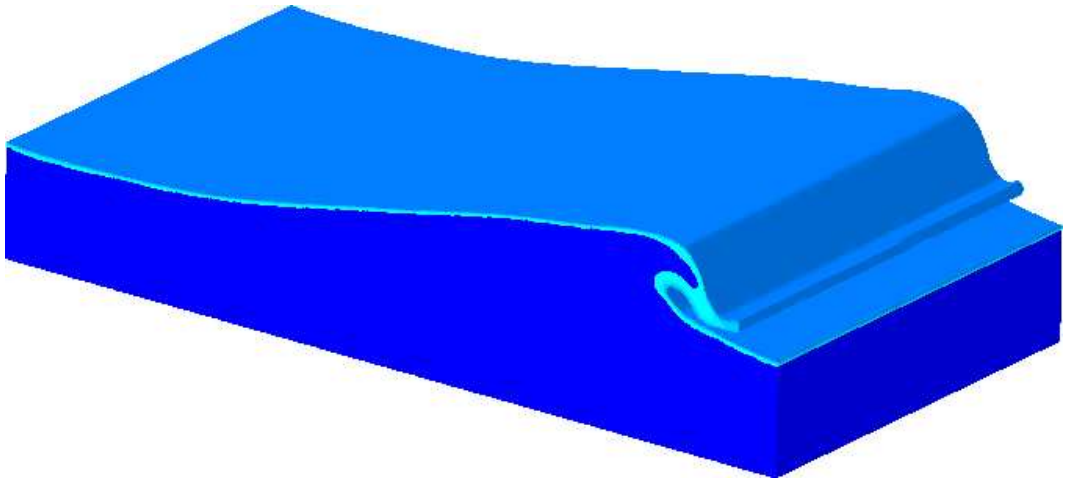

(a) $t = 0.18\ s$

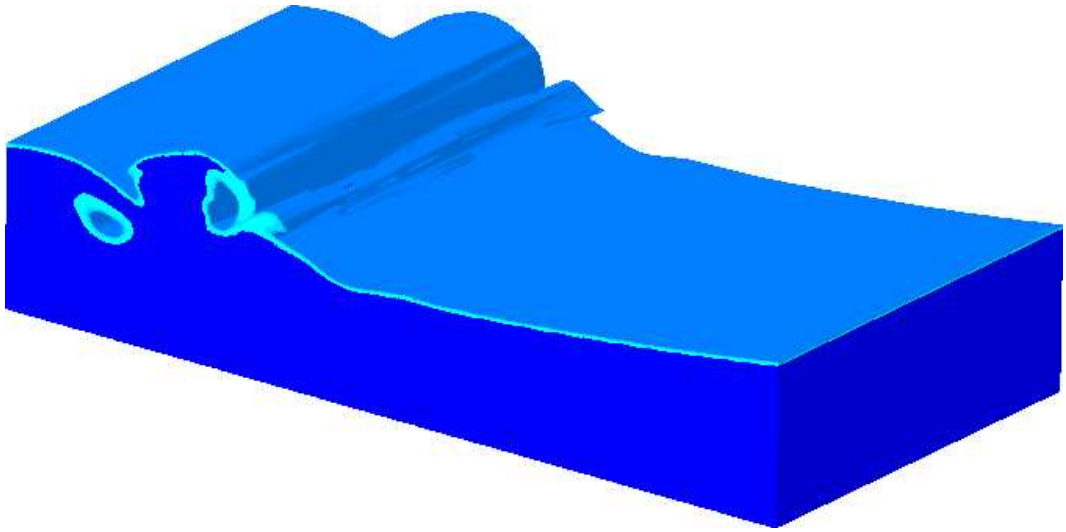

(b) $t = 0.28\ s$

Figure 5.24: Three-dimensional direct numerical simulation of a plunging breaker, with perturbation. $\frac{H}{L} = 0.13$, $\frac{d}{L} = 0.17$, $C \geq 0.5$.

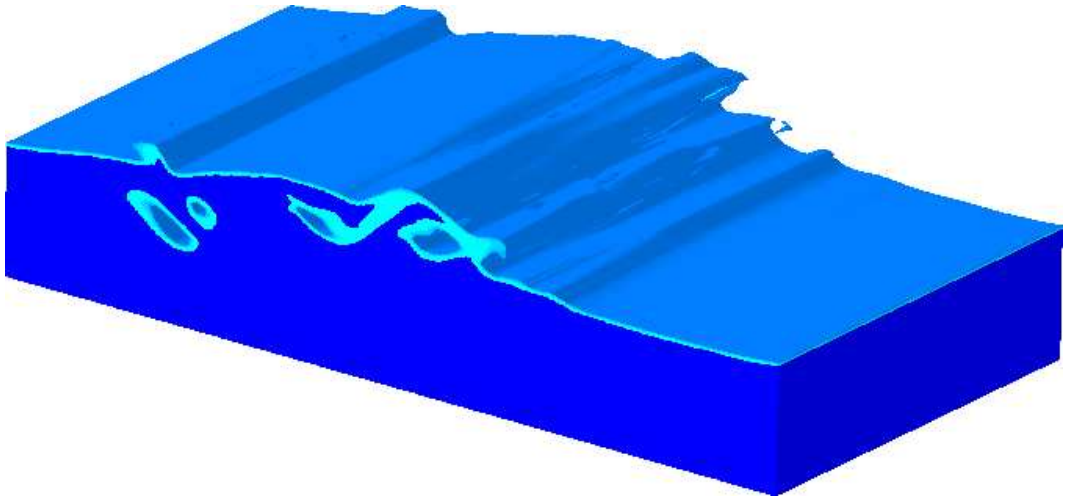

(c) $t = 0.35\ s$

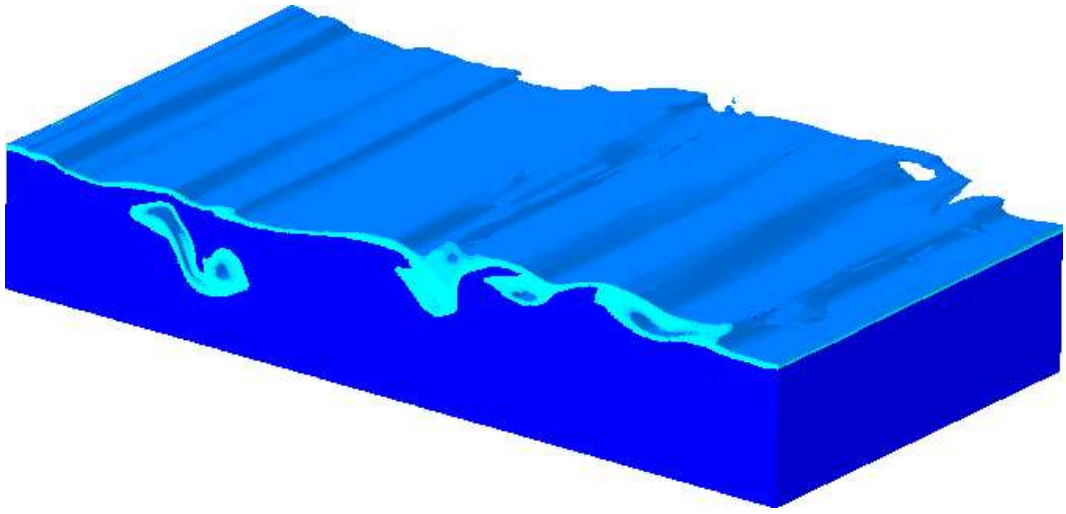

(d) $t = 0.42\ s$

Figure 5.25: See caption in figure (5.24). $\frac{H}{L} = 0.13$, $\frac{d}{L} = 0.17$, $C \geq 0.5$.

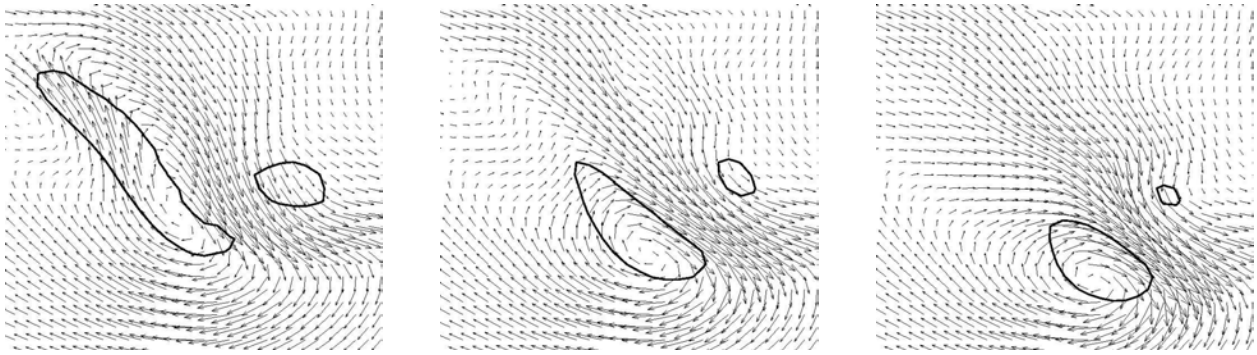

(a) Right side (b) Middle (c) Left side

Figure 5.26: Anisotropy of the counter-rotative vortices and the velocity field along the y-axis - zoom of vertical slices taken from the three-dimensional direct numerical simulation of a plunging breaker, with perturbation. $\frac{H}{L} = 0.13$, $\frac{d}{L} = 0.17$, $C = 0.5$, $t = 0.40\ s$.

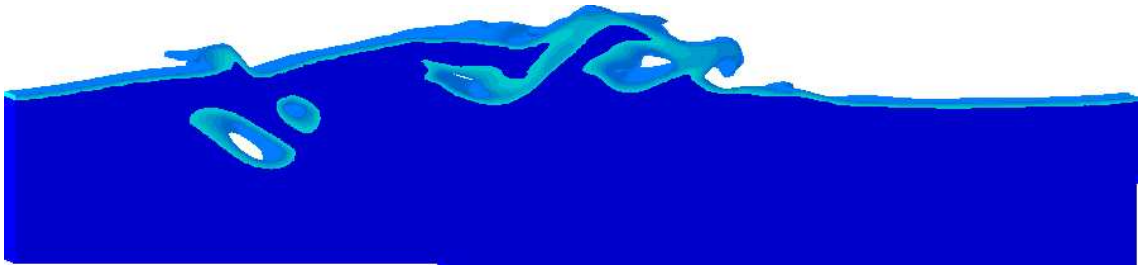

(a) $t = 0.35\ s$

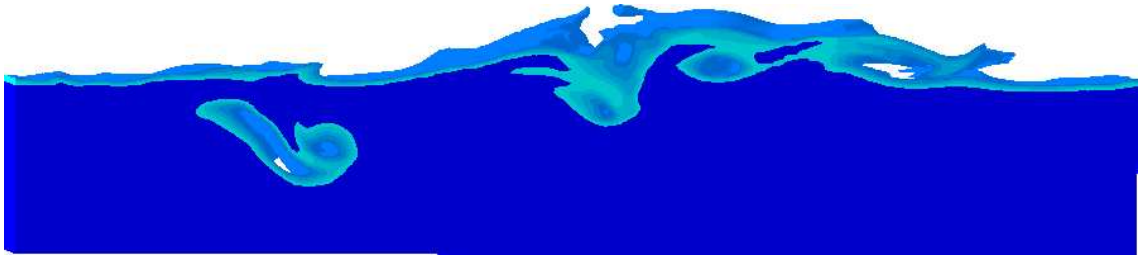

(b) $t = 0.41\ s$

Figure 5.27: Counter-rotative and co-rotative vortices - zoom, frontside view of the whole three-dimensional numerical domain. $\frac{H}{L} = 0.13$, $\frac{d}{L} = 0.17$.

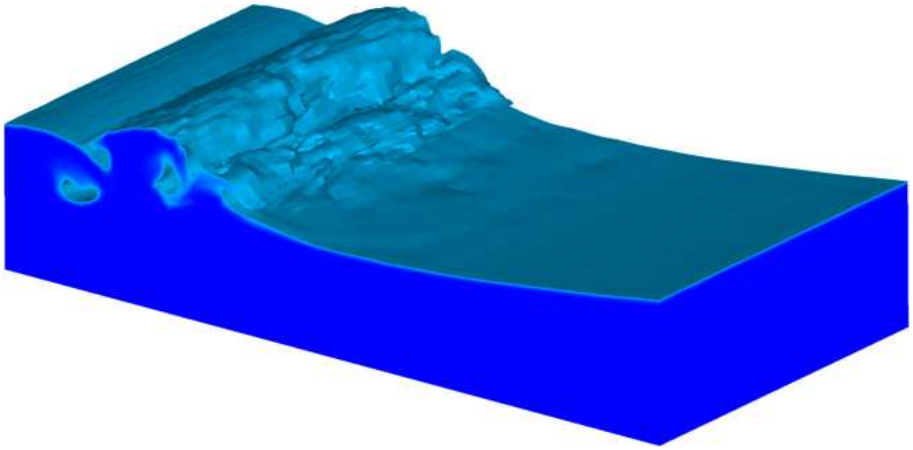

(a) $t = 0.28\ s$

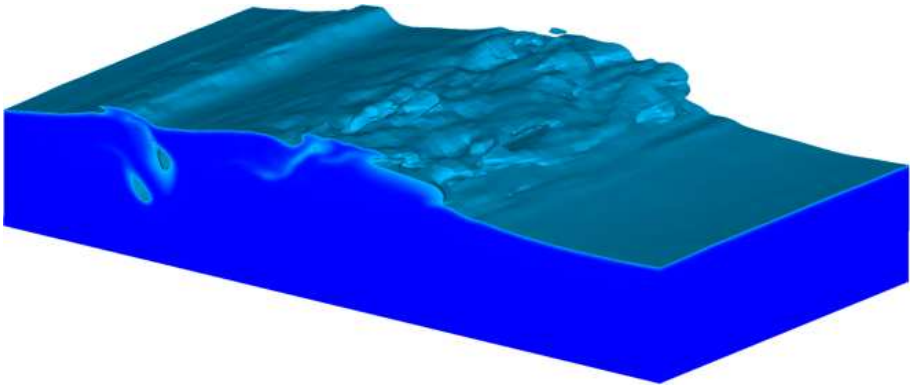

(b) $t = 0.35\ s$

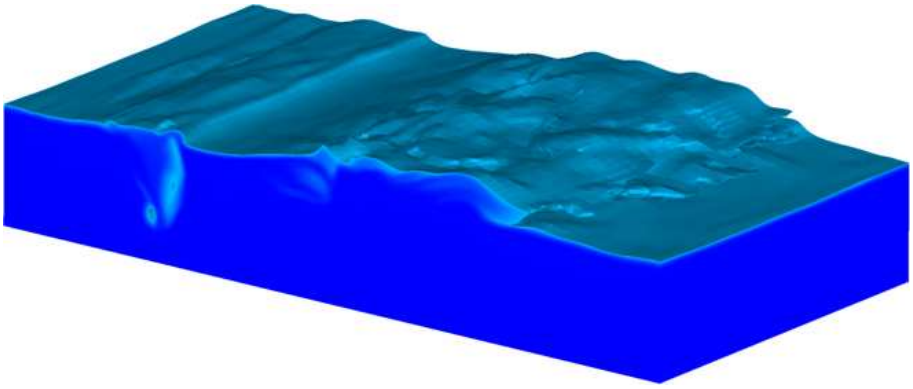

(c) $t = 0.42\ s$

Figure 5.28: Three-dimensional large eddy simulation of a plunging breaker. $\frac{H}{L} = 0.13$, $\frac{d}{L} = 0.17$, $C \geq 0.5$.

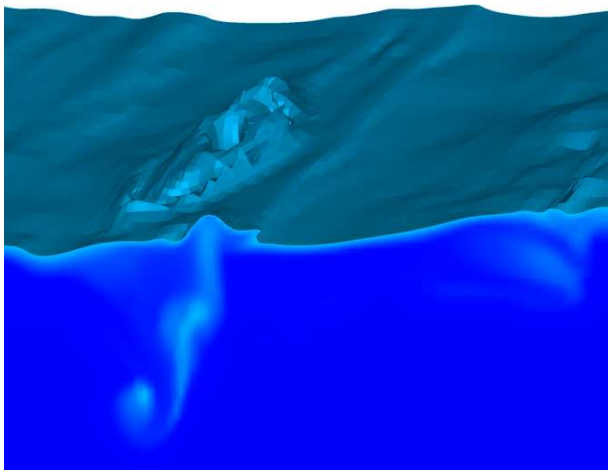

Figure 5.29: Main gas pocket exploding through the free surface - zoom of the three-dimensional numerical domain. $\frac{H}{L} = 0.13$, $\frac{d}{L} = 0.17$, $C = 0.5$, $t = 0.43$ s.

a first vortex is created, a pocket of air is entrapped and put into rotation due to the high circulation of water surrounding it (Figs. 5.28 a, 5.31 a and 5.33 a). A large amount of gas is entrained in the water. The air resists, as it is enveloped by the tongue of water, and induces a great shear rate at the free-surface. The flow becomes very turbulent and violent in both media. We can then see that we got a high splash-up generating counter-rotative vortices, as observed by Bonmarin (1989), and co-rotative vortices, as observed by Miller (1976) or Sakai et al. (1986).

After the jet touches down the forward face of the wave, a series of splash-ups induces some new vortices in front of the main one previously generated (Figs. 5.28 b, 5.31 b and 5.33 b). This phenomenon appears to repeat (Miller, 1976; Bonmarin, 1989) and decrease in size as it develops.

However, the entrapped gas pockets can have very various sizes. The length scales of these large structures can be approximately from third to half of the whole depth (Fig. 5.32 c and 5.34 c). They reach sometimes the same size as the water depth as they are rotating and stretching (Fig. 5.34 d). The speed of propagation of these vortices is observed to be smaller than the initial wave celerity.

The rapid compression of the entrained pockets of air forces some of the structures to rise and explodes through the free surface. We could see some gas pockets rising to the free surface and the air exploding as a spout of spray (Figs. 5.29, 5.32 f and 5.34 f). We can see the dipole has a short life time. They are separating as one of them is stretching and rising to the surface (Figs. 5.30), as due to the buoyancy effects. We can notice the topologically generated vorticity. The flow between the two counter-rotative vortices,

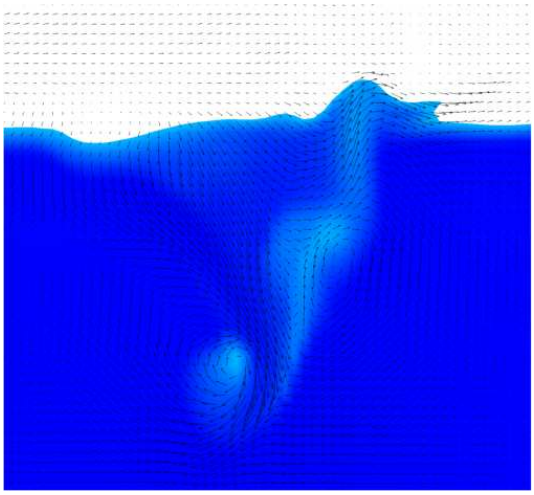

(a) Right side

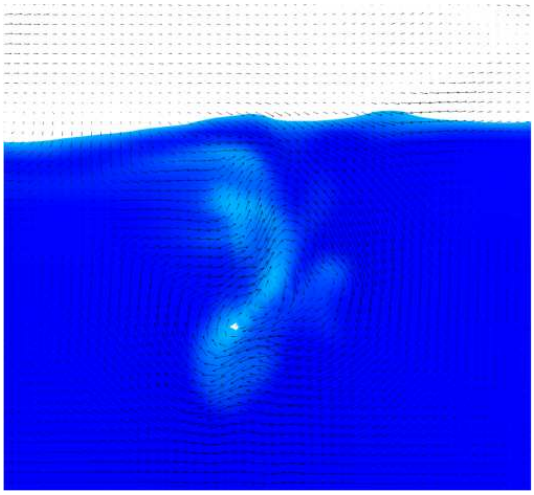

(b) Left side

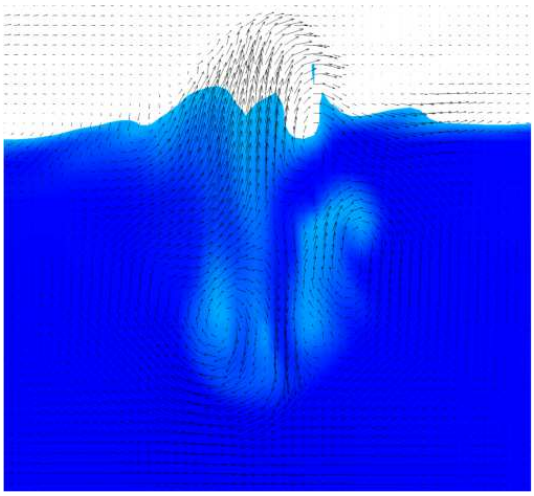

(c) Middle

Figure 5.30: Velocity field in both air and water media showing the main gas pocket once it has pierced the free surface - zoom of vertical slices taken from the three-dimensional large eddy simulation of a plunging breaker. $\frac{H}{L} = 0.13$, $\frac{d}{L} = 0.17$, $C = 0.5$, $t = 0.43$ s.

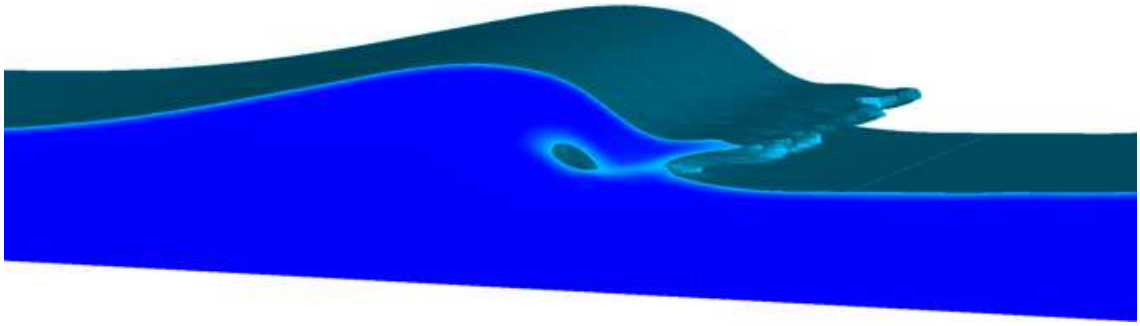

(a) $t = 0.16\ s$

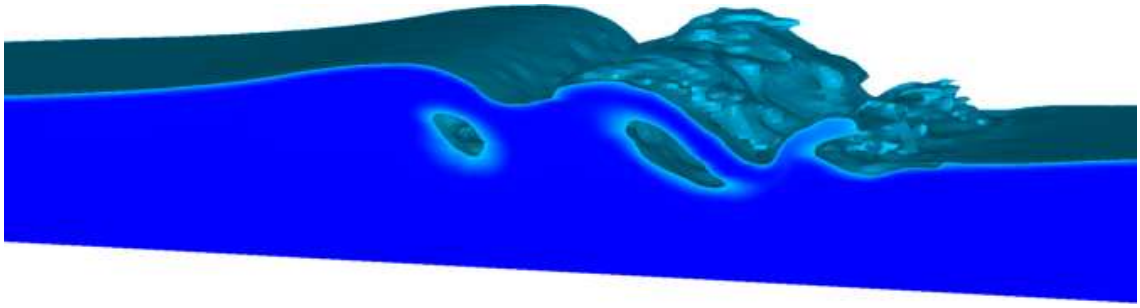

(b) $t = 0.22\ s$

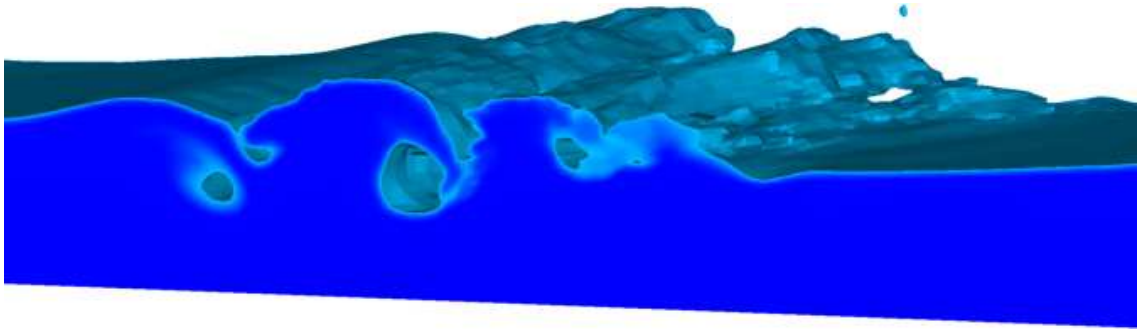

(c) $t = 0.27\ s$

Figure 5.31: Snap shots of a three-dimensional large eddy simulation of a plunging breaker. $\frac{H}{L} = 0.13$, $\frac{d}{L} = 0.13$, $C \geq 0.5$.

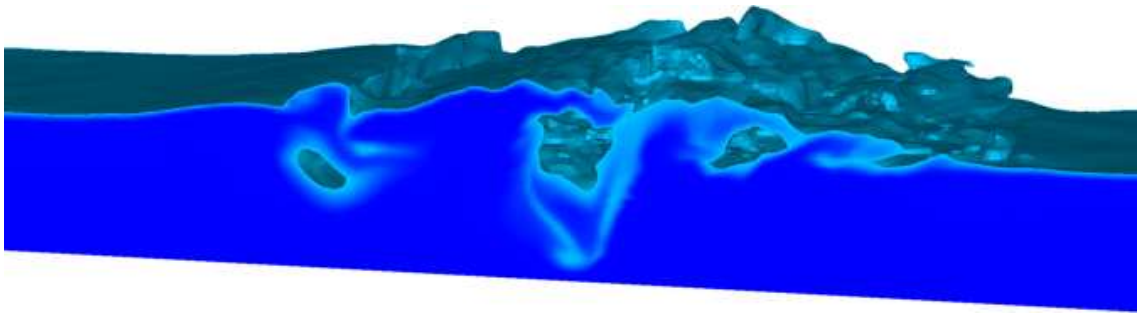

(d) $t = 0.30\ s$

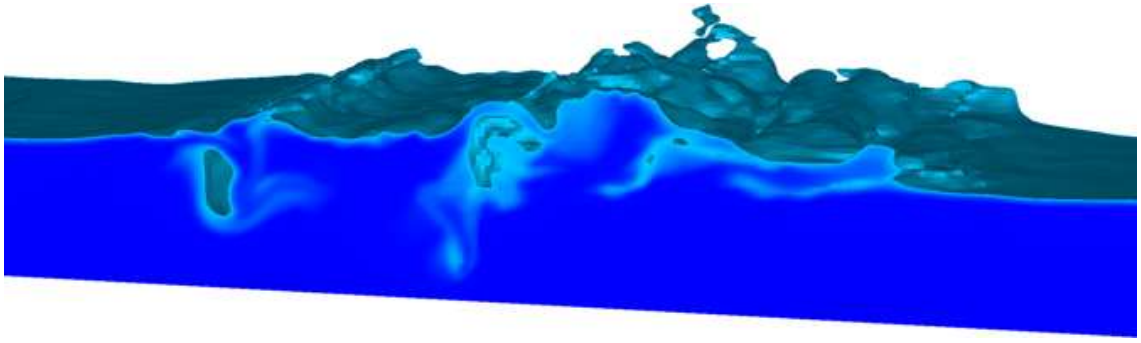

(e) $t = 0.34\ s$

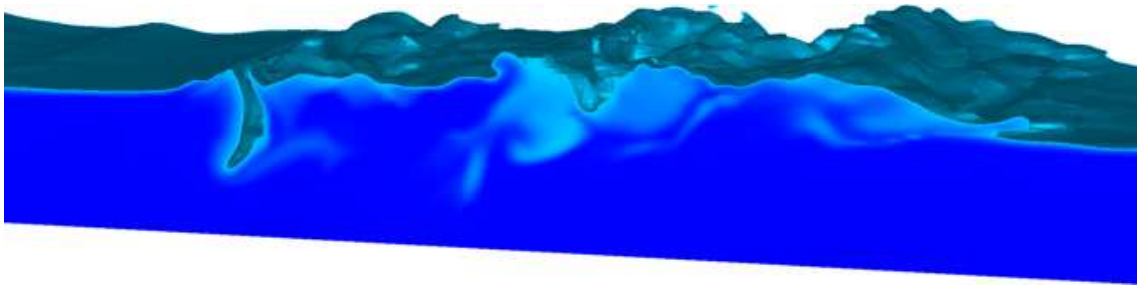

(f) $t = 0.37\ s$

Figure 5.32: See caption in figure (5.31). $\frac{H}{L} = 0.13$, $\frac{d}{L} = 0.13$, $C \geq 0.5$.

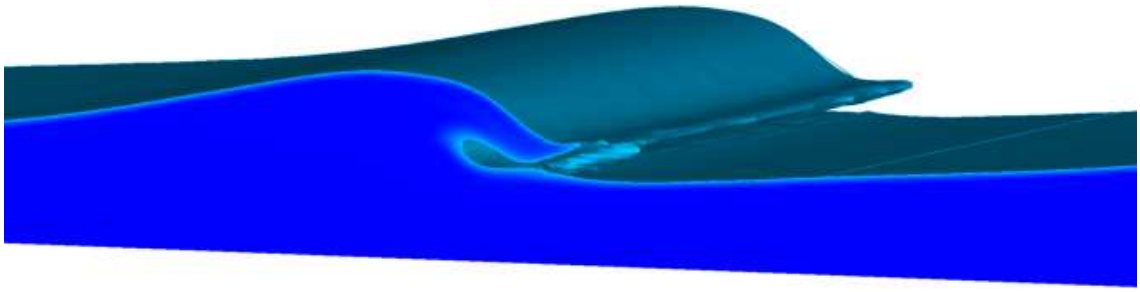

(a) $t = 0.16\ s$

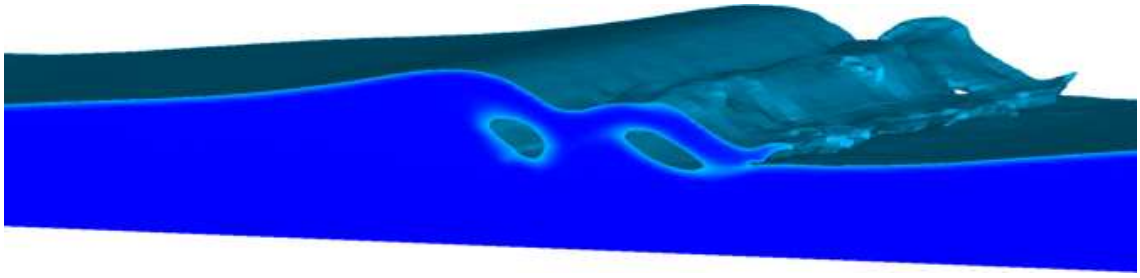

(b) $t = 0.21\ s$

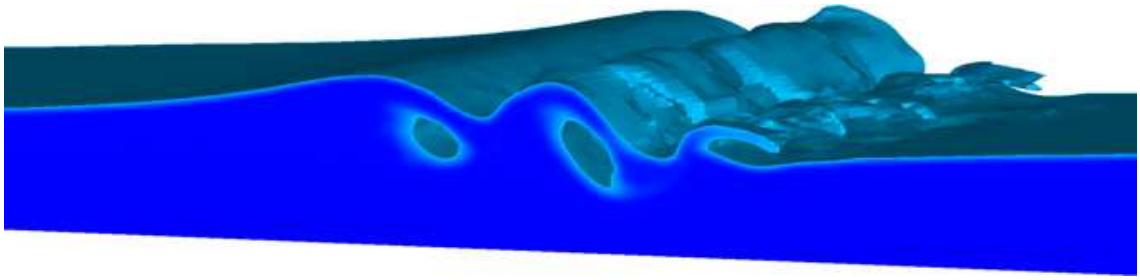

(c) $t = 0.23\ s$

Figure 5.33: Snap shots of a three-dimensional large eddy simulation of a plunging breaker. $\frac{H}{L} = 0.10$, $\frac{d}{L} = 0.10$, $C \geq 0.5$.

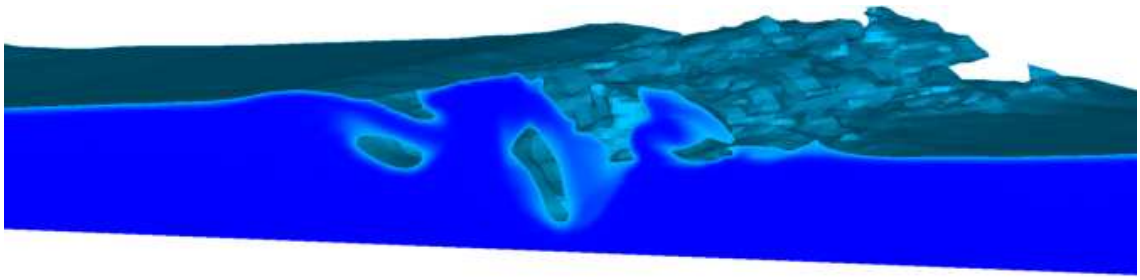

(d) $t = 0.28\ s$

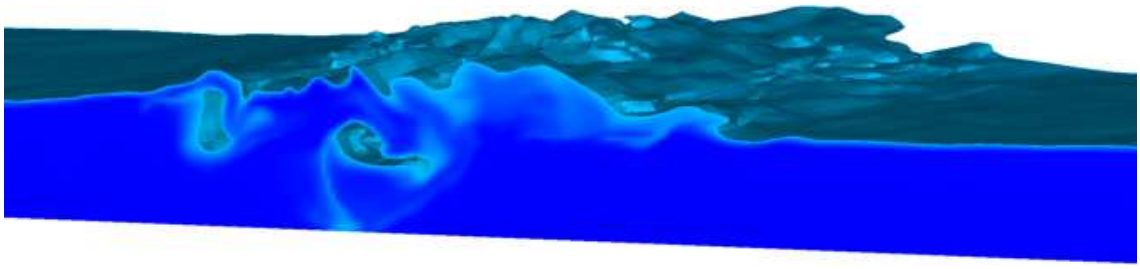

(e) $t = 0.35\ s$

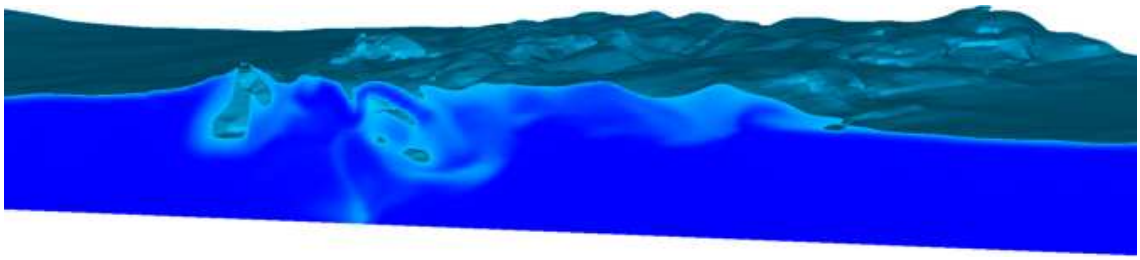

(f) $t = 0.38\ s$

Figure 5.34: See caption in figure (5.33). $\frac{H}{L} = 0.10$, $\frac{d}{L} = 0.10$, $C \geq 0.5$.

resulting from the impact of the projected tongue of water, is fed by the impacting jet.

The behavior, the quantities and the sizes of the generated vortices depend on their trajectories and the strength of the initial wave. We present in figures (5.35 a) the trajectory of the first main pocket of air, which is entrapped by the plunging jet. The trajectory of the next pocket of air, which is entrapped by the splash-up, is shown in figure (5.35 b). The trajectory is represented as the variation of normalized air pocket height (z/L) with the normalized distance (x/L), in order to compare results from the three test cases. When $(z/L) = 1$, the gas pocket has reached the free surface.

These observations have to be related to the sizes of the structures, as we visually estimated the average location of the core of each main pocket. We do not take into account the expansion and the stretching of the structures, we are only interested in describing the general entrainment process.

From the three lines plotted in both figures (5.35 a) and (5.35 b), the general behavior detailed previously is confirmed. In the case of the main tube of air, once it is generated, it is entrained in the water, then it rises very rapidly to the free surface. The structures are found to propagate less than half a wavelength of distance. The depth of penetration is found to be almost half of the initial water depth.

In the case of the first co-rotative spinning pocket of air, one of them is shown to be first risen before being entrained in the water. This is due to the fact that a large amount of water is pushed by the plunging jet to develop a high splash-up (Figs. 5.27 and 5.28 a). These pockets of gas are seen to stay near the free surface and do not propagate along a long distance.

Even if the wave breaking process seems more violent visually in the $\frac{H}{L} = 0.10$, $\frac{d}{L} = 0.10$ and $\frac{H}{L} = 0.13$, $\frac{d}{L} = 0.13$ configurations than the $\frac{H}{L} = 0.13$, $\frac{d}{L} = 0.17$ one, the general behavior is found to be very similar in the three cases.

Unfortunately, it can be observed that no foam is generated, as the number of grid points is not sufficient enough to take into account the dislocation of the pockets of gas into small bubbles. With past two-dimensional studies, we could check that the finer the grid was, the more pieces were produced from the entrained gas pockets, torn apart during the breaking of the wave. As pointed out by Lamarre and Melville (1991), the energy dissipation is dependent on this process. They observed experimentally that up to 50% of the wave energy is spent in entraining air and resisting against buoyancy forces, the turbulent behavior of the entrained and rising bubbles increasing this dissipation process.

Figures (5.36) show the time evolution of the turbulent viscosity μ_t in both air and

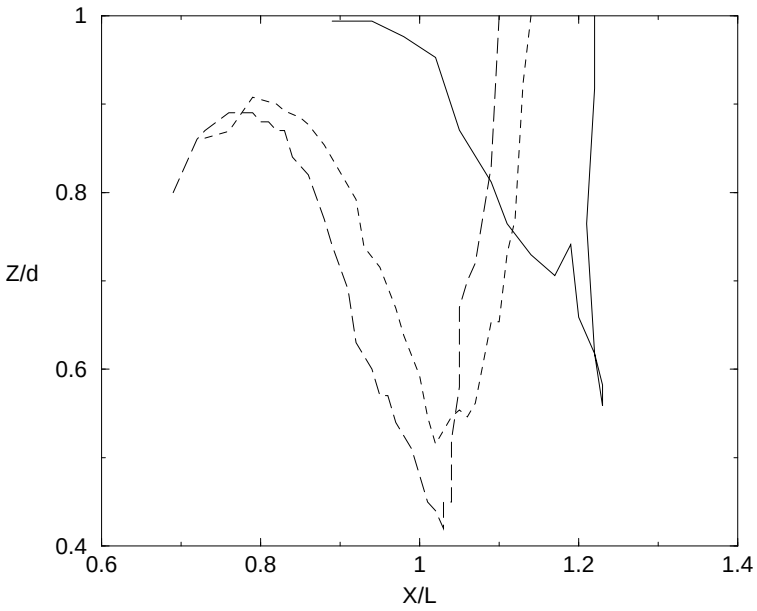

(a) Main pocket of air

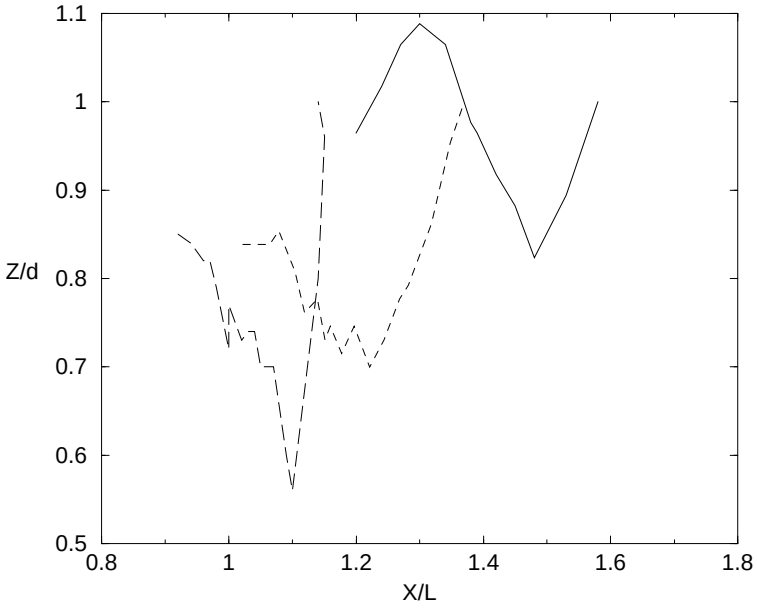

(b) First co-rotative spinning pocket of air

Figure 5.35: Trajectories of the main pocket of air entrained in the water for each three-dimensional large eddy simulations. The abscissae are divided by the wavelength L and the ordinates are divided by the initial water depth d. Solid line: $\frac{H}{L} = 0.13$, $\frac{d}{L} = 0.17$; long dashed line: $\frac{H}{L} = 0.10$, $\frac{d}{L} = 0.10$; dashed line: $\frac{H}{L} = 0.13$, $\frac{d}{L} = 0.13$.

water media. It can be used as an indicator for locating turbulent regions, as the models used to calculate the eddy viscosity are supposed to vanish if the flow is not fully turbulent.

As our study deals with a single breaking wave, the resulting flow is unstationary. Then, it is not possible to calculate any mean quantity and, so, any fluctuating value. This implies that we cannot have any information about the turbulent kinetic energy k, which is defined as $k = \frac{1}{2}(\overline{u'^2} + \overline{v'^2} + \overline{w'^2})$, where $\overline{u'^2}$, $\overline{v'^2}$ and $\overline{w'^2}$ are the mean of the squared fluctuating Cartesian component of the velocity field. Christensen and Deigaard (2001) averaged the velocity field over the transverse direction as an alternative method to the ensemble-averaging method. This is only possible in the case where the extension of the transverse direction is sufficiently large to obtain stable and reliable statistics. We choose not to follow this method and concentrate our work on the description of the larger-scale structures and the general behavior of the flow, as some numerical tests would be needed to ensure that the mean values are not influenced by a too narrow numerical domain.

We then use a more direct method based on a visual investigation of the turbulent viscosity and the velocity fields to study the behavior of the flow.

We can then see that the turbulent viscosity is mainly located where the large scale structures are. The maximum magnitudes of turbulent viscosity are observed in the regions of strong shear stress. These maxima correspond to some spotted areas. Thus, the successive impacting splash-ups generate higher shear stress during rebounds compared to penetrations (Figs. 5.36 a, b and c). This is why the co-rotative vortices do not propagate very deep (upper half of the water depth). These spinning structures produce high turbulent viscosity magnitudes. They explode to the surface very quickly, after propagating along less than half the wavelength. It is a strong plunging breaker and the main part of the energy of the initial wave is dissipated at the impingement. We can see that turbulence is spread straight to the bottom by the two counter-vortices generated by the violent impact of the initial impinging jet (Figs. 5.36 d to h). It is generally accepted that the energy dissipated during the breaking process is first converted into turbulent kinetic energy of organized vortices before being dissipated into small-scale turbulence.

Except in the initial impinging region, the turbulence remains located near the free-surface, where the co-rotative vortices propagate. If we pay attention to the propagating bore, it can be observed that turbulence is still active, even when the large structures disappeared. Some high values in magnitude of the turbulent viscosity can be noticed (Figs. 5.36 g and h), showing the interactions between some volumes of fluid put into rotation by the large spinning pockets of gas. It has been noticed that the behavior of the flow field was highly three-dimensional, as expected. These observations are all consistent

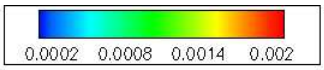

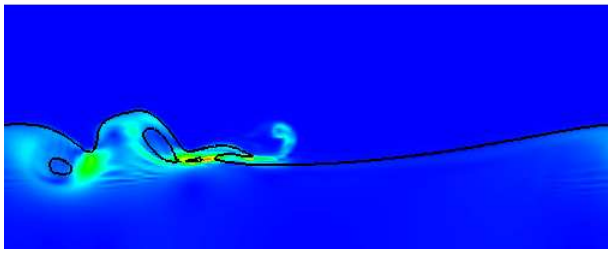

(a) $t = 0.27\ s$

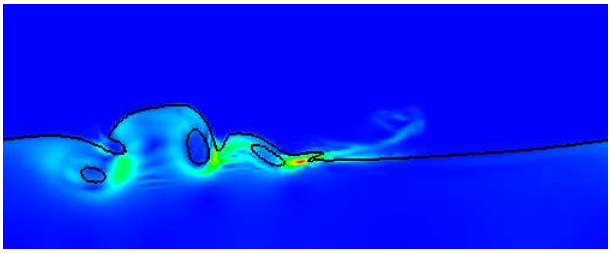

(b) $t = 0.30\ s$

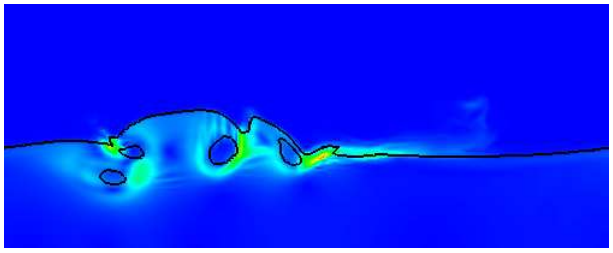

(c) $t = 0.33\ s$

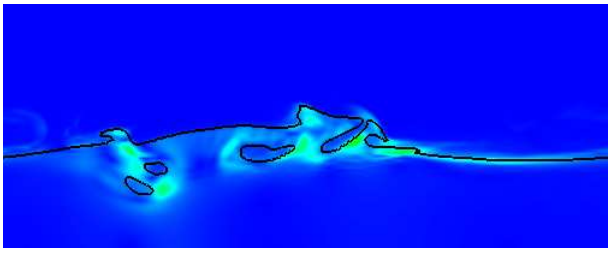

(d) $t = 0.34\ s$

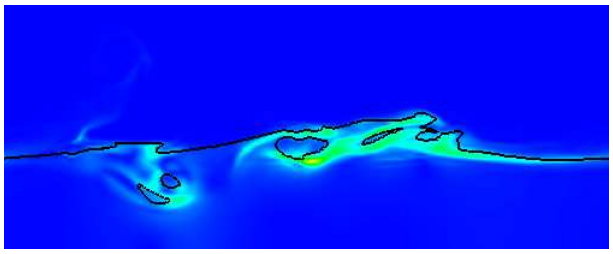

(e) $t = 0.36\ s$

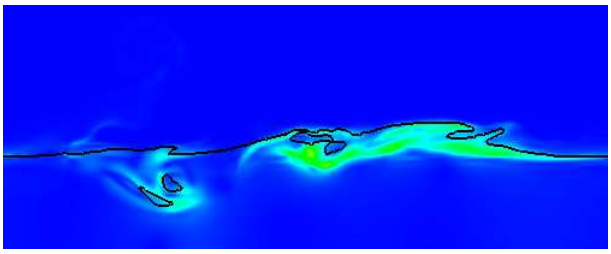

(f) $t = 0.40\ s$

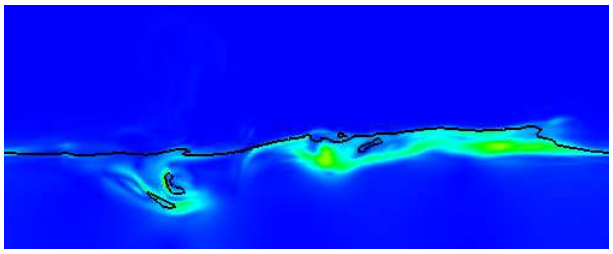

(g) $t = 0.43\ s$

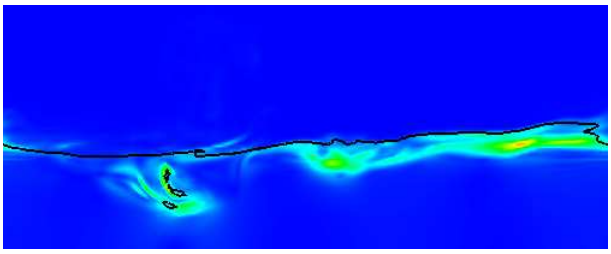

(h) $t = 0.45\ s$

Figure 5.36: Turbulent viscosity magnitude ($m^2.s^{-1}$) in both air and water media. The black line stands for $C = 0.5$. Slices taken in the middle plane of a 3D simulation. $\frac{H}{L} = 0.13$, $\frac{d}{L} = 0.17$.

with the results found in literature.

It can also be noticed that some turbulence is spreading towards the bottom after the propagation of the co-rotative vortices. Zhang and Sunamura (1990) indicated that the occurrence of spilling breakers provides a necessary condition for the formation of oblique vortices, but showed that these particular eddies can be found where a bore propagates even if a plunging breaker occurs. This confirms the observations of Sakai et al. (1986) and Nadaoka et al. (1989) who identified the generation of these fully three-dimensional structures. It is not possible to conclude with only the presented numerical simulations that we are able to observe these coherent structures. We can only detail, with a careful investigation of the velocity field, that some chaotic motion is spreading towards the bottom.

If we have a look at the velocity field in figures (5.30 a) and (5.30 b), we can see that a large volume of water is put into rotation. This eddy is as large as the water depth. This confirms that plunging breaking waves are found to be responsible for a large amount of sediment to be put into suspension and for the formation of sandbars, whereas spilling breaking waves are responsible to erode these sandbars. Moreover, the main flow is directed towards the shoreline, which implies that the sediment would be entrained in this direction.

5.2.3 Energy dissipation

As suggested in section (5.1), three-dimensional simulations exhibit different features from two-dimensional simulations. This has been discussed in terms of vortices behavior in the previous section. In the present section, we illustrate this point by examining the energy dissipation. The time evolution of the total energy, normalized by its initial value is shown in figure (5.37). The solid line stands for the three-dimensional result, compared to the two-dimensional result presented with the dashed line.

It is obvious that two-dimensional turbulence is less dissipative than three-dimensional turbulence. So, as expected, a very clear difference can be observed in terms of total wave energy decay, the main features being comparable with different magnitude. It can be seen than the discrepancy starts at the time of the impact of the jet on the forward face of the wave ($t \simeq 0.17\ s$) and increases with the turbulence generation, resulting from the splash-ups and the vortices occurrence. At $t \simeq 0.3\ s$, when the successive splash-ups entrain the gas pockets, about 50% of the total pre-breaking wave energy is dissipated in the two-dimensional simulation, compared to the 45% dissipated in the

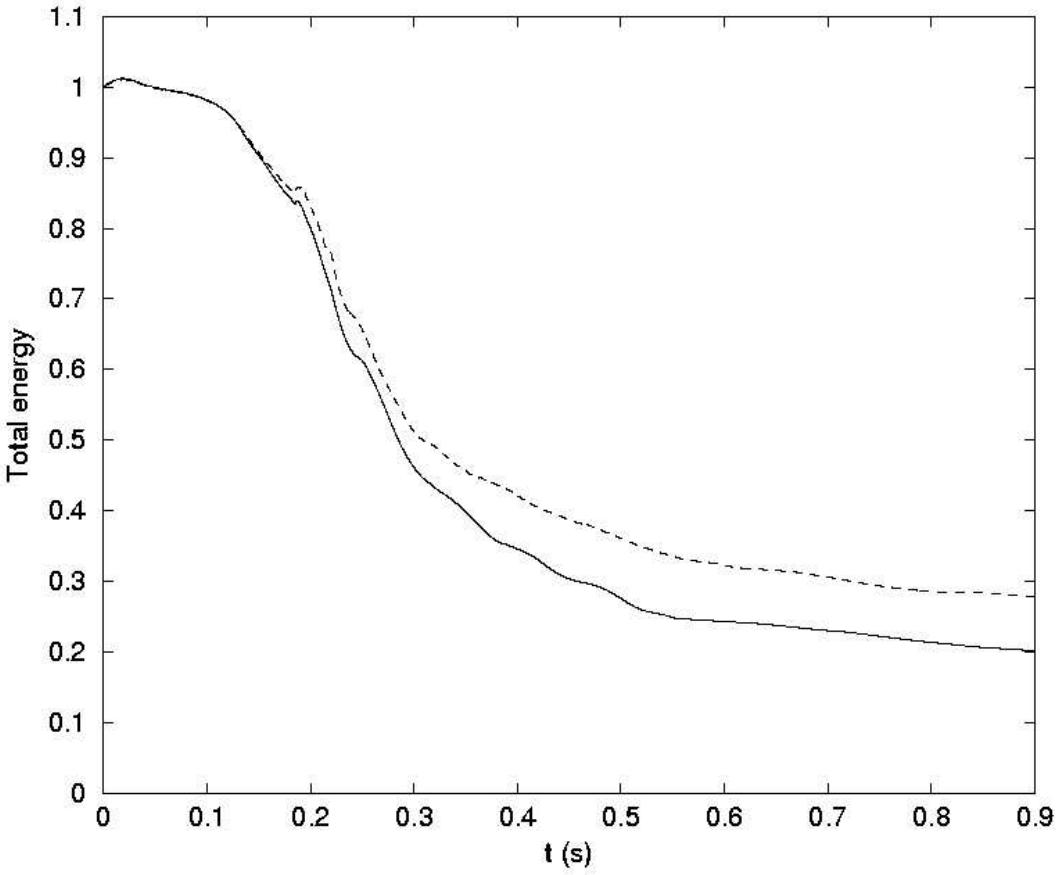

Figure 5.37: Time evolution of the non-dimensional energy. Solid line: total energy calculated from a 3D simulation; dashed line: total energy calculated from a 2D simulation. $\frac{H}{L} = 0.10$, $\frac{d}{L} = 0.10$.

three-dimensional simulation. The decay rate is much important for the three-dimensional result as the turbulence generation process is mainly observed at this time of the breaking phenomenon. The pockets of gas are entrained in the water and dislocated before rising to the free surface. At the time when all these large structures have disappeared, a large amount of water has been put into three-dimensional turbulent motion.

Two and a half wave period later ($t \simeq 0.9\ s$), almost 30% of the total pre-breaking wave energy remains in the two-dimensional numerical domain, whereas almost 20% of the total pre-breaking wave energy remains in the three-dimensional numerical domain. However, both curves seem to exhibit the same decay rate at the end of the breaking process. This has to be verified with a longer time simulated, but three-dimensional simulations have the negative aspect of taking a long time to run.

Summary and conclusion

We give in this section a detailed study of the abilities of the numerical tool to describe the plunging phenomenon. The Large Eddy Simulation of some two-dimensional configurations are first studied. Then some three-dimensional examples are investigated.

The overturning motion and the general flow motion is fully detailed. The splash-up process is described. We show that the plunging jet does not penetrate very deep though the forward face of the wave. The water from the splash-up is shown to come partly from the plunging crest and partly from the forward face of the wave, but always originates from the plunging jet.

The air entrainment has been shown to be very well described by the numerical methods. We illustrated the occurrence of large counter- and co-rotative gas pockets, entrained in the water during the breaking process. Their behavior and their importance in the flow has been presented. Moreover, we presented the importance of taking a turbulent viscosity into account.

The air entrainment in the water is the main process responsible for a large amount of energy to be dissipated during the breaking of a wave. We found that the maximum of the total pre-breaking wave energy is dissipated during the splash-ups occurrence, an average value of 40% of the total pre-breaking wave energy being estimated from the numerical results. This value has been shown to be greater in the case of a three-dimensional configuration.

It has also been shown that some great discrepancies can appear between two- and three-dimensional results. We also illustrated the importance of taking a turbulence model into account.

However, some points would need some more clarifications. The effect of the air on the general flow motion could be investigated thanks to some simulations without taking the air into account and compared to the results presented in this section. The influence of the boundary conditions has not been the subject of any numerical tests, but would be of great interest, especially in the three-dimensional configurations. The next step would be to study the effect of the size of our computational domain in the y-direction. A good care has to be taken to ensure that enough room is left to let any three-dimensional structures develop without being constrained by an artificial box effect. We could also vary the long-shore perturbation in order to investigate its influence on the flow. The flow induced in the air can also be investigated more in details. We should also perform some numerical tests to show the effect of the surface tension in the whole process of air entrainment.

Conclusion

Bilan des résultats

L'objectif de cette thèse est centré sur l'étude du déferlement plongeant des vagues par la simulation numérique des grandes échelles. Il apparaît dans ce travail deux contributions distinctes : l'implémentation des modèles de turbulence au sein d'un outil numérique adapté à cette étude et l'analyse physique des résultats numériques pour valider et améliorer la connaissance du phénomène.

Sur le plan numérique, une méthode originale du Lagrangien Augmenté pour la simulation numérique d'écoulements à plusieurs phases a été testé et validé grâce au cas d'étude du déferlement plongeant.

Le traitement de l'interface a été réalisé grâce à un schéma Lax-Wendroff TVD (Total Variation Diminishing), qui a été montré comme étant capable de décrire avec précision les problèmes de connexions et déconnexions d'écoulements diphasiques tridimensionnels. Ce schéma n'avait jamais été employé auparavant pour la description du déferlement des vagues.

Des modèles de turbulence adaptatifs ont été implémentés et validés dans l'outil de simulation Aquilon, afin de pouvoir décrire correctement la turbulence au sein d'un écoulement tel que celui généré lors du déferlement d'une vague. Une étude analytique du filtrage des équations de Navier-Stokes en formulation diphasique a été détaillée.

À cheval entre la partie numérique et la partie physique, l'outil de simulation Aquilon a été montré comme étant capable de fournir des résultats avec un niveau de précision très intéressant. Différentes configurations très complexes ont été étudiées afin de pouvoir analyser très précisément le comportement des méthodes et schémas numériques. Des cas comme la rupture de barrage sur fond mouillé, des cas de propagations et d'interactions d'ondes solitaires, des cas de déferlements d'ondes solitaires sur obstacles ou sur plages inclinées ont été comparés avec succès avec des mesures expérimentales ou des résultats

numériques, tout en permettant d'identifier les limitations et les problèmes. Nous avons ainsi pu aller au-delà des simples cas de validation pour décrire précisément certains des cas d'études et montrer l'étendue des possibilités offertes par la simulation numérique de manière générale.

Sur le plan physique, l'étude a porté sur la description du problème spécifique du déferlement plongeant des vagues en deux, puis en trois dimensions. Des conditions initiales correspondant à des ondes sinusoïdales de grandes amplitudes en domaines périodiques ont été utilisées.

Le processus du retournement de l'onde ainsi que l'écoulement global ont été pleinement détaillés. Une attention toute particulière a été portée à la description du phénomène du splash-up, celui-ci ayant été montré comme jouant un rôle prépondérant dans le piégeage et l'entraînement de l'air dans l'eau et dans le processus de dissipation de l'énergie de la vague.

Il a été illustré et expliqué comment le splash-up se formait à partir de l'eau provenant de la face avant de la vague et de la lèvre éjectée lors du retournement de l'onde. Les cas étudiés ont permis non seulement d'identifier clairement ce phénomène, mais aussi de montrer que le jet plongeant pénétrait peu profondément dans la vague, la quantité de mouvement étant transmise par percussion. La face avant de la vague, agissant comme une paroi solide, provoque un rebond du jet plongeant, le splash-up étant ainsi composé tout d'abord de l'eau du jet avant de se développer sous la pression du jet impactant.

L'entraînement de l'air dans l'eau a été illustré par des images des principales structures générées lors du déferlement de la vague. Ce phénomène est responsable d'une grande partie de la dissipation de l'énergie de la vague, puisqu'il a été évalué à partir des résultats numériques, qu'environ 40% de l'énergie totale de la vague disparaissait lors du phénomène du splash-up. Ainsi, une grande partie de l'énergie de la vague est dissipée en entraînant les poches d'air et en luttant contre leur force de flottaison.

Le caractère fortement tridimensionnel de l'écoulement a été illustré en comparant différents résultats numériques de simulations tests.

Perspectives

Certaines limitations sont cependant apparues lors des analyses des résultats numériques.

La principale est la constatation de l'importance de la diffusion numérique. En effet, sur la plupart des images, cette dissipation numérique apparaît sous la forme de ce dégradé de couleur pour la fonction de présence (*color function*) servant au suivi de l'interface. Le même problème, de manière un peu plus cachée est aussi présent pour les schémas utilisés

pour la discrétisation spatiale des équations de Navier-Stokes.

Plusieurs options s'offrent alors à nous.

D'autres schémas d'ordre plus élevé ou plus adaptés à la description de la turbulence peuvent être implémentés ou utilisés. De même, des comparaisons avec des simulations employant des traitements de suivi d'interface différents pourraient être instructives.

La solution plus simple, mais plus coûteuse, d'employer une résolution de maillage plus fine peut aussi être une solution. Il a été expérimenté durant cette thèse que les progrès incessants de l'informatique permettent d'envisager des simulations toujours plus importantes en nombre de points de maillage et plus rapide en temps de calcul. Un maillage plus fin donnerait alors accès à des informations plus précises en terme de description d'interface : la simulation de poches d'air disloquées en petites bulles peut-être dans un jour proche ? Les petites échelles seraient alors mieux évaluées pour un meilleur calcul des modèles de turbulence.

Dans ce même esprit de vouloir atteindre des échelles de discrétisation spatiale plus fines, des techniques de raffinement de maillage automatique sont actuellement implémentées dans Aquilon. On peut alors, grâce à certains critères tels que le gradient de la fonction de présence ou la vorticité, suivre plus finement uniquement certaines régions du domaine numérique en raffinant et déraffinant le maillage. Ces méthodes restent assez difficiles à mettre en œuvre, mais sont tout de même une piste à envisager.

Le code numérique Aquilon est actuellement développé dans sa version parallèle, avec la possibilité de diviser la domaine numérique en plusieurs bloc de discrétisation. Les temps de simulation pourraient ainsi être fortement diminués, mais, surtout, le principal avantage de ces techniques est pouvoir utiliser des maillages très importants.

De nombreux cas traités dans ce document sont encore en cours d'étude, tel que le déferlement d'ondes solitaires en comparaison avec des résultats expérimentaux. Certains cas de validation sont très originaux. En effet, les cas d'interactions d'une onde solitaire avec une paroi ou d'ondes solitaire rencontrant une autre onde solitaire n'ont jamais été traités aussi en détail avec un outil de simulation basé sur les équations de Navier-Stokes. Il serait donc très intéressant d'aller plus loin dans cette direction. De plus, une étude plus approfondies de déferlement d'ondes sinusoïdales instables en trois dimensions, avec des maillages plus fins, seraient nécessaires afin de visualiser plus clairement les structures entraînées dans l'eau ou de mieux décrire les mécanismes de dissipation de l'énergie. Toutes les amélioration citées permettraient de pallier à nos limitations dans la description de la turbulence ou l'entraînement de l'air dans l'eau, ou l'étude en trois dimensions de cas réels de déferlement d'ondes sur plages inclinées.

L'application de tout ce travail à l'étude de la mise en suspension et au transport du sédiment est prévue. De plus, des cas d'impact de vagues sur des structures seront testés afin de valider les potentialités de l'outil de simulation Aquilon pour des cas d'étude réels, tels que des digues, des récifs plus ou moins immergés ou des digues. Le passage à des configurations plus réalistes de déferlements de train de houles régulières sur plages inclinées a déjà fait l'objet de tests aux résultats prometteurs, mais n'a pas été présenté dans ce document afin de lui conserver son homogénéité.

De plus, une étude plus systématique de certains aspects du déferlement plongeant sera à compléter, tel que le splash-up et la dissipation d'énergie.

Enfin, le cas du déferlement déversant sera prochainement abordé. La complexité de ce cas en fait un défi très intéressant à relever: sa nature très fortement turbulente, tout en étant organisée, cette grande quantité de mélange d'air et d'eau se propageant, etc. Il reste encore beaucoup de choses à expliquer et à décrire, mais une étude préliminaire telle que celle qui a été réalisée dans ce document est une étape importante vers ce cas plus difficile et motivant.

Appendix A

The adaptative augmented Lagrangian method

An adaptative augmented Lagrangian method for three-dimensional multi-material flows [1]

Stéphane Vincent, Jean-Paul Caltagirone, Pierre Lubin, Tseheno Nirina Randrianarivelo

A.1 Introduction

The direct numerical simulation of incompressible multi-material flows, in the sense of free surface or fluid/particle motions, is subjected to two fundamental constraints: the incompressibility which must be verified to an almost computer error and, at the same time, the momentum conservation which is solved with discontinuous densities and viscosities, through the interface between the different media. Two approaches are currently found in literature to solve these problems. On the one hand, only one medium is discretized thanks to a curvilinear or an unstructured grid which is adapted in time and space to the Lagrangian evolutions of the interface (Magnaudet et al., 1995). The fluid dynamics are solved thanks to the Navier-Stokes equations in the considered fluid with standard projection methods (Goda, 1978). These methods are very accurate to take into account the forces acting on the interface. However, they become difficult to implement in three dimensions and are very time consuming. Moreover, they cannot handle merging or tearing

[1] The following section is taken from the pre-print version of the work which has been published by Vincent et al. (2004). I truly thank my co-authors for authorizing me to use their material in this report to keep the text's integrity and comprehensibility.

of interfaces. On the other hand, the discontinuous multi-material medium can be merged into a global structured grid (Eulerian approach). A Volume Of Fluid (VOF) function (Hirt and Nichols, 1981) allows to locate the materials and the evolutions of the physical characteristics are solved according to an advection equation on the VOF function. The challenge in this approach is to solve the Navier-Stokes equations in their multi-material formulation (Scardovelli and Zaleski, 1999) in the presence of discontinuous densities and viscosities. The Eulerian approach has been widely used over the last 10 years for its easy programming in three dimensions and its potential application to interface distortion or rupture.

Our motivation is to study three dimensional, unsteady incompressible multi-material flows such as the wave breaking on a beach, the flow induced by a solid particle falling into a cylindrical tube or the interaction between a liquid film and a turbulent gaseous jet. All these problems induce strong variations of the topology and position of the interface, and consequently of the physical characteristics of the flow. We have chosen to use an Eulerian approach for its wide adaptability to various geometries and interface conditions. The aim of this article is to present an original numerical solver dedicated to the Navier-Stokes equations in their single fluid formulation. Let $\mathbf{u}$ be the velocity field, C the volume of fluid function, p the pressure, $\mathbf{g}$ the gravity vector, t the time, σ the surface tension coefficient, k the average curvature of interface, $\mathbf{n}_i$ its normal, δ_i a Dirac function indicating interface Σ, ρ the density and μ the dynamic viscosity. If Ω is the physical domain, Ω_0 and Ω_1 the subdomains corresponding to media 0 and 1 (see figure A.1), Γ the limit of Ω and $\mathbf{n}$ the unit normal to Γ, the conservation equation system reads:

$$\nabla \cdot \mathbf{u} = 0 \text{ in } \Omega \tag{A.1}$$

$$\begin{aligned} \rho \left(\tfrac{\partial \mathbf{u}}{\partial t} + (\mathbf{u} \cdot \nabla)\mathbf{u} \right) &= \rho \mathbf{g} - \nabla p \\ &+ \nabla \cdot [\mu(\nabla \mathbf{u} + \nabla^T \mathbf{u})] + \sigma k \mathbf{n}_i \delta_i \text{ in } \Omega \end{aligned} \tag{A.2}$$

$$\frac{\partial C}{\partial t} + \mathbf{u} \cdot \nabla C = 0 \text{ in } \Omega \tag{A.3}$$

$$\begin{cases} \rho = \rho_0 \text{ and } \mu = \mu_0 \text{ if } C \geq 0.5 \\ \rho = \rho_1 \text{ and } \mu = \mu_1 \text{ else} \end{cases} \tag{A.4}$$

$$\mathbf{u} = 0 \text{ or } \frac{\partial \mathbf{u}}{\partial \mathbf{n}} = 0 \text{ on } \Gamma \tag{A.5}$$

where ρ_0, ρ_1, μ_0 and μ_1 are the densities and the viscosities in the media Ω_0 and Ω_1 respectively. The advection equation (A.3) on C can be discretized by classical VOF algorithms such as Piecewise Linear Interface Construction (Youngs, 1982) or Total Variation Diminishing TVD schemes (Vincent and Caltagirone, 1999).

The approximation of the Navier-Stokes equations (A.1-A.2) is difficult, due to the velocity-pressure coupling and the incompressibility constraint. Historically, a first idea has been proposed by Uzawa (1958) and applied, later on, for numerical computations based on spectral and finite element methods. Applied in 3D orthogonal geometries, such a method cannot be considered as optimal from the viewpoint of the computational complexity. With this difficulty, the time splitting strategy offers a convenient practical method for realistic modelling of fluid problems (complex geometries, direct numerical simulations of turbulence, ...etc). Here, the uncoupling between velocity and pressure is intrinsically related to the time scheme chosen for the Navier-Stokes problem. Nevertheless, this scheme suffers from some fundamental difficulties, namely consistency, global stability, easiness to the extension to high temporal orders and physically relevant determination of the pressure field. Since the introduction of the concept of projection methods by Chorin (1968) and Temam (1964) in the late 60's, there has been a lot of work devoted to the implementation of various versions of these techniques (Goda, 1978; Kan, 1986; Guermond, 1998). The projection approach is based on a time-marching algorithm with two sub-steps which require to solve a predicted non-divergence free velocity field, thanks to an explicit pressure and to correct these unknown variables to ensure mass balance. Second order formulation of the projection method can be dealt with by leading, for example, an algebraic analysis of the projection step (Quarteroni et al., 2000). Based on the time splitting approach, an alternative formulation has been proposed by Caltagirone and Breil (1999) to solve the Navier-Stokes equations. It consists in adding a vectorial projection step to an augmented Lagrangian method introduced by Fortin and Glowinski (1982). The projection step suggests to estimate a velocity correction by solving a differential operator, coupling all the velocity components.

For the sake of simplicity, the present article is based on a standard time splitting method (Goda, 1978) even if it can be generalized to all the previously cited works. The predictor/corrector steps involve the following splitting of unknown variables:

$$\begin{cases} \mathbf{u}^{n+1} = \mathbf{u}^* + \mathbf{u}' \\ p^{n+1} = p^* + p' \end{cases} \tag{A.6}$$

where $\mathbf{u}^*$ and p^* are predictor solutions of velocity and pressure, $\mathbf{u}'$ and p' the corrector solutions and n the time discretization subscripts related to time $t = n\Delta t$. Following the work of Scardovelli and Zaleski (1999) for example, the projection approaches are proofed to be restricted to moderate density gradient problems (ρ_1/ρ_0 less than several hundreds) because they need a Poisson equation to be solved in the corrector step, whose conditioning depends on the inverse of the density. Moreover, scalar projection methods are restricted to Dirichlet boundary conditions leading to Neumann conditions on the pressure (Peyret and Taylor, 1983). The previous drawbacks can be avoided using a vectorial projection method (Caltagirone and Breil, 1999) which acts directly on the velocity field and does not depend on the physical characteristics of the problem nor on the boundary conditions. This approach has been implemented in this work to solve 2D and 3D multi-material flows.

However, the key point is to approximate a prediction solution $(\mathbf{u}^*, p^*)$ of the velocity verifying the boundary conditions, the inertial, viscous or gravity forces as well as the divergence free constraint with a low as possible residual. Indeed, the corrector step only ensures mass conservation, but it does not improve the other physical meanings of the numerical solution. For these reasons, this article is focused on the numerical solving of the prediction step $(\mathbf{u}^*, p^*)$ by optimization or augmented Lagrangian methods (Fortin and Glowinski, 1982). We chose these approaches as they implicitly deal with both the conservation equations and the constraints at the same time. Referring to previous works concerning penalty methods (Carey and Krishman, 1987; Bernardi et al., 2002) and augmented Lagrangian (Fortin and Glowinski, 1982), the penalty parameter is often difficult to estimate for constant density incompressible flows. Based on our numerical experiments, we have observed the need to have a variable penalty parameter in space and time to optimize the numerical solving and the physical meaning of the numerical solution $(\mathbf{u}^*, p^*)$. The previous remarks are emphasized by multiphase flow problems. Our main contribution is to formulate a dynamic a priori estimate of the penalization parameter, adaptative in time and space, based on the physical characteristics of the studied flow. Several stiff numerical experiments are presented to demonstrate the efficiency and interest of the adaptative augmented Lagrangian.

Our article is structured in four parts. After the introduction, the second section is devoted to the presentation of an original method for the prediction step of the motion

equations, based on optimization techniques requiring the determination of a velocity-pressure saddle point. The third section illustrates the ability of the direct numerical simulation on several two and three-dimensional problems. Concluding remarks are given in the last section.

A.2 Uzawa algorithms for predictor velocity fields

A Finite-Volume method on a staggered mesh (MAC, (Harlow and Welsh, 1995)) is implemented to discretize the Navier-Stokes equations through a second-order Euler scheme, or GEAR scheme, on the time derivatives, while a second order Hybrid Centered scheme (Patankar, 1990) is devoted to the non-linear convective term and a second order centered scheme is chosen for the approximation of the viscous and the augmented Lagrangian terms. The boundary conditions (BC) are imposed thanks to implicit penalty terms added to the Navier-Stokes equations (Vincent and Caltagirone, 2000):

$$\left\{ \begin{array}{rl} \rho \left(\dfrac{\partial \mathbf{u}}{\partial t} + (\mathbf{u} \cdot \nabla)\mathbf{u} \right) & = \rho \mathbf{g} - \nabla p \ + \nabla \cdot [\mu(\nabla \mathbf{u} + \nabla^T \mathbf{u})] + \sigma k \mathbf{n}_i \delta_i \\ \dfrac{\partial \mathbf{u}}{\partial \mathbf{n}} & = \mathbf{B}_\mathbf{u}(\mathbf{u} - \mathbf{u}_\infty) \end{array} \right. \tag{A.7}$$

where $\mathbf{B}_\mathbf{u}$ is a diagonal matrix. For $B_{ii} = 0$, Neuman BC are modelled while Dirichlet BC are obtained choosing $B_{ii} = +\infty$.

Following the work of Goda (1978) on time splitting schemes, the predictor velocity field is calculated by standard time discretizations:

$$\left\{ \begin{array}{rl} \rho \left(\dfrac{\mathbf{u}^* - \mathbf{u}^n}{\Delta t} + (\mathbf{u}^n \cdot \nabla)\mathbf{u}^n \right) & = \rho \mathbf{g} - \nabla p^n + \nabla \cdot [\mu(\nabla \mathbf{u}^n + \nabla^T \mathbf{u}^n)] + \sigma k \mathbf{n}_i \delta_i \\ p^* & = p^n \end{array} \right. \tag{A.8}$$

for the explicit version and

$$\left\{ \begin{array}{rl} \rho \left(\dfrac{\mathbf{u}^* - \mathbf{u}^n}{\Delta t} + (\mathbf{u}^n \cdot \nabla)\mathbf{u}^* \right) & = \rho \mathbf{g} - \nabla p^n + \nabla \cdot [\mu(\nabla \mathbf{u}^* + \nabla^T \mathbf{u}^*)] + \sigma k \mathbf{n}_i \delta_i \\ p^* & = p^n \end{array} \right. \tag{A.9}$$

for the implicit one, the linear system being solved for example by the iterative technique described in section (A.2.3).

The explicit discretization is generally discarded, even for unsteady flows, because it is very restricting with respect to Δt. The implicit version is unconditionally stable but the higher the time step, the longer the convergence of the iterative solver is. Moreover, the incompressibility constraint is not solved in this predictor algorithm, which can lead to poor precision solutions in strong density or viscosity ratio problems. In this section, we present an implicit predictor step based on the optimization augmented Lagrangian algorithm. The main originality consists in adding a control, or penalty, term in the Navier-Stokes equations, which uses an adaptative Lagrangian parameter in time and space. No stability criterion is needed and the predicted solution satisfies the Navier-Stokes equations, the boundary conditions, as well as the divergence free property, with a maximum error lower than the errors obtained with Goda's method (A.8-A.9). The behavior of both Goda's and augmented Lagrangian methods for the calculation of $\mathbf{u}^*$ are illustrated and commented in section (A.3).

A.2.1 Standard augmented Lagrangian (SAL)

The standard augmented Lagrangian method was first introduced by Fortin and Glowinski (1982). It consists in solving an optimization problem by solving a velocity-pressure saddle point with an Uzawa algorithm (Uzawa, 1958). Starting with $\mathbf{u}^{*,0} = \mathbf{u}^n$ and $p^{*,0} = p^n$, the predictor solution reads:

$$\text{while } ||\nabla \cdot \mathbf{u}^{*,\mathbf{m}}|| > \epsilon,$$

$$\text{solve} \begin{cases} (\mathbf{u}^{*,0}, p^{*,0}) = (\mathbf{u}^n, p^n) \\ \\ \rho \left(\dfrac{\mathbf{u}^{*,m} - \mathbf{u}^{*,0}}{\Delta t} + \mathbf{u}^{*,m-1} \cdot \nabla \mathbf{u}^{*,m} \right) - r \nabla (\nabla \cdot \mathbf{u}^{*,m}) \\ = -\nabla p^{*,0} + \rho \mathbf{g} + \nabla \cdot [\mu (\nabla \mathbf{u}^{*,m} + \nabla^T \mathbf{u}^{*,m})] + \sigma k \mathbf{n}_i \delta_i \\ \\ p^{*,m} = p^{*,0} - r \nabla \cdot \mathbf{u}^{*,m} \end{cases} \tag{A.10}$$

where r is a numerical parameter used to impose the incompressibility constraint, m is an iterative convergence index and ϵ a numerical threshold controlling the constraint. Usually, a constant value of r is used. From numerical experiments, optimal values are found to be of the order of ρ_i and μ_i to accurately solve the motion equations in the related zone (Vincent and Caltagirone, 2000). The momentum, as well as the continuity equations are accurately described by the predictor solution $(\mathbf{u}^*, p^*)$ coming from (A.10)

in the medium, where the value of r is adapted. However, high values of r in the other zones act as penalty terms inducing the numerical solution to satisfy only the divergence free property. Indeed, if we consider for example $\frac{\rho_1}{\rho_0} = 1000$ (characteristic of water and air problems) and a constant $r = \rho_1$ to impose the divergence free property in the denser fluid, the asymptotic equation system solved in the the predictor step is:

$$\begin{cases} \rho\left(\dfrac{\mathbf{u}^* - \mathbf{u}^n}{\Delta t} + (\mathbf{u}^n \cdot \nabla)\mathbf{u}^*\right) - r\nabla(\nabla \cdot \mathbf{u}^*) \\ = \rho\mathbf{g} - \nabla p^n + \nabla \cdot [\mu(\nabla\mathbf{u}^* + \nabla^T\mathbf{u}^*)] + \sigma k\mathbf{n}_i\delta_i \text{ in } \Omega_1 \\ \\ \dfrac{\mathbf{u}^* - \mathbf{u}^n}{\Delta t} - r\nabla(\nabla \cdot \mathbf{u}^*) = 0 \text{ in } \Omega_0 \end{cases} \tag{A.11}$$

Our idea is to locally estimate the augmented Lagrangian parameter in order to obtain satisfactory equivalent models and solutions in all the media.

A.2.2 Adaptative augmented Lagrangian (AAL)

Instead of choosing an empirical constant value of r fixed at the beginning of the simulations, we propose at each time step to locally estimate the augmented Lagrangian parameter r. Then, $r(t, M)$ becomes a function of time t and space position M. It must be two to three orders of magnitude higher than the most important term in the conservation equations.

Let L_0, t_0, u_0, C_0 and p_0 be reference space length, time, velocity, volume fraction and pressure respectively. If we consider one iterative step of the augmented Lagrangian procedure (A.10), the non-dimensional form of the momentum equations can be rewritten as:

$$\begin{aligned} &\rho\frac{u_0}{t_0}\frac{\mathbf{u}^{*,m} - \mathbf{u}^n}{\Delta t} + \rho\frac{u_0^2}{L_0}(\mathbf{u}^{*,m-1} \cdot \nabla)\mathbf{u}^{*,m} - r\frac{u_0}{L_0^2}\nabla(\nabla \cdot \mathbf{u}^{*,m}) \\ &= \rho\mathbf{g} - \frac{p_0}{L_0}\nabla p^n + \frac{u_0}{L_0^2}\nabla \cdot [\mu(\nabla\mathbf{u}^{*,\mathbf{m}} + \nabla^T\mathbf{u}^{*,m})] + \frac{\sigma}{L_0^2}k\mathbf{n}_i\delta_i \end{aligned} \tag{A.12}$$

Multiplying the right and left parts of equation (A.12) by $\frac{L_0^2}{u_0}$, we can compare the augmented Lagrangian parameter to all the contributions of the flow (inertia, gravity, pressure and viscosity). We obtain:

$$\begin{aligned}&\rho\frac{L_0^2}{t_0}\frac{\mathbf{u}^{*,m}-\mathbf{u}^n}{\Delta t}+\rho u_0 L_0(\mathbf{u}^{*,m-1}\cdot\nabla)\mathbf{u}^{*,m}-r\nabla(\nabla\cdot\mathbf{u}^{*,m})\\&=\rho\frac{L_0^2}{u_0}\mathbf{g}-\frac{p_0L_0}{u_0}\nabla p^n+\nabla\cdot[\mu(\nabla\mathbf{u}^{*,m}+\nabla^T\mathbf{u}^{*,m})]+\frac{\sigma}{u_0}k\mathbf{n}_i\delta_i\end{aligned}\tag{A.13}$$

It can be noticed that r is comparable to a viscosity coefficient. It is then defined as:

$$\begin{gathered}r(t,M)=Kmax\left(\rho(t,M)\tfrac{L_0^2}{t_0},\rho(t,M)u_0L_0,\rho(t,M)\tfrac{L_0^2}{u_0}g,\tfrac{p_0L_0}{u_0},\mu(t,M),\tfrac{\sigma}{u_0}\right)\\10<K<1000\end{gathered}\tag{A.14}$$

If $\frac{\rho_1}{\rho_0}=1000$ and $\mu_0<\mu_1<<\rho_0<<\rho_1$ for example, the semi-discrete form of the momentum equations resulting from the new values of $r(t,M)$ given by (A.14) then becomes:

$$\left\{\begin{array}{l}\rho_1\left(\dfrac{\mathbf{u}^{*,m}-\mathbf{u}^n}{\Delta t}+(\mathbf{u}^{*,m-1}\cdot\nabla)\mathbf{u}^{*,m}\right)-r\nabla(\nabla\cdot\mathbf{u}^{*,m})\\=\rho_1\mathbf{g}-\nabla p^n+\nabla\cdot[\mu_1(\nabla\mathbf{u}^{*,m}+\nabla^T\mathbf{u}^{*,m})]+\sigma k\mathbf{n}_i\delta_i\text{ in }\Omega_1\\\text{with }r=K_1\rho_1L_0^2u_0\rho_0\left(\dfrac{\mathbf{u}^{*,m}-\mathbf{u}^n}{\Delta t}+(\mathbf{u}^{*,m-1}\cdot\nabla)\mathbf{u}^{*,m}\right)-r\nabla(\nabla\cdot\mathbf{u}^{*,m})\\=\rho_0\mathbf{g}-\nabla p^n+\nabla\cdot[\mu_0(\nabla\mathbf{u}^{*,m}+\nabla^T\mathbf{u}^{*,m})]+\sigma k\mathbf{n}_i\delta_i\text{ in }\Omega_0\text{ with }r=K_0\rho_0L_0^2u_0\end{array}\right.\tag{A.15}$$

where K_0 and K_1 are in between 10 and 1000. In this way, thanks to expression (A.13), the adaptative Lagrangian parameter is at least 10 to 1000 times the order of magnitude of the most important term between inertia, viscosity, pressure or gravity in both Ω_1 and Ω_0 domains. Compared to the SAL approach (A.11), the AAL is consistent with the expected conservation equation system (A.1-A.2). The new method (A.14) can be easily extended to other forces such as surface tension and Coriolis or specific source terms. Comparisons between standard and adaptative augmented Lagrangian (AAL) methods are presented in section (A.3). In particular, the influence of the penalty parameter on the convergence speed of the Bi-CGSTAB solver and time and space variations of $r(M)$ are discussed.

As a summary, the complete time-marching procedure of the predictor-corrector algorithm including the AAL method is the following:

$\otimes$ Step 1: defines initial values $\mathbf{u}^0$ and p^0 and boundary conditions on Γ,

$\otimes$ Step 2: knowing $\mathbf{u}^n$, p^n and a divergence threshold ϵ, estimates the predictor values $\mathbf{u}^*$ and p^* with the Uzawa algorithm (A.10) associated to the local estimate of $r(t, M)$ defined in expression (A.14), so that $\mathbf{u}^* = \mathbf{u}^{*,m}$ and $p^* = p^{*,m}$ when m verifies $||\nabla \cdot \mathbf{u}^{*,\mathbf{m}}|| < \epsilon$,

$\otimes$ Step 3: projects the solution $(\mathbf{u}^*, p^*)$ on a divergence free subspace thanks, for example, to projection approaches (Goda, 1978; Caltagirone and Breil, 1999) to get the correction solution $(\mathbf{u}', p')$. Then, the numerical solution at time $(n+1)\Delta t$ is $(\mathbf{u}^{n+1}, p^{n+1}) = (\mathbf{u}^* + \mathbf{u}', p^* + p')$,

$\otimes$ Step 4: iterates n in steps 3 and 4 until the physical time is reached.

A.2.3 Numerical solver

The use of implicit discretization for the approximation of the predictor and corrector steps in the time splitting approach, induces the determination of the inverse of a matrix. As the matrices resulting from the previous discretizations are nonsymmetric, the linear algebra problem is solved numerically with an iterative Bi-CGSTAB (Bi-Conjugate Gradient Stabilised) algorithm (Vorst, 1992), preconditioned under a Modified and Incomplete LU (MILU) algorithm of Gustafsson (1978).

A.3 Simulation of three-dimensional multi-material flows

For the treatment of incompressibility, the main advantage of augmented Lagrangian-like methods is that they lead unconditionally to solutions satisfying the constraint. However, taking constant penalization parameter r for flows with strongly varying characteristics ($\frac{\rho_1}{\rho_0} = 1000$ for example) requires high values of r with respect to ρ_1, which leads to unsatisfactory simulations in Ω_0 (see equation (A.11)). In this section, we illustrate the improvements brought by the adaptative r, calculated thanks to expression (A.14), following the example of the Laplace law, the falling of a solid particle into a tube and the unsteady sinusoidal wave breaking over a flat bottom. In all applications, the mass conservation is verified to a 10^{-3} error after the prediction step. It can be reduced to 10^{-15} by using a scalar or a vectorial projection method in all cases. Comparisons to Goda's algorithm are only performed for the Laplace law problems because the two other

test cases involve high density ratios that cannot be managed by this method.

A.3.1 The 2D Laplace law

Without gravity, an initial cylindrical drop of fluid 1, centered in a square domain full of fluid 0, represents a static fluid mechanics situation called the Laplace law. The drop radius R is the characteristic length of the problem. In this case, the stationary analytic solution is:

$$\left.\begin{array}{c} \Delta p = \dfrac{\sigma}{R} \\ \mathbf{u} = 0 \end{array}\right\} \text{ in } \Omega \tag{A.16}$$

In the momentum equations (A.2), the surface tension force can be approximated with the Continuum Surface Force (CSF) of Brackbill et al. (1992). This method is well adapted for Volume Of Fluid formulation on Eulerian grids because it does not require the exact position of interfaces. However, as shown by Vincent and Caltagirone (2004), the approximation of curvature in CSF is incomplete and it can lead to spurious parasitic currents which destroy interfaces for low Onhesorge numbers $\dfrac{\mu}{(\sigma\rho R)^{1/2}}$ (Scardovelli and Zaleski, 1999; Jamet and Brackbill, 2002). In this article, we use the Hessian Approximation of the surface tension Redistributed over an Extended Mesh (HAREM), based on the differential geometry of surfaces and on a discretization on a dual grid, proposed by Vincent and Caltagirone (2004). If $f(x,y,z) = 0$ is the implicit parametrization of interface, HAREM reads:

$$\left\{\begin{array}{c} k = \dfrac{1}{R_1} + \dfrac{1}{R_2} \\ R_i = \dfrac{\|\mathbf{n}_i\|}{Hes(\mathbf{t}_i, \mathbf{t}_i)} \\ Hes = \mathbf{t}_i^T \mathbf{H} \mathbf{t}_i \\ \mathbf{H} = \begin{bmatrix} \frac{\partial^2 f}{\partial x^2} & \frac{\partial^2 f}{\partial x \partial y} & \frac{\partial^2 f}{\partial x \partial z} \\ \frac{\partial^2 f}{\partial y \partial x} & \frac{\partial^2 f}{\partial y^2} & \frac{\partial^2 f}{\partial y \partial z} \\ \frac{\partial^2 f}{\partial z \partial x} & \frac{\partial z \partial x}{\partial z \partial y} & \frac{\partial^2 f}{\partial z^2} \end{bmatrix} \end{array}\right. \tag{A.17}$$

where $\mathbf{t}_1$ and $\mathbf{t}_2$ are a basis of the local tangent plane to the interface. As a definition, $\mathbf{t}_1 \cdot \mathbf{n}_i = 0$ and $\mathbf{t}_2 \cdot \mathbf{n}_i = 0$.

To understand the influence of the Lagrangian parameter on the numerical solution, we compare simulations of the cylindrical drop equilibrium, achieved with three different time discretizations of the Navier-Stokes equations: an implicit Uzawa prediction ($r = 0$) and a Goda projection on pressure and velocity (Goda, 1978) called **Sim1**, a standard augmented Lagrangian prediction and a vectorial projection (Caltagirone and Breil, 1999) referenced as **Sim2** and the new adaptative augmented Lagrangian prediction (A.14) and a vectorial projection named **Sim3**. Choosing $\Delta t = 10^{-3}\ s$ and a 128×128 Cartesian grid, figure (A.2) presents the results obtained for a stabilized average pressure jump in **Sim1** and **Sim2** (about 200 time iterations) and a steady state flow in **Sim3** (10 iterations). We demonstrate the appearance of parasitic currents in **Sim1** and **Sim2** with velocities of the order $10^{-6}\ m.s^{-1}$, whereas **Sim3** maintains a stabilized pressure from the first iteration onward and velocities lower than $10^{-15}\ m.s^{-1}$ for all the 10 time iterations. Comparing the numerical results to the theoretical solution (A.16) thanks to table 1, it is easily understood that solutions **Sim1** and **Sim2** are not analytical with respect to the velocity, and induce a strong error on the pressure jump (about 16 %). The adaptative augmented Lagrangian solution is exact with respect to velocity, but a 4 % error is observed on pressure. It is directly bound to the non-conformity of the cylindrical shape of the drop with the Cartesian mesh. However, we have demonstrated (Vincent and Caltagirone, 2004) that the pressure converges to the Laplace solution with first order accuracy. The same behavior is observed in three-dimensions.

A.3.2 Flow induced by a spherical particle

The problem of a solid spherical particle falling into a cylindrical tube is characteristic of liquid-solid interactions. It has been widely studied over the last forty years Happel and Brenner (1963) for its many applications in fundamental fluid mechanic and industrial researches. We assume R_p and R_t as the radii of the particle and the tube respectively. The solid media is modelled according to a penalization technique (Ritz and Caltagirone, 1999; Vincent and Caltagirone, 2001) as a fluid with specific density and viscosity ($\rho_1 = 5000\ kg.m^{-3}$ and $\mu_1 = 10^3\ Pa.s$) while the cylinder is full of a "real" fluid whose characteristics are $\rho_0 = 800\ kg.m^{-3}$ and $\mu_0 = 1\ Pa.s$. According to the Reynolds number$Re = \dfrac{2\rho_1 R_p u_s}{\mu_0}$, based on the particle parameters, which is equal to 0.73, the comparison to the Stokes theory is valid in our problem. In this configuration, we have the following theoretical results (Happel and Brenner, 1963) for the velocity:

$$u_s = \frac{2(\rho_1 - \rho 0)gR_p^2}{9\mu_0 C_w}$$
$$C_w = \frac{1 - 0.75857C_p^5}{1 - 2.105C_p + 2.0865C_p^3 + 0.72603C_p^6} \tag{A.18}$$

with $C_p = \frac{R_p}{R_t}$ the characteristic aspect ratio and $C_w = 1$ in an infinite medium.

Within the limit of the Stokes's theory $Re \to 0$, it can be demonstrated that the streamlines are symmetrical and centered at the particle center. If we examine the 3D axisymmetrical simulations on a 114×700 grid (figure A.3), we see that the solution arising from the standard augmented Lagrangian method is strongly disymmetrical with an artificial drag effect in the torque of the particle. On the contrary, the numerical simulation which uses the adaptative augmented Lagrangian approach is almost symmetrical according to the particle center. The weak dissymmetry of this solution is due to the magnitude of the Reynolds number that reaches the limit of the Stokes theory. If we have a look at the comparison between the theoretical correction parameter C_w estimated from Happel and Brenner (1963) and the one calculated numerically (figure A.4), we see that for various aspect ratios, the numerical flow induced by the spherical particle is comparable to the analytical and experimental ones. In agreement with the analysis of the asymptotic approach in power law developed by Happel and Brenner (1963), the numerical simulation diverges from the analytical solution for $\frac{R_p}{R_t} \geq 0.7$. Indeed, the terms discarded in the theoretical solution are not negligible in this case.

Even if the AAL parameter must be estimated locally at each calculation time, it induces a weak numerical overcost of about 5% in terms of computer storage and less than 1% with respect to calculation time (see table 2). Concerning the iterative Bi-CGSTAB solver presented on figure (A.5), the behavior is comparable with the SAL and the AAL methods, even if the decreasing of the residual is slightly slower with the last one. To finish with, it is observed that the space distribution of $r(M)$ is directly linked to the order of magnitude of the viscosity, so that $r(M,t) = K\mu_1$ in Ω_1 and $r(M,t) = K\mu_0$ in Ω_0. This observation is characteristic of low Reynolds numbers and Stokes flows.

A.3.3 Wave breaking in shallow water

To demonstrate the interest of the AAL method to deal with free surface flows, we study the propagation of an unstable periodic sinusoidal water wave on a flat bottom in an air

medium, as already shown in Abadie (1998) or Lubin et al. (2003a,b). All our calculations are made with the densities and the viscosities of air and water media ($\rho_a = 1.1768\ kg.m^{-3}$ and $\rho_w = 1000\ kg.m^{-3}$, $\mu_a = 1.85^{-5}\ kg.m^{-1}.s^{-1}$ and $\mu_w = 1^{-3}\ kg.m^{-1}.s^{-1}$), and $\sigma = 7.5.10^{-2}\ N.m^{-1}$. The calculation domain is periodic in the flow direction (one wavelength long), with a symmetry boundary condition in the lower and lateral limits, and a free boundary condition in the upper limit. Based on the linear theory, the reference variables of the initial incident wave are the celerity c, the period T and the wavelength L. The depth is defined by d and the waveheight is referred to as H. The flow motion is driven by the initial steepness, $\frac{H}{L}$, and the dispersion parameter, $\frac{d}{L}$, which are two dimensionless numbers respectively representative of the non linearity degree of the wave and the influence of the bottom on oscillatory movement. As already mentioned, the initial incident wave is not a steady travelling wave. The overturning motion is therefore controlled by the initial steepness and the dispersion parameter, which makes our approach interesting as we are then able to study any breaker type by only varying these two parameters. We can accurately study the breaking phenomenon in a smaller numerical domain, as it is periodical in the flow direction, compared to simulations involving a shoaling wave breaking over a sloping beach.

Three-dimensional simulations are carried out with the two-dimensional initial (x,z) solution spread in the y-direction. The x, y and z axis are the streamwise, spanwise and vertical directions respectively. As a periodic condition is imposed in the x direction of wave propagation, the wave moves out of the domain on the right side to re-enter on the left side. We choose to simulate and present a plunging breaker with $\frac{H}{L} = 0.13$ and $\frac{d}{L} = 0.17$, as shown hereafter (figures A.6 and A.7). The Reynolds number of the initial wave is $Re = \frac{\rho_w L c}{\mu_w} = 35\ 100$, corresponding to $T = 0.285\ s$, $c = 0.351\ m.s^{-1}$ and $L = 0.1\ m$. We use a regular Cartesian grid of $250 \times 100 \times 25$ points. The time step is approximately $0.1ms$. In figure (A.6), we present a picture of the three-dimensional wave breaking at $t = 0.13\ s$. The interface being chosen to be at $C = 0.5$, we show the color function for the water medium.

Using the same non-dimensional parameters, we show in figure (A.7), comparisons of the results obtained by doing the simulation with and without the AAL method. The velocity field and the free surface are presented in a (x, z) plane, parallel to the wave propagation axis. Differences can be very easily observed. The flow in the air medium is not well resolved without the AAL method. Indeed, as explained in section (A.2.1),

imposing the incompressibility through a constant Lagrangian parameter induces incorrect behavior of the air medium which acts as a solid wall and resists against the plunging jet. Moreover, it creates flow instabilities near the interface that propagate in the gas. Local artificial accelerations can be observed in this medium and therefore, the whole simulation suffers from these numerical drawbacks. On the contrary, using the AAL methods, the velocity field is well balanced in both phases and respects the descriptions of Peregrine (1983). During the ejection and the impact of the jet, the shape of the free surface looks like a tongue of water as generally observed in (Bonmarin, 1989) or (Miller, 1976), whereas strong spurious interface deformations appear with a constant r. A comprehensive representation of time and space variations of $r(M)$ are proposed on figure (A.8). In this problem, the inertial effects are predominant which lead to strong disparities of r in the water. The same type of variations could be observed in air if the scale range was adapted near value 1.

A.4 Conclusions

An augmented Lagrangian method is proposed for the numerical simulation of multi-material flows. The originality of the method is an adaptative estimate of the augmented Lagrangian parameter r according to the dimensionless form of the Navier-Stokes equations. by means of several examples, we have demonstrated that a good choice of r is necessary for multi-material flows, to avoid parasitic currents and worsen fluid and interface behavior. The adaptative augmented Lagrangian method can be interpreted as a penalty method for the numerical treatment of incompressibility. Future work will be devoted to the extension of this approach to other constraints, such as shearing, compressibility or elasticity in solids. The idea is to build a general model on a fixed grid for fluid-solid interactions and liquid-vapor phase change.

A.5 Acknowledgements

We acknowledge the reviewers for their fruitful remarks and helpful suggestions that guide us in improving this article. The authors thank M. Azaiez for his critical reading and interesting discussions on time splitting methods.

A.6 Tables and figures

Numerical method	Pressure jump (Pa)	Maximum velocity ($m.s^{-1}$)
Sim1	1.16	10^{-6}
Sim2	1.16	10^{-6}
Sim3	0.96	10^{-16}
Laplace law	1	0

Table 1: pressure jump and maximum velocity for the Laplace law.

Numerical method	Grid	Memory (Mo)	Computer time (s)
SAL	175 x 28	8.15	3.48210^2
SAL	350 x 57	23.3	1.51010^3
SAL	700 x 114	95.0	6.00510^3
AAL	175 x 28	8.2	3.66810^2
AAL	350 x 57	23.4	1.62110^3
AAL	700 x 114	95.7	6.41610^3

Table 2: Memory and time costs induced by the SAL and AAL methods for the numerical simulation of particle settling.

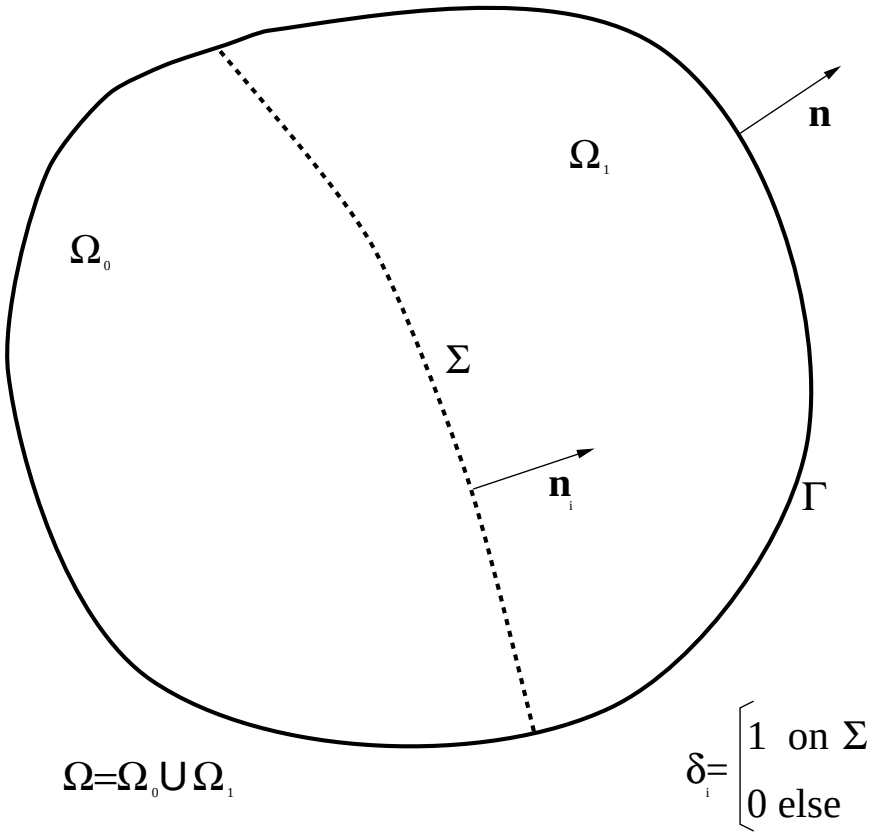

Figure A.1: Definition of the physical space.

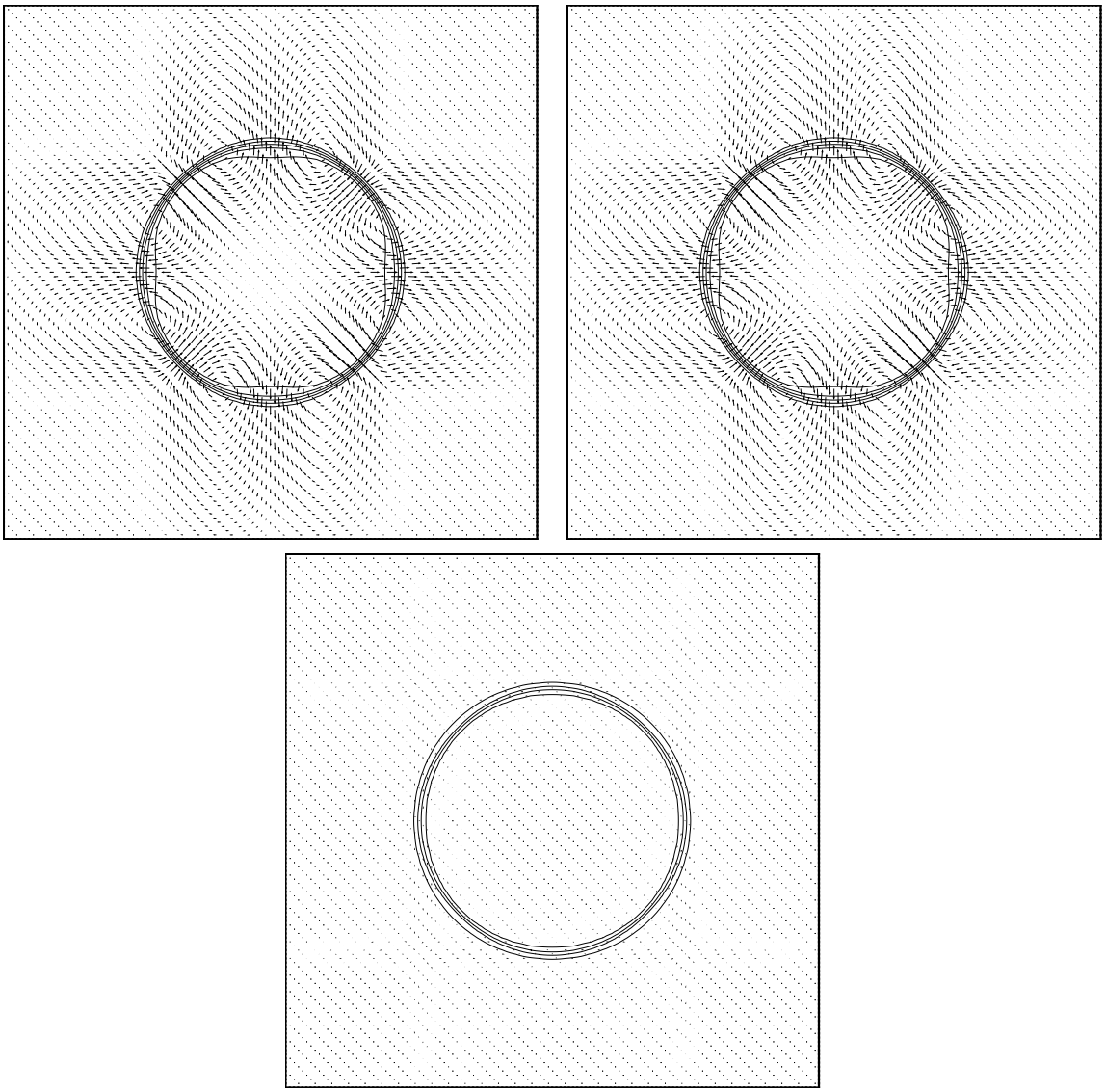

Figure A.2: Direct numerical simulation of spherical droplet equilibrium - $\frac{\rho_1}{\rho_0} = 1000$, $R = 0.25m$ and $\sigma = 0.25N.m^{-1}$ - **Sim1**, **Sim2** and **Sim3** are plotted from left to right and top to bottom - Velocity profiles (1 vector over 4) and pressure isolines are presented with the same magnitude scales.

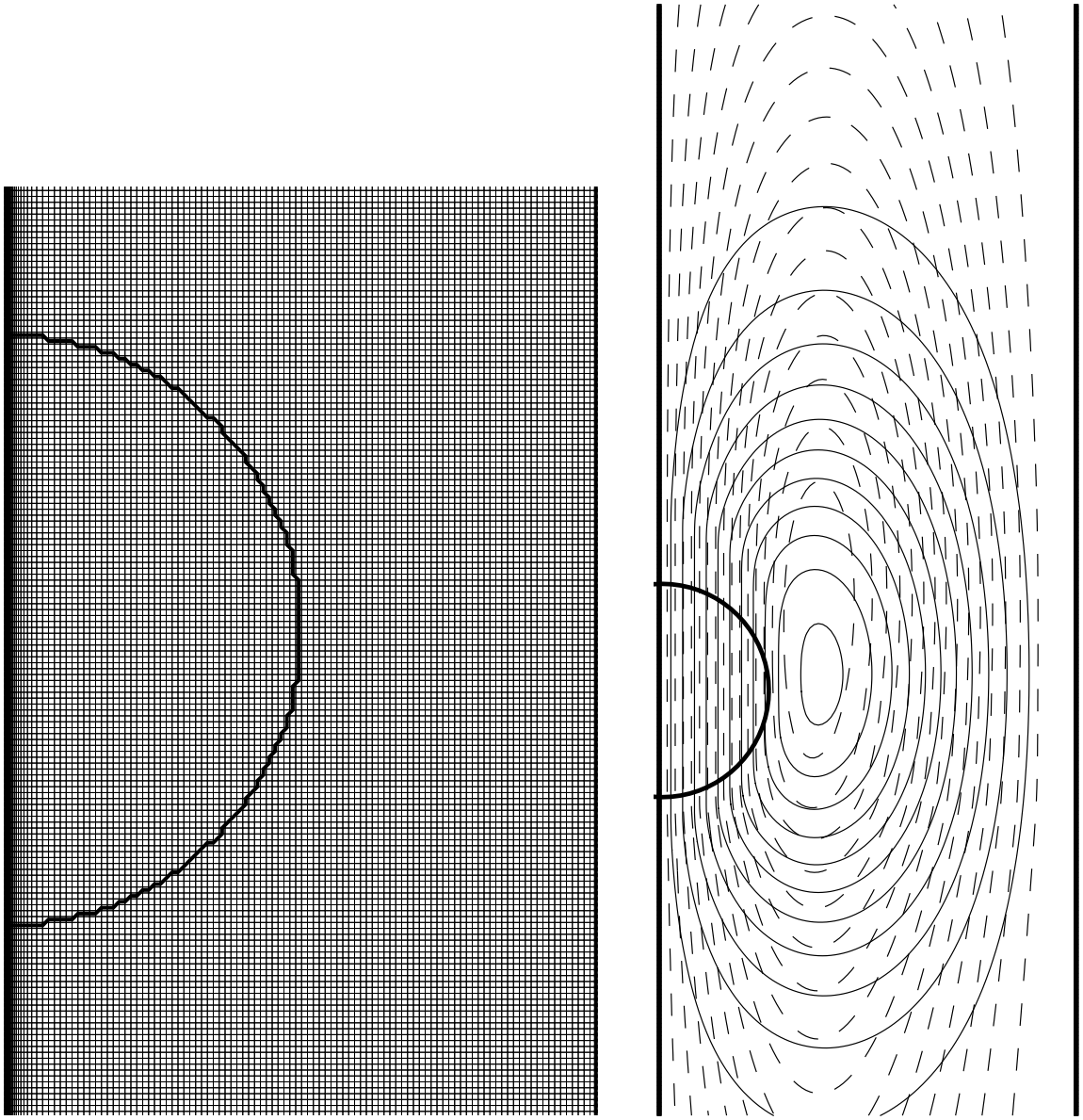

Figure A.3: Direct numerical simulation of spherical particle in a cylindrical vein - $\frac{\rho_1}{\rho_0} = 6.25$, $Re = 0.73$, $R_p = 0.002m$ and $R_t = 0.008m$ - Left: initial particle shape and grid - Right: particle shape and streamlines (adaptative augmented Lagrangian in solid lines and standard augmented Lagrangian in dashed lines) - Simulations are implemented on a 3D axisymetrical 114 x 700 irregular grid.

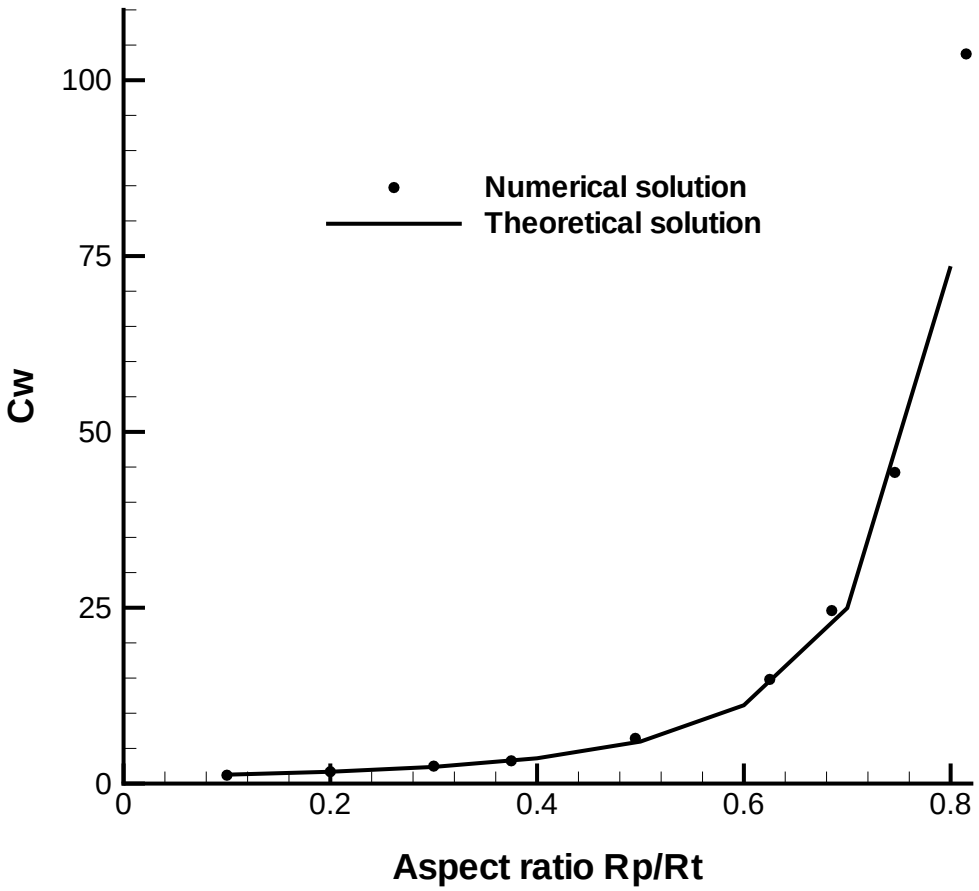

Figure A.4: Correction coefficients for the Stokes velocity - Comparison between theoretical and numerical solutions for various aspect ratios $\frac{R_p}{R_t}$.

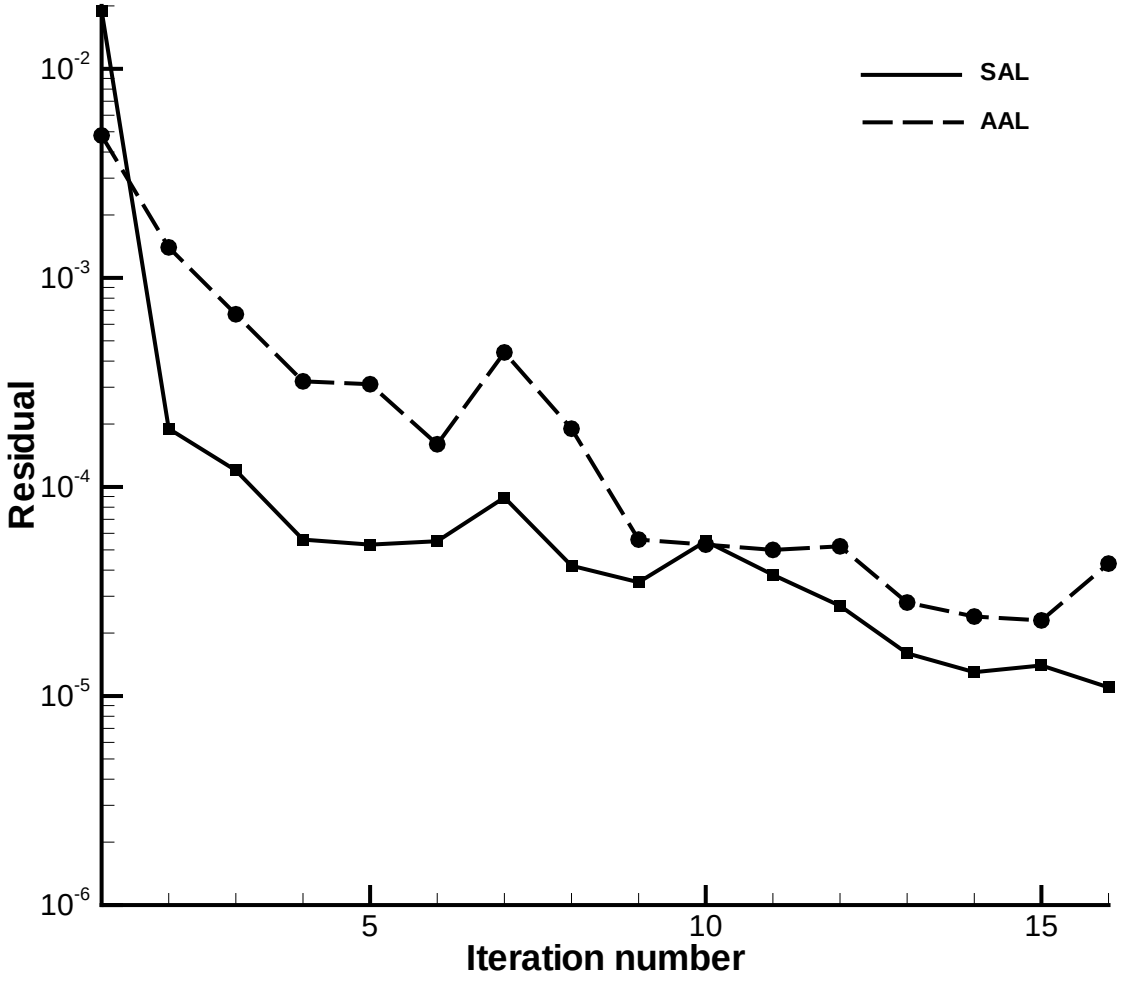

Figure A.5: Effects of the SAL and AAL methods on the behavior of the Bi-CGSTAB solver.

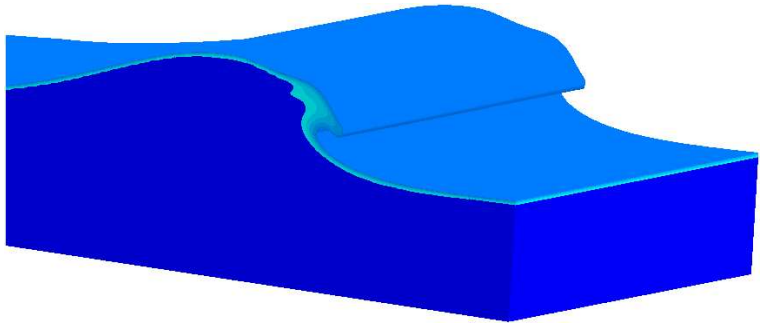

Figure A.6: Direct numerical simulation of wave breaking - 3D free-surface before impact of the plunging jet at $t = 0.13s$ - $\frac{H}{L} = 0.13$ and $\frac{d}{L} = 0.17$.

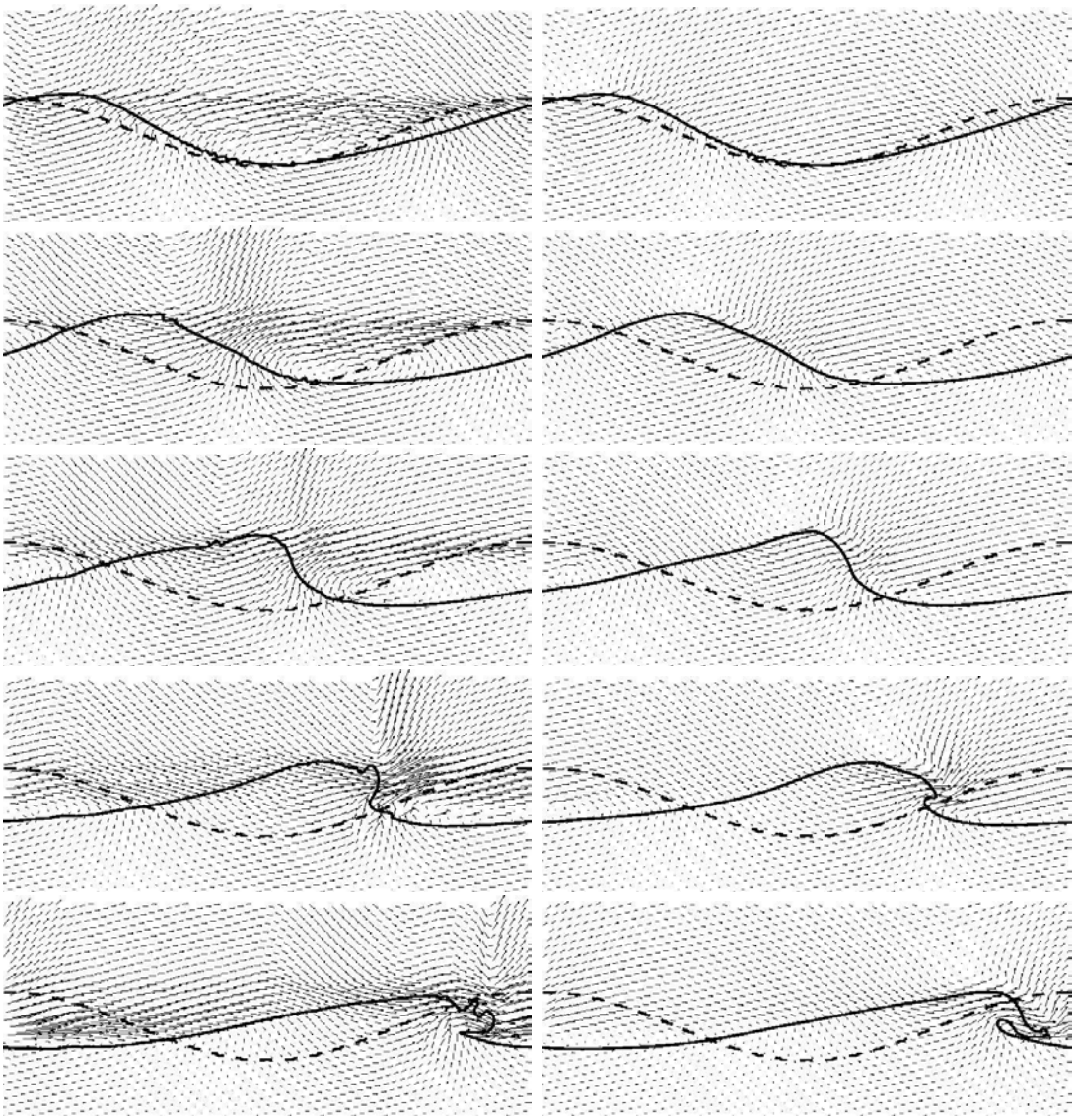

Figure A.7: Direct numerical simulation of wave breaking - standard augmented Lagrangian method (left column) and adaptative one (right column) at time $t = 0.018$, $t = 0.056$, $t = 0.09$, $t = 0.13$ and $t = 0.17$ s - Velocity profiles (1 vector over 15), free surface (solid line) and initial condition (dashed line) are plotted - $\frac{H}{L} = 0.13$ and $\frac{d}{L} = 0.17$.

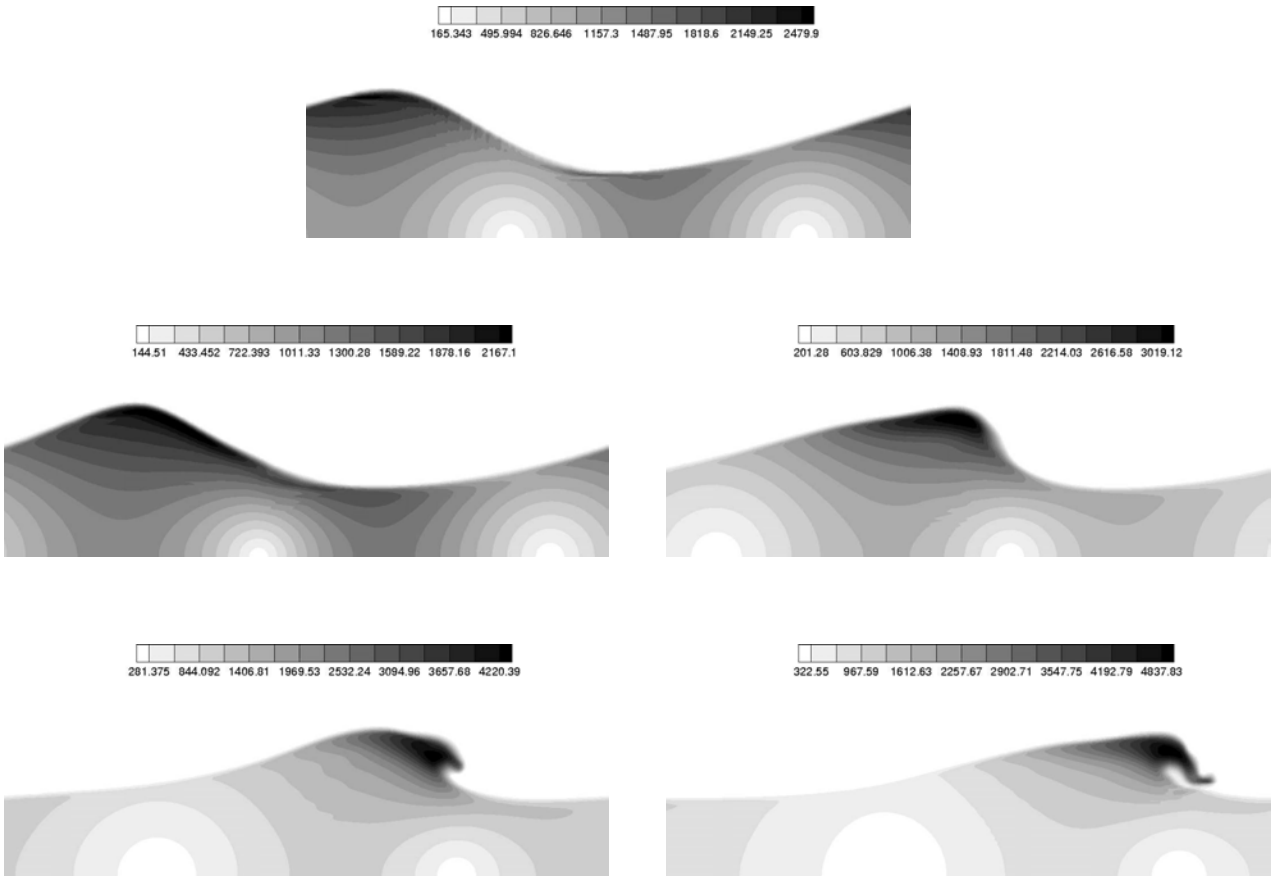

Figure A.8: Order of magnitude and space variations of $r(M)$ for the wave breaking problem at time t=0.018 s, t=0.056 s, t=0.09 s, t=0.13 s and t=0.17 s - $\frac{H}{L} = 0.13$ and $\frac{d}{L} = 0.17$.

Appendix B

Analytical solution of the two-phase Poiseuille flow

We consider the two-dimensional laminar flow of two incompressible non-miscible viscous fluids between two fixed parallel walls, which length is called L (m) and the separation distance H (m). The two fluids will be referred to as fluid 1 and 2. The motion is driven by a pressure gradient (Eq. B.1):

$$\frac{\partial p}{\partial x} = \frac{p_d - p_g}{L} = \Delta p \tag{B.1}$$

in the longitudinal X direction. The governing equations system (see section 2.4) now then reads (Eqs. B.2):

$$\begin{cases} \dfrac{\partial u_x}{\partial t} = 0 \\ \\ \dfrac{\partial u_x}{\partial t} = -\dfrac{1}{\rho}\dfrac{\partial p}{\partial x} + \dfrac{1}{\rho}\nabla \cdot \left[\mu(\dfrac{\partial u_x}{\partial x} + \dfrac{\partial u_x}{\partial y})\right] \\ \\ \dfrac{\partial p}{\partial y} = 0 \end{cases} \tag{B.2}$$

According to the system of equations (B.2), we have $u(u_x, 0, 0) = (u_x(y,t), 0, 0)$ and $p = p\,(x,t)$. The resulting velocity field has thus only one cartesian component along the same direction.

Moreover, if we consider a stationary flow condition, we then have the following equation (B.3), which is valid for both fluids:

$$\frac{\partial p}{\partial x} = \frac{\partial}{\partial y}\left[\mu \frac{\partial u_x}{\partial y}\right] \tag{B.3}$$

After integration of equation (B.3), we have (Eq. B.4):

$$\begin{cases} u_{x,1}(y) = \dfrac{\Delta p}{2\mu_1} y^2 + C_1 y + C_1^{'} \\ \\ u_{x,2}(y) = \dfrac{\Delta p}{2\mu_2} y^2 + C_2 y + C_2^{'} \end{cases} \tag{B.4}$$

where $u_{x,1}$ and $u_{x,2}$ are the respective longitudinal cartesian velocity components of each fluid 1 and 2, and C_1, $C_1^{'}$, C_2 and $C_2^{'}$ being constants obtained during the integration.

If we add no-slip conditions at the walls (Eqs. B.5 and B.6),

$$u_{x,1} = 0 \text{ at } y = 0 \tag{B.5}$$

$$u_{x,2} = 0 \text{ at } y = H \tag{B.6}$$

and jump relations at the interface between both fluids (Eqs. B.7 and B.8),

$$[u_x] = u_{x,2} - u_{x,1} = 0 \text{ at fluid}_1\text{/ fluid}_2 \tag{B.7}$$

$$\left[\mu \frac{\partial u_x}{\partial x}\right] = \mu_2 \frac{\partial u_{x,2}}{\partial x} - \mu_1 \frac{\partial u_{x,1}}{\partial x} = 0 \text{ at fluid}_1\text{/fluid}_2 \tag{B.8}$$

it is then possible to find an analytical solution for the pressure and velocity fields for this two-dimensional two-phase Poiseuille flow (Eqs. B.3, B.5, B.6, B.7 and B.8). To do so, we must determine the constants C_1, $C_1^{'}$, C_2 and $C_2^{'}$ thanks to equations (B.4, and B.5, B.6, B.7 and B.8).

We can re-write the system of equations (B.4) by using equation (B.8), as (Eq. B.9):

$$\begin{cases} \mu_1 \dfrac{\partial u_{x,1}}{\partial y} = \mu_1 \left(\dfrac{1}{\mu_1} \Delta p y + C_1 \right) \\ \\ \mu_2 \dfrac{\partial u_{x,2}}{\partial y} = \mu_2 \left(\dfrac{1}{\mu_2} \Delta p y + C_2 \right) \end{cases} \tag{B.9}$$

If d is the distance between the interface and the lower wall, we then have (Eq. B.10):

$$\Delta p d + \mu_1 C_1 = \Delta p d + \mu_2 C_2 \tag{B.10}$$

So, we can determine the constant C_1 (Eq. B.11):

$$C_1 = \frac{\mu_2}{\mu_1} C_2 \tag{B.11}$$

The boundary condition at the lower wall (Eq. B.5) allow us to determine the constant $C_1^{'}$ (Eq. B.12):

$$C_1^{'} = 0 \tag{B.12}$$

We can write the constant $C_2^{'}$ as a function of the constant C_2 (Eq. B.13), thanks to the condition (B.6) on $u_{x,2}$:

$$C_2^{'} = -\frac{1}{2\mu_2} \Delta p H^2 - C_2 H \tag{B.13}$$

By injecting the system of equations (B.4) concerning the velocities $u_{x,1}$ and $u_{x,2}$ in relation (B.7), we get (Eq. B.14):

$$\frac{1}{2\mu_1} \Delta p d^2 + C_1 d = \frac{1}{2\mu_2} \Delta p d^2 + C_2 d + C_2^{'} \tag{B.14}$$

So, by replacing C_1 (Eq. B.11) and $C_2^{'}$ (Eq. B.13) by their respective values in equation (B.14), we then have a relation depending only on the constant C_2 (Eq. B.15):

$$C_2 = \frac{\Delta p}{2\mu_2} \left(\frac{\mu_1 (d^2 - H^2) - \mu_2 d^2}{\mu_2 d - \mu 1 (H - d)} \right) \tag{B.15}$$

By identifying the value of the constant $C_2^{'}$ given by equation (B.15) in the system of equations (B.11-B.12-B.13), we can determine all the constants which define $u_{x,1}$ et $u_{x,2}$ (Eqs. B.16):

$$\begin{cases} C_1 = \dfrac{\Delta p}{2\mu_1}\left(\dfrac{\mu_1(d^2-H^2)-\mu_2 d^2}{\mu_2 d-\mu_1(H-d)}\right) \\ C_1' = 0 \\ C_2 = \dfrac{\Delta p}{2\mu_2}\left(\dfrac{\mu_1(d^2-H^2)-\mu_2 d^2}{\mu_2 d-\mu 1(H-d)}\right) \\ \\ C_2' = \dfrac{\Delta p H}{2\mu_2}\left(\dfrac{(\mu_2-\mu_1)(d^2-Hd)}{\mu_2 d-\mu_1(H-d)}\right) \end{cases} \tag{B.16}$$

We can then express analytically the velocity of the two-dimensional stationary two-phase Poiseuille flow in each fluid thanks to (Eq. B.17):

$$\begin{cases} u_{x,1} = \dfrac{\Delta p}{2\mu_1}\left(y^2 + \dfrac{\mu_1(d^2-H^2)-\mu_2 d^2}{\mu_2 d-\mu_1(H-d)}y\right) \\ \\ u_{x,2} = \dfrac{\Delta p}{2\mu_2}\left(y^2 + \dfrac{(\mu_1(d^2-H^2)-\mu_2 d^2)y + H(d^2-Hd)(\mu_2-\mu_1)}{\mu_2 d-\mu_1(H-d)}\right) \end{cases} \tag{B.17}$$

The analytical solution for the pressure field comes directly from equation (B.3), in which we inject the analytical solution we obtain for the velocity field from the system of equations (B.17). We can also integrate equation (B.1) and get the following system of equations (Eq. B.18):

$$\begin{cases} p_1(x) = \Delta p x + K_1 \\ p_2(x) = \Delta p x + K_2 \end{cases} \tag{B.18}$$

where K_1 and K_2 are the integrating constants with respect to x. But $p_1(x) = p_2(x)$ at $y = d$, thus $K_1 = K_2$. Moreover, we have $p = p_{left}$ at $x = 0$ and $p = p_{right}$ at $x = L$.

Finally, the analytical solution for the pressure field reads (Eq. B.19):

$$p(x) = \frac{(p_{right} - p_{left})}{L}\ x\ +\ p_{left} \tag{B.19}$$

Appendix C

Solitary waves theories

C.1 Description of the various theories

We deal hereafter with the problem of a perturbation propagating at the free-surface of fluid layer of depth d, its amplitude H being non-negligible compared to d, and located over a length L. It has been shown (Stoker, 1957; Dean and Dalrymple, 1991; Guyon et al., 2001) that, thanks to a compensation effect, such a perturbation can propagate with uniform speed without any change of shape: it has been called a *solitary wave*. This phenomena has been first reported by John Scott Russel in 1834 (Russel, 1844).

A solitary wave (or *soliton*) is solution of a non-linear equation and maintains its individuality (no dispersion), even in case of collisions and in spite of the non-linearity of the equation. D. J. Kotreweg et G. de Vries (Korteweg and Vries, 1895) first gave in 1895 a complete analytical solution of a hydrodynamics non-linear equation, showing that there could be localized non dissipative waves. The Kotreweg-de Vries equation (KdV) is defined by (Eq. C.1):

$$\frac{\partial \eta}{\partial t} + \frac{\partial \eta}{\partial x} + \frac{3}{4}\epsilon\eta\frac{\partial \eta}{\partial x} + \frac{\mu}{6}\frac{\partial^3 \eta}{\partial x^3} = 0 \tag{C.1}$$

Several analytical solutions can be found in the literature (Boussinesq, 1871; McCowan, 1891; Grimshaw, 1971; Fenton, 1972; Lee et al., 1982). These analytical solutions and a related experiment are discussed here. The experiment is devoted to the propagation of a solitary wave in a wave tank. In particular, the water surface profiles and corresponding water particle velocities of several solitary waves have been measured. The reference variables of the initial wave are the celerity, c, the depth, d, of the water channel and the wave height, H. All the solutions detailed in the following sections will give solitary

waves propagating from the left to the right end of the numerical domain.

C.1.1 Boussinesq's solution - 1^{st} order

The initial wave shape, and the shape at any time t, celerity and velocity fields (u and v being the cartesian components) can be computed from the first order solitary wave theory (Boussinesq, 1871), given by (Eq.C.2):

$$\eta(x,t) = H sech^2\Big(\sqrt{\frac{3H}{4d^3}}(x - x_0 - ct)\Big) \tag{C.2}$$

where x_0 is the initial position of the wave crest. The celerity is defined by:

$$c = \sqrt{g(d+H)} \tag{C.3}$$

In the following, it will be considered that η is a sole function of the coordinate x' which is the longitudinal coordinate in the frame attached to the wave:

$$\eta = \eta(x'(x,t)) \text{ with } x'(x,t) = x - x_0 - ct. \tag{C.4}$$

So, at the instant $t = 0\ s$, we have:

$$\eta(x) = H sech^2\Big(\sqrt{\frac{3H}{4d^3}}(x - x_0)\Big) \tag{C.5}$$

Next the velocity field is given by:

$$\begin{aligned} \frac{u}{\sqrt{gd}} &= \epsilon\Big[\eta_* - \frac{1}{4}\epsilon {\eta_*}^2 + \frac{d^2}{3c^2}\Big[1 - \frac{3}{2}\frac{z^2}{d^2}\Big]\frac{\partial^2\eta_*}{\partial t^2}\Big] \\ \frac{v}{\sqrt{gd}} &= z\frac{\epsilon}{c}\Big[\Big(1 - \frac{1}{2}\epsilon\eta_*\Big)\frac{\partial\eta_*}{\partial t} + \frac{d^2}{3c^2}\Big(1 - \frac{z^2}{2d^2}\Big)\frac{\partial^3\eta_*}{\partial t^3}\Big] \end{aligned} \tag{C.6}$$

with $\epsilon = H/d$, $\eta_* = \eta/H = sech^2\Big(\sqrt{\frac{3H}{4d^3}}(x - ct)\Big)$, and:

$$\frac{\partial \eta_*}{\partial t} = \frac{2c\sqrt{\frac{3}{4}\frac{H}{d^3}}sinh\Big(\sqrt{\frac{3}{4}\frac{H}{d^3}}(x-ct)\Big)}{cosh^3\Big(\sqrt{\frac{3}{4}\frac{H}{d^3}}(x-ct)\Big)}$$

$$\frac{\partial^2 \eta_*}{\partial t^2} = \frac{c^2\frac{3}{2}\frac{H}{d^3}\Big[2cosh^2\Big(\sqrt{\frac{3}{4}\frac{H}{d^3}}(x-ct)\Big)-3\Big]}{cosh^4\Big(\sqrt{\frac{3}{4}\frac{H}{d^3}}(x-ct)\Big)} \tag{C.7}$$

$$\frac{\partial^3 \eta_*}{\partial t^3} = \frac{6c^3\frac{H}{d^3}\sqrt{\frac{3}{4}\frac{H}{d^3}}sinh\Big(\sqrt{\frac{3}{4}\frac{H}{d^3}}(x-ct)\Big)\Big[cosh^2\Big(\sqrt{\frac{3}{4}\frac{H}{d^3}}(x-ct)\Big)-3\Big]}{cosh^5\Big(\sqrt{\frac{3}{4}\frac{H}{d^3}}(x-ct)\Big)}$$

A lower order solution can be given:

$$\begin{aligned}\frac{u}{\sqrt{gd}} &= \frac{\eta}{d} \\ \frac{v}{\sqrt{gd}} &= \frac{z}{d}\frac{1}{c}\frac{\partial \eta}{\partial t}\end{aligned} \tag{C.8}$$

Note that this solution is a very rough one as the horizontal velocity component u is independent of depth d.

C.1.2 Grimshaw's solution - 3^{rd} order

It is also possible to initialize simulations with the solution developed by Grimshaw (1971) (also corrected and given in Fenton (1972) and Lee et al. (1982)). The initial wave shape, celerity and velocity field are then given by (Eq.C.9):

$$\frac{\eta}{d} = \epsilon s^2 - \frac{3}{4}\epsilon^2 s^2 t^2 + \epsilon^3\Big(\frac{5}{8}s^2t^2 - \frac{101}{80}s^4t^2\Big) \tag{C.9}$$

$$
\begin{aligned}
\frac{u}{\sqrt{gd}} &= \epsilon s^2 - \epsilon^2\Big[-\frac{1}{4}s^2 + s^4 + \Big(\frac{z}{d}\Big)^2\Big(\frac{3}{2}s^2 - \frac{9}{4}s^4\Big)\Big] \\
&\quad - \epsilon^3\Big[\frac{19}{4}s^2 + \frac{1}{5}s^4 - \frac{6}{5}s^6 + \Big(\frac{z}{d}\Big)^2\Big(-\frac{3}{2}s^2 - \frac{15}{4}s^4 + \frac{15}{2}s^6\Big) \\
&\quad + \Big(\frac{z}{d}\Big)^4\Big(-\frac{3}{8}s^2 + \frac{45}{16}s^4 - \frac{45}{16}s^6\Big)\Big] \\
\frac{v}{\sqrt{gd}} &= (3\epsilon)^{\frac{1}{2}}\Big(\frac{z}{d}\Big)t\Big[-\epsilon s^2 + \epsilon^2\Big[\frac{3}{8}s^2 + 2s^4 + \Big(\frac{z}{d}\Big)^2\Big(\frac{31}{2}s^2 - \frac{3}{2}s^4\Big)\Big] \\
&\quad + \epsilon^3\Big[\frac{49}{640}s^2 - \frac{17}{20}s^4 - \frac{18}{5}s^6 + \Big(\frac{z}{d}\Big)^2\Big(-\frac{13}{16}s^2 - \frac{25}{16}s^4 + \frac{15}{2}s^6\Big) \\
&\quad + \Big(\frac{z}{d}\Big)^4\Big(-\frac{3}{40}s^2 + \frac{9}{8}s^4 - \frac{27}{16}s^6\Big)\Big]\Big]
\end{aligned}
\tag{C.10}
$$

with $\epsilon = H/d$, $\alpha = (\frac{3}{4}\epsilon)^{\frac{1}{2}}(1 - \frac{5}{8}\epsilon + \frac{71}{128}\epsilon^2)$, $s = \mathrm{sech}(\alpha x') = 1/\cosh(\alpha x')$ et $t = \tanh(\alpha x')$.

The pressure is then given by (Eq.C.11):

$$
\begin{aligned}
\frac{p}{\rho g d} &= 1 - \Big(\frac{z}{d}\Big) + \epsilon s^2 + \epsilon^2\Big[\frac{3}{4}s^2 - \frac{3}{2}s^4 + \Big(\frac{z}{d}\Big)^2\Big(-\frac{3}{2}s^2 + \frac{9}{4}s^4\Big)\Big] \\
&\quad + \epsilon^3\Big[-\frac{1}{2}s^2 - \frac{19}{20}s^4 + \frac{11}{5}s^6 + \Big(\frac{z}{d}\Big)^2\Big(\frac{3}{4}s^2 + \frac{39}{8}s^4 - \frac{33}{4}s^6\Big) \\
&\quad + \Big(\frac{z}{d}\Big)^4\Big(\frac{3}{8}s^2 - \frac{45}{16}s^4 + \frac{45}{16}s^6\Big)\Big]
\end{aligned}
\tag{C.11}
$$

and the celerity is defined by (Eq. C.12):

$$
c = \sqrt{gd}\Big(1 + \epsilon - \frac{1}{20}\epsilon^2 - \frac{3}{70}\epsilon^3\Big)^{\frac{1}{2}} \tag{C.12}
$$

C.1.3 Tanaka's exact solution

The solitary wave can also been initialized from the exact solution developed by Tanaka (1986), which is widely used (Tanaka et al., 1987; Guignard, 2001; Guignard et al., 2001;

Grilli et al., 2001). The initial free-surface shape and the values of the velocity potential are obtained from the algorithm given by Tanaka (1986). It is then possible to calculate the velocity field below the free-surface thanks to Cauchy's integral formula, as detailed by Vinje and Brevig (1981), calculations being based of the potential theory.

Let consider, in complex space, $z = x + iy$. In the fluid domain, Laplace's equation is satisfied for both velocity potential, ϕ, and the stream function, ψ. We then have $f(z) = \phi(x;y) + i\psi(x;y)$ an analytical function of z. In this case, Cauchy's theory is valid:

$$\oint_C \frac{f(z)}{(z-z_0)}dz = \oint_C \frac{\phi(x;y)+i\psi(x;y)}{(z-z_0)}dz = 0 \tag{C.13}$$

with z_0 being outside a closed contour C. If z_0 is inside C, the complex potential can be found from (C.14):

$$f(z) = \frac{1}{2\pi i}\oint_C \frac{\phi(x;y)+i\psi(x;y)}{(z-z_0)}dz = 0 \tag{C.14}$$

In the same way, $w(z) = u(x;y) - iv(x;y)$ can be calculated in z_0 from (C.15):

$$w(z) = \frac{1}{2\pi i}\oint_C \frac{\phi(x;y)+i\psi(x;y)}{(z-z_0)^2}dz = 0 \tag{C.15}$$

The numerical solution of equations (Eqs. C.14) and (C.15) can be calculated from the sums (Eq. C.16):

$$\begin{aligned} f(z_0) &= \frac{1}{2\pi i}\oint_C \frac{\phi(x;y)+i\psi(x;y)}{(z-z_0)}dz \cong \sum_j \Gamma_j(z_{j-1},z_j,z_{j+1},z_0)f_j(z_j) \\ w(z_0) &= \frac{1}{2\pi i}\oint_C \frac{\phi(x;y)+i\psi(x;y)}{(z-z_0)^2}dz \cong \sum_j \Gamma 2_j(z_{j-1},z_j,z_{j+1},z_0)f_j(z_j) \end{aligned} \tag{C.16}$$

with Γ_j and $\Gamma 2_j$ being called the influence functions. All the calculations are detailed by Vinje and Brevig (1981). So, for any point contained inside a domain limited by a contour C, we have the relations (Eq. C.17):

$$\begin{aligned}\Gamma_j(z_{j-1},z_j,z_{j+1},z_0) &= \frac{z_0-z_{j-1}}{z_j-z_{j-1}}\ln\frac{z_j-z_0}{z_{j-1}-z_0} \\ &+ \frac{z_0-z_{j+1}}{z_j-z_{j+1}}\ln\frac{z_{j+1}-z_0}{z_j-z_0}\end{aligned} \tag{C.17}$$

$$\begin{aligned}\Gamma 2_j(z_{j-1},z_j,z_{j+1},z_0) &= \int_{z_{j-1}}^{z_j}\frac{z-z_{j-1}}{z_j-z_{j-1}}\frac{1}{(z-z_0)^2}dz \\ &+ \int_{z_j}^{z_{j+1}}\frac{z-z_{j+1}}{z_j-z_{j+1}}\frac{1}{(z-z_0)^2}dz\end{aligned}$$

the last equation being integrated by parts. We then have (C.18):

$$\Gamma 2_j(z_{j-1},z_j,z_{j+1},z_0) = \frac{1}{z_j-z_{j-1}}\ln\frac{z_j-z_0}{z_{j-1}-z_0} + \frac{1}{z_j-z_{j+1}}\ln\frac{z_{j+1}-z_j}{z_j-z_0} \tag{C.18}$$

C.2 Comparison between the various theories

Some other solutions can be found in the literature, as McCowan's analytical solution (McCowan, 1891), Fenton's 9^{th} order solution (Fenton, 1972), the latter one being numerically obtained as Tanaka's solution. But we will not go any further than the three solutions detailed previously, the 1^{st} order, the 3^{rd} order and Tanaka's exact solution. We want here to give a quick comparison between the solutions used in chapter 4, which is mostly dedicated to the validation tests that have been conducted on the basis of the results published by Lee et al. (1982). We present here the experimental data they recorded to demonstrate the wide range of possibilities of a new technique of measurement. They gave indications of free-surface profiles and corresponding velocity fields at several depths, the results being presented for three initial non-dimensional amplitudes ϵ. We show hereafter in table (C.1) a summary of the experimental data which have been compared with the existing theories, giving an idea of the different orders of approximation. Experiments have not been conducted for the last case, $\epsilon = 0.70$, but theoretical profiles are shown.

We present in the following figures (C.1) the free-surface profiles, η/d, plotted versus the non-dimensional time, $t\sqrt{g/d}$. We can note a good agreement between the experiments and the solutions coming from the theories. The asymmetric aspect of the experimental profiles has been explained as a consequence of the way that waves have been generated (Lee et al., 1982). It can be mention that the differences between the theoretical profiles are mainly observed at the bottom of the wave. Indeed, the theories give all the

Test-case	ϵ	$d(m)$	H (m)
1	0.11	0.3020	0.03322
2	0.19	0.4046	0.076874
3	0.29	0.2040	0.05916
4	0.70	0.3020	0.2114

Table C.1: Values of the parameters describing the experiments by Lee et al. (1982), with $\epsilon = H/d$.

same maximum values for the crests' ordinates, but shows discrepancies in the width of the bottom profile. The wider profile is given by the lowest order of approximation (Eq. C.2), being anyway very close to the exact solution given by Tanaka (1986).

In the figures (C.2), (C.3) and (C.4), the non-dimensional horizontal velocities are presented for several ϵ values, at different depths within solitary waves.

In the figures (C.5) and (C.6), the non-dimensional vertical velocities are presented for several ϵ values, at different depths within solitary waves. It can be mentioned that there is a great difference in magnitude between the horizontal and the vertical components of the velocity.

Tables (C.2), (C.3) and (C.4) give the corresponding values of the maximum of the non-dimensional velocity components at given non-dimensional depths (z/d).

As expected, the lower the order of approximation is, the more the theories disagree. The 1^{st} order theory (Eq. C.2) overestimates the solutions. Moreover, the greater the value of ϵ is, the more the theories diverge from each other. This can be checked with table (C.5) showing the values of the wave celerities for test-case 4. However, the theories we use to initialize our simulations are close to each other, Tanaka's solution being exact and allowing to study the largest waves, under the limit of $\epsilon = 0,833$.

1^{st} order				
c (m.s^{-1})	1.8134			
$c/\sqrt{gd}$	1.054			
z/d	0.92	0.78	0.62	0.45
$u_{max}/\sqrt{gd}$	0.109	0.106	0.104	0.103
$v_{max}/\sqrt{gd}$ ($.10^{-1}$)	$\pm$ 0.202	$\pm$ 0.170	$\pm$ 0.133	$\pm$ 0.0958
3^{rd} order				
c (m.s^{-1})	1.81288			
$c/\sqrt{gd}$	1.053			
z/d	0.92	0.78	0.62	0.45
$u_{max}/\sqrt{gd}$	0.107	0.106	0.104	0.103
$v_{max}/\sqrt{gd}$ ($.10^{-1}$)	$\pm$ 0.195	$\pm$ 0.163	$\pm$ 0.129	$\pm$ 0.0927
Tanaka				
c (m.s^{-1})	1.81284			
$c/\sqrt{gd}$	1.053			
z/d	0.92	0.78	0.62	0.45
$u_{max}/\sqrt{gd}$	0.106	0.105	0.103	0.102
$v_{max}/\sqrt{gd}$ ($.10^{-1}$)	$\pm$ 0.195	$\pm$ 0.165	$\pm$ 0.128	$\pm$ 0.0952

Table C.2: Values of the maximum of the non-dimensional velocity components at given non-dimensional depths (z/d). Test case 1, $d = 0.3020$ m, $\epsilon = 0.11$.

1^{st} order				
c (m.s^{-1})	2.1733			
$c/\sqrt{gd}$	1.09			
z/d	1.05	1.02	0.92	0.45
$u_{max}/\sqrt{gd}$	0.193	0.191	0.186	0.168
$v_{max}/\sqrt{gd}$ $(.10^{-1})$	$\pm$ 0.500	$\pm$ 0.484	$\pm$ 0.429	$\pm$ 0.199
3^{rd} order				
c (m.s^{-1})	2.1714			
$c/\sqrt{gd}$	1.089			
z/d	1.05	1.02	0.92	0.45
$u_{max}/\sqrt{gd}$	0.182	0.181	0.178	0.169
$v_{max}/\sqrt{gd}$ $(.10^{-1})$	$\pm$ 0.465	$\pm$ 0.450	$\pm$ 0.402	$\pm$ 0.189
Tanaka				
c (m.s^{-1})	2.1713			
$c/\sqrt{gd}$	1.089			
z/d	1.05	1.02	0.92	0.45
$u_{max}/\sqrt{gd}$	0.184	0.183	0.179	0.170
$v_{max}/\sqrt{gd}$ $(.10^{-1})$	$\pm$ 0.469	$\pm$ 0.457	$\pm$ 0.408	$\pm$ 0.198

Table C.3: Values of the maximum of the non-dimensional velocity components at given non-dimensional depths (z/d). Test case 2, $d = 0.4046$ m, $\epsilon = 0.19$.

1^{st} order				
c (m.s^{-1})	1.6067			
$c/\sqrt{gd}$	1.136			
z/d	1.05	1.03	0.92	0.67
$u_{max}/\sqrt{gd}$	0.296	0.294	0.280	0.255
$v_{max}/\sqrt{gd}$ $(.10^{-1})$	$\pm$ 0.876	$\pm$ 0.855	$\pm$ 0.745	$\pm$ 0.522
3^{rd} order				
c (m.s^{-1})	1.6035			
$c/\sqrt{gd}$	1.133			
z/d	1.05	1.03	0.92	0.67
$u_{max}/\sqrt{gd}$	0.260	0.259	0.253	0.245
$v_{max}/\sqrt{gd}$ $(.10^{-1})$	$\pm$ 0.786	$\pm$ 0.770	$\pm$ 0.680	$\pm$ 0.485
Tanaka				
c (m.s^{-1})	1.6032			
$c/\sqrt{gd}$	1.133			
z/d	1.05	1.03	0.92	0.67
$u_{max}/\sqrt{gd}$	0.273	0.271	0.264	0.251
$v_{max}/\sqrt{gd}(.10^{-1})$	$\pm$ 0.788	$\pm$ 0.770	$\pm$ 0.672	$\pm$ 0.471

Table C.4: Values of the maximum of the non-dimensional velocity components at given non-dimensional depths (z/d). Test case 3, $d = 0.204$ m, $\epsilon = 0.29$.

$\epsilon = 0.70$			
	1^{st} order	3^{rd} order	Tanaka
c (m.s^{-1})	2.2442	2.2182	2.2012
$c/\sqrt{gd}$	1.303	1.289	1.279

Table C.5: Values of the wave celerities. Test case 4, $d = 0.3020$ m, $\epsilon = 0.70$.

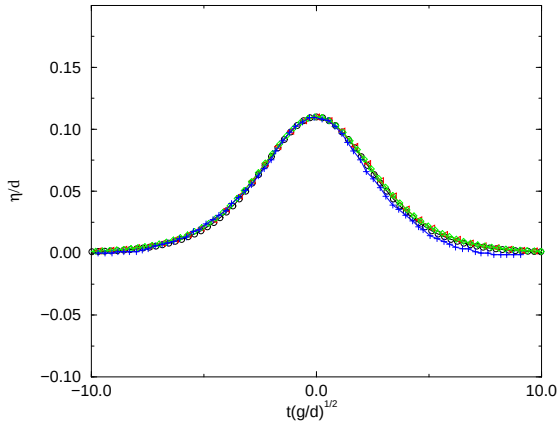

(a) $d = 30.20\ cm$, $\epsilon = 0.11$

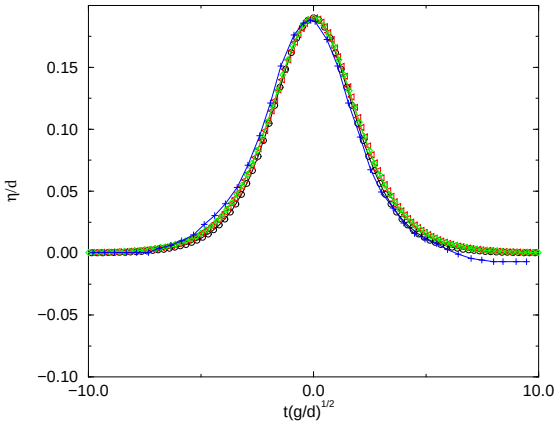

(b) $d = 40.46\ cm$, $\epsilon = 0.19$

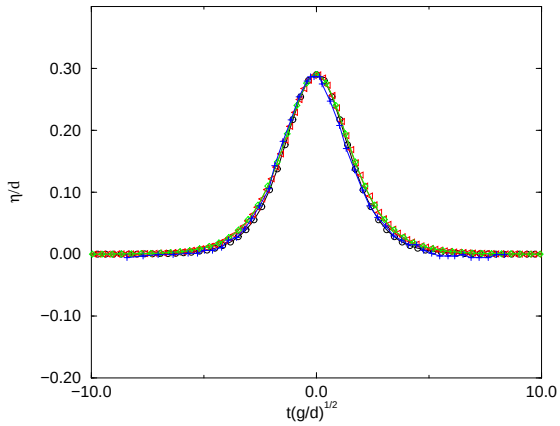

(c) $d = 20.40\ cm$, $\epsilon = 0.29$

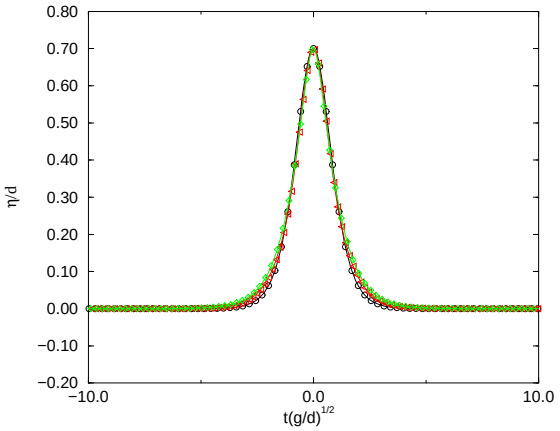

(d) $d = 30.20\ cm$, $\epsilon = 0.70$

Figure C.1: Solitary wave profiles: water surface elevation, η/d, is plotted versus non-dimensional time, $t\sqrt{g/d}$. Comparison of theories and experiments. $\circ$ 1^{st} order (black), $\triangleleft$ 3^{rd} order (red), $\diamond$ Tanaka (green), $+$ Lee (blue).

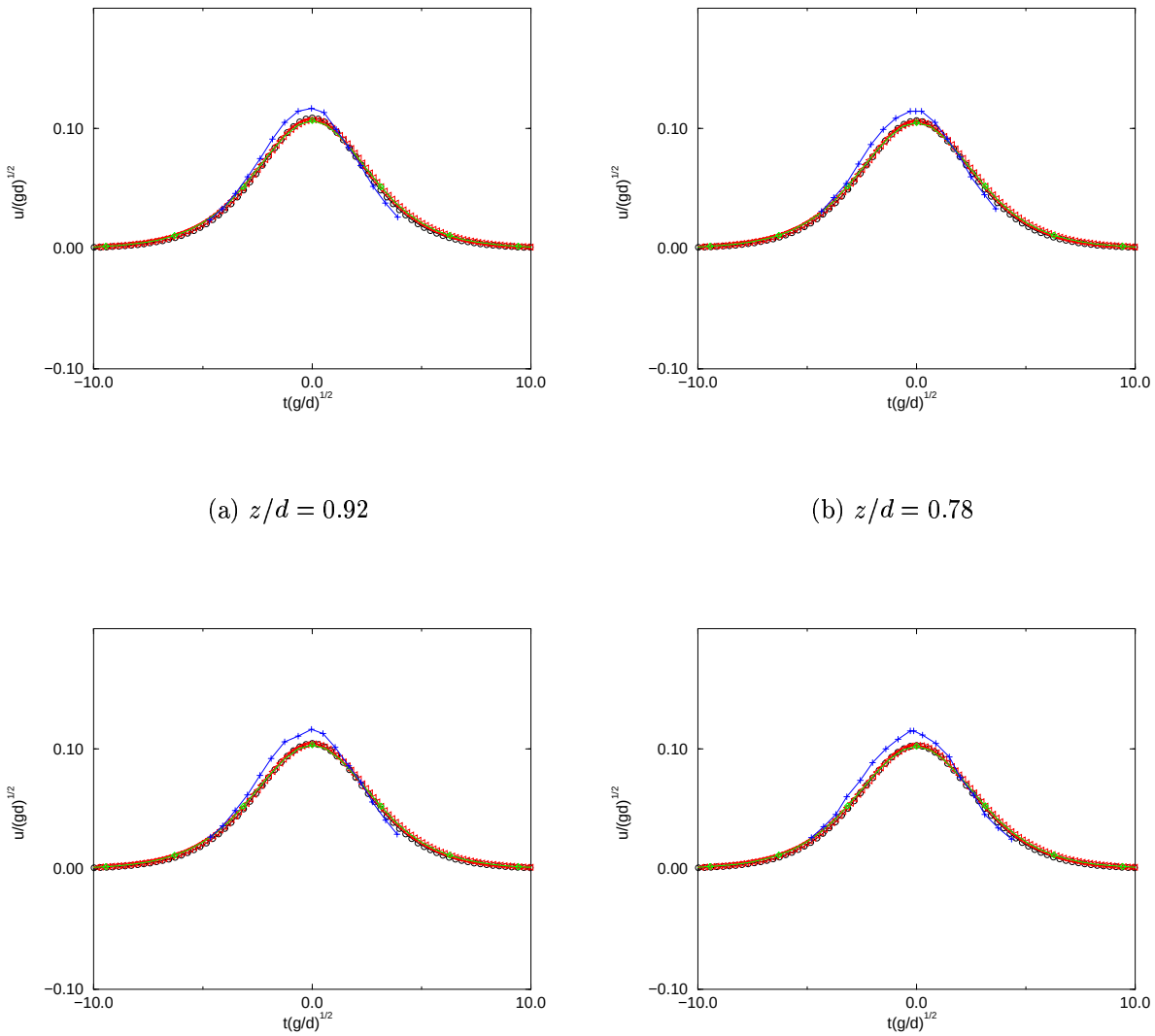

(a) $z/d = 0.92$ (b) $z/d = 0.78$

(c) $z/d = 0.62$ (d) $z/d = 0.45$

Figure C.2: Horizontal velocities at various depths z/d: non-dimensional water particle velocities, $u/\sqrt{gd}$, are plotted versus non-dimensional time, $t\sqrt{g/d}$. Comparison of experiments and theories for $d = 0.3020$ m, $\epsilon = 0.11$. $\circ$ 1^{st} order (black), $\triangleleft$ 3^{rd} order (red), $\diamond$ Tanaka (green), $+$ Lee (blue).

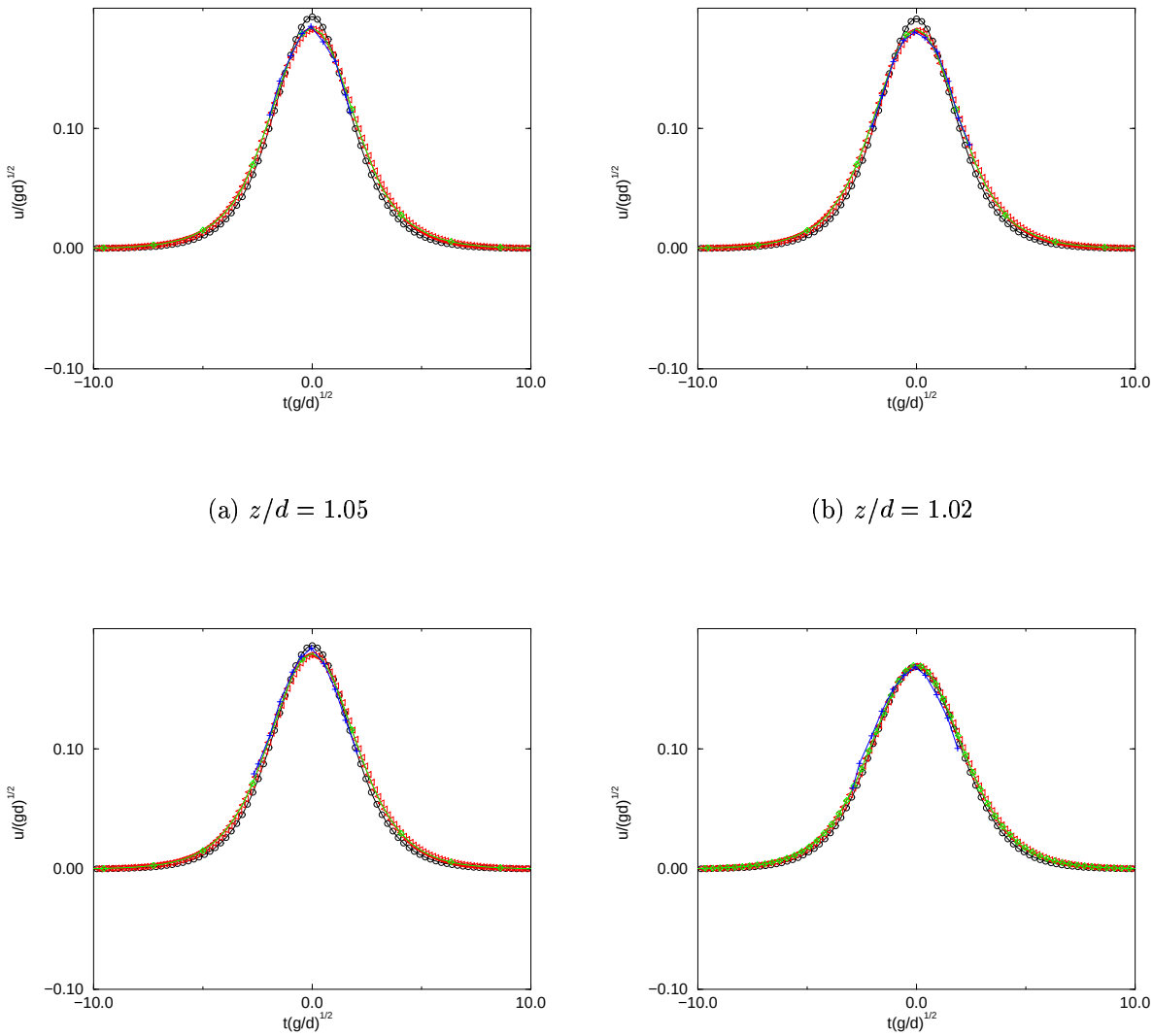

(a) $z/d = 1.05$

(b) $z/d = 1.02$

(c) $z/d = 0.92$

(d) $z/d = 0.45$

Figure C.3: Horizontal velocities at various depths z/d: non-dimensional water particle velocities, $u/\sqrt{gd}$, are plotted versus non-dimensional time, $t\sqrt{g/d}$. Comparison of experiments and theories for $d = 0.4046$ m, $\epsilon = 0.19$. $\circ$ 1^{st} order (black), $\triangleleft$ 3^{rd} order (red), $\diamond$ Tanaka (green), $+$ Lee (blue).

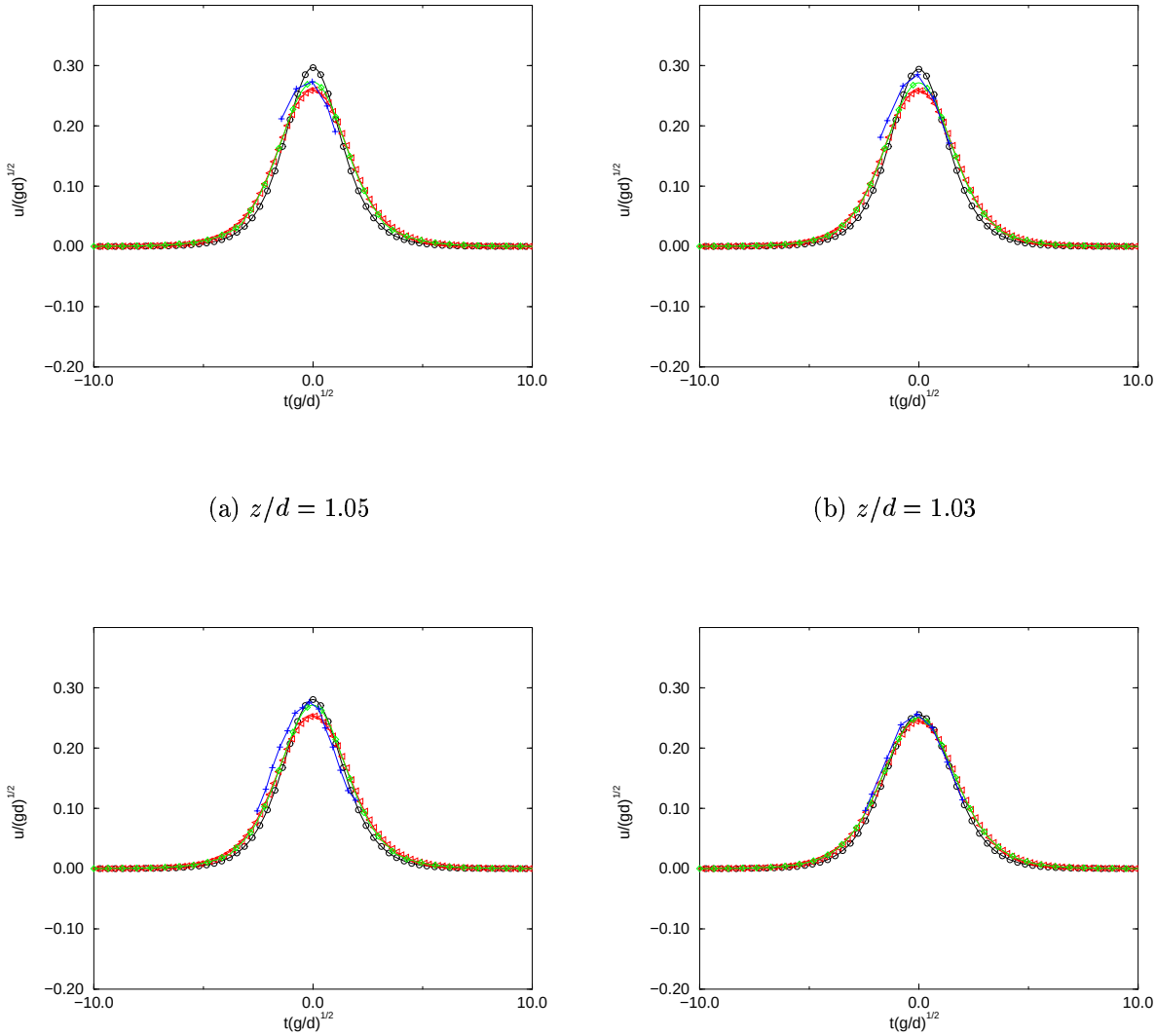

(a) $z/d = 1.05$

(b) $z/d = 1.03$

(c) $z/d = 0.92$

(d) $z/d = 0.67$

Figure C.4: Horizontal velocities at various depths z/d: non-dimensional water particle velocities, $u/\sqrt{gd}$, are plotted versus non-dimensional time, $t\sqrt{g/d}$. Comparison of experiments and theories for $d = 0.204$ m, $\epsilon = 0.29$. $\circ$ 1^{st} order (black), $\triangleleft$ 3^{rd} order (red), $\diamond$ Tanaka (green), $+$ Lee (blue).

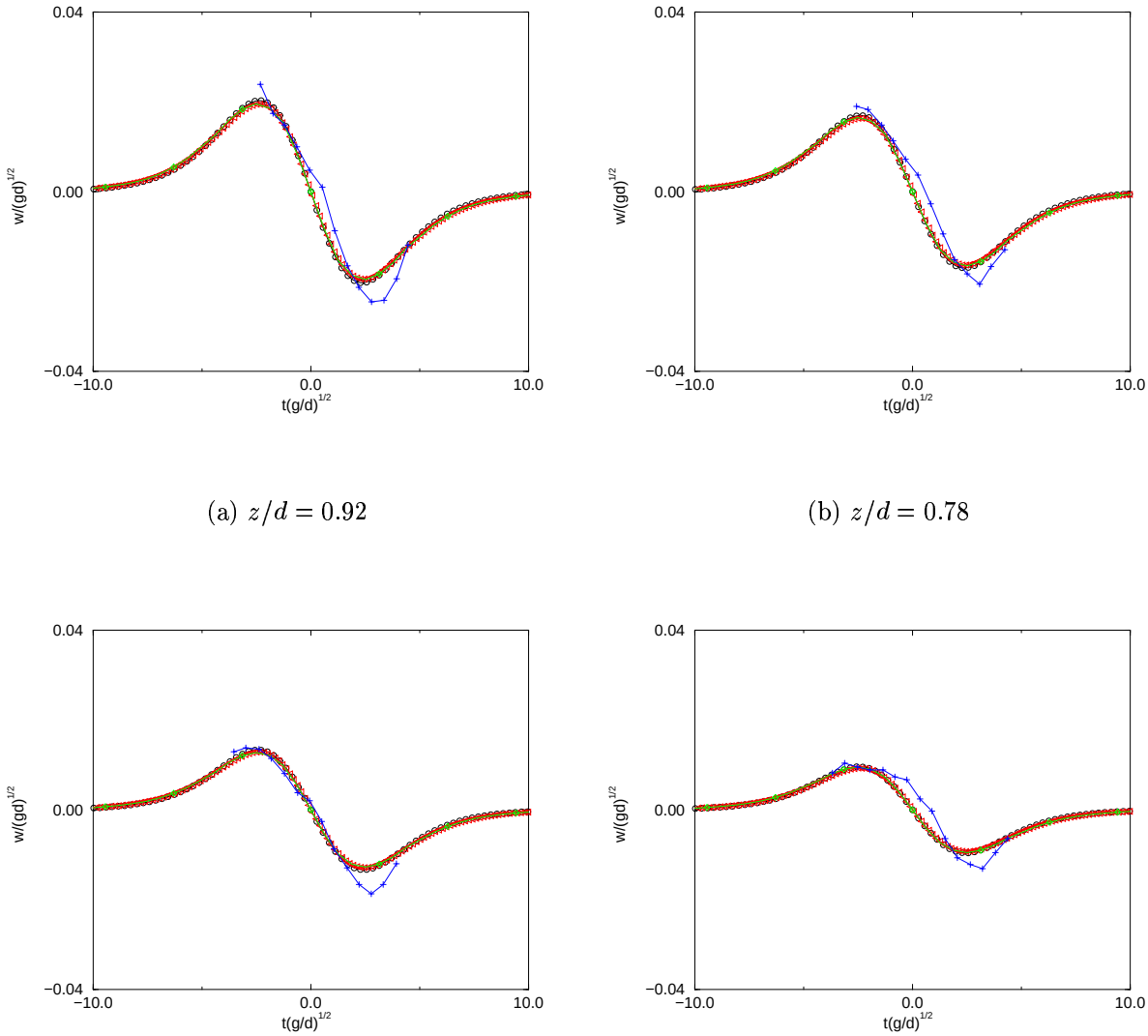

(a) $z/d = 0.92$

(b) $z/d = 0.78$

(c) $z/d = 0.62$

(d) $z/d = 0.45$

Figure C.5: Vertical velocities at various depths z/d: non-dimensional water particle velocities, $v/\sqrt{gd}$, are plotted versus non-dimensional time, $t\sqrt{g/d}$. Comparison of experiments and theories for $d = 0.302$ m, $\epsilon = 0.11$. $\circ$ 1^{st} order (black), $\triangleleft$ 3^{rd} order (red), $\diamond$ Tanaka (green), $+$ Lee (blue).

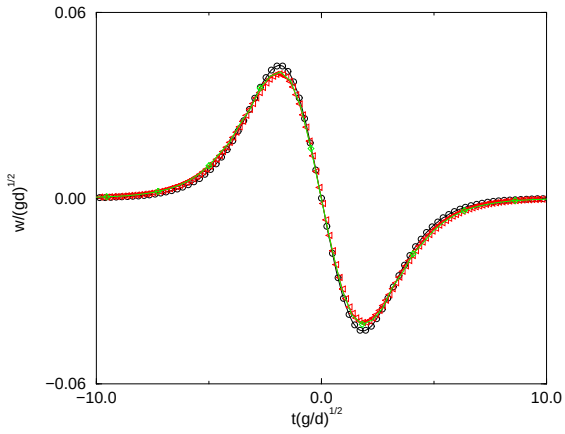

(a) $d = 40.46\ cm$, $\epsilon = 0.19$, $z/d = 0.92$

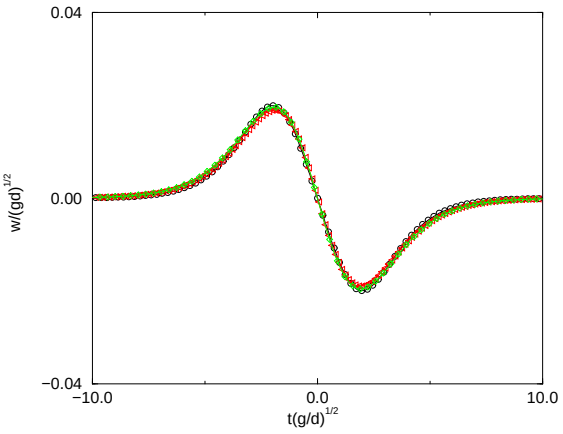

(b) $d = 40.46\ cm$, $\epsilon = 0.19$, $z/d = 0.45$

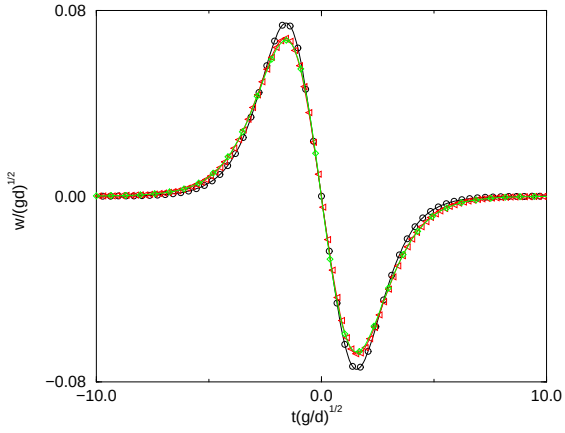

(c) $d = 20.40\ cm$, $\epsilon = 0.29$, $z/d = 0.92$

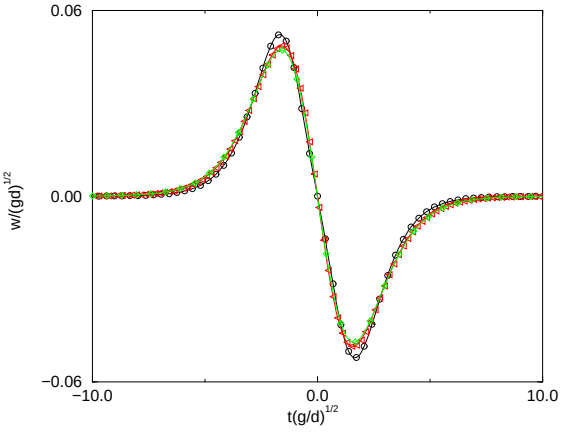

(d) $d = 20.40\ cm$, $\epsilon = 0.29$, $z/d = 0.67$

Figure C.6: Vertical velocities at various depths z/d: non-dimensional water particle velocities, $v/\sqrt{gd}$, are plotted versus non-dimensional time, $t\sqrt{g/d}$. Comparison of the different theories for several ϵ values. $\circ$ 1^{st} order (black), $\triangleleft$ 3^{rd} order (red), $\diamond$ Tanaka (green).

Bibliography

S. Abadie. *Modélisation numérique du déferlement plongeant par méthode VOF.* PhD thesis, Université Bordeaux I, 1998.

S. Abadie. Numerical modelling of the flow generated by plunging breakers. In *Proceedings Coastal Dynamics 2001*, pages 202–211, 2001.

S. Abadie, J.-P. Caltagirone, and P. Watremez. Mécanisme de génération du jet secondaire ascendant dans un déferlement plongeant. *C. R. Mécanique*, 326:553–559, 1998.

R. J. Adrian, C. D. Meinhart, and C. D. Tomkins. Vortex organization in the outer region of the turbulent boundary layer. *Journal of Fluid Mechanics*, 422:1–54, 2000.

P. Angot. *Contribution à l'étude des transferts thermiques dans des systèmes complexes; application aux composants électroniques.* PhD thesis, Université Bordeaux I, 1989.

P. Angot, C.-H. Bruneau, and P. Fabrie. A penalization method to take into account obstacles in viscous flows. *Numer. Math.*, 81:497–520, 1999.

P. Arbez. *Stabilité de couche limite incompressible sur surface rugueuse.* PhD thesis, Université Bordeaux I, 1998.

E. Arquis and J.-P. Caltagirone. Sur les conditions hydrodynamiques au voisinage d'une interface milieu fluide - milieu poreux : application à la convection naturelle. *C. R. Acad. Sci. Série II b*, 299:1–4, 1984.

J. Bardina, J. H. Ferziger, and W. C. Reynolds. Improved subgrid scale models for large eddy simulation. *AIAA Paper*, pages 80–1357, 1980.

J. A. Battjes. Surf-zone dynamics. *Annu. Rev. Fluid Mech.*, 20:257–293, 1988.

A. Benkenida and J. Magnaudet. Une méthode de simulation d'écoulements diphasiques sans reconstruction d'interfaces. *C. R. Acad. Sci. Paris, Série II b*, 328:25–32, 2000.

C. Bernardi, V. Girault, and F. Hecht. *A posteriori analysis of a penalty method and application to the Stokes problem.* Laboratoire Jacques-Louis Lions, R02033, 2002.

B. Biausser. *Suivi d'interface tridimensionnel de type Volume Of Fluid : application au déferlement.* PhD thesis, Université de Toulon et du Var, 2003.

P. Bonmarin. Geometric properties of deep-water breaking waves. *Journal of Fluid Mechanics*, 209:405–433, 1989.

R. Bonnefille. *Cours d'hydraulique maritime.* Masson, 1992.

J. Boussinesq. Théorie de l'intumescence liquide appelée onde solitaire ou de translation se propageant dans un canal rectangulaire. *C. R. Mécanique*, page 755, 1871.

J. U. Brackbill, B. D. Kothe, and C. Zemach. A continuum method for modelling surface tension. *J. Comput. Phys.*, 100:335–354, 1992.

S. F. Bradford. Numerical simulation of surf zone dynamics. *J. of Waterway, Port, Coastal, and Ocean Eng.*, 126(1):1–13, 2000.

H. Bredmose, M. Brochini, D. H. Peregrine, and L. Thais. Experimental investigation and numerical modelling of steep forced water waves. *Journal of Fluid Mechanics*, 2002. Under consideration for publication.

J. Breil. *Modélisation du remplissage en propergol de moteur à propulsion solide.* PhD thesis, Université Bordeaux I, 2001.

M. Brochini and D. H. Peregrine. The dynamics of turbulence at free surfaces: Part 1. description of strong turbulence at a free surface. *Journal of Fluid Mechanics*, 449: 225–254, 2001a.

M. Brochini and D. H. Peregrine. The dynamics of turbulence at free surfaces: Part 2. free surface boundary conditions. *Journal of Fluid Mechanics*, 449:255–290, 2001b.

I. Calmet. *Analyse par simulation des grandes échelles des mouvements turbulents et du transfert de masse sous une interface plane.* PhD thesis, Institut National Polytechnique de Toulouse, 1995.

J.-P. Caltagirone and J. Breil. Sur une méthode de projection vectorielle pour la résolution des équations de navier-stokes. *C. R. Acad. Sci. série II b*, 327:1179–1184, 1999.

G. F. Carey and R. Krishman. Convergence of iterative methods in penalty finite element approximation of the navier-stokes equations. *Comput. Methods Appl. Mech. Engrg.*, 60:1–29, 1987.

R. K. C. Chan and R. L. Street. A computer study of finite amplitude water waves. *J. Comput. Phys.*, 6:68–94, 1970.

K.-A. Chang, T.-J. Hsu, and P. L.-F. Liu. Vortex generation and evolution in water waves propagating over a submerged rectangular obstacle. *Coastal Eng.*, 44:13–36, 2001.

H. Chanson, S. Aoki, and M. Maruyama. Unsteady air bubble entrainment and detrainment at a pluging breaker: dominant time scales and similarity of water level variations. *Coastal Eng.*, 46:139–157, 2002.

H. Chanson and J.-F. Lee. Plunging jet characteristics of pluging breakers. *Coastal Eng.*, 31:125–141, 1997.

G. Chen, C. Kharif, S. Zaleski, and J. J. Li. Two-dimensional navier-stokes simulation of breaking waves. *Physics of Fluids*, 11:121–133, 1999.

S. Chen, D. B. Johnson, and P. E. Raad. *The surface marker method*, volume 1 of *Computational Modeling of Free and Moving Boundary Problems, Fluid Flow*, pages 223–324. W. de Gruyter, New-York, 1991.

A. Chorin. Numerical simulation of the navier-stokes equations. *Math. Comput.*, 22: 745–762, 1968.

E. D. Christensen. *Large eddy simulation of breaking waves.* PhD thesis, Technical University of Denmark, 1996.

E. D. Christensen and R. Deigaard. Large eddy simulation of breaking waves. *Coastal Eng.*, 42:53–86, 2001.

E. D. Christensen, D.-J. Walstra, and N. Emerat. Vertical variation of the flow across the surf zone. *Coastal Eng.*, 45:169–198, 2002.

E. D. Cokelet. *Mechanics of Wave-Induced Forces on Cylinders*, chapter Breaking waves, the plunging jet and interior flow-field, pages 287–301. Ed. T. L. Shaw, 1979.

G. Comte-Bellot. *Contribution à l'étude de la turbulence de conduite.* PhD thesis, Université de Grenoble, 1963.

D. T. Cox and S. L. Anderson. Statistics of intermittent surf zone turbulence and observations of large eddies using piv. *Coastal Eng. J. in Japan*, 43(2):121–131, 2001.

D. T. Cox and N. Kobayashi. Identification of intense, intermittent coherent motions under shoaling and breaking waves. *J. of Geophysical Research*, 105 (C6):14223–14236, 2000.

D. T. Cox, N. Kobayashi, and A. Okayasu. Bottom shear stress on the surf zone. *J. of Geophysical Research*, 101 (C6):14337–14348, 1996.

E. David. *Modélisation des écoulements compressibles et hypersoniques.* PhD thesis, Institut National Polytechnique de Grenoble, 1993.

R. B. Dean. Reynolds number dependences of skin friction and other bulk flow variables in two-dimensional rectangular duct flow. *Trans. ASME I : J. Fluids Engng*, 100:215–223, 1978.

R. G. Dean and R. A. Dalrymple. *Water wave mechanics for engineers and scientists.* World Scientific, 1991.

J. W. Deardorff. A numerical study of three-dimensional turbulent channel flow at large reynolds numbers. *Journal of Fluid Mechanics*, 41:453–465, 1970.

J. M. Delhaye. Jump conditions and entropy sources in two-phase systems; local instant formulation. *Int. J. Multiphase Flow*, 1:395–409, 1974.

V. Deschamps. Simulation numérique de la turbulence inhomogéne incompressible dans un écoulement de canal plan. Technical report, Office National d'Etude et de Recherches Aérospatiales, 1988.

J. C. Doering and M. A. Donelan. Acoustic measurements of the velocity field beneath shoaling and breaking waves. *Coastal Eng.*, 32:321–330, 1997.

D. G. Dommermuth, D. K. P. Yue, W. M. Lin, R. J. Rapp, E. S. Chan, and W. K. Melville. Deep-water plunging breakers : a comparison between potential theory and experiments. *Journal of Fluid Mechanics*, 189:423–442, 1988.

D. A. Drew. Mathematical modeling of two-phase flows. *Annu. Rev. Fluid Mech.*, 15: 261–291, 1983.

F. Ducros. *Simulations numériques directes et des grandes échelles de couches limites compressibles.* PhD thesis, Institut National Polytechnique de Grenoble, 1995.

F. Ducros, P. Comte, and M. Lesieur. Large-eddy simulation of transition to turbulence in a boundary layer developing spatialy over a flat plate. *Journal of Fluid Mechanics*, 326:1–36, 1996.

J. H. Duncan, H. Qiao, V. Philomin, and A. Wenz. Gentle spilling breakers: crest profile evolution. *Journal of Fluid Mechanics*, 39:191–222, 1999.

A. Favre, L. S. G. Kovasznay, R. Dumas, J. Gaviglio, and M. Coantic. *La turbulence en mécanique des fluides*. Gauthier-Villars, Bordas, Paris, 1976.

J. Fenton. A ninth-order solution for the solitary wave. *Journal of Fluid Mechanics*, 53: 257–271, 1972.

M. Fortin and R. Glowinski. *Méthodes de lagrangien augmenté. Application à la résolution numérique de problèmes aux limites*. Dunod, Paris, 1982.

J. Fredsoe and R. Deigaard. *Mechanics of coastal sediment transport*. World Scientific, 1992.

C. J. Galvin. Breaker type classification on three laboratory beaches. *J. of Geophysical Research*, 73:3651–3659, 1968.

M. Germano. The filtering approach. *Journal of Fluid Mechanics*, 238:325–336, 1992.

M. Germano, U. Piomelli, P. Moin, and W. H. Cabot. A dynamic subgrid-scale large eddy viscosity model. *Physics of Fluids*, 3(7):1760–1765, 1991.

S. Glockner. *Contribution à la modélisation de la pollution atmosphérique dans les villes*. PhD thesis, Université Bordeaux I, 2000.

K. Goda. A multistep technique with implicit difference schemes for calculating two- or three-dimensional cavity flows. *J. Comput. Phys.*, 30:76–95, 1978.

M. Greenhow. Free-surface related to breaking waves. *Journal of Fluid Mechanics*, 134: 259–275, 1983.

S. T. Grilli, R. Gilbert, P. Lubin, S. Vincent, D. Astruc, D. Legendre, M. Duval, D. Drevard, P. Fraunié, and S. Abadie. Numerical modeling and experiments for solitary wave shoaling and breaking over a sloping beach. In *Proc.* 14^{th} *Int. Offshore and Polar Engng. Conf.*, volume 3, pages 306–312, 2004.

S. T. Grilli, P. Guyenne, and F. Dias. A fully non-linear model for three-dimensional overturning waves over an arbitrary bottom. *Int. J. Numer. Meth. Fluids*, 35:829–867, 2001.

S. T. Grilli, I. A. Svendsen, and R. Subramanya. Breaking criterion and characteristics for solitary waves on plane beaches. *J. of Waterway, Port, Coastal, and Ocean Eng.*, 123(3):102–112, 1997.

R. Grimshaw. The solitary wave in water of variable depth. part 2. *Journal of Fluid Mechanics*, 46:611–622, 1971.

J.-L. Guermond. Un résultat de convergence d'ordre deux en temps pour l'approximation des équations de navier-stokes par une technique de projection incrémentale. *Modél. Math. Anal. Numér.*, 30:169–189, 1998.

S. Guignard. *Suivi d'interface de type VOF - application au déferlement des ondes de gravité d aux variations bathymétriques.* PhD thesis, Université de Toulon et du Var, 2001.

S. Guignard, R. Marcer, V. Rey, C. Kharif, and P. Fraunié. Solitary wave breaking on sloping beaches : 2-d two phase flow numerical simulation by sl-vof method. *Eur. J. Mech. B - Fluids*, 20:57–74, 2001.

I. Gustafsson. *On first and second order symmetric factorization methods for the solution of elliptic difference equations.* Chalmers University of Technology, 1978.

P. Guyenne and S. T. Grilli. Numerical study of three-dimensional overturning waves in shallow water. *Journal of Fluid Mechanics*, 20:57–74, 2003.

E. Guyon, J.-P. Hulin, and L. Petit. *Hydrodynamique physique.* EDP Sciences / CNRS Editions, 2001.

J. Happel and H. Brenner. *Low Reynolds number hydrodynamics.* Kluwer Academic Publishers, New York, 1963.

F. H. Harlow and J. E. Welsh. Numerical calculation of time dependent viscous incompressible flow with free surface. *Physics of Fluids*, 8:21–82, 1995.

D. J. Harvie and D. F. Fletcher. A new volume of fluid advection algorithm: the defined donating region scheme. *Int. J. Numer. Meth. Fluids*, 35(2):151–172, 2001.

P. D. Hieu, T. Katsutoshi, and V. T. Ca. Numerical simulation of breaking waves using a two-phase flow model. *Applied Mathematical Modelling*, 28(11):983–1005, 2004.

C. W. Hirt and B. D. Nichols. Volume of fluid (vof) methods for the dynamics of free boundaries. *J. Comput. Phys.*, 39:201–255, 1981.

A. Iafrati and E. F. Campana. A domain decomposition approach to compute wave breaking (wave breaking flows). *Int. J. Numer. Meth. Fluids*, 41:419–445, 2003.

A. Iafrati, A. Di Mascio, and E. F. Campana. A level set technique applied to unsteady free surface flows. *Int. J. Numer. Meth. Fluids*, 35:281–297, 2001.

D. Jamet and J. U. Brackbill. On the theory and computation of surface tension: the elimination of parasitic currents through energy conservation in the second gradient method. *J. Comput. Phys.*, 182:262–276, 2002.

P. C. M. Jansen. Laboratory observations of the kinematics in the aerated region of breaking waves. *Coastal Eng.*, 9:453–477, 1986.

J. Jeong, F. Hussain, W. Schoppa, and J. Kim. Coherent structures near the wall in a turbulent channel flow. *Journal of Fluid Mechanics*, 332:185–214, 1997.

J. Van Kan. A second-order accurate pressure-correction scheme for viscous incompressible flow. *SIAM J. Sci. Stat. Comput.*, 7:870–891, 1986.

I. Kataoka. Local instant formulation of two-phase flow. *Int. J. Multiphase Flow*, 12(5): 745–758, 1986.

K. Khadra. *Méthodes adaptatives de raffinement local multigrille, applications aux équations de Navier-Stokes et de l'énergie*. PhD thesis, Université Bordeaux I, 1994.

K. Khadra, P. Angot, S. Parneix, and J.-P. Caltagirone. Fictitious domain approach for numerical modelling of navier-stokes equations. *Int. J. Numer. Meth. Fluids*, 34: 651–684, 2000.

J. Kim, P. Moin, and R. Moser. Turbulence statistics in fully developed channel flow at low reynolds number. *Journal of Fluid Mechanics*, 177:133–166, 1987.

O. Kimmoun, H. Branger, and B. Zucchini. Laboratory piv measurements of wave breaking on a beach. In *Proc.* 14^{th} *Int. Offshore and Polar Engng. Conf.*, volume 3, pages 293–298, 2004.

S. J. Kline, W. C. Reynolds, F. A. Schraub, and P. W. Runstadler. The structure of turbulent boundary layers. *Journal of Fluid Mechanics*, 30:741–773, 1967.

D. J. Korteweg and G. De Vries. On the change of form of long waves advancing in a rectangular canal and on a type of a long stationary wave. *Phil. Mag.*, 39:422–443, 1895.

E. Labourasse, D. Lacanette, A. Toutant, P. Lubin, S. Vincent, O. Lebaigue, J.-P. Caltagirone, and P. Sagaut. Towards large eddy simulation of isothermal two-phase flows: governing equations and *a priori* tests. Submitted to Int. J. Multiphase Flow, 2004.

E. Lamarre and W. K. Melville. Air entrainment and dissipation in breaking waves. *Nature*, 351:469, 1991.

J.-J. Lee, J. E. Skjelbreia, and F. Raichlen. Measurements of velocities in solitary waves. *J. of Waterway, Port, Coastal, and Ocean Eng.*, WW2(108):200–218, 1982.

C. M. Lemos. *Wave breaking: A Numerical Study*, volume 71 of *Lecture Notes in Engineering*. Springer Verlag, 1992.

Y. Li and F. Raichlen. Non-breaking and breaking solitary wave run-up. *Journal of Fluid Mechanics*, 456:295–318, 2002.

D. K. Lilly. the representation of small-scale turbulence in numerical simulation experiments. In *IBM Scientific Computing Symposium on Environmental Sciences*, 1967.

D. K. Lilly. A proposed modification of the germano subgrid-scale closure method. *Physics of Fluids*, A 4(3):633–635, 1992.

C. Lin and H. H. Hwung. External and internal flow fields of plunging breakers. *Experiments in Fluids*, 12:229–237, 1992.

P. Lin and P. L.-F. Liu. A numerical study of breaking waves in the surf zone. *Journal of Fluid Mechanics*, 359:239–264, 1998a.

P. Lin and P. L.-F. Liu. Turbulence transport, vorticity dynamics, and solute mixing under plunging breaking waves in surf zone. *J. of Geophysical Research*, 103(C8): 15,677–15,694, 1998b.

P. L.-F. Liu. *Free surface tracking methods and their applications to wave hydrodynamics*, volume 5 of *Advances in Coastal and Ocean Eng.*, pages 213–240. World Scientific, 1999.

P. L.-F. Liu and Y. Cheng. A numerical study of the evolution of a solitary wave over a shelf. *Physics of Fluids*, 13(6):1660–1667, 2001.

P. L.-F. Liu, Y.-S. Cho, M. J. Briggs, U. Kanoglu, and C. E. Synolakis. Run-up of solitary waves on a circular island. *Journal of Fluid Mechanics*, 302:259–285, 1995.

M. S. Longuet-Higgins. Parametric solutions for breaking waves. *Journal of Fluid Mechanics*, 121:403–424, 1982.

M. S. Longuet-Higgins and E. D. Cokelet. The deformation of steep surface waves on water - i. a numerical method of computation. *Proc. R. Soc. Lond.*, A 350:1–26, 1976.

P. Lubin, S. Abadie, S. Vincent, and J.-P. Caltagirone. Etude du déferlement par modélisation numérique 2d et 3d. In Centre Francais du Littoral, editor, *Génie Civil - Génie Cotier 7èmes Journées Nationales*, volume 1, pages 85–92, 2002.

P. Lubin, S. Vincent, J.-P. Caltagirone, and S. Abadie. Fully three-dimensional direct simulation of a plunging breaker. *C. R. Mécanique*, 331:495–501, 2003a.

P. Lubin, S. Vincent, J.-P. Caltagirone, and S. Abadie. Fully three-dimensional direct simulation of a plunging breaker. In WIT Press, editor, *Coastal Engineering VI - Computer Modelling and Experimental Measurements of Seas and Coastal Regions*, pages 253–262, 2003b.

P. Lubin, S. Vincent, J.-P. Caltagirone, and S. Abadie. Three-dimensional direct simulation of a plunging breaker. 5th Euromech Fluid Mechanics Conference, 2003c.

P. A. Madsen and H. A. Schäffer. *A review of Boussinesq-type equations for surface gravity waves*, volume 5 of *Advances in Coastal and Ocean Eng.*, pages 1–94. World Scientific, 1999.

J. Magnaudet. Simulation d'écoulements en présence d'interfaces. Lecture Notes, École de Printemps de Mécanique des Fluides Numérique, 1997.

J. Magnaudet and I. Eame. The motion of high-reynolds-number bubbles in inhomogeneous flows. *Annu. Rev. Fluid Mech.*, 32:659–708, 2000.

J. Magnaudet, M. Rivero, and J. Fabre. Accelerated flows around a rigid sphere or a spherical bubble. *Journal of Fluid Mechanics*, 284:97–136, 1995.

J. C. Martin and W. J. Moyce. An experimental study of the collapse of liquid columns on a rigid horizontal plane. *Phys. Trans. Serie A, Path. Phys. Sci.*, 244:312–325, 1952.

T. Maxworthy. Experiments on collisions between solitary waves. *Journal of Fluid Mechanics*, 76:177–185, 1976.

J. McCowan. On the solitary wave. *Philosophy Magazine*, 32(5):45–58, 1891.

E. McCurdy. *Les carnets de Léonard de Vinci*, volume 1 and 2. Collection Tel, 1942.

W. K. Melville. The instability and breaking of deep-water waves. *Journal of Fluid Mechanics*, 115:165–185, 1982.

W. K. Melville, F. Veron, and C. J. White. The velocity field under breaking waves : coherent structures and turbulence. *Journal of Fluid Mechanics*, 454:203–233, 2002.

O. Métais and M. Lesieur. Spectral large-eddy simulation of isotropic and stably stratified turbulence. *Journal of Fluid Mechanics*, 256:157–194, 1992.

R. L. Miller. *Role of vortices in surf zone predictions : sedimentation and wave forces*, chapter 24, pages 92–114. Soc. Econ. Paleontol. Mineral. Spec. Publ., R. A. Davis and R. L. Ethington, 1976.

P. Moin and J. Kim. Numerical investigation of turbulent channel flow. *Journal of Fluid Mechanics*, 118:341–377, 1982.

E. Montreuil. *Simulations numériques pour l'aérothermique avec des modèles sous-maille*. PhD thesis, Office National d'Etude et de Recherches Aérospatiales, 2000.

K. Nadaoka, M. Hino, and Y. Koyano. Structure of the turbulent flow field under breaking waves in the surf zone. *Journal of Fluid Mechanics*, 204:359–387, 1989.

K. Nadaoka and T. Kondoh. Laboratory measurements of velocity field structure in the surf zone by ldv. *Coastal Eng. J. in Japan*, 25:125–145, 1982.

H. M. Nepf, E. A. Cowen, S. J. Kimmel, and S. G. Monismith. Longitudinal vortices beneath breaking waves. *J. of Geophysical Research*, 100 (C8):16211–16221, 1995.

A. L. New. A class of elliptical free-surface flows. *Journal of Fluid Mechanics*, 130: 219–239, 1983.

A. L. New, P. McIver, and D. H. Peregrine. Computations of overturnings waves. *Journal of Fluid Mechanics*, 150:233–251, 1985.

S. Osher and R. P. Fedkiw. Level set methods: an overview and some recent results. *J. Comp. Phys.*, 169:463–502, 2001.

S. Osher and J. A. Sethian. Fronts propagating with curvature dependent speed: algorithm based on hamilton-jacobi formulations. *J. Comp. Phys.*, 79:12–49, 1988.

S. V. Patankar. *Numerical heat transfer and fluid flow.* Hemisphere Publishing Corporation, New York, 1990.

S. Pennell. On a series expansion for the solitary wave. *Journal of Fluid Mechanics*, 179: 557–561, 1987.

S. Pennell and C. H. Su. A seventeenth-order series expansion for the solitary wave. *Journal of Fluid Mechanics*, 149:431–443, 1984.

D. H. Peregrine. The fascination of fluid mechanics. *Journal of Fluid Mechanics*, 106: 59–80, 1981.

D. H. Peregrine. Breaking waves on beaches. *Annu. Rev. Fluid Mech.*, 15:149–178, 1983.

D. H. Peregrine, E. D. Cokelet, and P. McIver. The fluid mechanics of waves approaching breaking. In *Proc.* 17^{th} *Conf. Coastal Eng.*, pages 512–528, 1980.

R. Peyret and T. D. Taylor. *Computational methods for fluid flow.* Springer Verlag, 1983.

N. Picard. *Ecoulement bidimensionnel turbulent isotherme entre deux plaques - Fiche de validation ESTET.* EDF, 1995.

U. Piomelli. Large eddy simulation: achievements and challenges. *Progress in Aerospace Sciences*, 35:335–362, 1999.

A. Quarteroni, F. Saleri, and A. Veneziani. Factorization methods for the numerical approximation of navier-stokes equations. *Comput. Methods. Appl. Mech. Engrg.*, 188: 505–526, 2000.

J.-B. Ritz and J.-P. Caltagirone. Efficient solving method for unsteady incompressible interfacial flow problems. *Int. J. Numer. Meth. Fluids*, 30:795–811, 1999.

J. S. Russel. Report on waves. Technical report, British Association Reports, 1844.

P. Sagaut. *Large Eddy Simulation for incompressible flows - An introduction.* Springer Verlag, 1998.

P. Sagaut, P. Comte, and F. Ducros. Filtered subgrid-scale models. *Physics of Fluids*, 12 (1):233–236, 2000.

P. Sagaut and R. Grohens. Discrete filters for large eddy simulation. *Int. J. Numer. Meth. Fluids*, 31:1195–1220, 1999.

P. Sagaut, E. Montreuil, and O. Labbé. Assessment of some self-adaptative sgs models for wall bounded flows. *Aerospace Science and technology*, 6:335–344, 1999.

P. Sagaut, E. Montreuil, O. Labbé, and C. Cambon. Analysis of the near-wall behaviour of some self-adaptative subgrid-scale models in finite-differenced simulations of channel flow. *Int. J. Numer. Meth. Fluids*, 40:1275–1302, 2002.

T. Sakai, T. Mizutani, H. Tanaka, and Y. Tada. Vortex formation in plunging breaker. In *Proc. ICCE*, pages 711–723, 1986.

T. Sawaragi and K. Iwata. Turbulence effect on wave deformation after breaking. *Coastal Eng. J. in Japan*, 17:39–49, 1974.

R. Scardovelli and S. Zaleski. Direct numerical simulation of free-surface and interfacial flow. *Annu. Rev. Fluid Mech.*, 31:567–603, 1999.

F. J. Seabra-Santos, D. P. Renouard, and A. M. Temperville. Numerical and experimental study of the transformation of a solitary wave over a shelf or isolated obstacle. *Journal of Fluid Mechanics*, 176:117–134, 1997.

A. Sergent. *Approche numérique d'écoulements de convection naturelle turbulente en cavité par la simulation des grandes échelles.* PhD thesis, Université de La Rochelle, 2000.

H. A. Sethian. *Level set methods.* Cambridge University Press, 1996.

S. Shin and D. Juric. Modeling three-dimensional multiphase flow using a level contour reconstruction method for front tracking without connectivity. *J. Comp. Phys.*, 180: 427–470, 2002.

D. Skyner. A comparison of numerical predictions and experimental measurements of the internal kinematics of a deep-water plunging wave. *Journal of Fluid Mechanics*, 315: 51–64, 1996.

J. Smagorinsky. General circulation experiments with the primitive equations. i : The basic experiments. *Month. Weath. Rev.*, 91(3):99–165, 1963.

D. Sous, N. Bonneton, and J. Sommeria. Turbulent vortex dipoles in a shallow water layer. *Physics of Fluids*, 16(8):2886–2898, 2004.

P. K. Stansby, A. Chegini, and T. C. D. Barnes. The initial stages of dam-break flows. *Journal of Fluid Mechanics*, 374:407–424, 1998.

M. J. F. Stive. A scale comparison of waves breaking on a beach. *Coastal Eng.*, 9:151–158, 1985.

J. J. Stoker. *Water waves: The Mathematical Theory With Applications*. John Wiley and Sons - Interscience Publishers, Inc., New York, 1957.

C. H. Su and R. M. Mirie. On head-on collision between two solitary waves. *Journal of Fluid Mechanics*, 98:509–525, 1980.

M. Sussman, P. Smereka, and S. Osher. A level set approach for computing solutions to incompressible two-phase flow. *J. Comp. Phys.*, 114:146–159, 1994.

I. A. Svendsen. Analysis of surf zone turbulence. *J. of Geophysical Research*, 92 (C5): 5115–5124, 1987.

I. A. Svendsen and U. Putrevu. *Surf-zone hydrodynamics*, volume 2 of *Advances in Coastal and Ocean Eng.*, pages 1–78. World Scientific, 1996.

C. E. Synolakis. The run-up of solitary waves. *Journal of Fluid Mechanics*, 185:523–545, 1987.

K. Takikawa, F. Yamada, and K. Matsumoto. Internal characteristics and numerical analysis of plunging breaker on a slope. *Coastal Eng.*, 31(1-4):143–161, 1997.

M. Tanaka. The stability of steep gravity waves. part 2. *Journal of Fluid Mechanics*, 156: 281–289, 1985.

M. Tanaka. The stability of solitary waves. *Physics of Fluids*, 29:650–655, 1986.

M. Tanaka, J. W. Dold, M. Lewy, and D. H. Peregrine. Instability and breaking of a solitary wave. *Journal of Fluid Mechanics*, 185:235–248, 1987.

R. Temam. Une méthode d'approximation de la solution des équations de navier-stokes. *Bull. Soc. Math. France*, 98:115–152, 1964.

H. Tennekes and J. L. Lumley. *A first course in turbulence*. MIT Press, 1972.

F. C. K. Ting and J. T. Kirby. Observation of undertow and turbulence in a laboratory surf zone. *Coastal Eng.*, 24:51–80, 1994.

F. C. K. Ting and J. T. Kirby. Dynamics of surf-zone turbulence in a strong plunging breaker. *Coastal Eng.*, 24:177–204, 1995.

F. C. K. Ting and J. T. Kirby. Dynamics of surf-zone turbulence in a spilling breaker. *Coastal Eng.*, 27:131–160, 1996.

C. D. Tomkins and R. J. Adrian. Spanwise structure and scale growth in turbulent boundary layer. *Journal of Fluid Mechanics*, 490:37–74, 2003.

M. P. Tulin and T. Waseda. Laboratory observations of wave group evolution, including breaking effects. *Journal of Fluid Mechanics*, 378:197–232, 1999.

S. O. Unverdi and G. T. Tryggvason. A front-tracking method for viscous, incompressible, multi-fluid flows. *J. Comp. Phys.*, 100:25–37, 1992.

H. Uzawa. *Iterative method for concave programming.* K. J. Arrow, L. Hurwicz and H. Uzawa, editors, Studies in linear and Nonlinear Programming, Stanford University Press, Stanford, CA, 1958.

S. Vincent. *Modélisation d'écoulements incompressibles de fluides non-miscibles.* PhD thesis, Université Bordeaux I, 1999.

S. Vincent and J.-P. Caltagirone. Efficient solving method for unsteady incompressible interfacial flow problems. *Int. J. Numer. Meth. Fluids*, 30:795–811, 1999.

S. Vincent and J.-P. Caltagirone. A one cell local multigrid method for solving unsteady incompressible multi-phase flows. *J. Comput. Phys.*, 163:172–215, 2000.

S. Vincent and J.-P. Caltagirone. Tensorial penalisation method for solving navier-stokes equations. *C. R. Acad. Sci. série IIb*, 329:607–613, 2001.

S. Vincent and J.-P. Caltagirone. Harem: A hessian approximation redistributed over an extended mesh of surface tension forces. Submitted to J. Comput. Phys., 2004.

S. Vincent, J.-P. Caltagirone, P. Lubin, and T. N. Randrianarivelo. An adaptative augmented lagrangian method for three-dimensional multi-material flows. *Computers and Fluids*, 33:1273–1289, 2004.

T. Vinje and P. Brevig. Numerical simulation of breaking waves. *J. Adv. Water Resour.*, 4:77–82, 1981.

H. A. Van Der Vorst. Bi-cgstab: a fast and smoothly converging variant of bi-cg for the solution of non-symmetric linear systems. *SIAM J. Sci. Stat. Comput.*, 13:631–644, 1992.

Y. Watanabe and H. Saeki. Three-dimensional large eddy simulation of breaking waves. *Coastal Eng. J. in Japan*, 41(2):281–301, 1999.

Y. Watanabe and H. Saeki. Velocity field after wave breaking. *Int. J. Numer. Meth. Fluids*, 39:607–637, 2002.

G. B. Whitam. *Linear and non-linear waves.* John Wiley and Sons - Interscience Publication, 1974.

T. Yasuda, H. Mutsuda, and N. Mizutani. Kinematics of overturning solitary waves and their relations to breaker types. *Coastal Eng.*, 29:317–346, 1997.

T. Yasuda, H. Mutsuda, N. Mizutani, and H. Matsuda. Relationships of plunging jet size to kinematics of breaking waves with spray and entrained air bubbles. *Coastal Eng. J. in Japan*, 41:269–280, 1999.

H. C. Yee. Upwind and symmetric shock-capturing schemes. Technical report, NASA, 1987.

D. L. Youngs. *Time-dependent multimaterial flow with large fluid distortion.* K.W. Morton and M.J. Baines, Numerical Methods for Fluid Dynamics, Academic Press, New-York, 1982.

Y. Zang, R. L. Street, and J. R. Koseff. A dynamic subgrid-scale model and its application to turbulent recirculating flows. *Physics of Fluids*, A 5(12):3186–3196, 1993.

D. Zhang and T. Sunamura. Conditions for the occurence of vortices induced by breaking waves. *Coastal Eng. J. in Japan*, 33(2):145–155, 1990.

H. Zhao and P. R. Voke. A dynamic subgrid-scale model for low-reynolds-number channel flow. *Int. J. Numer. Meth. Fluids*, 23(1):19–27, 1996.

Q. Zhao, S. Armfield, and K. Tanimoto. Numerical simulation of breaking waves by multi-scale turbulence model. *Coastal Eng.*, 51:53–80, 2004.

Q. Zhao and K. Tanimoto. Numerical simulation of breaking waves by large eddy simulation and vof method. In *Proc. of the 26th Int. Conf. Coastal Eng.*, volume 1, pages 892–905. ASCE, 1998.

J. Zhou, R. J. Adrian, S. Balachandar, and T. M. Kendall. Mechanisms for generating coherent packets of hairpin vortices in channel flow. *Journal of Fluid Mechanics*, 387: 353–396, 1999.

SIMULATION DES GRANDES ÉCHELLES DU DÉFERLEMENT PLONGEANT DES VAGUES

Résumé

Une étude tridimensionelle du déferlement plongeant des vagues est proposée sur la base de résultats obtenus par Simulation des Grandes Échelles des équations de Navier-Stokes en formulation diphasique. Après une étude bibliographique situant le problème, la première partie du travail est consacrée au développement et à la validation des méthodes numériques employées pour la résolution des équations. Dans une seconde partie de travail, l'outil numérique est exploité afin d'étudier différents problèmes bidimensionnels de propagation d'ondes solitaires. La dernière partie du travail consiste à appliquer les méthodes numériques au déferlement tridimensionnel d'ondes sinusoïdales périodiques de larges amplitudes. Une description complète du phénomène est proposée, incluant la gnration du splash-up ainsi que la dissipation de l'énergie par les différentes structures turbulentes présentes dans l'écoulement.

Mots clé : Simulation des Grandes Échelles ; Écoulement diphasique ; Ondes solitaires ; Déferlement plongeant ; Entraïnement d'air ; Splash-up ; Structures turbulentes.

LARGE EDDY SIMULATION OF PLUNGING BREAKING WAVES

Abstract

The scope of this work is to show the results obtained for simulating three-dimensional plunging breaking waves by solving the Navier-Stokes equations in air and water, coupled with a subgrid scale turbulence model (Large Eddy Simulation, LES). After a bibliographical study of the problem, the first part of the document is dedicated to the presentation and the validation of the numerical models and methods. In the next part, the numerical tool is used to treat two-dimensional configurations of solitary waves propagations. The last part of the document presents the application of the numerical methods for the complete decription of the breaking processes including overturning, splash-up and breaking induced vortex-like motion beneath the surface, by using 3D initial conditions corresponding to unstable periodic sinusoidal waves of large amplitudes in periodic domains.

Key words: Large Eddy Simulation; Two-phase flow; Solitary waves; Plunging breaking waves; Air entrainment; Splash-up; Turbulent structures.